

Growth and Thermal Decomposition of Metal-Halide
Perovskite Thin Films Analyzed by In Situ X-Ray Diffraction

Dissertation

zur Erlangung des Doktorgrades der Naturwissenschaften
(Dr. rer. nat.)

der

Naturwissenschaftlichen Fakultät II
Chemie, Physik und Mathematik

der Martin-Luther-Universität
Halle-Wittenberg

vorgelegt von

Herrn Thomas Burwig

Erstgutachter:	Prof. Dr. Roland Scheer
Zweitgutachter:	Dr. Jan Paul Pistor
Drittgutachter:	Prof. Dr. Michael Saliba
Datum der Verteidigung:	02.06.2023

0.1 Abstract

In recent years metal-halide perovskites (MHPs) have seen an ever-increasing attention in view of their potential use as optoelectronic semiconductors. They have shown promising results in implementations as solar cell absorbers, high-energy photon detectors and LEDs. Due to MHPs being a relatively new technology, there is still an abundance of open questions, especially relating to their long-term stability and how this and other properties are related to the conditions of their preparation. Most current day research on these perovskites focuses on spin-coated films, which leaves a gap in knowledge regarding the growth and characteristics of MHPs which were prepared using other methods. For this reason, this work aims to provide insights into the preparation and properties of films prepared via co-evaporation in vacuum. To prepare thin films of below $1\ \mu\text{m}$ in thickness, we used a vacuum chamber operated under high vacuum and thermally evaporated the precursor materials from two or more sources onto a glass substrate. A key element of the analytical setup used in this work is an in situ X-ray diffraction (XRD) system. Crystal phase changes during growth and decomposition can be observed in quasi-real-time as they occur and can thus be more easily attributed to a change in process parameters, for example the substrate's temperature.

Assuming the general perovskite sum formula ABX_3 , the constituents on all three positions were systematically varied to produce a series of MHPs which include MAPbI_3 , MAPbBr_3 , MAPbCl_3 , CsPbI_3 , CsPbBr_3 , CsPbCl_3 , FAPbI_3 , FAPbBr_3 , CsSnBr_3 and $\text{Cs}_2\text{AgBiBr}_6$. These MHPs were then studied with regards to a variety of aspects: their preparation via thermal co-evaporation in vacuum, the process conditions to achieve single phase films, phase segregations, their preferred crystal phases at different temperatures, their thermal stability, the kinetics of their thermal decay, their thermal expansion, influence of environmental factors and their suitability for solar energy harvesting devices. The results were published in peer reviewed scientific journals and these publications provide the framework for this cumulative thesis.

The first paper focuses on MAPbI_3 , MAPbBr_3 and MAPbCl_3 [Bu1]. The films were prepared in high vacuum via co-evaporation and subsequently exposed to a temperature ramp. In situ XRD data is presented that details the crystal phase evolution during growth, annealing and the thermally induced decay. Additionally, experiments have been conducted which show in situ XRD data on the conversion of MAPbI_3 to MAPbBr_3 and MAPbBr_3 to MAPbI_3 via the exposure of, respectively, MABr - or MAI -vapor. The data on the thermal decomposition indicates a concerning low thermal stability for all three materials in respect to the use case as photovoltaic absorber materials.

The next experiments on CsPbI_3 and CsPbBr_3 [Bu2] and $\text{Cs}_2\text{AgBiBr}_6$ [Bu3] followed the same general principle of preparation and subsequent thermal decomposition, observed by in situ XRD. The results indicate a significant increase in thermal stability for these Cs based perovskites as opposed to the MA based ones.

The work on the decomposition experiments which used a temperature ramp to decompose the samples has highlighted the following issue: Different research groups employ a vast variety of different experimental setups and thermal regimes and use different physical properties as a measure for the progress of the decomposition reaction. In consequence, their results can be very difficult to compare to one another. This has motivated an alternative approach, where data

obtained from isothermal decomposition experiments is used to determine the activation energy E , frequency factor A and reaction model of the thermal decomposition reaction. A simple first order model, a model fitting approach and, in the case of MAPbI_3 , an isoconversional method were used to calculate these values from the data gained from the isothermal experiments and the results were compared with one another and with the results of other research groups. This has been done explicitly for MAPbI_3 [Bu4] and FAPbI_3 [Bu5].

In addition to the main line of results described above, there have been experiments on $\text{Cs}_2\text{AgBiBr}_6$ solar cells, which highlight the unsuitability of this material as a photovoltaic absorber material [Bu6]. In further research, MAPbI_3 solar cells have been prepared and it was studied how the MAI induced increase in chamber pressure and the temporal offset between the start of MAI and PbI_2 evaporation correlate to their performance [Bu7].

List of Publications

- [Bu1] Paul Pistor, Thomas Burwig, Carlo Brzuska, et al. “Thermal stability and miscibility of co-evaporated methyl ammonium lead halide (MAPbX₃, X = I, Br, Cl) thin films analysed by in situ X-ray diffraction”. In: *Journal of Materials Chemistry A* (2018). DOI: 10.1039/c8ta02775g.
- [Bu2] Thomas Burwig, Wolfgang Fränzel, and Paul Pistor. “Crystal Phases and Thermal Stability of Co-evaporated CsPbX₃ (X = I, Br) Thin Films”. In: *The Journal of Physical Chemistry Letters* 9.16 (2018), pp. 4808–4813. DOI: 10.1021/acs.jpcclett.8b02059.
- [Bu3] Thomas Burwig, Maxim Guc, Victor Izquierdo-Roca, et al. “Synthesis and Crystal Structure Evolution of Co-Evaporated Cs₂AgBiBr₆ Thin Films upon Thermal Treatment”. In: *The Journal of Physical Chemistry C* (2020). DOI: 10.1021/acs.jpcc.0c02480.
- [Bu4] Thomas Burwig and Paul Pistor. “Reaction kinetics of the thermal decomposition of MAPbI₃ thin films”. In: *Physical Review Materials* 5.6 (June 2021), p. 065405. DOI: 10.1103/physrevmaterials.5.065405.
- [Bu5] Thomas Burwig, Karl Heinze, and Paul Pistor. “Thermal decomposition kinetics of FAPbI₃ thin films”. In: *Physical Review Materials* 6.6 (June 2022), p. 065404. DOI: 10.1103/physrevmaterials.6.065404.
- [Bu6] T. Burwig, K. Heinze, V. Naumann, et al. “Co-Evaporated Cs₂AgBiBr₆ Double Perovskites for Solar Cells”. In: *Proceedings of the 36th European Photovoltaic Solar Energy Conference and Exhibition* (Marseille, France). 2019, pp. 728–732. ISBN: 3-936338-60-4. DOI: 10.4229/EUPVSEC20192019-3BV.2.11. URL: <https://www.eupvsec-proceedings.com/>.
- [Bu7] Karl L. Heinze, Oleksandr Dolynchuk, Thomas Burwig, et al. “Importance of methylammonium iodide partial pressure and evaporation onset for the growth of co-evaporated methylammonium lead iodide absorbers”. In: *Scientific Reports* 11.1 (July 2021). DOI: 10.1038/s41598-021-94689-1.

Contents

0.1	Abstract	1
1	Introduction	6
2	Theory and Current State	9
2.1	Perovskites	9
2.1.1	Perovskite Crystal Structure	9
2.1.2	Properties of Perovskites	11
2.1.3	Stability	14
2.1.4	Co-Evaporated Perovskites	22
2.2	Photoactive Perovskite Devices	23
2.2.1	Perovskite Solar Cells	23
2.2.2	Other Photoactive Perovskite Devices	27
2.3	Thin Film Growth	28
2.4	Reaction Kinetics	31
2.5	Characterization Methods	36
2.5.1	X-ray Diffraction	36
2.5.2	Scanning Electron Microscopy and EDX	41
2.5.3	Other Methods	44
3	Experimental Methods	46
3.1	Experimental Setup	46
3.2	Analysis via In-Situ XRD	47
3.3	Thin Film Growth via Thermal Co-Evaporation	48
3.4	Limitations of the Analytical Setup	50
4	Main Results	54
4.1	General Notes	54
4.2	Preparation and Thermal Stability of MAPbX ₃	56
4.3	Preparation and Thermal Stability of CsPbX ₃	70
4.4	Preparation and Thermal Stability of Cs ₂ AgBiBr ₆	79
4.5	Kinetics of the Thermal Decomposition of MAPbI ₃	88
4.6	Kinetics of the Thermal Decomposition of FAPbI ₃	104

5	Additional Results	118
5.1	General Notes	118
5.2	Cs ₂ AgBiBr ₆ Solar Cells	119
5.3	Influence of MAI Onset on Growth of MAPbI ₃	126
5.4	Additional Decomposition Experiments	127
5.5	Comparison of Thermal Stabilities	128
6	Summary and Outlook	130
A	Appendix	133
A.1	Estimation of X-ray Induced Damage	133
A.2	Evaporation Temperatures for the Preparation of Various MHPs	134
A.3	XRD Results of the Additional Experiments	135
	Bibliography	156

Chapter 1

Introduction

The material class of *perovskites* is defined by its crystal structure, which has first been observed in the naturally occurring mineral CaTiO_3 . This mineral was discovered by the mineralogist GUSTAV ROSE in 1839 and he dedicated his find to LEV ALEKSEYEVICH VON PEROVSKI. In the year 2009 Kojima et al. demonstrated that metal-halide perovskites (MHPs) can be used as photo absorbers for solar cell devices. They combined TiO_2 and MAPbI_3 to produce a solar cell with a power conversion efficiency (PCE) of 3.8% [1]. From this point onward, perovskite based solar cells have seen a remarkable progress with respect to their PCEs, achieving efficiencies of up to 25.5% in the year 2021 under laboratory conditions [2]. Metal-halide perovskites can be made out of a variety of different materials, most of which are very abundant [3] and they can be synthesized via solution based processing methods, such as spin-coating and roll-to-roll printing. The latter of which allows for a very flexible, energy efficient and scalable production [4]. This, in turn, can lead to reduced cost and reduced complexity of production, resulting in a potentially much lower energy payback time (EPBT) when compared to more established solar cell technologies [5, 6, 7]. Beside their use as light harvesting materials, they have also shown promising results as high resolution, direct UV-, X-ray- and γ -detectors, showing an exceptional radiation hardness and a high radiation stopping power, owing to them containing heavy elements such as Pb, Cs, Bi and I [8, 9, 10, 11, 12, 3].

The two main challenges that currently hold back the wide scale application of perovskite solar cells are the use of lead and a low environmental stability. The detrimental effects of lead on health and the environment are well known. The European Restriction on Hazardous Substances (RoHS), which aims to restrict the wide-scale use of hazardous materials in electronic devices, explicitly allows certain potentially harmful materials in solar cells, as long as they are handled by trained professionals [13]. Nevertheless, the social acceptance of the technology might be hindered by this, as a contamination risk, however small, always remains. Nonetheless, the key question for the application of MHPs is their stability. Because MHPs can be formed from a wide variety of precursors, certain degradation pathways are more or less likely, depending on the composition. For example, many MHPs incorporate organic molecules such as methylammonium (MA), which is itself inherently prone to decomposition from a variety of environmental factors. Fully inorganic MHPs, on the other hand, cannot suffer from this specific type of degradation. There is also the open question of how the conditions and methods

employed in the preparation of an MHP influence the properties and stability of the resulting material. Most current day research focuses on spin-coating, which is difficult to scale up to an industrial magnitude, has a comparably low material efficiency and might negatively influence the resulting layer's stability [14]. Liu et al. have shown in 2013 that efficient MHP solar cells can be prepared using a planar hetero-junction architecture with a perovskite absorber layer prepared via co-evaporation in vacuum [15]. Despite of the fact that co-evaporation presents numerous advantages when compared to spin-coating, like easier scalability, better material efficiency, potentially better reproducibility and increased stability of prepared films, spin-coating has remained the dominant preparation method for laboratory research to this day. As a consequence, most of the information found on various MHPs has been collected using spin-coated films, while the side of co-evaporated MHPs has remained under-examined.

To address this issue, this work aims to provide insights into the preparation and properties of various MHP thin films prepared via co-evaporation in high vacuum. The experiments follow the general structure of first choosing an MHP to grow, then trying to prepare a single-phase film via the co-evaporation of the precursors in a high vacuum environment and then exposing the film to thermal stress. The core of the analytical setup is an in situ X-ray diffraction system that enables a time-resolved assessment of the crystal structure of the sample during the experiment. This allows for the gathering of information on the growth of the perovskite, the existence of secondary phases, the different crystal structures that are assumed by the MHP at different temperatures, the thermal expansion coefficient, the temperature of the thermal decomposition and the remaining products after the decomposition.

Taking the general perovskite sum formula of ABX_3 , this work combines a multitude of different constituents, to form perovskites with $A = MA, FA$ and Cs ; $B = Pb, Sn$ and $AgBi$; $X = I, Br$ and Cl . The first set of experiments focused on the prototypical MHP system, which is $MAPbX_3$ ($X = I, Br, Cl$). The results of these experiments have been summarized in the publication [Bu1]. When exposing $MAPbI_3$ to a temperature ramp, the sample started decomposing at roughly $120^\circ C$, which confirms a concerning lack of thermal stability of the MA-based perovskites. Since the remaining species after the decomposition was PbX_2 for all the studied $MAPbX_3$, it can be assumed that the limiting factor of the stability of these perovskites is the organic molecule MA. For the next leg of research, this MA molecule was substituted with Cs, forming $CsPbX_3$ ($X = I, Br$). This substitution resulted in a significantly increased thermal stability. The remaining material after the decomposition experiment was CsX , which is the AX component, which again suggests that the organic MA component is the main culprit leading to the low thermal stability of the $MAPbX_3$ perovskites. These findings also indicate that the respective constituent that limits the thermal stability of these compounds is the one with the lower sublimation temperature. To investigate a Pb-free MHP, $Cs_2AgBiBr_6$ was chosen as the next candidate material. Its thermal stability lies in between that of $MAbPX_3$ and $CsbPX_3$ but the results obtained from $Cs_2AgBiBr_6$ based solar cells suggest a very low photocurrent density, which might be an inherent issue with the material. Despite this, it is a promising candidate for high energy photon detectors [16, 9, 10, 11, 17]. During these experiments it was also found that the differences in experimental setups and procedures between research groups make comparisons of thermal stability experiments difficult. A more general way to characterize the thermal decomposition behavior of a material is to determine the kinetic parameters, consisting

of the activation energy E and pre-exponential factor A of the thermal decomposition reactions. These parameters have been determined for the thermal decomposition of MAPbI_3 and FAPbI_3 , which is the focus of the last two papers, which also compare a variety of approaches to determine these parameters from the data of isothermal in situ XRD decomposition experiments. In addition to the main experiments described above, thermal ramp decomposition experiments have been conducted on CsPbCl_3 , CsSnBr_3 and FAPbBr_3 , which have not yet had their results seen published. Finally, the relative thermal stabilities of all studied perovskites is discussed and compared by looking at the results of the temperature ramp experiments.

The chapter *Theory and Current State* gives information on the necessary theory concerning MHPs with regard to their stability and other properties, thin film growth and decomposition, the analytical systems that were employed in this work and the relevant theory that was used to interpret the data. The third chapter (*Experimental Methods*) gives some detail on the experimental setup and the procedure of growing and decomposing the MHPs, as well as how the resulting data was collected. The fourth chapter (*Main Results*) presents the publications which were produced in the course of these works. Each subsection contains a preliminary discussion, followed by a reprint of the publication, in turn followed by a closing discussion. The fifth chapter (*Additional Results*) shows a supplementary paper on $\text{Cs}_2\text{AgBiBr}_6$ and another paper that was co-authored by the author of this thesis, which investigates the correlation between MAI induced chamber pressure increase, MAI evaporation onset and solar cell performance. The sixth and last chapter (*Summary*) gives an overview over the results.

Chapter 2

Theory and Current State

This chapter will give a summary of the current state of knowledge on the main topics that are relevant to this thesis. First, there is an overview over perovskites in general, their properties and their potential for use in optoelectronic devices. After that, there is an outline of the theory of thin film growth, followed by a look into the characterization methods that were utilized.

2.1 Perovskites

2.1.1 Perovskite Crystal Structure

The crystal structure that defines the perovskite material class was first described by VICTOR MORITZ GOLDSCHMIDT and THOMAS FREDRIK WEIBY BARTH in 1926 in their seminal work *Die Gesetze der Krystallochemie* [18]. They indicated that the general perovskite sum formula is of the form ABX_3 . An image of such a perovskite structure is depicted in figure 2.1 **a**. In the case of *metal-halide perovskites* there is a metal like Cs or an organic ion such as methylammonium (MA) in the A-position, a metal, like Pb, in the B-position and a halide, typically one of either I, Br or Cl in the X-position. A structure that is derived from this general ABX_3 system is the so called *double perovskite* structure, as seen in figure 2.1 **b**. Double perovskites have the general sum formula $A_2B^1B^2X_6$ and their unit cell is a combination of one AB^1X_3 unit cell and one AB^2X_3 unit cell.

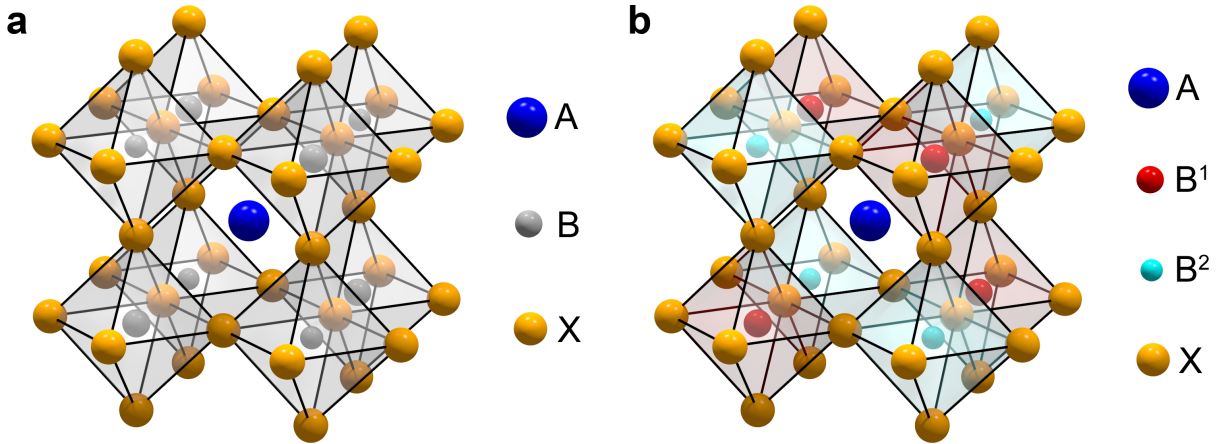


Figure 2.1: **a**: Perovskite crystal structure with the sum formula ABX₃. **b**: Double perovskite crystal structure with the sum formula A₂B¹B²X₆.

Goldschmidt et al. found that, for a stable perovskite, the ion radii r_i of the ABX₃-structure fulfill the following formula:

$$r_A + r_X = \alpha \cdot \sqrt{2}(r_B + r_X) \quad (2.1)$$

where the value of α lies between 0.8 and 1.0. According to GOLDSCHMIDT, the system will prefer the corundum structure if α is below 0.8. For an α that is above 1.0 the crystal will assume a structure like calcite and even larger values will result in an aragonite structure. This factor α came to be known as the *Goldschmidt tolerance factor* and is now usually represented by t according to the formula:

$$t = \frac{r_A + r_X}{\sqrt{2}(r_B + r_X)} \quad (2.2)$$

which is equivalent to equation 2.1. This factor is an indication for the distortion of the crystal structure in reference to a cubic one with the space group $Pm\bar{3}m$. $t = 1$ indicates an undistorted cubic structure while a $t < 1$ indicates a tetragonal ($I4/mcm$) or orthorhombic ($Pbnm$) crystal structure. Stable perovskites exist for values $0.75 < t < 1.0$ [19]. While this tolerance factor gives an easy-to-use indicator, later works have found the need to refine this concept to achieve a higher accuracy. Li et al. introduced what they termed the *octahedral factor* μ :

$$\mu = \frac{r_B}{r_X} \quad (2.3)$$

where, for stable perovskites, $0.442 < \mu < 0.895$ and $0.85 < t < 1.1$ [20]. There are several compounds that are within the perovskite range in regard to t , but most of them don't form a perovskite if their μ falls below the lower limit. Since these considerations about t and μ were done with the ternary perovskite structure of ABX₃ in mind, they are not applicable to double perovskites. Calculating a simple average over the radii of r_{B^1} and r_{B^2} might seem reasonable at first, but it is obvious that this logic would break down for very large mismatches between the two ion radii. Filip et al. tried to generalize the octahedral factor's applicability to double

perovskites by defining the average octahedral factor $\bar{\mu}$ and the octahedral mismatch $\Delta\mu$. For a double perovskite of the form $A_2B^1B^2X_6$ these factors are calculated as follows:

$$\bar{\mu} = \frac{r_{B^1} + r_{B^2}}{2r_X} \quad \Delta\mu = \frac{|r_{B^1} - r_{B^2}|}{2r_X} \quad (2.4)$$

The boundary for a stable perovskite is then defined as $\Delta\mu \leq \bar{\mu} + \sqrt{2} - 1$. They also derive a generalized tolerance factor t_g as

$$t_g = \frac{r_A/r_X + 1}{\sqrt{2(\bar{\mu} + 1)^2 + \Delta\mu^2}} \quad (2.5)$$

The condition $t_g \leq 1$ remains intact for this new tolerance factor. Filip et al. claim an accuracy of 80 % for their method, which is remarkable, considering that it is applicable to a much greater scope of perovskites than previous tolerance factors. For $B^1 = B^2$ these formulae express the case of a ternary perovskite and $\bar{\mu}$ becomes equivalent to μ and t_g becomes equivalent to t . Therefore, this approach can be seen as a direct generalization of the previous method [21].

Bartel et al. presented an approach that respects the oxidation state of the A component. They proposed a new tolerance factor τ :

$$\tau = \frac{r_X}{r_B} - n_A \left(n_A - \frac{r_A/r_B}{\ln(r_A/r_B)} \right) \quad (2.6)$$

with n_A being the oxidization state of ion A . Stable perovskites are predicted for $\tau < 4.18$. They claim an accuracy of 91 % in a test-set consisting of 1,034 perovskites, which included not only single perovskites but, remarkably, double perovskites as well. In the case of double perovskites, r_B is the arithmetic mean of the radii of the two B ions. An interesting property of this classification method is that τ is monotonically related to the probability of a given material being a perovskite, with lower values for τ implying a higher probability [22].

The most thorough method known for calculating the stability of a given combination of materials are density functional theory (DFT) calculations. These, however, tend to be mathematically complex and are very computationally expensive. In recent works, Li et al. used a machine learning approach to map the ionic radii to the probability of the components forming a perovskite crystal. They used high-throughput DFT-analysis to construct a training data set and used this set to train a neural network. They also used experimental data to further validate their results [23, 24]. In their test database of double perovskites the tolerance factor t predicted their stability correctly with an $F_1 = 77\%$ while their machine learning approach had a success rate of $F_1 = 95.9\%$. Given these promising results, further research into this topic might yield highly reliable and computationally efficient machine learning approaches for predicting which materials form perovskites.

2.1.2 Properties of Perovskites

The exceptional optoelectronic properties of perovskites are often cited as one of the main reasons for the attention they have been given in current day research. This section will give an overview over these and other properties of this material class.

Photon Absorption

One of the reasons for the attention given to MAPbI₃ in photovoltaic research is its remarkably sharp absorption onset. It is highly transparent for photons with energies below its band gap of around 1.51 eV [25] and has an absorption onset with an Urbach energy of 15 meV, reaching absorption coefficients of $3 \times 10^4 \text{ cm}^{-1}$ for photon energies of around 1.6 eV [26]. These absorption characteristics make it particularly interesting for the application as the top cell in tandem solar cells, as a high transparency for photon energies below the band gap and a sharp absorption onset limit parasitic absorption. Similar Urbach energies were found for CsPbI₃ (15.9 meV [27]) and FAPbI₃ (14 meV [28]), indicating that this characteristic is generalizable to other MHPs. Another important aspect in this regard is the adjustable band gap of perovskites. The lattice constant and thus the band gap of a mixed halide perovskite follow Vegard's law [29, 30], which means that with a mixed halide perovskite, the band gap can be adjusted to any value in between the two pure halides, as long as there is no miscibility gap that forbids the specific mixture. In a two-absorber tandem solar cell, there exists a specific optimal band gap for the top cell, which depends on the band gap of the absorber used for the bottom cell. Hence an adjustable band gap is a great benefit for such an application.

Charge Transport

Due to their nature as organic-inorganic hybrid materials, it is not by itself obvious whether an absorbed photon leads to the formation of an electron-hole pair or to the formation of an exciton. The exciton binding energy of MAPbI₃ is around 25 meV [31] to 57.21 meV [32], with a more recent calculation putting it around 18 meV [33]. In the case of the fully inorganic perovskites, an excitonic binding energy of 15 meV has been discovered for CsPbI₃ and 33 meV for CsPbBr₃ [34]. These values are in the order of magnitude of the thermal energy at room temperature of $k_B T = 26 \text{ meV}$, which means that any exciton would quickly dissociate, and the charge transport is therefore conducted via free charge carriers. Wehrenfennig et al. note that the charge carrier mobility of MAPbI₃ is remarkably high at around $10 \text{ cm V}^{-2} \text{ s}^{-1}$ [35]. Herz gives an overview of a large variety of MHPs prepared by different research groups and the mobilities that were determined. For MAPbI₃ films, the mobilities (electron-hole sum) range from $8 \text{ cm V}^{-2} \text{ s}^{-1}$ to $71 \text{ cm V}^{-2} \text{ s}^{-1}$ with many values around $30 \text{ cm V}^{-2} \text{ s}^{-1}$. The electron-hole sum mobilities for other perovskites, like FAPbI₃, FAPbBr₃ and many mixed halide and mixed cation perovskites are also within that range [36].

The intrinsic charge carrier density n_i of perovskites can vary by the exact type of MHP studied. Liu et al. compare literature values for a variety of single crystalline perovskites. They show values in the order of $1 \times 10^{10} \text{ cm}^{-3}$ to $1 \times 10^{12} \text{ cm}^{-3}$ for MAPbI₃, $5 \times 10^9 \text{ cm}^{-3}$ to $1 \times 10^{12} \text{ cm}^{-3}$ for MAPbBr₃, around $5 \times 10^9 \text{ cm}^{-3}$ for MAPbCl₃ and around $3 \times 10^9 \text{ cm}^{-3}$ for FAPbI₃ [37].

Metal-halide perovskites can exhibit very long charge carrier diffusion lengths. Using a combination of light and atmospheric treatment, Brenes et al. created a polycrystalline MAPbI₃ solar cell with a PCE of 19.2%, a charge carrier diffusion length of $72 \mu\text{m}$ (by lifetime-mobility product), charge carrier lifetimes of $32 \mu\text{s}$ and an internal luminescence quantum efficiency of 89% and a recombination velocity of 0.4 cm s^{-1} , which approaches that of fully passivated crys-

talline silicon [38].

These results show the enormous potential for metal-halide perovskite photovoltaics, but there is, as of yet, no definitive answer as to why the members of this material class exhibit these outstanding optoelectronic properties.

Defect Tolerance

Up to the present day the preferred method for the preparation of metal-halide perovskites has been spin coating, which naturally results in comparably defect-rich thin films. Solar cells with more conventional semiconductors, like GaAs, would not be operational at all with a similar defect density, while the record efficiencies of PSCs were achieved in spite of this fact [39]. This defect tolerance was also nicely demonstrated by Slavney et al. who prepared the double perovskites $\text{Cs}_2\text{AgBiBr}_6$ in thin film and in powder form and measured similar charge carrier lifetimes of around 660 ns in both cases [40]. This also shows that this defect tolerance is not a particular feature of the highly studied MAPbI_3 , but is also generalizable to other metal-halide perovskites, including fully inorganic ones. There are multiple explanations that have been put forth to explain this peculiarity:

- **Shallow defects:** Yin et al. found that the defects in MAPbI_3 which have the lowest formation energy are shallow defects close to the valence band maximum (VBM), while deep defects, close to the middle of the band gap, have a high formation energy [41]. Haruyama et al. have conducted DFT calculations and concluded that the termination of the (110), (001), (100) and (101) surface maintain the electronic structure of the bulk MAPbI_3 quite well and so reduce the amount of mid-gap states at the grain boundary [42]. Buin et al. agrees with the assessment that the surfaces of a MAPbI_3 crystal are relatively free of deep trap states. However, they note that interstitial Pb and I provide trap states close to the middle of the band gap. They found that I rich conditions promote the formation of deep defect states, which are suppressed when Cl, for example in the form of PbCl_2 , is added to the precursors. They propose that this Cl does not in itself promote large diffusion lengths, but instead leads to an I poor preparation, which reduces the probability of interstitial I [43]. Agiorgousis et al. found, based on first principle calculations, that a MAPbI_3 crystal has a notable likelihood of developing Pb dimers and I trimers, which do provide deep defects and thus centers for non-radiative recombination [44]. Overall, whether it is a low amount of deep trap states that is truly responsible for the long charge carrier lifetimes in metal-halide perovskites does not yet have a conclusive answer. It is, however, plausible that the amount of deep trap states in a particular metal-halide perovskite crystal depends significantly on the conditions of its preparation.
- **Charge neutral defect clusters:** Walsh et al. calculated the Shottky defect formation energy of MAPbI_3 (regarding MA, Pb and I vacancies) to be 0.14 eV, which results in an equilibrium vacancy concentration of 0.4% at room temperature. The Shottky defect formation energy of MAI is especially low at 0.08 eV, leading to 4% of the MA and I being vacant [45]. In spite of this, MHPs show very high charge carrier lifetimes, which they explain by the low charge and thus small interaction cross section of these defects. Additionally, the high number of vacancies leads to a high ion mobility, which allows defects

to aggregate into charge neutral clusters, which further reduce their effect on charge-carrier recombination. It follows that: “The stoichiometric hybrid perovskites can simultaneously be highly defective and electronically benign.” [45].

- **Charge carrier screening:** Since the organic MA^+ and FA^+ ions in organic-inorganic hybrid perovskites constitute rotational dipoles, they can rotate to screen the charges of electrons and holes. This screening shields the charge carriers from the surrounding lattice and increases the time of thermalization for hot charge carriers, which also increases the overall charge carrier lifetimes. Zhu et al. prepared MAPbBr_3 , FAPbBr_3 and CsPbBr_3 and observed hot fluorescence emission with a lifetime of 10×10^2 ps in the former two, but not in the latter. They also did not detect any hot fluorescence emission for orthorhombic MAPbBr_3 , where the MA^+ ions are rotationally frozen. This provides some evidence that the rotationally free dipoles of the organic-inorganic hybrid perovskites do indeed delay the thermalization of hot charge carriers [46].
- **Charge carrier separation:** Simulations conducted by Pecchia et al. demonstrate that a antiferroelectric ordering of the MA^+ dipoles in MAPbI_3 will lead to electrons and holes being lead along different pathways through the perovskite crystal, enhancing charge separation [47]. Many perovskites, like BaTiO_3 (with tetragonal crystal symmetry), are well known ferroelectrics of the displacive type and so it is plausible that MHPs might be as well. But not only do many MHPs exhibit the asymmetric crystal structures (at least at lower temperatures) that are necessary for displacive-type ferroelectricity, but the ones with an organic molecule, like MA or FA, on their A position also have a rotationally free dipole, that might allow order-disorder type ferroelectricity. Ferroelectric domains have been observed in MAPbI_3 , FAPbI_3 and $\text{MAPbI}_x\text{Br}_{3-x}$ ($0 < x < 1.5$) [48]. Interestingly, Li et al. have prepared CsPbBr_3 quantum dots that, in their orthorhombic phase, showed evidence of ferroelectricity of the displacive type due to an off center Cs^+ and a distortion of the $[\text{PbBr}_6]^{4-}$ sublattice [49].

2.1.3 Stability

The main issue that is holding back PSCs from being a viable alternative or complement to existing solar cell technologies is their lack of stability towards a number of environmental factors. These factors include, most notably, heat, moisture, oxygen and light. However, any perovskite device also consists of a variety of layers besides the perovskite, and those can also degrade or induce degradation in one another. This section gives an overview over different intrinsic and extrinsic factors that concern perovskite stability. It is of note that our experiments were conducted in a high vacuum chamber, thereby excluding potentially disruptive influences of light, oxygen and moisture during the preparation and annealing of our samples.

Intrinsic Stability

As of yet it is controversial, whether MAPbI_3 is intrinsically stable. For the reaction formula $\text{MAI} + \text{PbI}_2 \rightarrow \text{MAPbI}_3$ the reaction enthalpy of formation has been calculated to be positive by some groups and negative by others [50]. In contrast to that, the enthalpies of formation for

MAPbBr₃ and MAPbCl₃ are agreed upon to be negative [51, 52]. A positive formation enthalpy, or negative decomposition enthalpy, would imply that MAPbI₃ spontaneously separates into PbI₂ and MAI, at room temperature without any external influence. Such an intrinsic instability would be impossible to combat without changing the chemical makeup of the substance itself. The general instability of MAPbI₃, that has often been observed in experiments, might support such an intrinsic instability, however, there are many preparation methods for MAPbI₃ that work by combining MAI and PbI₂ at room temperature: Co-evaporation (with the substrate at RT), solution processing, mechanically grinding a combination of the precursor powders [53] or subjecting solid PbI₂ to MAI vapor [54]. Even the non-stoichiometric reaction of exposing PbI₂ to CH₃NH₂ vapor in the presence of water results in the formation of MAPbI₃ with additional PbO as by-product [55]. If separated MAI and PbI₂ were energetically preferred compared to MAPbI₃, the success of these methods would be unlikely. Another thing of note is that this uncertainty of intrinsic stability only applies to MAPbI₃, as MAPbBr₃ and MAPbCl₃ are predicted to be much more stable [52]. At this point, it needs to be emphasized that an assessment of the reaction enthalpy depends critically on the correct identification of the reaction's educts and products. For example, a positive reaction enthalpy of the MAI + PbI₂ → MAPbI₃ reaction does not exclude the possibility of a spontaneous decomposition of the MAI component, according to CH₃NH₃I → HI + CH₃NH₂ or CH₃NH₃I → CH₃I + NH₃. As noted by Zhang et al., no study, as of yet, has shown solid MAI as a byproduct of MAPbI₃ decomposition [52], but whether this dissociation of the MAI component occurs during or shortly after the perovskites decomposition is difficult to determine.

Ion Migration

Ion migration is another important aspect of metal-halide perovskite stability. It is likely a major factor in the current-voltage hysteresis that is often observed in perovskite solar cells and it is also the driving force behind phase separation in mixed perovskites [56]. The activation energies for ionic migration in the case of MA₂PbI₃ are 0.58 eV for I, 0.84 eV for MA and 2.31 eV for PbI₂, which are comparably low [57]. Migrating ions can potentially react with the perovskite's interface layers or the electrodes, reducing the overall lifespan of a device [52]. This ion migration is exacerbated under illumination or voltage biases, while perovskites with low defect density significantly diminish this phenomenon [52]. In the case of MAPbI₃, DFT calculations by Son et al. have indicated that it is possible for the MA molecule to rotate, which can spontaneously occur under room temperature. This rotation leaves a space where an I-ion can move in, creating a Frenkel defect and leaving behind an I-vacancy [58]. This process occurs preferably at grain boundaries. The additive KI has been shown to significantly reduce this type of ion migration, by introducing I that can fill the vacancy and a possible grain boundary passivation by the local accumulation of K [59]. The KI additive also enabled the preparation of hysteresis free solar cells [58]. Quasi-2D perovskites have also been shown to be less susceptible to all types of ion migration [52].

Heat

As solar cells can reach working temperatures of up to 85 °C [60], the stability of a material towards heat needs to be taken into account. A low stability under thermal stress is a particular challenge for solar cells, as they are operated in direct sunlight. Active cooling would reduce the overall energy efficiency. Heat spreaders would combat local heat buildup and might slightly enhance passive heat removal but would likely have a very limited effect during continuous operation. Encapsulation would not reduce the heat itself but can trap decomposition products so that they could re-react to form the perovskite again, once the device cools down over night.

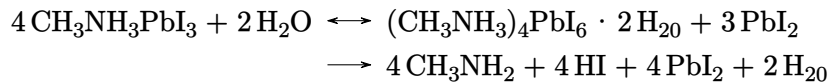
Thermal stress can also lead to mechanical stress, which can reduce the operational longevity of a PSC device. Large mismatches in the thermal expansion coefficients of the layers can lead to the worsening of contacts and delamination [61]. Another factor to consider is the thermal conductivity. Low thermal conductivity means that localized heat-ups will take longer to diminish, increasing the thermal stress on a particular area. Additionally, the resulting temperature mismatch can also lead to mechanical stress. MAPbI₃ has a very low thermal conductivity with 0.5 W K⁻¹ m⁻¹ [62].

A sustainable solution to the heat problem would ideally entail a material that is by itself more robust towards heat. It is therefore of paramount importance to understand how the different constituents of a perovskite influence its thermal stability. A more thorough overview over the current literature on the topic of the thermal stability of MHPs is found in chapter 4, where this work's results on the thermal stability of MHPs are discussed.

Moisture

One of the earliest known factors in metal-halide perovskite degradation is water. Even before these perovskites have gained attention as light harvesting materials, it was known that MAPbI₃ has a high tendency to hydrate to MAPbI₃ · H₂O when in contact with water. Freshly prepared, black MAPbI₃ will develop a gray color in ambient air due to MAPbI₃ · H₂O forming on its surface [63].

Christians et al. exposed MAPbI₃ to water vapor and concluded that a “hydrate product similar to (CH₃NH₃)₄PbI₆ · 2H₂O is formed” and that the transition to this phase decreased the absorption and changed the crystal structure of the material [64]. The existence of a hydrated intermediate phase was later confirmed by Yang et al., who propose the following reaction pathway [65]:



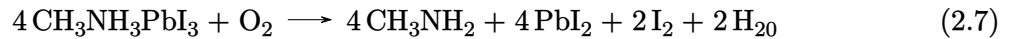
They note that the former reaction is reversible, but the strong propensity of PbI₂ to crystallize into a secondary phase makes the backwards reaction unlikely. After this first step, the CH₃NH₃ component further decomposes into the volatile products of CH₃NH₂ and HI [65]. Fang et al. conducted molecular dynamics simulations on the decomposition of the (CH₃NH₃)₄PbI₆ · 2H₂O intermediate phase. They found that the O²⁻ ion of the H₂O is attracted to the MA⁺ and that the H⁺ is attracted to the PbI₃⁻ sublattice. This traps the H₂O molecule in the perovskite lattice, between the MA⁺ and the PbI₃⁻. Then, the water molecule moves in between two I⁻

ions, guided by its two H^+ ions. In this position, the O^{2-} is pointing towards one of the two Γ^- , pushing it away, which moves it closer towards the MA^+ , where the Γ^- captures a H^+ from the MA, forming HI and leaving behind CH_3NH_2 and PbI_2 [66].

The interdiffusion of moisture can be combated by encapsulating the device or by using hydrophobic interface layers [67]. Another important factor affecting moisture stability is the grain size of the polycrystalline layer, as larger grain sizes result in a reduced surface area for water influx, thus increasing stability [68]. Given that this decomposition pathway is directly related to the MA molecule, modifications to the composition of the perovskite are likely to significantly increase its moisture stability. FA-based PSCs have already shown great increases in stability compared to their MA counterparts [69, 70]. All inorganic perovskites, such as CsPbBr_3 , show a remarkable moisture stability [71]. CsPbI_3 and FAPbI_3 do not irreversibly degrade under moist conditions, but instead they will recrystallize into a high-bandgap phase (see the section on “Phase Stability”) [72].

Oxygen

As Senocrate et al. showed, the interaction of a perovskite with oxygen seems to depend strongly on the presence of light. They exposed MAPbI_3 samples to a pure $^{18}\text{O}_2$ atmosphere for 20 h at 333 K and found a monotonic dependence of the amount of oxygen incorporated into the perovskite on the illumination intensity [73]. Conversely, Aristidou et al. showed the influx of oxygen into a perovskite under an atmosphere of 20 % O_2 and 80 % N_2 , even in complete darkness. However, the absorption of the films did not change while in the dark. Only when exposed to dry air under illumination did the absorption of the samples change measurably [74]. According to them, the degradation pathway of MAPbI_3 under O_2 atmosphere is as follows [75]:



This reaction is not thermodynamically favored and should therefore not occur spontaneously. However, photogenerated charge carriers in the MAPbI_3 can bind to the oxygen, creating a superoxide O_2^- , which is much more reactive and, as a result, it can react with the MA component of the perovskite [75]. They also found that I vacancies in the perovskites are the preferred sites for this oxygen activation to occur [74].

Light

For the usage of perovskites as light harvesting materials, it is of paramount importance to understand how light influences their stability. The interplay between light and oxygen has been explained in the previous paragraph, which concludes that, at least for MAPbI_3 , the light stability is directly related to the presence of oxygen. The response of perovskites to light is especially puzzling, given that an initial light soaking often leads to increased performance, while long term exposure can degrade a device. Tsai et al. have found that illumination led to a uniform lattice expansion in their $\text{FA}_{0.7}\text{MA}_{0.25}\text{Cs}_{0.05}\text{PbI}_3$ which relieved lattice strain and increased the PCE of the solar cell from 18.5 % to 20.5 %. They also found such an increase in PCE with MAPbI_3 based solar cells. Long term, the $\text{FA}_{0.7}\text{MA}_{0.25}\text{Cs}_{0.05}\text{PbI}_3$ based cells retained 95 % of their initial PCE after 300 min of 10 sun illumination, while the MAPbI_3 based ones,

under the same conditions, lost almost 50 % of their initial PCE after only 200 min [76]. These results provide a plausible explanation of the initial PCE increase while also demonstrating the stability benefits of mixed cation perovskites in comparison to pure MAPbI₃. Motti et al. have demonstrated, that illumination of MAPbI₃ leads to increased ion migration, which in turn results in both defect formation and annihilation as simultaneous, competing processes. High temperature and a high initial trap density favor the process of defect formation, as two I combine to form I₂, which will then concentrate on the grain boundaries, reducing the overall efficiency of the PSC. In contrast to this, if the initial defect density is low and the grain boundaries are passivated, the balance shifts in favor of defect healing [77]. This might explain the disparate results on the influence of light on perovskite absorbers. Bag et al. determined that the transport of MA⁺ ions was responsible for the observed degradation in MAPbI₃. They also found that for photodegradation to occur, both infrared and a component of visible light needed to be available, as they did not observe any degradation under white illumination and under illumination with simulated sunlight, if an IR-filter was used. FA showed a lower diffusivity and thus decreased the effects of the light induced degradation [78].

Light has been shown to be a driving force behind a phase segregation of mixed halide MAPb(I_{1-x}Br_x)₃ perovskites. Brivio et al. conducted DFT calculations that predicted a miscibility gap in the MAPb(I_{1-x}Br_x)₃ system, where there is a metastable region at 0.3 < x < 0.6. They reported that the decomposition might be slow, but light can overcome the kinetic barriers, which significantly speeds up the phase segregation [79]. Hoke et al. reported a reversible splitting of XRD peaks upon illumination [80]. The reversion to the mixed phase after 5 min in the dark contradicts Brivio et al.'s conclusion that the tendency for phase segregation inherently exists but is just very slow without light.

As stated in the section on the influence of oxygen, it is likely that for a lot of experiments done on films under ambient atmosphere, the mechanism of oxygen induced decomposition plays a significant role. However, some experiments have shown decomposition of MAPbI₃ under illumination in vacuum. Juarez-Perez et al. have shown via X-ray photoelectron spectroscopy, that MAPbI₃ thin films emitted I₂, CH₃NH₂, HI, CH₃I and NH₃ when illuminated in vacuum, even at room temperature [81]. They also noted that the degradation pathway that releases CH₃NH₂ and HI is reversible while the one that releases CH₃I and NH₃ is not.

High Energy Photons and Particles

Yang et al. investigated the radiation tolerance of solar cells with a mixed cation, mixed halide Cs_{0.05}FA_{0.81}MA_{0.14}PbI_{2.55}Br_{0.45} absorber to γ -rays and found that after an accumulated dose of 2.3 Mrad they retained 96.8 % of their initial PCE, while the covering glass showed significant darkening. Lang et al. demonstrated a MAPbI₃ solar cell that showed higher resistance to proton radiation than a commercially available c-Si photo diode [82]. According to Wei et al., perovskites have a remarkable radiation stopping power due to the fact that MHPs incorporate many heavy elements such as (from high to low atomic number) Bi (83), Pb (82), Cs (55), I (53), Sn (50), Ag (47) and Br (35) [3].

Self Healing

A peculiar observation that a lot of researchers made with MHPs, was that a device that experienced light induced performance degradation could partially or fully recover its lost efficiency when kept in the dark [83, 84]. Nie et al. demonstrated a complete self-recovery after a time below 1 min and a complete elimination of the light induced degradation, if the device was kept at 0 °C [85]. The perovskites used were $\text{MAPbI}_x\text{Cl}_{3-x}$, prepared with PbI_2 and MACl . They discuss different explanations for the origin of the degradation in light and the self-healing in the dark. They exclude intrinsic defect states as an explanation, because the timescale would be in the order of nano- to microseconds, as opposed to the hours the observed degradation effects took to manifest. The second possibility is ion migration, where they presented four markers of ion migration (reversible phase segregation of mixed halide perovskites, jV hysteresis, photo voltage changes after light-dark-cycles, external field dependent behavior) and analyzed their samples with respect to those factors. Since they did not observe any of the markers in their samples, they tentatively excluded ion migration as a plausible explanation for the observed degradation, without conclusively ruling it out. The third explanation pertains to ferroelectric domains, which, however, would also show its influence in very small timescales. They also note that the existence of ferroelectricity has not been conclusively shown for 3D MHPs. Their favored thesis for the observed degradation is the existence of photo generated polaronic states, which constitute deep trap states for the charge carriers. They note that polaron formation is prominently observed in highly ionic crystals, which MHPs are. Some MHPs also have rotationally free dipoles, which would further exacerbate this effect [85]. They also conducted Raman measurements that showed evidence of photo induced lattice distortions and noted that Gottesman et al. also observed this phenomenon [86].

Khenkin et al. used $\text{Cs}_{0.05}(\text{MA}_{0.15}\text{FA}_{0.85})_{0.95}\text{PbI}_{2.55}\text{Br}_{0.45}$ perovskites to study the phenomenon of reversible light induced degradation and found that, under illumination, the photoluminescence (PL) intensity and short circuit current density decreased, while the PL peak shifted slightly towards higher wavelengths. All of these effects were reversible and repeatable with the same samples. They excluded phase separation as a possible explanation due the low Br content of their samples and attributed them to non-radiative recombination centers that formed in the bulk of the material [87], proposing that the observed behavior could be explained by Nie's [85] or Bag's [78] findings.

Further complicating the issue, is the observation of a regeneration under illumination: Lee et al. observed a recovery of a PSC's performance after UV light induced photodegradation under 1 sun illumination [88]. Khenkin et al. identified two modes of degradation and self-recovery: A recovery in the dark after a period of illumination, observed with a $\text{Cs}_{0.05}(\text{MA}_{0.15}\text{FA}_{0.85})_{0.95}\text{PbI}_3$ absorber (referred to as type I), and a degradation of the perovskite layer in the dark with recovery under illumination, observed with a MAPbI_3 absorber (type II). Notably, the mixed cation PSC switched from type I behavior to type II behavior after 11 days [89]. In a later work they had shown that the $\text{Cs}_{0.05}(\text{MA}_{0.15}\text{FA}_{0.85})_{0.95}\text{PbI}_3$ absorbers also showed type II behavior if they were aged to 50 % of their initial PCE, where the PCE further dropped upon storage in the dark and recovered partially under illumination [87]. They put forward the following explanation for this type II behavior: The illumination leads the formation of shallow trap states close to the interface layers, which are, however, saturated by the photogenerated charge carriers during

illumination. When stored in the dark, these trap states desaturate and this leads to a charge extraction barrier. Upon further, continuous illumination the trap states saturate again and are neutralized.

Influence of Preparation Methods

It is well known by now, that the method of preparation has a significant influence of the stability of the resulting perovskite layer. Dewi et al. prepared PSCs via solution processing and via co-evaporation and stored the solar cells at 85 °C under 10 % RH. The PSCs with a co-evaporated layer dropped to 80 % of their original PCE after 3600 h while the solution processed ones dropped to 0 % of their initial PCE after only 1000 h [14]. A factor that might have a significant impact on the stability of solution processed layers are solvent residues, as many MAbPI₃ have been shown to release DMF upon decomposition [52].

Phase Stability

Some metal-halide perovskites can exist in one of two different crystal phases at room temperature. CsPbI₃ and FAPbI₃, for example, have a low band gap, black perovskite phase that is often referred to as their α phase and a yellow, high band gap δ phase. A transition from the α to the δ phase does not entail the irreversible destruction of the material, but rather a spatial reorganization of its constituents, therefore it is not a form of decomposition. However, it could limit the applicability of the material as a solar harvester just the same. In both cases, heating up the perovskite to a temperature of around 300 °C, in the case of CsPbI₃ [90], or 130 °C in the case of FAPbI₃ [91], leads to the crystal taking on the α phase. At room temperature, it will slowly (≈ 10 days for FAPbI₃ [92]) revert back to the δ phase. This process is significantly accelerated by the presence of moisture in the air, which can lead to the full conversion of a crystal in minutes [93]. This polymorphism in CsPbI₃ and FAPbI₃ arises due to the non-ideal ionic sizes of the FA⁺ and Cs⁺ ions. FA⁺ has a large ionic size, leading to a tolerance factor t slightly above 1, while Cs⁺ is small, resulting in $t \approx 0.8$ [94]. Because of this, most strategies for increasing the stability of the α phase focus on adjusting the tolerance factor by changing the composition of the crystals, usually via mixing other constituents into the A and X sites. Zheng et al. found that in FAPbI₃ there exists an inherent, anisotropic strain in the (111) plain, which drives the phase transition from the α to the δ phase. They prepared a FAPbI₃ perovskite that incorporated MABr, creating a MA_yFA_{1-y}PbI_xBr_{3-x} perovskite of unspecified stoichiometry. They found that this incorporation of MABr lead to a lattice contraction which alleviated the inherent strain and lead to a more stable α phase that showed an increased resistance towards humid air [95].

Interface layers

In 2017 Grancini et al. prepared a 10 by 10 cm² perovskite solar cell module using a 2D-3D perovskite that combined CH₃NH₃PbI₃ and (HOOC(CH₂)₄NH₃)₂PbI₄ that exhibited an efficiency of 11.2%. This module was operated in standard conditions (without controlled humidity or oxygen content of the air) for 10 000 h with no measurable loss in efficiency. A similar module

that used spiro-OMeTAD as an HTM retained 60% of its initial PCE after 300 h in Ar atmosphere. This result highlights that the interface layers do play a non-negligible role in the long-term stability of perovskite devices [96]. Khenkin et al. found that solar cells using the popular spiro-MeOTAD as the HTM have shown lowered stability under illumination compared to those using PTAA [87].

Due to the relatively low temperature stability of MHPs and the promise that MHPs enable low temperature preparation, such a preparation at low temperatures is usually preferred. However, inorganic HTLs usually show low crystallinity when prepared under low temperatures, which limits the conductivity [57]. Thus, the focus of current PSC research has been organic HTLs. These organic HTLs, however, can exhibit poor operational stability and low resistance to heat and moisture, while also being susceptible to the formation of pinholes [57]. In addition to a decomposition of the HTL itself, certain additives used in their production might also contribute to a loss in overall device longevity. Spiro-MeOTAD, for example, is often combined with additives such as 4-tert-butylpyridine (4-TBP) and acetonitrile (used as the solvent for Li-TFSI), which can corrode the perovskite [97]. Under illumination a barrier layer can form between spiro-MeOTAD and the perovskite absorbers, which limits charge collection [98].

The ETLs that are predominantly used in PSC research consist of either metal oxides, such as TiO_2 or SnO_2 , or fullerene-based compounds, such as C_{60} and PCBM. Similarly to the HTLs, the inorganic ETLs require a high temperature for the preparation of high-quality layers. In the case that the required temperature exceeds the thermal stability of the perovskite, the layer needs to be prepared prior to the perovskite itself. Under the influence of UV-light, TiO_2 can extract electrons from the I in the perovskite, which destabilizes its crystal structure [97]. Another factor is photoinduced desorption of surface-adsorbed oxygen on the TiO_2 , which induces trap states that act as recombination centers [99].

When it comes to long-term device performance, even the electrodes demand attention. Ag electrodes can corrode to AgI due to I that migrated from the perovskite through pin-holes in the HTL [100]. It is also possible for electrode material to migrate into the ETL and HTL, which can result in shunts between the layers [57].

Current Situation

As the elaborations on these different decomposition vectors show, the research field of MHPs is still very young and a lot of questions do not have a definitive answer. On the one hand, the fact that MHPs can exist in a very large variety of different compositions and allow for a multitude of different preparation methods increases these difficulties, as they can make comparisons between the results of different research groups challenging. On the other hand, this multiplicity provides many possible avenues of research, which gives hope that the challenge of stability might one day find its solution. Every research project is faced with the difficult choice of which material to focus on: They can report on the well-known-to-be-unstable MAPbI_3 , thereby creating data that is well comparable to the plentiful results of other groups on this material, but possibly sacrificing relevance, as any industrial application of pure MAPbI_3 is very unlikely at this point. Alternatively, they can focus on alternative MHPs, which might be better candidates for real world applications, but which introduce many more variables, like which constituents to choose and their stoichiometry, which will make comparisons to other groups more difficult. Ideally,

every path of research should provide results on MAPbI₃ in addition to another MHP, to achieve comparability as well as an insight into how the material modification from the MAPbI₃ to the chosen MHP affects the attributes of the resulting material.

As many of the degradation effects, like phase changes, phase segregation, light induced degradation and even the chemical decomposition of the perovskite can, under the right conditions, be fully or partially reversible, it is also evident that the peculiarities of MHPs require modifications to currently established stability testing protocols if those want to properly reflect the long-term behavior of PSC modules. During the International Summit on Organic Photovoltaic Stability (ISOS) multiple researchers, among them notable names such as Khenkin, Brunetti, Grätzel, Park, Saliba, Snaith and Stranks have come together to formulate a consensus statement for the stability testing of PSCs. Its abstract reads: “[...] Despite the great emphasis laid on stability-related investigations, publications lack consistency in experimental procedures and parameters reported. It is therefore challenging to reproduce and compare results and thereby develop a deep understanding of degradation mechanisms. [...]” [101] Notably, the proposed tests are not meant for the assessment of stability for industrial applications and cannot be “failed” or “passed”, but instead provide testing protocols for researchers to improve the comparability between the results of different research groups.

While the stability of PSCs is still the major concern for widespread application, it cannot be denied that very significant progress has been made in understanding and combating their different degradation pathways. The European Perovskite Initiative (EPKI) notes that Oxford PV has already passed some IEC accelerated stress tests with their silicon-perovskite tandem solar cells [102]. They also point to Turren-Cruz et al., who produced a Rb₅Cs₁₀FAPbI₃ solar cell using poly(methyl-methacrylate) (PMMA) as an interface between the perovskite and the HTL, and a PCBM:PMMA mixture layer at the interface to the ETL. After an initial “burn in”, where the efficiency dropped from 18.74% to 17.63%, they retained 99.4% of this latter efficiency for 1000 h. They propose that this heightened stability is due to the shielding of the perovskite by the PMMA, as their PMMA free PSCs did not achieve that same stability [103]. The 10 000 h stable (HOOC(CH₂)₄NH₃)₂PbI₄ device prepared by Grancini et al. also shows that stable perovskite solar cells are very much possible [96], even if the multitude of factors pertaining to their stability require further research.

2.1.4 Co-Evaporated Perovskites

The experiments in this work use the method of high-vacuum co-evaporation to prepare MHP thin films. With this method, multiple evaporation sources are mounted within a vacuum chamber. These sources contain the precursor powders. For example, for preparing MAPbI₃, one source would contain PbI₂ and the other MAI. When the desired vacuum level is reached, the sources will be heated, which will cause molecules of the precursors to sublime from the powder. These molecules will later reach the substrate, where they condense to combine the perovskite layer. Snaith et al. have demonstrated in 2013 that efficient solar cells can be prepared using MHP absorber layers that were prepared via thermal co-evaporation in vacuum [15]. From this point on, vacuum evaporated MHPs have seen increasing interest among perovskite researchers, but the dominant method of MHP preparation to this day is spin coating. Vaynzof notes that there exist multiple thousands of papers on the optimization of PSCs with solution processed ab-

sorbers, while fewer than one hundred cover the optimization of PSC using evaporated absorber layers [104]. They note that this imbalance is mostly because spin coating has many benefits when it comes to laboratory scale preparation of PSCs, such as generally cheap equipment, a less complicated introduction of additives and a greater ease of preparation, leading to a high sample throughput and thus more reliable statistics of the results. Because of spin coating's head start in MHP preparation, there is also a much greater existing understanding in how certain additives and other process modifications influence the resulting layer in terms of the stability and the performance of resulting PSCs [104]. However, they also point out that in 2018 the record efficiency for spin coated PSCs was 23.7% [2] and the record efficiency for evaporated PSCs was not far off, at 20.8% [105]. The current record PCE for thermally evaporated perovskite films is 21.3% and was achieved by Feng et al. using a sequential deposition process to prepare $\text{Cs}_{0.15}\text{FA}_{0.85}\text{PbI}_3$ films. The highest PCE achieved with spin coated perovskite layers is 25.5%, achieved by UNIST [2]. While there is a clear lead for spin coated perovskites, it is remarkable that evaporated perovskites could keep up so well, despite the large discrepancy in the amount of research. Additionally, PSCs with evaporated absorber have shown good scalability properties, with Li et al. achieving a PCE of 18.1% [106] with a mini module with an area of 21 cm² [106]. This scalability is also demonstrated by Feng et al., who managed to prepare a continuous, highly uniform perovskite layer with an area of 400 cm² on glass [107]. Besides making it easier to prepare large scale, uniform films, there are other advantages of the vacuum evaporation of perovskites over spin coating, like a higher material efficiency, easier control of the resulting film's thickness, omission of potentially toxic solvents, no solvent residue in the finished layers, a high vacuum environment which excludes confounding factors like oxygen and moisture, an easier preparation of high purity films and easier preparation of some fully inorganic perovskites, such as CsPbBr_3 [108, 104, 109].

2.2 Photoactive Perovskite Devices

2.2.1 Perovskite Solar Cells

History

Organic-inorganic metal-halide perovskites were first proposed as a viable photo absorber material by Kojima et al. in 2009. Their dye-sensitized solar cell (DSSC) – see figure 2.2 a – with MAPbI_3 absorber reached a PCE of 3.8% [1]. This first solar cell used mesoporous TiO_2 that was coated with perovskite, which was in turn surrounded by a liquid electrolyte that acted as the hole conductor. Improvements on this architecture made by Park et al. in 2011 resulted in a PCE of 6.5% [110]. These first perovskite solar cells had a very low stability due to the liquid HTL that could easily corrode the perovskite. Using the solid spiro-MeOTAD as an HTL, the group around Park et al. achieved a solar cell with a PCE of 9.7% with increased longevity in 2012. In the same year, Snaith et al. used an architecture in which a solid TiO_2 layer was coated with mesoporous Al_2O_3 . As an absorber they used MAPbI_2Cl and as HTL they used spiro-MeOTAD. With this meso-superstructured solar cell (MSSC), depicted in figure 2.2 b, they achieved a PCE of 10.9% [111]. In 2013, Seok et al. modified this concept by fully filling up the pores of mesoporous TiO_2 with perovskite and creating a pillar-like structure of

perovskite on top of the infused TiO_2 layer (see 2.2 c). They reached a PCE of 12% using a MAPbI_3 absorber and polytriarylamine (PTAA) as the HTL. Grätzel achieved a PCE of 15% by using this structure, where the TiO_2 was coated with perovskite using a two-step coating method [112]. Later in 2013, Snaith et al. introduced perovskite solar cells with the planar heterojunction architecture, which consists of a solid HTL atop a solid perovskite layer atop a solid ETL. Using spiro-MeOTAD as the HTL, TiO_2 as the ETL and vapor deposited $\text{MAPbI}_{3-x}\text{Cl}_x$ as the absorber, they reached a PCE of 15.4%, while they reached 8.6% with a solution processed perovskite [15]. To this day, this planar heterojunction architecture is the most common architectures that is employed in perovskite solar cell research. The current record efficiency of perovskite solar cells under laboratory conditions, as recorded by the NREL, is 25.5%, achieved by the South Korea's Ulsan National Institute of Science and Technology (UNIST) in 2021 [2].

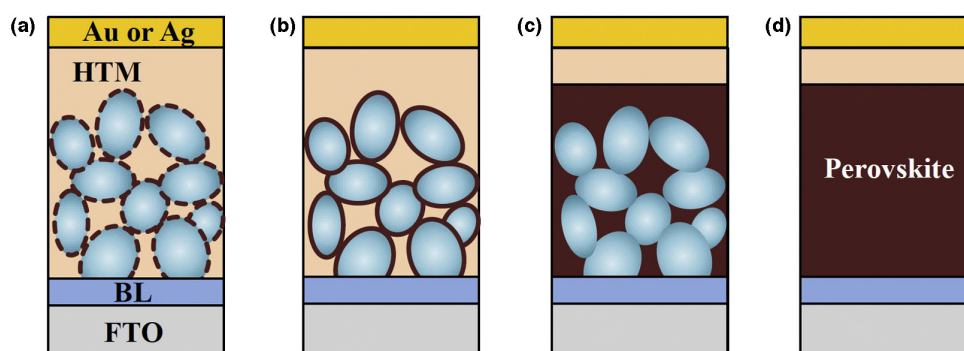


Figure 2.2: Different architectures of perovskite solar cells. **a:** Dye-Sensitized Solar Cell (DSSC); **b:** Meso-Superstructured Solar Cell (MSSC); **c:** Pillared Structure Solar Cell; **d:** Planar Heterojunction Solar Cell [113] Licensed under CC BY-NC-ND: <https://creativecommons.org/licenses/by-nc-nd/4.0/>

Current Challenges

Toxicity

To this day, the best efficiencies with perovskite solar cells (PSCs) have been achieved using Pb as the B-ion. Pb is well known to be highly toxic, as the body treats it as Ca which leads to its incorporation into various body structures, such as bone and hair, and leads to its ability to pass the blood-brain barrier. When in the brain, lead can inhibit and kill neurons, resulting in possibly severe brain damage and developmental problems in children [114]. It is for these reasons that the usage of lead in any technology should be eliminated or, at the very least, minimized. Over the years, there have been multiple attempts to substitute Pb in PSCs in favor of non-toxic alternatives. The most prominent substitute for this has been Sn, as it can exist in the same ionization state as lead (2+) and exhibits a similar ionic radius. The best PSCs achieved with Sn have, however, stayed short of the high efficiencies of their Pb based counterparts, with the highest certified PCE to date being 12.4% [115]. Additionally, the usage of Sn exacerbates the perovskites stability issue, as Sn^{2+} has a tendency to oxidize to Sn^{4+} [116].

According to Park, a typical PSC with a film thickness of around 400 nm contains roughly

0.4 g of Pb. For a given area of PSC, they calculated the equivalent depth of ground soil of the same area that would result in a volume that contained the same amount of Pb as the PSC and the result was merely 1 cm [117]. Additionally, a lot of commercial solar cells use solder that contains Pb. The amount of solder used per area of such a solar cell would contain around 50 times the amount of solder than a PSC contains Pb [117]. This means, that if the Pb content of the solder exceeds 2 %, the resulting Pb content per area of the solar cell would be larger than that of a PSC.

The toxicity of Cs is most often discussed in the context of radioactive Cs, as the body treats Cs like K and incorporates it into the body. This, of course, can have devastating effects should the substance in question be radioactive. Naturally occurring Cs, which is the Cs used for the preparation of PSCs, consists of the non-radioactive and only mildly toxic isotope ^{133}Cs . Due to its chemical similarity to K, very large quantities can lead to low blood-presence of K, cardiac arrhythmia and cardiac arrest [118]. However, studies with mice have determined a median lethal dose of CsCl of around 2.3 g per kg of body mass, which is similar to that of NaCl and, interestingly, KCl [119]. The personal and environmental risk of the Cs contained in PSCs can therefore be considered minimal.

The European Restriction on Hazardous Substances (RoHS), which aims to limit the industrial use of toxic materials, explicitly excludes solar cells, as it reads: “This Directive does not apply to [...] photovoltaic panels intended to be used in a system that is designed, assembled and installed by professionals for permanent use at a defined location to produce energy from solar light for public, commercial, industrial and residential applications.” [13] (last updated 08.07.2011, accessed 23.09.2021) All in all, while the complete omission of toxic substances, especially Pb, is not a requirement for the large scale application of PSCs, the omission of such materials would certainly still be a benefit to the overall operational security and it would also be conducive to a positive public image of such a technology.

Scalability

While the current record efficiency of PSCs is at 25.2 % for an active area of 0.09 cm^2 the current record efficiency of a module is held by Panasonic at 17.9 % for an active area of 804 cm^2 [120]. As with all solar technologies, there is a challenge in maintaining high efficiencies as the active area of a solar cell becomes larger. An additional factor for PSCs is that the dominant method for preparation, up to this point, has been spin coating, which is notoriously hard to scale up to larger substrates. Additionally, many modifications of the spin-coating method, like anti-solvent dripping, exacerbate the difficulty of upscaling. For this reason, the area of many PSCs in research has usually been around 1 cm^2 . Lee et al. have compared how the method of preparation impacts the drop in PCE as the active area increases and found that spin-coated mini modules showed the lowest efficiencies. The main reason for the loss in PCE as the area active area becomes larger is a loss in FF, that in turn is a result from the sheet resistance of the transparent conducting oxide used. Another factor is non-uniformity (pin-holes in particular), which can reduce the open-circuit voltage and become more difficult to avoid as the area of a PSC becomes larger [121].

Economics

One of the main drivers behind the interest in PSCs is their combination of low-cost precursor materials with low-temperature preparation processes, which has the potential to result in low-cost devices. Park et al. estimated a price of around US\$2 per square meter of perovskite. Given that the sheet resistance of the TCO used is the main hindrance for PSC upscaling, FTO or ITO with a very low sheet resistance would need to be used, which cost around US\$10 per square meter. Overall, the price per square meter of solar module was estimated to be around US\$40, as compared to conventional silicon solar modules with around US\$80 [117]. They also estimated the energy amortization time to be around 0.7 years, as opposed to the 3 to 5 years of crystalline silicon solar cells [122]. Due to the fact that perovskites and their precursors can be dissolved with the usage of appropriate solvents, PSCs offer the ability to be easily recycled. Multiple research groups have demonstrated the ability to fully regain the lead component of PSCs and re-create the solar cells using the reclaimed materials. Impressively, the re-created devices showed no significant loss in performance in comparison to the fresh devices, even over multiple cycles [123, 124, 125, 126]. An efficient recycling strategy tackles three issues simultaneously: They solve the problem of what to do with the toxic Pb once a solar cell has spent its life, they allow the reuse of the TCO layer, which is the presumably most expensive part of a PSC [117] and they have the potential to substantially reduce the economic consequences of a lower device lifetime.

Stability

The aspects of PSC stability are discussed in section 2.1.3.

Functional Principle of PSCs

A PSC works by the principle of a p-i-n (p-type, intrinsic, n-type) heterojunction with the perovskite as the intrinsic absorber, enclosed by charge selective layers [127]. In contrast to organic solar cells, where an absorbed photon leads to the formation of an exciton, in PSCs free charge carriers are the species responsible for charge transport, as is further explained in section 2.1.2. An idealized version of a band diagram of a p-i-n solar cell is shown in figure 2.3. In a semiconductor in ground state, the valence band (VB) is completely filled and the conduction band (CB) is completely unoccupied. If a photon is absorbed by the intrinsic layer, an electron is excited from the VB into the CB, leaving behind a “hole”, which is a quasi-particle that represents a missing electron in the otherwise quasi-fully occupied VB. The *Fermi level* ϵ_F

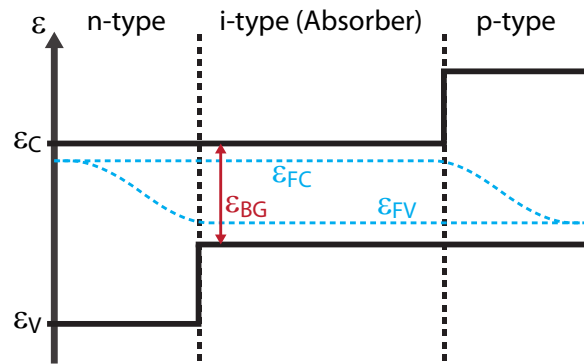


Figure 2.3: Stylized depiction of the band diagram of a p-i-n solar cell. ϵ_{BG} is the band gap of the absorber, ϵ_C is the energy level of the conduction band, ϵ_V is the energy level of the valence band and ϵ_{FC} and ϵ_{FV} are the quasi Fermi levels.

is an energy level that indicates to what degree the available electron states are occupied. States with energies far below ϵ_F are mostly filled and states with energies far above ϵ_F are mostly unfilled. A Fermi level close to the VB would indicate a lowered electron density — and therefore high hole density — in the VB and an almost unoccupied CB. Since the excitation of electron-hole pairs increases the concentration of electrons in the CB and also increases the concentration of holes in the VB, one value of ϵ_F can no longer properly describe the occupation of states of both the VB and the CB and thus two new quasi Fermi levels are introduced, ϵ_{FV} that describes the density of holes in the VB and ϵ_{FC} , that describes the amount of electrons in the CB. Shortly after the first charge carriers are generated, there is a concentration gradient of electrons in the CB, where there are many electrons in the CB of the intrinsic absorber, but none in the CBs of the adjacent layers. The situation is the same for the holes in the VB. The resulting gradient in the electrochemical potential drives a spread of the charge carriers from the absorber layer to the adjacent layers [128]. Due to its band offset in the VB, the n-type layer provides a barrier that blocks holes and lets only electrons through. Conversely, due to its energy offset in the CB, the p-type layer blocks electrons and only permits holes to pass. The result is an accumulation of electrons on the n-type side and an accumulation of holes on the p-type side, which leads to voltage between the two sides that can be calculated with respect to the two Fermi levels ϵ_{FC} and ϵ_{FV} and the elementary charge e :

$$U = \frac{\epsilon_{FC} - \epsilon_{FV}}{e} \quad (2.8)$$

2.2.2 Other Photoactive Perovskite Devices

Metal-halide perovskite first gained the attention of researchers as a potential absorber material for solar cells, but due to their interesting optoelectronic properties they also find increasing interest in fields other than photovoltaics.

LEDs

Metal-halide perovskites possess numerous characteristics that make them extremely interesting for the development of light emitting diodes (LEDs): A tunable band gap that allows for an influence over the wavelength of the emitted light, light emission that is energetically very narrow and a high photoluminescence quantum yield, that can theoretically reach up to almost 100 % [129]. While the concerns over stability and the toxicity of lead remain, they have the potential of being much cheaper and simpler to prepare than other common technologies, while also providing a superior color gamut, thanks to their very narrow emission peaks [129]. This has spurred the interest in this material class and LEDs have been prepared with metal-halide perovskite quantum dots, nanoplates, nanorods and polycrystalline films [129]. As Shan et al. point out, a low mobility of electrons and holes is a benefit for LEDs, as this reduces to chances of an electron or hole to recombine non-radiatively by encountering a defect. This lower mobility can be achieved via quantum confinement. 2D perovskites have a structure that naturally results in multiple quantum wells which makes them particularly suited for this application [129]. Huang et al. managed to prepare a red perovskite LED with an EQE of 11.7 % [130].

High Energy Photon Detectors

Since metal-halide perovskites can contain many heavy elements, such as Pb, I, Cs and Bi, they exhibit a high stopping power towards high energy photons. Together with their other favorable properties, like high defect tolerance, a large mobility-lifetime product, tunable band gap and potentially cheap preparation, this has led to an increasing attention in the field of high energy photon detectors [3]. Remarkably, metal-halide perovskites exhibit very good radiation hardness. MHPs show large linear attenuation coefficients for hard X-rays (energies of about 100 keV), which is 10 cm^{-1} in the case of MAPbI_3 and 14 cm^{-1} for CsPbI_3 which, in this regard, makes them comparable to state of the art CZT ($\text{Cd}_{1-x}\text{Zn}_x\text{Te}$) detectors [3].

2.3 Thin Film Growth

When a particle from a gaseous species hits the solid surface of a substrate, there are multiple possible outcomes, depending on the kinetic energy of the particle. If the kinetic energy is low enough, the particle might be able to give off its kinetic energy when hitting the surface and it can be adsorbed. A slightly larger energy might result in the particle bouncing off of the surface multiple times, being drawn back to it by VAN-DER-WAALS forces. The particle loses energy with each bounce, until it can eventually be fully adsorbed. If the initial kinetic energy is too large, it might not be able to give off all its energy and bounce off completely. In extreme cases, the kinetic energy can be large enough for the particle to enter the substrates surface and be absorbed instead of being adsorbed. It is also possible that particles already present on the substrate can be loosened by the impact [131].

The adsorption of a particle from a gas phase onto a solid surface can be further separated into *physisorption* and *chemisorption*. Physisorption means that the adsorbed particle attaches to the surface without engaging in a chemical bond with the solid's molecules. It will be kept in place by VAN-DER-WAALS forces and, in a process that is called *accommodation*, needs to give off its kinetic energy in some way, which is usually done by means of inducing lattice vibrations within the substrate which are then dissipated as heat. From this follows, that this process is exothermic. If the particle cannot lose its kinetic energy, it will bounce off of the surface instead of staying attached [131].

In chemisorption, the adsorbed particle forms a chemical bond with the material on the surface of the substrate. For a reaction to occur spontaneously, the Gibbs free energy $\Delta G = \Delta H - T\Delta S$ (ΔH : change in free enthalpy, T : temperature, ΔS : change in entropy) needs to be negative. Usually, the molecule that gets chemisorbed loses degrees of freedom, which means that the term $T\Delta S$ is negative. In order to offset this, ΔH needs to be negative as well, which means that the reaction is exothermic. In exceptional circumstances the translational freedom of the chemisorbed particles is greater than that of the incoming particles, in which case the process is endothermic [131].

The evaporation rate Φ_e from liquid and solid surfaces is given by Ohring et al. as [132]:

$$\Phi_e = \frac{\alpha_e N_A (p_v - p_h)}{\sqrt{2\pi m R T}} \quad (2.9)$$

where α_e is the evaporation coefficient (between 0 and 1), N_A is the Avogadro constant, p_v is the vapor pressure and p_h the hydrostatic pressure of the material, m is the mass of the evaporated molecule and T is the absolute temperature. This evaporation rate Φ_e factors into the condensation rate Φ_c [132]:

$$\Phi_c = \frac{\alpha_s \Phi_e A \cos \theta}{\sqrt{4\pi r^2}} \quad (2.10)$$

where α_s is the sticking coefficient (between 0 and 1), A is the area of the surface of the evaporating material, θ is the angle between source and substrate and r is the distance between source and substrate. Equation 2.10 is valid for a point source (with small A) or a source that is far away from the substrate.

The particles that travel from the source have a certain chance of colliding with molecules of the atmosphere that remains inside the vacuum chamber. This collision probability can be calculated by [132]:

$$f = 1 - \exp\left\{-\frac{r}{\lambda}\right\} \quad (2.11)$$

where λ is the average free path, calculated by $\lambda = 0.667 \text{ cm Pa}/p_c$, with p_c being the pressure of the chamber's atmosphere. If f is to be taken into account, it is, in effect, a scalar factor on Φ_c . For the parameters of our vacuum chamber with a base pressure of $p_c = 5 \times 10^{-2} \text{ mbar}$ and a distance $r = 30 \text{ cm}$, this collision probability is $f \approx 9\%$.

Formation of Clusters

When particles of species B get introduced into a system A , these particles can spread out equally or form clusters. To distinguish between these two cases, one can consider an existing cluster of species B with radius r and determine how the free enthalpy G changes upon the introduction of new B particles: The particles of B that are bound within the volume of the cluster are in strong interaction between one another. The removal of such a particle requires the expenditure of energy, which increases the volume free energy of the droplet, while the introduction of a new particle decreases the volume free energy. This volume free energy scales with the size of the system in a cubic relation and decreases when r is increasing ($-r^3$). On the surface, the B particles interact with the particles inside the droplet, but since there are no B particles on the outside, there is no counter action to this. This results in what is known as surface tension, which acts to draw particles towards the inside of the droplet. The introduction of new atoms increases the radius of the droplet, which means that particles will be moved outwards, which is in opposition to the surface tension. It follows that for the addition of new particles, energy needs to be expended and the

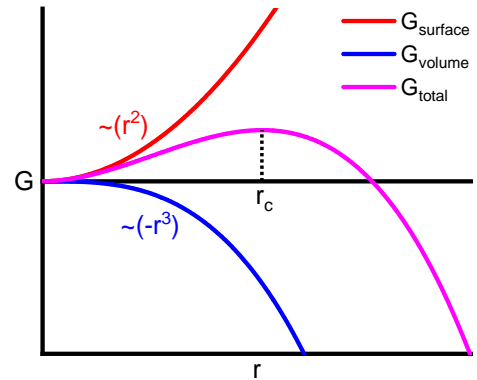


Figure 2.4: Qualitative depiction of how the surface free energy, volume free energy and total free energy of a droplet scale with its radius.

surface energy of the system increases, which is the converse case compared to the volume energy. The surface free energy scales with the size of the system squared (r^2). It follows from these deliberations, that for small values of r the surface free energy dominates and B tends to exist in the form of dispersed, singular particles. For large values of r , the volume free energy dominates, and the B particles will tend towards forming large clusters. The point of demarcation between these two states is known as the critical radius r_c . This is illustrated in figure 2.4, which shows how the surface and volume free energies scale and how they add together. Since a process will occur spontaneously when $\Delta G < 0$, for $r < r_c$ a decrease in radius is preferred, while for $r > r_c$ an increase in radius is preferred [132]. The considerations described here apply to free particle clusters without considering interactions with the environment. The next subsection will detail the relevant energies for the growth of a thin film on a substrate.

Growth Modes

When examining the formation of thin films on a substrate, one needs to take into account the contributions of the surface energies that exist between the substrate A and the growing species B : the surface energy of the substrate A itself (γ_A), the surface energy (or surface tension) of a droplet of the growing species B (γ_B) and the interface energy between A and B (γ_{AB}). γ_A acts to increase the surface wetting of B on A . This is counteracted by the interface energy γ_{AB} and the contribution of the surface tension, which depends on the wetting angle Θ and is $\Theta \cdot \gamma_B$. In equilibrium, these energies equal out and it follows that:

$$\gamma_A = \gamma_{AB} + \gamma_B \cdot \Theta \quad (2.12)$$

As a consequence of this, the wetting angle can be calculated as follows:

$$\Theta = \arccos\left(\frac{\gamma_A - \gamma_{AB}}{\gamma_B}\right) \quad (2.13)$$

Depending on the relative magnitude of the involved energies and the resulting wetting angle, one can classify thin film growth processes into different modes [133]:

- **Frank–van der Merwe Mode:** If $\Theta = 0^\circ$ ($\gamma_A = \gamma_B + \gamma_{AB}$), the growing species B will wet the substrate and will tend towards forming closed layers of species B before another layer begins growing. (This will also be the case, if $\gamma_A > \gamma_B + \gamma_{AB}$) The resulting layers will exhibit a low surface roughness.
- **Volmer–Weber Mode:** If $0^\circ < \Theta < 180^\circ$ ($\gamma_A < \gamma_B + \gamma_{AB}$), a formation of three-dimensional clusters of B is favored, compared to the formation of compact layers. Additional particles of species B that are introduced will have a higher tendency towards binding to the existing B clusters, as opposed to forming new ones. The resulting film will exhibit a high surface roughness. According to Chen et al., this is the preferred growth mode of MHPs on a conductive transparent oxide (CTO) or glass substrate. Additionally, they note that lower evaporation rates lead to larger grain sizes [134].
- **Stranski–Krastanov Mode:** In this growth mode the layer starts out growing layer-by-layer (like in the Frank–van der Merwe case) and will later, after reaching a critical

thickness, change to a growth of separate clusters (like in the Volmer–Weber case). The reasons for this can be manifold and depend on how the B -layer’s increasing thickness changes the ratios of γ_A , γ_B and γ_{AB} . Two examples that can cause this are lattice strain within B that results from epitaxial growth with a lattice mismatch between A and B , or due the fact that, for large layer thicknesses, the newly introduced B particles grow effectively on a B substrate, while the interactions with the actual substrate A become weaker.

2.4 Reaction Kinetics

A good mathematical description of how a reaction progresses can be constructed by using the following formula, that describes how the rate of a reaction $d\alpha/dt$ changes with the extent of conversion α [135]:

$$\frac{d\alpha}{dt} = A \exp\left(-\frac{E}{RT}\right) f(\alpha) \quad (2.14)$$

t is the time, R is the universal gas constant and T the absolute temperature. The activation energy E , the pre-exponential factor A and the reaction model $f(\alpha)$ are sometimes referred to together as the “kinetic triplet”. Another term that is often referenced is the rate constant k , that is calculated by:

$$k(T) = A \exp\left(-\frac{E}{RT}\right) \quad (2.15)$$

leading to a more compact form of equation 2.14:

$$\frac{d\alpha}{dt} = k(T)f(\alpha) \quad (2.16)$$

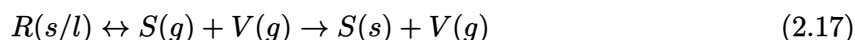
This rate constant describes how the rate of the process scales with the temperature T . The exponential part of k , that is $\exp\left(-\frac{E}{RT}\right)$, describes a Maxwell-Boltzmann distribution. In the classical gas theory of reaction kinetics, this term describes the relative fraction of collisions within a gas that occur with an energy of at least E [136]. It will always be between 0 and 1 and can also be interpreted as the “degree of activation” of the process, which is closer to 0 if the temperature, and thus the product RT , is low compared to the activation energy and it is close to 1 for very high temperatures. A collision with an energy of at least E is seen as a requirement for the reaction to occur, which is why the speed of the reaction is directly proportional to this exponential term. The base frequency of collisions, on the other hand, is expressed with the frequency factor A . This factor can also be seen as a “maximum rate constant”, since for cases were $RT \gg E$ the degree of activation will be at 1 and thus k will equal A . This illustration must be taken with the caveat that, depending on the process and the temperature range in question, A itself might have a non-negligible dependence on temperature [137, 131]. This frequency factor is also a stand-in for what can be a variety of factors that make collisions more likely or restrict the type of collision that would lead to a reaction. For example, some reactions might require the collision of specific bonds [136]. This theoretical framework works well for gases and for liquids. In the case of liquids, there are further complications arising from the low diffusivity of the reactive species (when compared to gases) and from the possibility

of solute ions bonding to solvent ions. As a consequence, these influences change the effective values for E and A , but do not invalidate the general application of the Arrhenius theory. The situation is different for reactions from the solid state.

Applicability of the Arrhenius Relation to Solid-State Decomposition Reactions

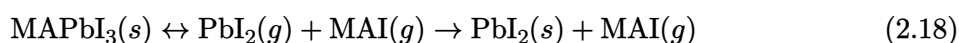
There has been some contention in the physical chemistry community over whether the assumptions of the Arrhenius model hold true for in-homogeneous, solid state reactions [138, 139, 136, 140]. Garn has pointed out, that there is no discrete activated state in solids, as any energy influx spreads out very quickly over the constituents of the material, so that no significant deviation from the average energy exists [141]. In essence, the Maxwell-Boltzmann distribution does not apply in such a case. This would contradict one of the central assumptions of the Arrhenius model and thus render it inapplicable to this class of reaction. While experiments can still be evaluated using the mathematical relations from equations 2.14 and 2.15, the obtained values for E and A would be purely empirical, without any physical significance [140]. Galwey and Brown have proposed two possible mechanisms, by which the use of the Arrhenius equation could be justified: For a reaction to occur, electronic bonds need to be redistributed. The energy levels of electrons near the reaction interface can be described similarly to the electron energy levels in crystalline solids, i.e. they can be described using Fermi-Dirac statistics: $F = \{1 + \exp[(E_e - E_f)/k_B T]\}^{-1}$. If $E_e \gg E_f$, this relation can be simplified and approximates that of the Maxwell-Boltzmann distribution. Similarly, reactions can be driven by vibrations in the reaction coordinate. Such vibrations are described by phonons, whose energetic distribution can be expressed by the Bose-Einstein statistic: $n(\omega) = \{\exp(h\omega/2\pi k_B T)\}^{-1}$. Again, if the energy $h\omega$ is large compared to $2\pi k_B T$, this approximates the Maxwell-Boltzmann distribution. The detailed derivations of these models can be found in the references [139, 138] and [136].

A different approach at resolving this issue has been chosen by L'vov, who proposed a theory of what he initially called the “physical approach” in contrast to the original, chemical justification for the use of the Arrhenius model [142]. This theory is based on the works of Hertz and Langmuir and their “[...] prediction of the proportional dependence of the evaporation rate on the equilibrium partial pressure of the vapor which, in its turn, depends exponentially on temperature” [142]. While this theory retains the validity of equation 2.15, the interpretation of the values thus obtained changes. Within this theoretical framework, the activation energy directly corresponds to the specific reaction enthalpy, thus it successfully relates the values obtained from the Arrhenius analysis to actual physical characteristics of the studied material [142]. This can be seen as a major achievement of their work, as previously the activation energy in solid state decompositions lacked any physical significance whatsoever. Of great importance within this approach is the reaction type of the congruent dissociative volatilization (CDV). This describes the dissociation of a solid (or liquid) educt R into a volatile product V and a non-volatile, stable product S , the latter of which then condenses, forming a solid [140]:



The theoretical framework developed by L'vov also allows for a physico-chemical and quantitative interpretation of, among other things, the effect of the slowing of the reaction due to gaseous

product, the Topley-Smith effect and the kinetic compensation effect [142]. Especially the latter one has often been observed, but was up to now only regarded as an “interesting observation”, but remained without an actual physical interpretation [140]. L’vov explains this effect by the buildup of gaseous product inside the reactor, which influences the values for A and E in a way that is consistent with the kinetic compensation effect [142]. The type of reaction described in equation 2.17 can easily model the typical decomposition reactions of organic-inorganic hybrid metal-halide perovskites. As can be seen in the results of this work (chapter 4), the major limiting factor of the stability of MAPbX₃ and FAPbX₃ (X = I, Br, Cl) is their respective organic molecule. Upon decomposition, the organic molecule leaves the material and leaves behind the respective lead halide as PbX₂. Therefore, the volatile species V corresponds to the organic molecule while the non-volatile one corresponds to PbX₂. Thus, equation 2.17, rewritten for MAPbI₃, would have the form (excluding any further dissociation of the MAI component):



This, of course, predicts that the PbI₂ evaporates upon decomposition and then immediately condenses into the solid phase. According to L’vov, a more direct reaction of $R(s/l) \rightarrow S(s) + V(g)$ would only give an incomplete description of the reaction: “It is difficult to imagine such a transformation of a solid reactant into solid product(s), with the different from initial spatial distribution, without any intermediate stage related to a change of its aggregate state.” [143]

Reaction Models

Beside the rate constant A and the activation energy E , there is also the reaction model $f(\alpha)$ to consider when examining the overall rate of a process. The reaction model describes how the rate of the process changes with the changing extent of conversion α . Very often, the reaction model is derived from the reaction geometry and an assumption on which part of the changing geometry (e.g. surface area, volume or a diffusing species) is the rate limiting factor of the process. Despite that, not all reaction models allow for an easy conclusion towards the underlying process. Some model fitting methods employ “order fitting”, where an n^{th} order process is described via $f(\alpha) = (1-\alpha)^n$ and a value for n is obtained. This allows for an adequate empirical description of the process, but an actual physical interpretation of the results might prove very challenging.

A selection of reaction models is shown in table 2.1. For every reaction model $f(\alpha)$ there exists an integrated form $g(\alpha)$ [135]:

$$g(\alpha) = \int_0^\alpha [f(\alpha)]^{-1} \quad (2.19)$$

This $g(\alpha)$ gives a value, that when divided by k , gives the time t at which a certain α has been reached. This can be written as [135]:

$$g(\alpha) = k \cdot t \quad (2.20)$$

Table 2.1: The selection of models that were used for the calculations presented here. This selection was taken from Khawam et al. [144], who also go into detail on how to derive these relations. $g(\alpha)$ denotes the integrated reaction model as calculated by equation 2.19.

Symbol	Model Name	$f(\alpha)$	$g(\alpha)$
F0	Zeroth Order	1	α
F1	First Order; Mampel	$1 - \alpha$	$-\ln(1 - \alpha)$
F2	Second Order	$(1 - \alpha)^2$	$(1 - \alpha)^{-1} - 1$
F3	Third Order	$(1 - \alpha)^3$	$(1/2)[(1 - \alpha)^{-2} - 1]$
R2	Contracting Area	$2(1 - \alpha)^{1/2}$	$1 - (1 - \alpha)^{1/2}$
R3	Contracting Volume	$3(1 - \alpha)^{2/3}$	$1 - (1 - \alpha)^{1/3}$
D1	1D Diffusion	$1/2\alpha^{-1}$	α^2
D2	2D Diffusion	$-1/\ln(1 - \alpha)$	$((1 - \alpha)\ln(1 - \alpha)) + \alpha$
D3	3D Diffusion	$2(1 - \alpha)^{2/3}(1 - (1 - \alpha)^{1/3})^{-1}$	$[1 - (1 - \alpha)^{1/3}]^2$
D4	Ginstling-Brounshtein	$3/[2((1 - \alpha)^{-1/3} - 1)]$	$1 - (2/3)\alpha - (1 - \alpha)^{2/3}$
P2	Power Law	$2\alpha^{1/2}$	$\alpha^{1/2}$
P3	Power Law	$3\alpha^{2/3}$	$\alpha^{1/3}$
P4	Power Law	$4\alpha^{3/4}$	$\alpha^{1/4}$
P2/3	Power Law	$2/3\alpha^{-1/2}$	$\alpha^{3/2}$
A2	Avrami-Erofeev	$2(1 - \alpha)[- \ln(1 - \alpha)]^{1/2}$	$[- \ln(1 - \alpha)]^{1/2}$
A3	Avrami-Erofeev	$3(1 - \alpha)[- \ln(1 - \alpha)]^{2/3}$	$[- \ln(1 - \alpha)]^{1/3}$
A4	Avrami-Erofeev	$4(1 - \alpha)[- \ln(1 - \alpha)]^{3/4}$	$[- \ln(1 - \alpha)]^{1/4}$
B1	Prout-Tompkins	$\alpha(1 - \alpha)$	$\ln[\alpha/(1 - \alpha)] + c$

Even if a given set of experimental data fit a model quite well, one needs to be careful when trying to deduce the physics behind the process from this. This has multiple reasons:

- There is not *one* well defined set of models to test every experiment against and so any given selection of models is somewhat arbitrary. The “correct” model, that fits the process best, might not be included in the set or might not even have been conceived of yet.
- Often a multitude of models will fit the experimental data and so the results are ambiguous. A different model will yield different values for E and A to compensate for the difference in the reaction model [135].
- A good fit of a given model to a set of experimental data constitutes a purely mathematical motivation for assuming that model. This, taken by itself, includes no physical perspective. Since there is an infinitude of mathematically possible models, it is not surprising to find a multitude that fit the data well. If the goal is a more definitive statement about which model describes the process, complementary analysis (i.e. microscopy) needs to be employed in order to lend support for the choice of a given reaction model [138].
- Some processes might exhibit a dependence of their reaction model on different experimental conditions. Changes in surrounding temperature, pressure, atmosphere and the

contaminants contained within that atmosphere can significantly influence the rate limiting subprocess of the reaction. In extreme cases, even a different reaction path might be preferred by the system.

- It is typically assumed that the value A is a constant, which only holds true for limited temperature ranges [138].
- Most approaches focus on obtaining a single value for A and E , which assumes that the reaction consists of only one reactional step. A multistep reaction ought to be described by a separate kinetic triplet for every reaction step, but, depending on the experimental setup and the reaction in question, the multistep nature of a process can very easily be overlooked [135].
- For some models, different physical descriptions can lead to the same function for $f(\alpha)$. For example: A more abstract definition of the Avrami-Erofeev model is as follows: $f(\alpha) = n(1 - \alpha)[\ln(1 - \alpha)]^{n-1/n}$, with $n = \eta + \lambda$, where η describes how the number of nuclei increases ($\eta = 0$: fixed amount of nuclei, $\eta = 1$: linear increase of the number of nuclei, etc.) and λ describes the dimensionality of the growth of these nuclei. Thus a fixed amount of nuclei ($\eta = 0$) with a three-dimensional growth ($\lambda = 3$) would result in $n = 3$, as would a linearly increasing amount of nuclei ($\eta = 1$) combined with two-dimensional growth ($\lambda = 2$) [138].

Additional complications arise, when one tries to interpret the data obtained from a single ramp experiment. To explain why, one can recall equation 2.16 from section 2.4:

$$\frac{d\alpha}{dt} = k(T)f(\alpha) \quad (2.21)$$

An isothermal experiment keeps the temperature T constant, so that only α will change over the course of the process. When conducting a temperature ramp experiment, both T and α change simultaneously, which can have a considerable impact on the reliability of the obtained data [135]. The change in the obtained values for E and A which compensate for a different model is thus particularly significant for non-isothermal experiments.

When keeping these limitations in mind, the evaluation of the kinetics of a thermal decomposition reaction can give valuable information. Irrespective of the physical interpretation of the data, the kinetic triplet allows for an extrapolation from the experimental data into other temperature ranges, thereby making comparisons between the results of different experiments easier. Having a reasonably robust theoretical foundation for such an extrapolation is especially important for solar cells, as their target “time of life” should ideally be measured in the dozens of years for typical operating temperatures. Because of this, decomposition experiments at those specific temperatures might prove unfeasible. Additionally, the kinetic triplet can be evaluated using a variety of different experimental setups. As long as the temperature can be controlled with reasonable accuracy and the measured attribute of the sample can be translated into an extent of conversion, there is the potential to evaluate the experiment in view of its reaction kinetics.

A detailed reaction kinetical analysis on the isothermal decomposition of co-evaporated MAPbI₃ thin films, using the development of XRD reflexes as the indicator for α , was conducted in reference [Bu4]. That paper also gives more detailed information into the process of obtaining a kinetic triplet from the experimental data. A similar experiment was later conducted for co-evaporated FAPbI₃ thin films [Bu5]. That investigation was complemented by an SEM analysis of a sample that was partially decomposed, to study in which way the perovskite layer decomposes and the PbI₂-product film forms.

2.5 Characterization Methods

2.5.1 X-ray Diffraction

Since its inception, X-ray analysis has become an important tool for a variety of analytical purposes. The penetrative power of X-rays is used in medicine to study the internal structure of living organisms, eliminating the need for a vivisection and their properties are also exploited in physics in a variety of analytical methods. The arguably most common use case in solid state physics and crystallography is in X-ray diffraction. Since the wavelengths of X-rays are within the order of magnitude of the interatomic distances of a typical crystal lattice, which is a few Å, the atoms of a crystal will act as a diffraction lattice on the X-rays. The resulting diffraction pattern can then be interpreted to gain information on the crystal structure.

Generation of X-rays

Any charged particle that experiences a deceleration will release radiation in the form of *Bremsstrahlung*. The energy of the released photons will be proportional to the difference in kinetic energy of the charged particle before and after the deceleration. This Bremsstrahlung is one of the main sources of naturally occurring X-ray- and γ -radiation, as decelerating charged particles can be found within ionized gases, β -decay and strong electric discharges, like lightning, which can ionize gases and lead to electrons being scattered among air molecules. To artificially create Bremsstrahlung, the two most widely used methods are: *Synchrotrons*, which keep charged particles in a circular motion, which makes them release Bremsstrahlung upon each change in direction, and *X-ray tubes*, where charged electrons are accelerated in an electric field towards an anode, where they abruptly decelerate upon impact. A voltage U_a is applied between the cathode and the anode to extract electrons from the cathode and send them to the anode. To facilitate the extraction of electrons, a heating voltage U_h is applied to the cathode. The electrons will impact onto the anode, each with a kinetic energy that is equal to 1 eV per 1 V of potential difference between cathode and anode. In this sudden deceleration, most of the electrons kinetic energy will be converted into thermal energy and only a small fraction is released in the form of X-rays.[145, p.135] The overall energy that is transferred to the anode is $W = U_a \cdot I_a$, where I_a is the current between anode and cathode. Typical values for W are in the order of magnitude of kilowatts. Because of the large amount of heat that is transferred to the anode, it needs to be continuously cooled, which is usually realized using a water-cooling system. Some setups also combine a water-cooling loop with a rotating anode, so that the impact point of the electrons is changing continuously. This need for cooling also affects the choice of anode material, as it

needs to have a sufficient heat conductivity to allow for efficient heat removal, while the melting point of the anode material must never be exceeded. The X-rays that are released directly by the decelerating electrons are usually called *white X-rays*, because their energetic spectrum spans a wide, continuous range. If the acceleration voltage U_a is large enough, the energy of the incoming electrons becomes sufficient to knock electrons out of the inner orbitals of the atoms of the anode material. If atoms exhibit such induced electron vacancies, electrons from higher orbitals will fall into these lower orbitals, filling the vacancies and releasing their surplus energy as *characteristic X-rays*. The intensity peaks that result from the transition from the 2p orbital are called the $K\alpha$ -peaks, further distinguished into $K\alpha_1$ for the higher energy transition and $K\alpha_2$ for the lower energy transition. If the originating electron is from the 3p orbital, the resulting radiation is labeled with $K\beta$. The frequency f of the photons resulting from these transitions can be calculated using Moseley's Law [146]:

$$f = f_R(N - S)^2 \left(\frac{1}{n_1^2} - \frac{1}{n_2^2} \right) \quad (2.22)$$

where f_R is the Rydberg frequency, N is the ordinal number of the atom, S is a constant that describes the shielding of the atomic nucleus by the surrounding electrons, n_1 is the quantum number of the target orbital and n_2 is the quantum number of the source orbital. Since the energies of the $K\alpha_1$ - and $K\alpha_2$ -peaks are very close together, they can sometimes appear as one peak, depending on the resolution of the detecting system. Since the wavelengths and the relative intensities of these characteristic X-rays are specific to each material, they are also an important consideration when choosing the anode material. The most commonly used materials for X-ray tube anodes are Copper (Cu), tungsten (W), molybdenum (Mo) and rhodium (Rh).

X-Ray Diffraction

The interaction of X-rays with the electron cloud that surrounds the atomic nucleus can take various forms. In Compton scattering, the photon is scattered inelastically and some of its energy is imparted onto the electron cloud. Thomson scattering, on the other hand, is the edge case whereby the photon energy is low enough so that the impulse transferred to the electron is negligible and only the photon is scattered. In Thomson scattering the incoming photon gets absorbed by the electron which then itself oscillates. This oscillating charge releases dipole radiation with the same energy as the absorbed photon.[147, p.2] The measured intensity I of a beam diffracted in such a way depends on the incident beam strength I_0 , the detector angle 2θ , the classical electron radius r_e , and the distance of the detector from the sample R according to [147, p.3]:

$$I = I_0 \frac{r_e^2}{R^2} \frac{1 + \cos 2\theta^2}{2} \text{ with} \quad (2.23)$$

The outgoing electromagnetic wave is phase shifted and attenuated compared to the incoming one. This behavior is described by the atomic form factor f [147]:

$$f = \int_{|r|=0}^{|r|=\infty} \rho(\mathbf{r}) \exp\{-i\mathbf{Q}\mathbf{r}\} d\mathbf{r} \quad (2.24)$$

where $\mathbf{Q} = \mathbf{K} - \mathbf{K}_0$ is the momentum transfer, \mathbf{r} is the position vector with $\mathbf{r} = 0$ corresponding to the center of the atomic nucleus and $\rho(\mathbf{r})$ is the electron density at position \mathbf{r} . The resulting f is complex-valued, where the real part indicates the phase shift of the outgoing wave while the imaginary part corresponds to its attenuation.

When a beam of X-rays hits a solid object, the electrons scatter the photons of the beam in the described way. In the case of an amorphous substance, the scattered X-rays are not coherent and do not interfere constructively. If the substance is a crystal, i.e. a periodic lattice of atoms, the scattered photons exhibit a path difference and therefore a phase shift, that depends on the distance between the lattice points a , the wavelength of the photons λ and their exit angle ϕ . If the path difference is an integer multiple of the wavelength λ , the photons interfere constructively, increasing the X-ray intensity in this direction. In the case of a path difference that is an integer multiple of half the wavelength, but not an integer multiple of the full wavelength, the outgoing photons interfere destructively, and the X-ray intensity is extinguished for this direction. For all other directions, the beam intensity is between the two extremes. Due to the large number of photons that exist within a typical X-ray beam, the beam components that do not interfere constructively are almost completely eliminated, leaving only the ones that interfere constructively.[145, p.136] In the case of a one-dimensional diffraction lattice with lattice parameter a , the condition for this constructive interference can be expressed as:

$$n\lambda = a \sin \phi \quad (2.25)$$

where n is an integer that denotes the order of diffraction. $n = 0$ corresponds to the incident beam at $\phi = 0$. For a three-dimensional crystal this condition must be fulfilled for all three spatial directions at once, which leads to the Laue-equations [145, p.138]:

$$\begin{aligned} n\lambda &= a_1 \sin \phi_1 \\ n\lambda &= a_2 \sin \phi_2 \\ n\lambda &= a_3 \sin \phi_3 \end{aligned}$$

A simplified model that was introduced by Bragg treats the crystal as a periodic structure of atomic layers, where the distance d from one layer to the next is equal to the lattice constant a . Here, a beam with the incoming angle θ is reflected back with the same outgoing angle on every layer. The path difference of the beams reflected off of two adjacent layers is $2d \sin \theta$ and if this path difference equals $n\lambda$, constructive interference occurs. This condition is known as Bragg's law [145, p.139]:

$$n\lambda = 2d \sin \theta \quad (2.26)$$

In a simple cubic lattice, the distance of the lattice plains in a specific direction given by the Miller indices (hkl) is:

$$d = a / (h^2 + k^2 + l^2)^{1/2} \quad (2.27)$$

Additionally, the diffraction order n is often incorporated as a factor to the Miller indices, because the n^{th} order diffraction on a lattice plain (hkl) is equivalent to a reflection on the $(nh \ nk \ nl)$ plain. The version of Bragg's law that results from these considerations is:

$$\sin \theta = \frac{\lambda \sqrt{h^2 + k^2 + l^2}}{2a} \quad (2.28)$$

Structure Factor

The diffracted beams intensity depends to a large part on the structure factor of the studied material. This structure factor F can be calculated for a set of miller indices (hkl) using the formula [147, p.19]:

$$F(hkl) = \sum_{n=1}^N f_n \exp\{[2\pi i(hx_n + ky_n + lz_n)]\} \quad (2.29)$$

n iterates over the N atoms of the unit cell, f_n are the atomic scattering factors of the atoms and the coordinates x , y , and z refer to the atoms position within the unit cell. The intensity of the scattered beam I is proportional to F^2 .

Collection of an XRD Pattern

Depending on the type of sample and the desired information, there are multiple ways to acquire XRD data. Some notable examples are listed here:

- **Laue Method / Debye-Scherrer Method:** Here, a single crystalline sample (Laue method) or powder sample (Debye-Scherrer method) is placed between an X-ray source and a photo plate, which acts as the detector. In the case of a single crystalline sample, multiple dots will appear on the photo plate which correspond to the lattice planes which fulfill the Laue condition. If a powder sample is used, instead of discrete dots, rings will be visible, because a powder contains a large amount of randomly oriented grains.
- **θ - 2θ Scans:** Here, the X-ray source and a point detector are placed on goniometer arms, so that they both point to the same point on the surface of the sample from opposite directions, but under the same angle θ to the sample plane. The angle between the incident and outgoing beam is $2 \cdot \theta$. This geometry is also referred to as the Bragg-Brentano geometry. To analyze the sample, it is scanned by continually changing the angle of source and detector, but keeping the condition of $\theta_{\text{source}} = \theta_{\text{detector}}$.
- **GIXD:** Grazing incidence X-ray diffraction (GIXD) is usually used in combination with a 2-dimensional detector, and it provides information about the texture (preferential orientation of the grains) of a sample. The low incidence angle leads to a large interaction volume of the X-rays with the sample, which makes this method suitable for very thin samples, samples with low X-ray reflectivity and for samples that are prone to be damaged by the X-rays, such as those that consist of organic compounds.
- **Fixed Angles with 1D-Detector:** The setup used for the work in this thesis uses a fixed source-sample-detector geometry over the course of the experiment. A 1D-detector is used to capture and angular range of the exiting x-rays. The θ - 2θ condition is valid only for the middle of the 1D-detector.

Peak Shape

The idealized X-ray peak shape is a δ function, which describes an infinitesimally thin and infinitely high peak whose area corresponds to the diffracted intensity. In any real measurement however, there are several factors that lead to a broadening of the peaks. The two most commonly used definitions of peak width are: 1) the full-width-half-maximum (FWHM), which is the width of the peak at the point of half its maximum, and 2) the integral peak width, which is the width of a rectangle that has the same area and the same height as the peak. Another important attribute of a peak is its asymmetry. In order to mathematically define the peaks of an XRD pattern, one can fit a peak function onto them. The most commonly used ones are the Gaussian function (2.30) and the Lorentzian function (2.31):

$$I_G(2\theta) = I_{\max} \exp\left\{-\pi \cdot (2\theta - 2\theta_0)^2 / \beta^2\right\} \quad (2.30)$$

$$I_L(2\theta) = I_{\max} w^2 / [w^2 + (2\theta - 2\theta_0)^2] \quad (2.31)$$

Here, $2\theta_0$ is the position of the peak maximum, I_{\max} is the intensity at the peaks maximum, β is the integral breadth and w is half of the FWHM. There are also combinations like the Pseudo Voigt function, that mix these two peak shapes:

$$I_{PS}(2\theta) = I_{\max} [\eta L + (1 - \eta)G] \quad (2.32)$$

η is the Lorentz fraction with $0 < \eta < 1$, L is a Lorentzian peak and G is a Gaussian peak. Additionally, to describe an asymmetric peak, a split function can be used, that uses two separate peak shape definitions, one for $2\theta < 2\theta_0$ and one for $2\theta > 2\theta_0$. The following will give an overview over the main physical factors that influence a peaks appearance:

- **Instrument Function:** The overall XRD peak shape can be described as a convolution of the above mentioned delta function with the so called *instrument function*. This function determines how the instrumental setup itself leads to a broadening of the peaks and it is influenced mainly by the energetic dispersion of the incident beam and the geometry of the setup.
- **Crystallite Size:** The idealized model for X-ray diffraction on a crystal usually assumes a single crystal of infinite extent. Real crystals however, have a finite size and a polycrystalline sample is composed of multiple smaller crystallites. Every grain boundary is a deviation from the idealized lattice and is a break in the crystals symmetry. The smaller these grains are, the more such grain boundaries exist and the broader the XRD peaks will be. The Scherrer equation relates the width of a peak B at the angle θ to the grain size via $B = \frac{K\lambda}{L \cos \theta}$. L is the crystallite size and K is the Scherrer constant, which depends on

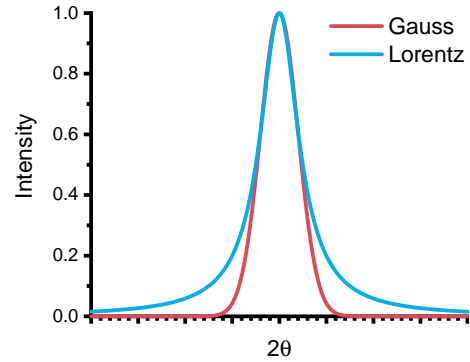


Figure 2.5: Example for peaks with $I_{\max} = 1$ in Gaussian shape ($\beta = 1$) and Lorentzian shape ($w = 0.5$).

the shape of the grains, the miller indices that correspond to the peak and also the chosen definition of peak width [148].

- **Lattice Strain:** If a lattice is homogeneously strained, this will simply lead to a change in the effective lattice constant and in turn to a shift of the positions of the XRD peaks. With inhomogeneous strain, however, there is a continuous shift from the unstrained lattice constant to the strained one, which leads to a continuous angular dispersion of the XRD reflexes and, therefore, to a broadening of the observed peaks. Inhomogeneous crystal strain can be the result of defects (vacancies, interstitial atoms, doping with foreign atoms), inhomogeneous temperature distribution (leading to inhomogeneous lattice expansion) or crystalline interface layers, which can induce epitaxial stress. The peak width B that results from lattice strain can be calculated via $B = C\epsilon \tan \theta$, where C is the strain factor and ϵ is the crystal strain [147].

2.5.2 Scanning Electron Microscopy and EDX

Microscopy is used to analyze small structures whose dimensions are far too small to be observed by the naked eye. Classical optical microscopes usually work by focusing a beam of white light onto a sample. As the photons of the beam pass through the sample, they will be either absorbed, transmitted or reflected. The absorbance, reflectance and transmittance of the sample at a specific point will depend on the material, the thickness and it is also wavelength specific. In this way, the sample – in a sense – “imprints” information onto the beam and when the beam later hits a spatially resolved detector, like a human eye or a camera sensor, the information can be interpreted. The focusing of the light is achieved via optical lenses. The relevant attribute of such a lens is its *focal length* f . The focal length defines a plane that is parallel to the plane of the lens, a distance equal to f away. Parallel light rays that hit the lens will be focused onto a point on its focal plane and light rays that originate from the focal plane will be transferred into parallel rays.

According to ERNST ABBE, the smallest distance d that can be resolved by an optical system is given by

$$d = \frac{0.61\lambda}{A_N} \quad (2.33)$$

where A_N is the *numeric aperture* of the optic system, that is calculated via

$$A_N = n \cdot \sin \alpha \quad (2.34)$$

where α is half the opening angle of the beam and n is the refractive index of the material between the objective and the focal point. The wavelengths of visible light range from 780 nm down to 380 nm. If the material between the objective and the sample is air or vacuum then $n \approx 1$. With the theoretically maximum half opening angle of $\alpha = 90^\circ$ we get $A_N \approx 1$ and thus $d \approx \lambda$. This already shows the limits of working with visible light, since structures beyond 380 nm would not be resolvable. The wavelength of a photon is given by

$$\lambda = \frac{h \cdot c}{E} \quad (2.35)$$

where h is the Planck constant, c is the speed of light and E is the energy of the photon. Increasing the energy of the photon would decrease the wavelength and thus increase the potential resolution, but this might create other issues: Consider the $K\alpha$ wavelength of a copper source, which is around $1.54 \text{ \AA} = 154 \text{ pm}$. Photons of this wavelength will have a high propensity for being transmitted through the sample without interacting. This issue would be especially noticeable with samples that are thin or consist of light elements.

To realistically achieve better resolutions, one can use particle beams, like ones made of electrons. The wavelength of a particle is called its DE-BROGLIE wavelength and is defined as:

$$\lambda = \frac{h}{p} \quad (2.36)$$

where p is the relativistic impulse of the particle. An electron under an acceleration voltage of just 1 keV has a wavelength of around 39 pm, which would result in a much finer resolution than what would be realistically achievable with high-energy photons and, by their very nature, particle beams have a much higher tendency to interact with the matter that they come into contact with.

To change the direction of an electron beam, one can use capacitor plates. To focus and defocus, a *magnetic lens* is required. When current is applied to such a system, it creates a rotationally symmetric magnetic field, which influences the electron beam in a way that can be mathematically described as analogous to an optical lens with a given focal distance. This focal distance can then be varied by changing the current that is applied to the magnetic lens.

When the electron beam hits the sample, a pear-shaped area, the so-called interaction volume, will be excited by the beam. This excitation results in a multitude of different types of radiation that can be detected, given the proper detector setup. These include:

- Secondary electrons
- Backscattered electrons
- Transmitted electrons
- Auger electrons
- Bremsstrahlung
- Characteristic radiation

The most significant ones for our analysis are the secondary electrons for the morphological SEM-analysis and the characteristic radiation for energy-dispersive X-ray spectroscopy (EDX).

Secondary Electrons (SE)

When the electron beam interacts with the sample, it creates a pear-shaped interaction volume in the sample within which the atoms get partially ionized, creating secondary electrons (SE). Because these electrons have a low kinetic energy, only the ones that are generated near the surface can escape the sample. The amount of escaping electrons also depends on the slope of

the sample: If the pear shaped interaction volume is in contact with a sloped surface, a larger portion of it is close to the surface than when a horizontal surface is hit. This results in the images having a good topographical contrast. To collect the freed electrons, the SE detector has an electrode that can be positively charged. SE-images also show a slight material contrast, since the number of freed electrons directly depends on the kind of atoms that the material consists of. Materials with a higher electron density lead to a stronger signal. Additionally, a material with a lower work function will more easily give off electrons, also increasing the signal strength. Modern SEM systems most commonly employ so called Everhart–Thornly (ET) detectors, which are mounted on the side of the specimen chamber, and In-Lens (IL) detectors, which are mounted, slightly off-center, in the beam column. According to Griffin et al., there are four main types of secondary electrons that an SE detector detects: SE generated from the previously described interaction of the beam with the sample (SE1), SE generated by high energy back scattered electrons interacting with the sample (SE2), SE generated by back scattered electrons that collide with chamber and column components (SE3) and SE generated by the primary beam interacting with the beam aperture (SE4). Only the latter type (SE4) provides no information on the sample. The signal of ET type SE detectors is dominated by SE2 and SE3, the signal of an IL detector is dominated by SE1. This results in a better material contrast of the IL detectors [149]. Due to the ET detector being positioned at a non-parallel angle to the samples normal, the electrons that are generated on surfaces that face the detector have a higher chance to be detected, compared to electrons originating from surfaces that face away from the detector. This results in detector-facing surfaces to appear slightly brighter, enhancing the topographical contrast. An IL detector, on the other hand, is located effectively above the sample and the SE are guided to it by the same magnetic fields that guided the electron beam. Therefore, the incoming electrons do not convey as much information on the samples topography [150].

Characteristic radiation (for use in energy-dispersive X-ray spectroscopy)

Energy-dispersive X-ray spectroscopy (EDX or EDS) has its primary purpose in providing an insight into the chemical composition of a specimen. As described in section 2.5.1, when a particle or photon beam of a high enough energy hits an atom, it can dislocate one of the electrons from a core energy level. An electron of a higher shell will fall into the resulting vacancy, releasing the energy difference in the form of a photon. The key to EDX is that the energy differences between the energy levels of these shells are specific to each type of atom. A spectrometer that analyses the energy of the photons emanating from a sample can therefore provide information on the chemical composition of the material. Because an electron beam can be used to excite the sample's atoms, EDX systems are often integrated into SEM setups.

Interaction with Perovskites

The electron beams used in electron microscopy are high energy particle beams and consequently there is always the possibility of beam induced damage to keep in mind. This is also a well known phenomenon in the realm of MHPs [151]. Some layers that were observed during the work on this thesis showed significant damage upon observation using the SEM, especially those where the target perovskite layer didn't form properly. After reducing the acceleration voltage from 10 kV to 4 kV, most layers only showed damage for very large magnifications. An example of such beam damage can be seen in figure 2.6. The rectangular shape of the damaged area is the result of previous scans with higher magnification. The dwell spots of the electron beam on the top left of the damaged areas are clearly visible.

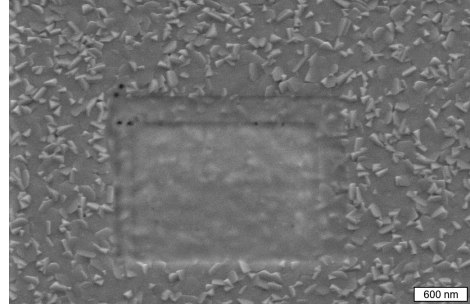


Figure 2.6: Electron beam damage on an improperly formed $\text{MAPbI}_x\text{Br}_{3-x}$ layer.

2.5.3 Other Methods

Quartz Micro Balance

If a mass is deposited on a quartz crystal scale, its resonant frequency diminishes. Therefore, a comparison of two frequencies allows for the calculation of the weight of the material that has been deposited in the time between the two frequency measurements. The change in frequency Δf is related to the change in mass Δm according to the Sauerbrey-Equation [152]:

$$\Delta f = -\Delta m \cdot \frac{2f_0^2}{A\sqrt{\rho_q\mu_q}} \quad (2.37)$$

where f_0 is the unaltered resonant frequency of the quartz crystal, A is the active crystal area, ρ_q is the density of the quartz crystal and μ_q is its shear modulus. Therefore, with the knowledge of the materials density and the cross section of the quartz scale, one can calculate the deposited films thickness. Since the quartz scale is in a different position as the substrate, the film's thickness on the quartz scale will usually not be the same as the thickness of the film deposited on the substrate. To correct for this discrepancy, a value is determined by measuring the actual thickness of the film on the substrate by other means (e.g. cross-sectional SEM analysis) and dividing it by the thickness predicted by the quartz scale. The resulting value is called the tooling factor and multiplying the thickness determined from the quartz scale by this value yields the actual thickness of the film on the substrate for later experiments.

Laser Light Scattering

The measurement of the change of a film's thickness via laser light scattering (LLS) works by the principle that a beam of light gets partially reflected upon crossing a boundary between two media with different indices of refraction. When the laser light hits the deposited thin film,

one part is reflected at the films surface (vacuum to film boundary) and another is reflected at the films backside (film to glass boundary). The two exiting beams exhibit a path difference and therefore a phase difference that depends directly on the films thickness and its index of diffraction. While the film is growing, the signal received from the LLS system grows and shrinks as the exiting beams experience constructive and destructive interference. If the index of diffraction n of the growing film is known, one can calculate the amount of material deposited per peak-to-peak or valley-to-valley transition in the signal. The deposited film thickness per such transition is [153]:

$$\Delta d = \frac{\lambda}{2} \left(\frac{n}{\cos \vartheta'_L} + \tan \vartheta'_L \cdot \sin \vartheta_D \cdot \sin(90^\circ - \varphi_A + \varphi_Z) \right)^{-1} \quad (2.38)$$

with $\vartheta'_L = \arcsin \frac{\sin \vartheta_L}{n}$

where, λ is the wavelength of the laser light, φ_L is the angle of the incident beam, φ_D is the angle of the detector, φ_Z is the polar angle and φ_A is the azimuthal angle.

Chapter 3

Experimental Methods

3.1 Experimental Setup

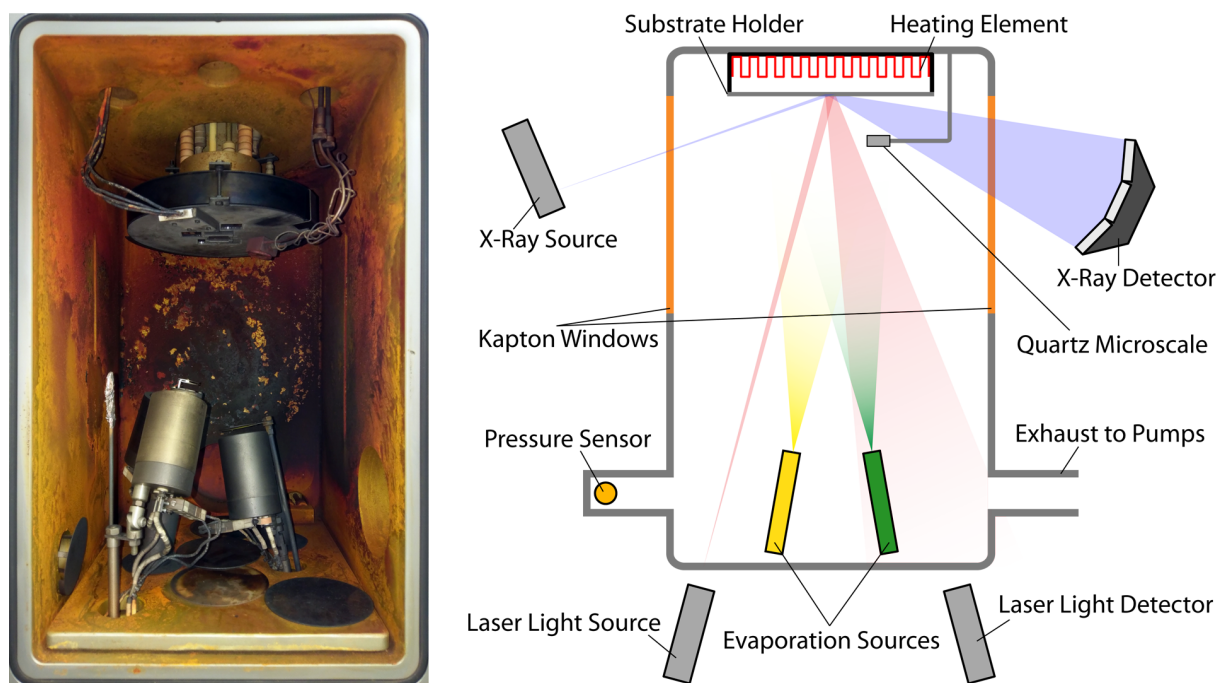


Figure 3.1: Left: A photo of the inside of the evaporation chamber. The sample holder is at the top with the quartz scale visible just below. The thermal evaporation sources are at the bottom. The entry and exit slits for the X-rays are visible at the sides of the chamber and they are covered with Kapton on the outside. The circular hole at the right is the connection to the vacuum pumps. Right: Schematic depiction of the evaporation chamber together with the XRD system. The X-rays enter and exit the evaporation chamber through the Kapton windows. The consecutive XRD scans can be translated into color maps.

Figure 3.1 shows a schematic depiction of the vacuum co-evaporation chamber. The vacuum system consists of a scroll pump (Edwards XDS 5) as the pre pump, which achieves a pressure of around 5×10^{-2} mbar, and a turbo molecular pump (Edwards STP 201). Additionally, there is a vacuum cold trap which is water-cooled. This system reaches a pressure of 2×10^{-5} mbar, which is also the background pressure of the processes examined in this work. To measure the pressure, a WRG (Wide Range Gauge) of the company Edwards is used.

To thermally evaporate the precursor materials, effusion cells from the companies LUXEL (model RADAK II) and CREATEK (model DFC-40-10-180-MO-WK-SHE-SC) were used. The crucibles consisted of quartz glass in the case of the LUXEL models and Al_2O_3 in the case of the CREATEK models. The effusion cells were equipped with shutter blades.

The substrate holder is a circular, stainless steel sheet with 6 square holes that each hold one of the 2.5 cm times 2.5 cm soda lime glass substrates. As is visible in figure 3.1, the samples are mounted above the crucibles, so the evaporated material is deposited on their underside. A carbon heating element is located above the samples and a thermocouple is in contact with the upper side of the middle substrate to monitor its temperature. The temperature of the heating element itself is also measured using a similar thermocouple that is electrically shielded from the heating element via a ceramic sheath.

There are two implementations in place to measure the film thickness: A quartz scale and a laser light scattering (LLS) system. Their exact workings and the way in which their data is interpreted is described in section 2.5.3. The quartz scale (produced by INFICON) is mounted off-center below the substrate holder and collects material from the evaporation sources. A continuous measurement of its resonant frequency provides information on the momentary deposition rate and the deposited films thickness. The LLS system measures the film thickness via scattered laser light. In keeping with the notation of equation 2.38, the angle of the incident laser beam (ϑ_L) and of the detector (ϑ_D) are both 15° , while the azimuth (φ_A) and polar angle (φ_Z) are both 45° . The system uses a red laser with a wavelength of 650 nm and an infrared laser with a wavelength of 1550 nm.

3.2 Analysis via In-Situ XRD

A core piece of the analytical setup employed for the experiments presented in this thesis is the in situ XRD setup. As the name implies, it is a system with which the sample can be continuously monitored by XRD during the experiment, without removing it from the chamber for analysis. This allows for a much more direct correlation of process parameters to the film's crystal phase relations than what would be possible with an analysis that is done after the experiment has finished. Using this setup, one can alter process conditions like the evaporation temperature of the precursor materials or the substrate temperature and directly observe any changes that this induces in the growing film in quasi real-time. This allows for an easy assessment of temperature induced expansion, phase changes and decomposition of a material.

Figure 3.1 shows a photo and a schematic of the vacuum evaporation chamber with the XRD setup. The detector consists of the three Dectris Mythen 1 K modules that are attached to one another at a slight angle and can cover a 2θ range of 28° . Above these 1D detectors is a point detector which is used for the calibration steps. The setup uses a Cu X-ray source with

a $K\alpha$ wavelength of 1.540 592 92 nm. The rays of the $K\beta$ wavelength (1.392 246 nm) get filtered through a Ni window, however, a small contribution of the $K\beta$ -rays remains. The intensity (by peak area) of the resulting $K\beta$ peaks is around 5% of the respective $K\alpha$ peak. The source and the detector are each attached to one goniometer arm, with the substrate situated approximately in the center of their rotation. The sample holder inside the chamber can be adjusted in height. The middle position of the middle detector segment fulfils the Bragg-Brentano geometry.

Initial Calibration

Before every experiment, a number of calibration steps are run by an automated program. First, the source and the detector are set in line, the sample is set to the highest possible position and the measured intensity is logged. Then the sample is slowly being lowered, until the measured intensity drops to zero. The point at which the intensity was half that of the initially logged one is assumed as the position of the sample. To correct for a tilt in the sample, the source and detector take on a $\theta - 2\theta$ position to a sample with an assumed tilt of 0° . They are then both rotated by the same offset-angle δ in one direction and then slowly rotate over an angle of 2δ in the other direction. The detected intensity is highest for the angle where the $\theta - 2\theta$ condition is fulfilled. When coming close to this angle, the detected intensity rises to a maximum and then, when having exceeded this optimal angle, drops. The function of the measured intensity over the offset angle has the shape of a peak. The angles of the left and right half-height points of this peak are taken and the middle between these two is taken as the new 0° reference. At the start of the experiment, a fixed source detector geometry is set which is retained throughout the experiment. The source, sample and the middle spot of the middle detector fulfil the Bragg-Brentano geometry. The choice of the θ angle is done in a way so that the 28° angle coverage of the 1D detector includes the most relevant XRD reflexes of the materials that are being studied.

3.3 Thin Film Growth via Thermal Co-Evaporation

The co-evaporation processes were controlled and monitored using a LabVIEW program, which allowed to define a sequence of temperatures and heating times for the evaporation sources and the substrate heating element, together with the corresponding shutter states. This program also monitored the temperatures, the signal strength from the LLS system and the output of the quartz scale.

Flux Measurements

Flux measurements are necessary to properly relate the temperature of a crucible to the resulting flux of that precursor. The evaporation chamber contains a quartz crystal scale located close to the substrate holder, which is connected to a computer so its data can be read out by suitable programs. To conduct a flux measurement, the program was set to the density of the evaporated material, the Z-factor was set to 1 and the tooling factor was set to 100%. The Z-factor only plays a role, if the layer deposited on the quartz crystal scale is thick enough to reduce the frequency of the crystal to less than 95% of its original frequency [154]. We exchanged our quartz crystals before reaching that point. To measure the flux at a given temperature, the

respective temperature was set for the crucible and after reaching it, the crucible was given a few minutes time to properly heat through. Then, the current thickness was read from the program and a stop watch was used to wait for around 10 min. After that, the thickness was read again, and the difference was calculated. To determine the tooling factor, the thickness that was displayed at the end of the process was compared to the thickness as determined by a cross-sectional SEM analysis. With this data, one can calculate the deposition rate for a given material and source temperature.

Finding the Correct Precursor Temperatures Using the XRD-System

The in situ XRD system can also help in finding the right preparation conditions for a given perovskite, as there is quick feedback if the given combination of substrate temperature and precursor fluxes results in the formation of the desired material. A method that has often been implemented to find the right precursor flux ratio, was to hold the temperatures of all but one precursor steady and to run a temperature ramp on the remaining one. At some temperature, the XRD peaks that indicate the existence of the desired crystal phase might appear and thus the correct temperature has been found.

Adjusting the Correct Precursor Temperatures using EDX

After a sample has been prepared, an analysis via EDX can give an indication of the ratio of the chemical components. This can be used to identify deviations from the expected stoichiometry. Since the flux measurements reveal how a given change in evaporation temperature changes the resulting flux, the temperatures can then be adjusted for the next trial.

Thermal Co-Evaporation

All materials were inserted into the crucibles in the form of a powder, the sole exception being CsI, which existed as small beads. Afterwards, the weight difference from before the filling was recorded and the crucibles were inserted into their respective evaporation sources. At the start of each evaporation process, with the shutters closed, the crucibles were heated to the target temperature, at which the actual evaporation was supposed to occur. The heating time was usually around 10 to 20 min. Some slight overshooting still commonly occurred and so there was an additional waiting period of 5 min with closed shutters, to allow the crucibles to properly settle into their target temperatures. If not otherwise stated, the shutters of the precursors were opened simultaneously to start the evaporation process and closed simultaneously after the process was finished.

There are some notable exceptions to this procedure, that are discussed in what follows: Usually the powders that were inserted into the crucibles remained in powder form during the process. In contrast, FAPbBr₃ exhibited a peculiar behavior, by which the powder completely liquefied and the material existed as a solid black mass after the process. During the first processes with this material, some droplets of liquid FAPbBr₃ sputtered onto the samples and in a later experiment the solid black mass (liquefied during a previous process) was ejected from the crucible during heating and it stuck to the shutter. To reduce the chance of these occurrences,

the FABr was heated over a time of 20 min to 20 °C above its target evaporation temperature, while keeping the shutter closed. It was kept there for 10 min and was afterwards allowed to cool down to the actual process temperature.

Thermal Decomposition

The aforementioned LabVIEW program was used to define the temperature regime for the thermal decomposition of the samples. During the decomposition experiments, the samples were continuously monitored using the in situ XRD system. The temperature ramp experiments used a heating rate between 3 °C and 4 °C per minute. The isothermal decomposition experiments used two temperature steps. The first one had the purpose to preemptively induce any potential temperature related recrystallizations, while the second step induced the thermal decomposition itself. The ramping time between those two steps was usually around 5 min. The specifics of the temperature control are described in the experimental sections of the respective publications.

3.4 Limitations of the Analytical Setup

In this section, some limitations and considerations about the analytical setup are discussed and some are quantified. Notably, the works on the kinetic triplet of the thermal decomposition of MAPbI₃ and FAPbI₃ depend significantly on the assumption that the area of the observed XRD peaks is proportional to the extent of the decomposition reaction. However, there are some effects that might decouple these two variables, which are discussed in the following sections.

X-ray absorption of the decomposition products

All of the metal-halide perovskites examined in this work, upon their decomposition, leave behind either a lead halide or a cesium halide. It is useful to know by how much such a layer of decomposition product reduces the strength of the XRD signal. To calculate the amount by which the X-ray intensity is reduced by the product layer, the following formula will be used:

$$I = I_0 \cdot e^{-\mu x} \quad (3.1)$$

$$x = 2 \cdot d / \sin \theta \quad (3.2)$$

where I is the final and I_0 the initial X-ray intensity, μ is the linear attenuation coefficient of the product and x is the length that the photons travel through the product layer, which is calculated using the product layer thickness d and the X-ray incidence angle θ . Additionally, one can consider the product layer coverage c , with $0 < c < 1$. With these parameters, the absorption A can be defined as:

$$A = c \cdot (1 - e^{-\mu x}) \quad (3.3)$$

With the SEM data obtained for the partial decomposition on FAPbI₃, which were published in reference [Bu5] and discussed in chapter 4.6, one can estimate the following properties for the covering PbI₂ layer: $d \approx 100$ nm and $c \approx 50$ %. The resulting values for the absorption A are shown in table 3.1 for the most significant perovskites analyzed in this thesis. All absorption values are below 5 %, which indicates that the absorption on the product layer will not have a

significant impact on the results. On an additional note, the thermal stability estimated via the temperature ramp experiments is determined by the onset of the XRD-peak's decline, at which point the sample cannot be significantly impacted by the absorption of the product layer.

Table 3.1: Absorption A calculated by equation 3.3 for a layer of product under the assumption of $\theta = 20^\circ$, $d = 100$ nm and $c = 50$ %.

Educt	Product	μ [cm^{-1}]	Absorption
MAPbI ₃ / FAPbI ₃	PbI ₂	1556.51	4.35 %
MAPbBr ₃ / FAPbBr ₃	PbBr ₂	1078.75	3.06 %
MAPbCl ₃ / FAPbCl ₃	PbCl ₂	1120.85	3.17 %
CsPbI ₃	CsI	1360.64	3.82 %
CsPbBr ₃	CsBr	1021.63	2.90 %
CsPbCl ₃	CsCl	1080.85	3.06 %

Deposition of X-ray absorbing material on the chamber windows

The sources are oriented towards the substrates, while the chamber windows are positioned roughly perpendicular to this direction. The films deposited on the chamber windows should therefore be significantly thinner than the films deposited on the substrates. The films on the substrate, even if partially converted to product, should not significantly reduce the signal strength, as was elaborated on earlier. It follows, that the film deposited on the windows should also not reduce the signal in any significant way. To substantiate this with experimental evidence, a few experiments were made, that did not see the Kapton windows exchanged between each process. These experiments consisted of the deposition of CsPbI₃ thin films. The values for signal strength were taken by adding together all counts received over all channels of the XRD detector and averaging this value over the first 10 scans, where no material has been deposited yet. The drop in this measure for signal strength from the first process to the second process was 1.5 %, from the second to the third it was 0.8 % (2.3 % from first to third). From this it can be concluded that the overall loss in signal strength over the course of one experiment is roughly 1 %, which can be considered negligible. Additionally, the material flux from the substrate during decomposition is likely to be much lower than the material flux from the sources during deposition. Usually, the material amount evaporated from the sources had a weight of a few dozen milli grams, while the overall weight of material on the substrate after the deposition, for a 500 nm CsPbI₃ film (2.5 cm · 2.5 cm substrate, $\rho = 4.81$ g cm⁻³), is roughly 1.5 mg.

Decomposition of the perovskite by X-rays

Svanström et al. have investigated the X-ray induced degradation of mixed cation (FA and MA) samples. They used X-rays from a synchrotron with a photon energy of 3 keV and took the ratio R of FA⁺ to Pb²⁺ as the indicator for the degradation, measured via XPS. They propose that the change in this ratio can be described by the formula:

$$R(x) = R_0 \exp\{-k_r \cdot x\} \quad (3.4)$$

where x is the photon fluence in photons per area, k_r is the radiolysis rate constant in area per photons, R_0 is the initial ratio and $R(x)$ is the new ratio after a photon fluence of x on the sample. The exponential term is 1 at the start of the experiment ($x = 0$) and approaches 0 as x increases. They obtained a value of $k_r = 1.68 \times 10^{-18} \text{ cm}^2 \text{ photon}^{-1}$ for their $\text{FA}_{0.83}\text{MA}_{0.17}\text{PbBr}_{0.51}\text{I}_{2.49}$ samples [155]. We estimated that over the course of an 8 h experiment with our X-ray setup the exponential term of equation 3.4 would be at 0.9973 which would correspond to a degradation by about 0.27%, which can be considered negligible. The detailed calculations can be found in appendix A.1.

A melting of the crystal without an actual decomposition

As has been pointed out by Galwey, many analyses into the thermal decomposition of materials do not properly account for the possibility of a melting of the material [140]. This would be especially crucial to consider, if XRD is used as the method of analysis. Singh et al. pointed out, that for metal-halide perovskites no melting point is known, because they decompose before a melting point can be reached [156]. Additionally, our results from the SEM analysis of a partially decomposed FAPbI_3 layer (see section 4.6) did not show any signs of melting, but instead indicated a layer that sublimated directly from the solid phase.

Rotation of the sample's particles

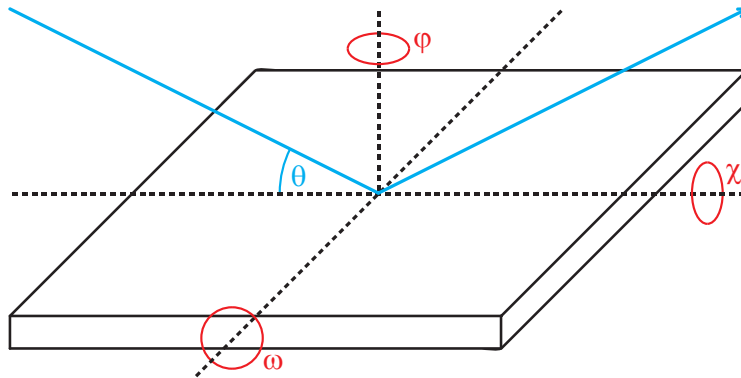


Figure 3.2: Rotational axes in relation to the sample plane, as they are referred to in the text. The blue line is the XRD beam, which lies in the plane spanned by the χ and φ axes.

- **Change in the Preferential Orientation Around the ω -axis:** When a specimen is observed via XRD using the Bragg-Brentano geometry, only the planes parallel to the sample plane can be observed. The polycrystalline perovskite layers usually show a strong preferential orientation in the (100) direction, which means that the (100) direction of the crystals is perpendicular to the sample plane. This results in the (100), (200) and (400) peaks being the most visible and other peaks being barely visible or not visible at all. If the

preferential orientation of the crystallites would change, one would expect the (100), (200) and (400) peak to decrease in intensity while other peaks would gain in intensity. Over the course of the decomposition experiments, no other peaks besides the (100), (200) and (400) peaks became visible that would indicate such a change in preferential orientation, so we considered this an indication that the film's crystallites retained their original orientation regarding this axis.

- **Change in the Preferential Orientation Around the χ -axis:** The distinction between the ω - and the χ -axis depends solely on the measurement geometry. If there is no rotation of the sample's particles around the ω axis, there is no reason to assume that a rotation around the χ -axis takes place.
- **Change in the Preferential Orientation Around the φ -axis:** The directions that correspond to different angles on the φ -axis depend on the measurement geometry, as rotating the sample itself would be equivalent to a rotation of all the sample's particles around the φ -axis. If the particles are randomly rotated around the φ -axis at the beginning of the experiment, their rotations will be just as randomly distributed at the end of it, as there is no mechanism that would introduce a bias in their orientation.

Chapter 4

Main Results

4.1 General Notes

Up to this day the preferred method for the preparation of metal-halide perovskites for research has been spin coating. In this wet chemical process, the desired material is dissolved within a solution. This solution is applied to a substrate, which is then spun with rotation speeds usually in the order of thousands of rotations per minute. As the solvent rapidly evaporates, the dissolved material crystallizes out and forms the desired layer. For research purposes spin coating has many advantages: Spin coating systems are relatively cheap to set up, easy to move and install and allow for quick processing and thus a high sample throughput. However, there are also some key disadvantages, especially when the end goal of industrial application is considered: Spin coating is much less scalable in regard to substrate sizes, as larger substrates can experience an immense amount of mechanical stress. Another factor is the very low material efficiency, as a macroscopic droplet of solution is used to create a film of around 500 nm in thickness, while the rest of the material is flung away. It is possible, but very complicated, to control the thickness of the deposited layer and the resulting film can exhibit a high thickness variation. This problem will be more pronounced with a higher roughness of the substrate and with lower wetting of the solution on that substrate. Small variations in the ratio of the solvents and their constituents can have a large influence on the resulting layer [157]. Constituents of the ambient atmosphere, like oxygen and moisture, can influence the results, potentially reducing the reproducibility, if the work is not conducted within a glovebox or a similarly controlled environment. There is also evidence, that solution processed films exhibit lower stability compared to co-evaporated films [52, 14], which at the very least highlights, that the attributes determined from spin coated films cannot necessarily be generalized to films obtained from other methods. Some precursors are also more difficult to dissolve than others, which might hinder the applicability of spin coating to certain materials. Additionally, certain solvents might be toxic. Therefore, if metal-halide perovskites want to reach industrial applications, the study of alternative methods of preparation will be necessary. This work will focus on thermal co-evaporation, which is a non-solution based method that is already being successfully implemented on an industrial scale, for example, in the production of OLED displays [158]. While the up-front costs of a vacuum co-evaporation setup are higher compared to a spin coating setup, this method has

some very significant advantages: The substrate size can be scaled much more easily and the material efficiency is much higher. Layers generally exhibit a much higher smoothness and the thickness can easily be controlled by variation of the deposition time. The preparation in vacuum removes influences from the atmosphere and the deposition parameters can easily be controlled, resulting in enhanced reproducibility. Furthermore, thermal post-treatment of the samples can be conducted without breaking the vacuum, which is, again, a benefit for reproducibility. While co-evaporation eliminates the need to find a suitable solvent for the precursors, some compounds, especially organic ones, can be difficult to thermally evaporate as they might dissociate upon heating.

As a direct consequence of the prevalence of spin coating in metal-halide perovskite preparation, most studies on the stability of perovskites focus on these solution processed films, which leaves a gap in the understanding of the properties of co-evaporated films. Our experimental setup, consisting of a high vacuum chamber built for preparation via co-evaporation, combined with the in situ XRD system, provides an opportunity to contribute to the closing of this gap. The in situ XRD setup constitutes the central piece of most of the analyses presented in this thesis. It provides an opportunity to analyze the crystal structure of the films during the experimental processes and thus allows great insight into the growth and — upon annealing — thermal expansion, phase changes and thermal decomposition of the films. Additionally, the setup allows to observe the downwards shift of the XRD peaks during a temperature ramp. This downward shift corresponds to the increase in lattice parameters of the observed crystal and with this information one can calculate the coefficient of linear expansion. Experiments of this nature have been conducted for MAPbI₃, MAPbBr₃ and MAPbCl₃ (section 4.2); CsPbI₃ and CsPbBr₃ (section 4.3) and Cs₂AgBiBr₆ (section 4.4). The crucible temperatures that have been used for the evaporation of these materials are shown in table A.1 in appendix A.2.

While the decomposition experiments that use a temperature ramp allow for a large variety of data to be gathered over the course of a single experiment, the results of the thermal decomposition experiments can be difficult to compare to the results of other research groups. Additionally, the onset of the decomposition can be difficult to determine. A more thorough, reaction kinetical analysis has been conducted for the decomposition of MAPbI₃ (section 4.5) and FAPbI₃ (section 4.6), which allows for the calculation of the activation energy E and the pre-exponential factor A of the thermal decomposition reaction.

Because it is very challenging to determine the exact onset of a decomposition with the temperature ramp experiments, the publications on MAPbI₃, MAPbBr₃, MAPbCl₃ (section 4.2), CsPbI₃ and CsPbBr₃ (section 4.3) referred to a point at which the XRD intensity dropped to roughly 50% to allow for a consistent comparison between the different materials. When decomposition temperatures are stated in this chapter, they refer to the first scan where a clear decline of the peak intensity is visible. This might result in a higher uncertainty in the stated value but given the fact that temperature ramp experiments tend to already over-estimate the temperature of decomposition, I decided that this gives a value closer to the “actual” temperature of thermal decomposition. I encourage the reader to use Fig. 5.1 for a plot of the observed XRD peak intensities over the temperature, to avoid uncertainty.

4.2 Preparation and Thermal Stability of MAPbX₃

Preliminary Discussion

Reference: [Bu1]

The metal-halide perovskite that has first sparked interest in this material class for photovoltaic applications is MAPbI₃. Because of this, MAPbI₃ and the related perovskites MAPbBr₃ and MAPbCl₃ have the largest amount of research dedicated to them. Consequently, the first major work of my thesis focuses on MAPbI₃, MAPbBr₃ and MAPbCl₃. I wanted to study the growth, thermal stability and crystal phase evolution between RT and the temperature of thermal decomposition. Another aspect investigated in this work is the creation of mixed halide MAPbI_xBr_{3-x} perovskites. MAPbI₃ has a band gap of 1.51 eV [25] and MAPbBr₃ has a band gap of 2.42 eV [29]. The lattice constant and the band gap of a MAPbI_xBr_{3-x} mixed halide perovskites have a roughly linear dependency on the ratio of I to Br, in accordance with VEGARDS law [30]. Because of this, the in situ XRD scans allow for an estimation of the ratio of I to Br from the position of the XRD peaks. Because the band gap can be manipulated in this way, these mixed halide perovskites are especially interesting for tandem applications. For a sub cell with a given band gap in a tandem arrangement, there exists an ideal band gap for the corresponding partner sub cell. If that required band gap lies within the range of available band gaps of an MHP, that MHP can have its band gap matched accordingly. Brivio et al., however, has shown by theoretical calculations that there might be a miscibility gap that would forbid a mixed MAPb(I_{1-x}Br_x)₃ perovskite for $0.3 < x < 0.6$ at RT [79]. We tried to prepare mixed MAPb(I_{1-x}Br_x)₃ perovskites using a variety of approaches: The first approach will focus on creating such a mixed halide perovskite directly by evaporating either PbI₂ and MABr or PbBr₂ and MAI. The second approach consists of trying to partially convert a pure halide perovskite by exposing it to the vapor of the respectively other MA halide. The expected observation of the in situ XRD would be a gradual shift of the peak positions from those corresponding to a pure perovskite of one halide to those of the pure perovskite of the other halide. If a miscibility gap is present, one would expect the observed peak to split into two peaks, one indicating I richness and one indicating Br richness.

The in situ character of our setup makes it very simple to measure the linear thermal expansion coefficients during heating. According to Cojocaru et al., the expansion coefficient of the perovskite absorber can have a significant impact on the performance a solar cell under thermal stress, as a large mismatch in expansion between the substrate and the absorber can lead to interfacial defects or even delamination [61]. This implies that it is crucial to know the thermal expansion coefficient of a given material before it can be used in actual devices.



Cite this: DOI: 10.1039/c8ta02775g

Thermal stability and miscibility of co-evaporated methyl ammonium lead halide (MAPbX₃, X = I, Br, Cl) thin films analysed by *in situ* X-ray diffraction†

Paul Pistor,^a Thomas Burwig,^a Carlo Brzuska,^a Björn Weber^b
and Wolfgang Fränzel^a

We present the identification of crystalline phases by *in situ* X-ray diffraction during growth and monitor the phase evolution during subsequent thermal treatment of CH₃NH₃PbX₃ (X = I, Br, Cl) perovskite thin films. The thin films are prepared by vacuum-based two-source co-evaporation using various methyl ammonium (MA) halide and lead halide (PbX₂) precursors. The single halide perovskite materials MAPbI₃, MAPbBr₃ and MAPbCl₃ are prepared without secondary phases and an upper thermal limit for decomposition into the corresponding lead halides is established. We show that at a substrate temperature of 120 °C, the halide in MAPbI₃/MAPbBr₃ thin films can be completely and reversibly exchanged upon exposure to the opposite MA halide. We monitor the temporal evolution of the conversion process *in situ* and discuss differences in the forward and backward conversion. For the deposition of mixed MAPb(I,Br)₃ perovskite thin films, different growth routes are suggested and evaluated in terms of growth with single phases or phase segregations. Our results are discussed in a broader context considering I/Br miscibility. Finally we propose a new growth route for the synthesis of single phase mixed MAPb(I_{1-x}Br_x)₃ thin films in the range from x = 0.3 to 1 by two source co-evaporation and discuss the implication of our results.

Received 26th March 2018
Accepted 17th May 2018

DOI: 10.1039/c8ta02775g

rscl.li/materials-a

Introduction

Hybrid organic–inorganic lead halide perovskites for solar cells

Research on photovoltaic (PV) energy conversion has been shaken in the last few years by the appearance of a new class of absorber materials called perovskites. These new hybrid organic–inorganic compounds were first explored as light harvesters in 2009 (ref. 1) and gained exponentially increasing interest during the last five years since their first successful application in 2012 with efficiencies exceeding 10%.^{2,3} Currently, the best cell efficiencies have well surpassed 20%,^{4,5} putting them on the same performance level as the best conventional polycrystalline PV technologies such as polycrystalline Si, Cu(In,Ga)Se₂ or CdTe.

The remarkable optoelectronic properties of thin film solar cells such as strong photoluminescence and long charge carrier diffusion lengths (>1 μm),^{6,7} the possibility to apply simple and

cheap non-vacuum-based deposition techniques (e.g. spin coating) and a tuneable band gap suitable for both single junction and tandem applications have further boosted scientific and industrial interest. While the race to highest efficiency solar cells is extremely fast and successful, reports about the intrinsic instability of hybrid halide perovskite materials when exposed to moderate levels of heat,^{8,9} moisture¹⁰ and even light^{11,12} currently are an obstacle to industrial considerations.^{13–15} This also severely limits the reproducibility of experimental results, especially because many of the fundamental properties have been reported for wet-chemical processes which depend critically on air exposure times, ambient conditions, surface conditioning and quality of solvents, precursors and substrates. It is therefore not an easy task to derive more general conclusions about this material class and there is still a strong need for further fundamental characterisation under very well-defined conditions.

Wet-chemical methodologies such as spin-coating allow very fast progress and high sampling rates on a laboratory scale and have up to now been applied in the grand majority of publications. However, we believe that vacuum-based technologies such as co-evaporation should not be ignored, as they allow precise parameter control, better reproducibility and fast processing on very large areas, which makes them attractive from a large-scale industrial point of view. Several groups have already successfully deposited MAPbI₃ thin films by two source

^aMartin-Luther-Universität Halle-Wittenberg, Institute of Physics, Von-Danckelmann-Platz 3, 06120 Halle (Saale), Germany. E-mail: paul.pistor@physik.uni-halle.de

^bMartin-Luther-Universität Halle-Wittenberg, Institute of Chemistry, Von-Danckelmann-Platz 3, 06120 Halle (Saale), Germany

† Electronic supplementary information (ESI) available. See DOI: 10.1039/c8ta02775g

co-evaporation^{16,17} yielding working solar cells with efficiencies of up to 15%.^{18,19} The two-source co-evaporation allowed dense planar films with large crystals to grow, where the thickness variations were much smaller as compared to solution-coated films.¹⁸ Additional intrinsic advantages of the co-evaporation technique over solution-based preparation are the ability to grow films with arbitrary thicknesses and the avoidance of toxic solvents. We follow this approach and report here on our progress in understanding the fundamental phase formation and decomposition mechanisms of perovskite thin films synthesized by co-evaporation of MAX and PbX₂ (X = I, Br, Cl) precursors investigated *in situ* by X-ray diffraction (XRD).

It is well known and has been extensively reported that MAPbI₃ decomposes easily under thermal stress and/or exposure to air/humidity.^{14,20,21} However, the rate of decomposition and the degree of instability is not well established and seems to be strongly related to the deposition pathway. More information on the intrinsic thermal stability of MAPbX₃ is therefore desirable. Furthermore, the air exposure time of grown films between synthesis and measurement (and relative humidity levels) is crucial for every decomposition analysis and is unfortunately usually not detailed. It is clear that if thin films had ever been exposed to air/humidity prior to any stability analysis, some moisture is likely to have soaked into the films. This will lead to a slow decomposition over a long time even if effective air exposure times have been kept short and the actual stability analysis afterwards is carried out under dry conditions. We find it therefore important to note that in contrast to most *ex situ* measurements, films in our experiments have not been exposed to air or humidity at any point during the investigation, which enables us to explore the fundamental thermal stability of unexposed perovskite films.

The prototype of the perovskite absorber material applied in solar cells is based on organic-inorganic methyl ammonium lead iodide (MAPbI₃). The most common variations and combinations of constituents are substitution of methyl ammonium (MA) by formamidinium (FA) and Cs or (partial) substitution of the iodine by Br or Cl. MAPbI₃ has a band gap of 1.51 eV,²² suitable for single-junction photovoltaic applications. Following the line I–Br–Cl, as the ionic radius decreases, the Pb–X bond strength increases²³ and consequently the band gap of the material is also increased (see Table 1). The analogous perovskite with bromine, MAPbBr₃, has a band gap of 2.42 eV,²⁴ which is suitable for light emitting diodes, but in principle too

high for efficient solar energy harvesting. MAPbCl₃ shows an even higher band gap of 3.16 eV.

A clear advantage of hybrid lead halides is the possibility to tune the bandgap by intermixing some of the perovskite components. As for the mixed halide MAPbX₃ perovskites, there is consensus that the MAPbBr₃–MAPbCl₃ system is completely miscible,^{25–27} while the MAPbI₃–MAPbCl₃ is not because the difference of the atomic radii is too large.^{26,28} The mixed MAPb(I,Br)₃ system allows band gaps interesting for tandem solar cell applications but the miscibility is still under debate.²⁹ While Bolink and co-workers have reported a sequential evaporation–conversion process,³⁰ up to our knowledge the deposition of mixed MAPb(I,Br)₃ thin films by co-evaporation from two sources has not been reported so far.

In our contribution we explore the possibility to control the growth of single phase perovskite thin films by two-source co-evaporation under high vacuum conditions. We focus on the most widely used methyl ammonium lead halide perovskites (MAPbX₃ with X = I, Br, and Cl). Firstly, we will investigate the growth mechanisms of the single halide perovskites and introduce the working principle and potential of our specialized *in situ* X-ray diffraction (XRD) setup. We continue studying in detail the behaviour of the grown MAPbX₃ thin films under thermal stress and monitor their decomposition routes.

We will then concentrate on the mixed MAPb(I,Br)₃ system, which is the most relevant one for photovoltaic applications. Here, we first investigate *in situ* the exchange of the halide anions in grown films and the conversion of MAPbI₃ into MAPbBr₃ and *vice versa*. Finally, the potential of different growth routes to prepare mixed MAPb(I,Br)₃ thin films using static two-source co-evaporation will be evaluated and the best growth route to obtain single phase material is identified.

Crystal structure of methyl ammonium lead halides (MAPbX₃, X = I, Br, Cl)

The ideal cubic crystal structure with the space group *Pm3m* (no. 221) and sum formula ABX₃ is the aristotype for the group of materials called perovskites.²² A sketch of the crystal structure is depicted in Fig. 1. In these materials, a large cation A is located at the Wyckoff position 1a coordinated to 12 X anions (position 3c). The position of the large cation A can be occupied not only by a large ion such as Ca or Cs, but also by small molecules such as methyl ammonium (MA) or formamidinium (FA) as in MAPbX₃. B is usually a smaller metal (position 1c) which is bonded to six X anions forming a dense framework of corner sharing octahedra. The larger A cations are located in the voids between these octahedra. The A and B cations and the X anions can come with different atomic radii R_A , R_B , and R_X which predict the stability of a perovskite according to the Goldschmidt equation:³¹

$$t = \frac{(R_A + R_X)}{\sqrt{2}(R_B + R_X)}$$

Here t is the tolerance factor which should lie between 0.9 and 1 for the ideal cubic structure. A non-ideal proportion of the A, B, and X atomic radii results in a distortion of the crystal structure

Table 1 Comparison of crystallographic properties of MAPbI₃, MAPbBr₃ and MAPbCl₃ perovskites. The lattice parameter a is given for MAPbBr₃ and MAPbCl₃ at room temperature and for MAPbI₃ at 70 °C

MAPbX ₃	X = I	X = Br	X = Cl
Ionic radius of the halide ³⁸	2.20 Å	1.96 Å	1.82 Å
Tolerance factor t	0.91	0.93	0.94
Band gap ^{22,24}	1.51 eV	2.42 eV	3.16 eV

Cubic high temperature α -phase

Space group	<i>Pm3m</i>	<i>Pm3m</i>	<i>Pm3m</i>
Lattice parameter a (ref. 22 and 36)	6.276 Å	5.901 Å	5.675 Å
Transition temperature ^{22,35}	330 K	237 K	178 K

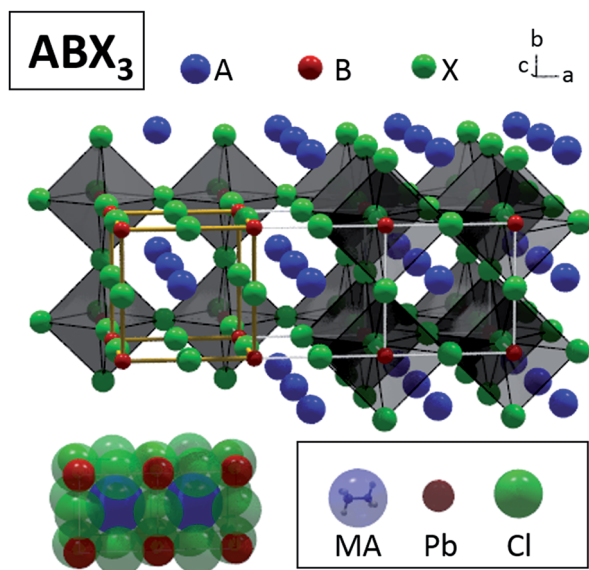


Fig. 1 Above: Sketch of the perovskite crystal structure for materials with the sum formula ABX_3 . Note that in this presentation the atoms are displayed smaller corresponding to their atomic radii for better visualization. Below: Presentation of $MAPbCl_3$ with properly scaled atomic radii.

where the B–X octahedra get tilted and form hettotypes with lower symmetry.³² Usually, the high temperature α -phase of perovskites crystallizes in the ideal cubic structure, as is the case for the three lead halide perovskites $MAPbI_3$, $MAPbBr_3$ and $MAPbCl_3$. Upon cooling, they undergo subsequent phase transitions towards one or several tetragonal β - and orthorhombic γ -phases with lowered symmetry. These polymorphs differ in the tilt and rotation of the PbX_6 octahedra.^{22,33,34}

The crystal structure and phase transitions of $MAPbX_3$ perovskites have been studied extensively.^{22,35,36} At 343 K, $MAPbI_3$ has the ideal cubic perovskite structure with the space group $Pm3m$ and lattice parameter $a = 6.276 \text{ \AA}$.²² The transition from the high temperature cubic α -phase to the tetragonal β -phase with the space group $I4/mcm$ takes place at 327–330 K,²² followed by a transition towards the orthorhombic γ - $MAPbI_3$ with the space group $Pnma$ at approximately 162 K. Similar transitions are observed for $MAPbBr_3$ and $MAPbCl_3$. $MAPbBr_3$ has a cubic crystal structure at room temperature ($a = 5.901 \text{ \AA}$)³⁶ and transforms into a tetragonal structure below 236.6 K.³⁵ Two different tetragonal configurations are reported for this compound and an orthorhombic γ -configuration is found for temperatures below 148.8 K. For $MAPbCl_3$, two different orthorhombic configurations have been found at low temperatures.³⁷ The transition temperatures of the cubic $MAPbX_3$ perovskites ($X = I, Br, Cl$) are listed together with other important crystallographic data in Table 1. Here, the Goldschmidt tolerance factors have been calculated with ionic radii provided by Shannon for the inorganic ions (Pb: 1.19 \AA)³⁸ and an estimated effective radius of 2.17 \AA for the protonated methyl ammonium $[CH_3NH_3]^+$ as reported by Kieslich and co-workers.³² From the transition temperatures it is clear that at room temperature only $MAPbI_3$ adopts a tetragonal crystal

structure, while the other two compounds are already in the high temperature cubic α -phase. An indication of the decomposition temperature as determined and described later on in this manuscript is added to a schematic representation of the phase transitions in Fig. 6.

Experimental *in situ* XRD monitoring and thin film co-evaporation setup

The growth of $MAPbX_3$ ($X = I, Br, Cl$) by co-evaporation in a vacuum can be achieved by evaporating the corresponding methyl ammonium halides (MAX) and the lead halide (PbX_2) simultaneously. In the following, we will show that the synthesis of thin films with this method is straightforward and use it as an example to introduce the capability to monitor thin films *in situ* by X-ray diffraction with the setup installed in our co-evaporation chamber. The chamber is usually operated at a base pressure of 2×10^{-5} mbar. The MAX crucible temperature is set in the temperature range between 110 $^\circ\text{C}$ and 130 $^\circ\text{C}$, while the PbX_2 evaporation sources are operated at slightly higher temperatures (PbI_2 : 300 $^\circ\text{C}$; $PbBr_2$: 300 $^\circ\text{C}$; $PbCl_2$: 350 $^\circ\text{C}$). During MAX evaporation, the chamber pressure usually increases to values around $(5.0\text{--}10.0) \times 10^{-4}$ mbar. The substrate is made of standard soda lime glass and, is usually not actively heating during the growth of the perovskite thin films. The thin film thickness can be monitored by the interferences of scattered laser light signals (650 nm and 1550 nm) and a quartz microbalance. If not stated otherwise, thin films in the following experiments had thicknesses between 500 and 700 nm. An entrance and exit window placed at opposing sides of the chamber allow the X-ray beam to enter and leave the chamber. These windows are freshly covered with Kapton tape before each process. The X-ray system is operated with a Cu K α source at a fixed incident angle and a position-sensitive X-ray detector covering an angular 2θ -range of approximately 12–40 $^\circ$. Counts within one scan are usually recorded over 60s. XRD peak positions and peak areas have been fitted with the analysis software PDX-L after background subtraction using a pseudo-Voigt profile. More details on the *in situ* XRD setup can be found in ref. 39 and 40.

Monitoring the growth and decomposition of $MAPbX_3$ thin films with *in situ* XRD

Monitoring the growth of $MAPbX_3$ ($X = I, Br, Cl$) thin films

Fig. 2 summarizes the data accumulated during the subsequent growth of the three different single halide $MAPbX_3$ thin films. In Fig. 2a, the growth of a $MAPbI_3$ thin film is presented. In these compact representations, in the lower part of the graph, information about the growth process is depicted. In this case, the temporal evolution of the PbI_2 /MAI crucible and the substrate temperatures during the growth are plotted. While during the other growth processes the substrate is usually not heated, in this case the substrate temperature was set to 70 $^\circ\text{C}$ because we wanted to grow $MAPbI_3$ also in the cubic phase for better

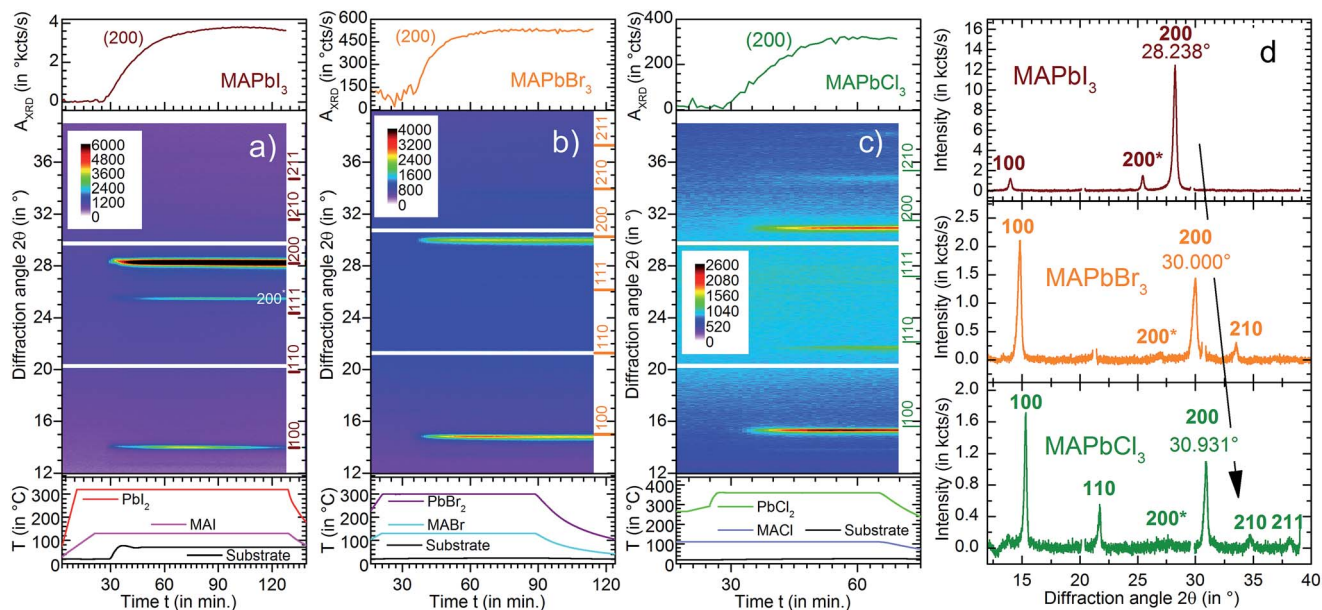


Fig. 2 Growth of single halide (a) MAPbI₃, (b) MAPbBr₃ and (c) MAPbCl₃ thin films by two-source co-evaporation. Each graph displays the evolution over time of the main process parameters such as the crucible and substrate temperatures (below), a color-coded representation of the *in situ* XRD data collected during the deposition process (middle graph) and the evolution of the integrated peak area of the (200) Bragg peak of the cubic MAPbX₃ perovskite phase. (d) Comparison of single XRD scans recorded at the end of each deposition process.

comparison. In the middle part, we present how the X-ray diffraction evolves over time (from left to right on the *x*-axis). Each pixel column corresponds to an XRD measurement over the angular range from 12° to 40° (from bottom to top on the *y*-axis). In these maps, the intensity of the X-ray diffraction is represented by a colour code. On the right hand side of this colour map, brown bars indicate the position of the main XRD peaks of cubic MAPbI₃ from the literature.²² After an initial heating phase of approximately 20–25 minutes, the PbI₂ shutter is opened and MAPbI₃ starts to grow. The (200) peak is observed with very high intensity, while other prominent peaks as, for example, the (110) or (210) are missing. This means that our film grows in a pronounced preferential orientation. The detection of the (100) peak is also suppressed in this preferential orientation due the fixed incident angle with static source-detector positions in these scans. Because of the very high intensity of the (200) peak, even the contribution from the Cu Kβ line can be observed at 25.47° and is marked in the picture with 200*. In the upper part, selected data extracted from the XRD analysis are plotted. As an example, in Fig. 2(a)–(c) we have plotted the integrated peak area of the most intense (200) peak as a function of time. Here, the increasing thin film thickness is reflected in an increasing intensity of the XRD contributions.

Similar graphs are obtained for the growth of MAPbBr₃ and MAPbCl₃, which are displayed in Fig. 2(b) and (c), demonstrating that the growth of MAPbX₃ thin films by co-evaporation is in fact straightforward. Although these films are also preferentially oriented to some extent, other peaks in addition to the (100) and (200) can still be observed with low intensities. The XRD analysis shows that the three single halide MAPbX₃ thin films grow in a single phase and no contributions from MAX or PbX₂ secondary phases can be observed. All three films grow in

a cubic perovskite crystal structure with decreasing lattice parameters from I to Br to Cl. This translates into a shift of the position of the (200) peak to higher diffraction angles (MAPbI₃: 28.24°, MAPbBr₃: 30.00°, MAPbCl₃: 30.93°), in agreement with expectation and the literature. The final XRD measurement for the three depositions can be compared in Fig. 2d.

Thermal decomposition of MAPbX₃ thin films in a vacuum

After proving the possibility to grow single halide perovskites by simple co-evaporation we are interested in comparing the thermal stability of the grown films. For this purpose, the grown films were heated without a vacuum break inside the chamber with a linear temperature ramp of 3 K min⁻¹. During the complete heating sequence, the evolution of phases was monitored with *in situ* XRD.

The results are depicted in Fig. 3. The lower graph shows how the substrate temperature increases linearly with time. In Fig. 3a we can clearly observe how the characteristic peaks of MAPbI₃ start to slowly lose intensity for temperatures above 150 °C, before they completely vanish at temperatures above 250 °C. Instead, new peaks arise above 200 °C, which can be easily identified as PbI₂ (see also the bars at the left side of the colour map). Above 320 °C, the PbI₂ also sublimates and its characteristic XRD peaks vanish. In the upper part, the evolution of the normalised integrated peak area A_{XRD} of the MAPbI₃ (200) and PbI₂ (003) peaks are displayed. The exact onset of decomposition cannot be determined from this simple experiment in a categorical manner. Nevertheless, for this comparative study we have deliberately elected and marked three points in the graphs: (I) the point where A_{XRD} (MAPbI₃) is diminished to 90% of its maximum value, (II) the point where the

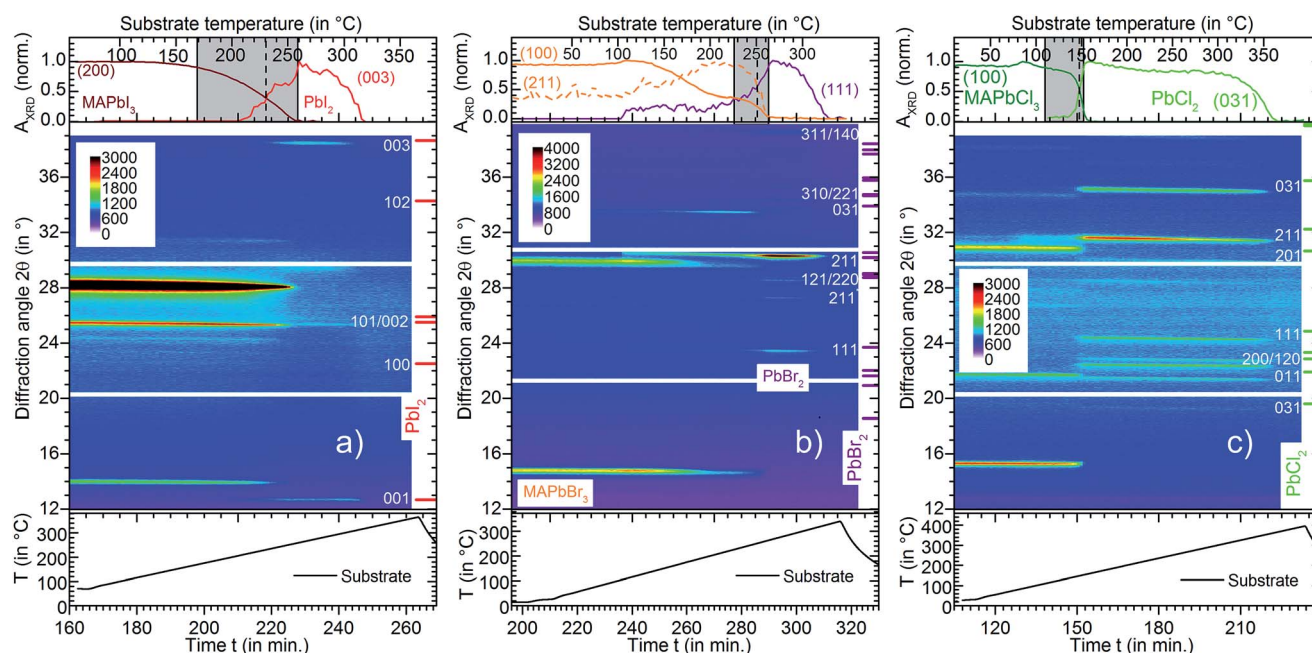


Fig. 3 Heating and decomposition of the three single halide MAPbX_3 thin films represented in Fig. 2. The lower graph shows the ramping of the substrate temperature. In the middle graph, a color-coded representation of the *in situ* XRD data collected during the annealing process is depicted. The upper graph shows the evolution of the normalized integrated peak intensity of the representative Bragg peaks of the observed phases. (a) MAPbI_3 , (b) MAPbBr_3 , and (c) MAPbCl_3 .

normalized $A_{\text{XRD}}(\text{MAPbI}_3) = A_{\text{XRD}}(\text{PbI}_2)$ and (III) the point where $A_{\text{XRD}}(\text{PbI}_2)$ has reached 90% of its maximum value. In the following discussions, we will treat these three points as indicators for (I) the onset of MAPbX_3 decomposition, (II) the critical temperature T_c where approximately half of the MAPbX_3 is decomposed and (III) the point where nearly all MAPbX_3 has been turned into the lead halide. These points are represented in the upper graph by the beginning (I) and the end (III) of a shaded area and a dashed line (II).

Similar to MAPbI_3 , the MAPbBr_3 thin film shows loss of MABr and decomposition into PbBr_2 upon heating (Fig. 3 b). However, before decomposing, the preferential orientation in the (200) direction is reduced in favour of a (211) orientation. Similar effects on the orientation have also been previously observed for MAPbI_3 films.³⁹ This induces additional changes in the MAPbX_3 peak intensities which complicate the interpretation, but it seems that the decomposition of MAPbBr_3 thin films occurs at slightly higher temperatures compared to MAPbI_3 . This is clearly not the case for MAPbCl_3 , which shows a very sharp change from MAPbCl_3 to PbCl_2 already at temperatures as low as 150 °C (Fig. 3 c). In conclusion, all three perovskite films show the same decomposition pathway at slightly different temperatures (150–250 °C). First, the organic MAX evaporates from the film leaving the pure lead halide behind. In our experiments with a linear temperature ramp of 3 K min^{-1} approximately half of the perovskite film is decomposed at the critical temperatures T_c of 230 °C (MAPbI_3), 251 °C (MAPbBr_3) and 148 °C (MAPbCl_3). At still higher temperatures, the lead halide also evaporates, leaving a blank glass substrate behind after the process. In the

following paragraphs, we will continue with an investigation of the mixed MAPb(I,Br) system.

Halide exchange

I. $\text{MAPbI}_3 \rightarrow \text{MAPbBr}_3$. Several groups have reported about the possibility to easily exchange the halide in methylammonium lead halide perovskites.^{41–43} We follow this line and will first try to convert MAPbI_3 into MAPbBr_3 inside the evaporation chamber. Theoretical calculations of Brivio *et al.* predict a miscibility gap of the MAPbI_3 – MAPbBr_3 system. The width of this miscibility gap however decreases with increasing temperature and at a critical temperature of 70 °C the gap should be closed and both compounds should intermix completely.⁴⁴ According to this, at a substrate temperature of 120 °C the two perovskite structures MAPbI_3 and MAPbBr_3 should be completely miscible.

In order to investigate this, we first deposit a MAPbI_3 thin film by co-evaporating MAI and PbI_2 the same way as described previously (Fig. 4 a). After a single phase MAPbI_3 perovskite thin film with a thickness of approximately 510 nm is grown, the PbBr_2 shutter is closed and the MABr and PbBr_2 sources are cooled down (t_1). Subsequently, the evaporation of MABr is started. In order to facilitate the halide exchange, the substrate is then heated to 120 °C (t_2). In consequence, the hot MAPbI_3 thin films are now exposed to a constant flux of MABr molecules.

Upon heating and exposure to MABr , the initial MAPbI_3 (200) peak gains intensity and then starts shifting continuously towards higher diffraction angles. Assuming Vegard's law,⁴⁵ the lattice parameter of MAPb(I,Br)_3 should vary linearly with

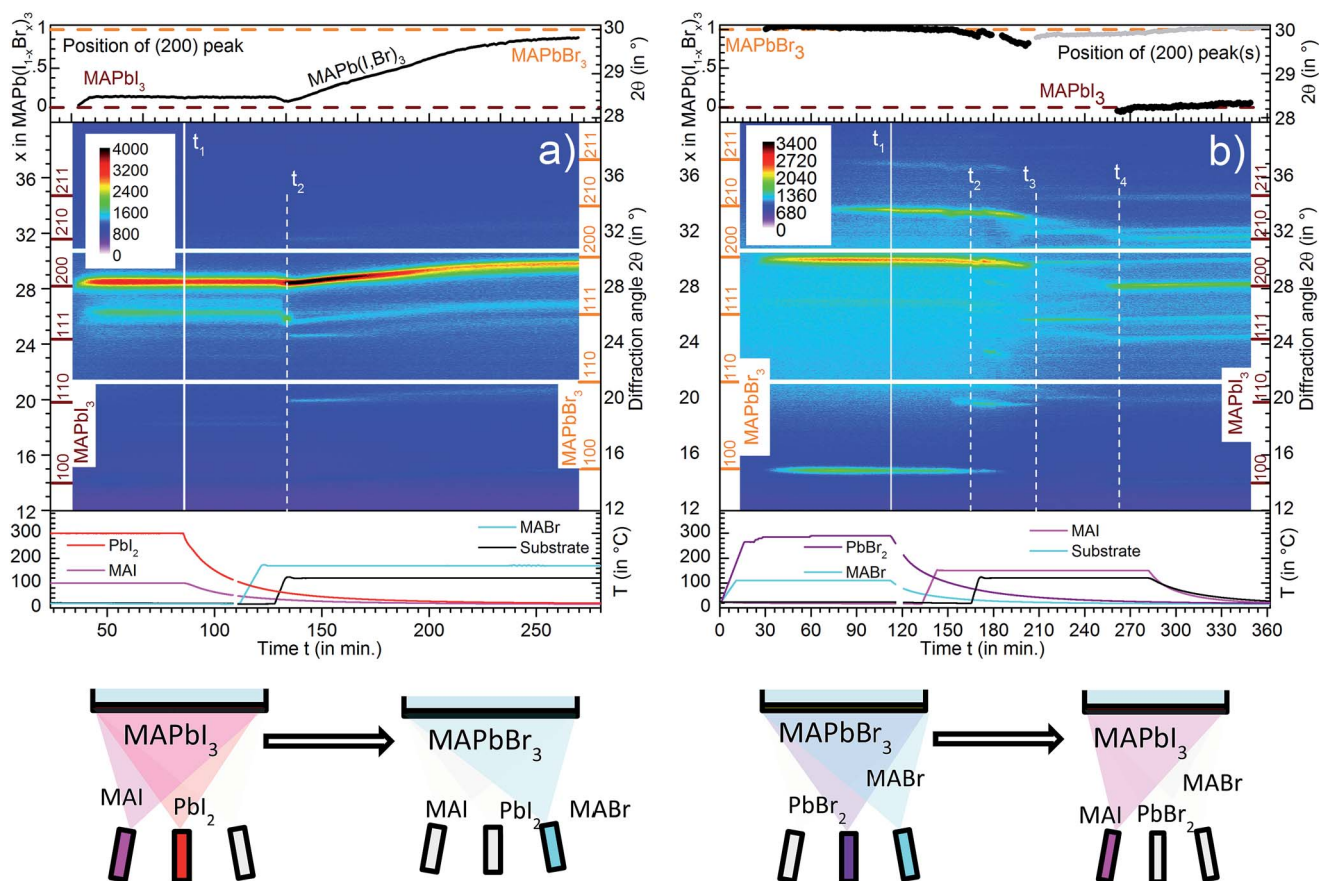


Fig. 4 (a) Growth of a MAPbI_3 thin film by two source co-evaporation and subsequent conversion into MAPbBr_3 upon exposure to MABr at a substrate temperature of 120°C . (b) Growth of a MAPbBr_3 thin film and subsequent conversion into MAPbI_3 . The top graph of both figures shows the evolution of the (200) peak position during the course of the experiment.

composition between the two single halide perovskites. The position of the (200) peak can therefore be directly translated into a $\text{Br}/(\text{I} + \text{Br})$ ratio x of the mixed compound $\text{MAPb}(\text{I}_{1-x}\text{Br}_x)_3$. In the upper part of the diagram in Fig. 4a, we have plotted the peak position of the (200) peak extracted from a fit to the XRD data. The peak positions of the two pure single halide perovskites are marked in this diagram with two dotted lines (brown: MAPbI_3 at 28.238° and orange: MAPbBr_3 at 30.000°). At the left hand side, the peak position is related to the I/Br ratio assuming Vegard's law.

After a continuous shift to higher diffraction angles, the $\text{MAPb}(\text{I},\text{Br})_3$ (200) peak position finally levels off at $29.80(2)^\circ$. This is only slightly below the peak position measured for the pure MAPbBr_3 (30.00°). As the higher substrate temperature already accounts for a small thermal shift of 0.16° to lower diffraction angles, we conclude that after the halide exchange the film is completely converted into MAPbBr_3 . In this case, the conversion took place through a gradual exchange of I by Br , without distorting the crystal structure. This means that the perovskite film underwent the complete compositional range from pure MAPbI_3 to MAPbBr_3 while maintaining and preserving the high crystallinity and ordering of the crystal lattice at all times, in agreement with the prediction of Brivio and co-workers.

These observations are in contrast to the following experiment, where the halide exchange is induced the other way around, starting with a single halide MAPbBr_3 perovskite.

II. $\text{MAPbBr}_3 \rightarrow \text{MAPbI}_3$. Fig. 4b shows the conversion of a MAPbBr_3 perovskite film into a MAPbI_3 thin film upon exposure to MAI . The experiment is conducted in the same way as the last one, except that we start with the co-evaporation of $\text{MABr}/\text{PbBr}_2$ to grow a MAPbBr_3 thin film first (590 nm), and then heat the substrate and expose the grown film to a flux of MAI . Fig. 4b shows clearly how from time t_2 on, the main peaks of the MAPbBr_3 perovskite start shifting to lower diffraction angles. However, and in contrast to the last experiment, at the same time their intensity is strongly reduced. Both, thermal expansion and the exchange of Br ions by I ions will cause a lattice expansion explaining the shift to lower diffraction angles. At time t_3 , the main (200) peak nearly vanished. Only a small broad band with a maximum at $29.83(3)^\circ$ remains. The position of this residual peak stays constant and only gradually shifts to higher diffraction angles again when the sample is cooled down at the end of the experiment, finishing at $30.03(3)^\circ$ and at less than 12% of its maximum intensity. Also around time t_3 a new peak arises at approximately 25.8° , which is assigned to the (111) peak of MAPbBr_3 . This change in the peak intensity of different MAPbBr_3 peaks is again interpreted as

a change in the preferential orientation of the MAPbBr₃ thin film, similar to the changing preferential orientation observed for the MAPbBr₃ thin film in Fig. 3b. At time *t*₄, a new peak arises at 28.17(3)° and soon becomes the most intense peak. This peak appears simultaneously with other peaks characteristic of the MAPbI₃ perovskite. At the end of the experiment, the remaining XRD peaks correspond to the single halide MAPbI₃, with small residues of the initial MAPbBr₃.

In summary, we were indeed able in this experiment to nearly completely exchange the Br in MAPbBr₃ and substitute it with I. However, the exchange was not based on a continuous exchange of halides as in the former experiment. In contrast, our results indicate that the crystal structure of the initial perovskite over time got severely distorted and then its crystalline structure was again built up upon incorporation of the I ions. This is not predicted by the theoretical calculations of Brivio *et al.*, in fact a similar behaviour would rather be expected if a fundamental miscibility gap between the two compounds existed.

We conclude with a simple remark: It is much easier in terms of the crystal lattice to replace I by Br, than the other way around. The implication of this will be discussed further in the Discussion section. Please note that during equivalent experiments with unheated substrates, we did not observe any halide exchange during the timescale of our experiments (1–3 hours).

Growing mixed MAPb(I,Br)₃ thin films by two source co-evaporation

I. Co-evaporation of MAI and PbBr₂. In the next step, we try to grow mixed MAPb(I,Br) thin films by co-evaporating MAI and

PbBr₂, in analogy to the initial work on co-evaporated MAPb(I,Cl)₃ thin films, where MAI and PbCl₂ were used as precursors.^{18,28} Since a relationship between the MAI/PbBr₂ flux ratio and the amount of I/Br inside the deposited final MAPb(I,Br)₃ thin film is expected, several different depositions with varying PbBr₂ fluxes at constant MAI evaporation rates have been realized. Fig. 5a summarizes the outcomes of these experiments in an illustrative manner. At the beginning, a low PbBr₂ crucible temperature leads to a small flux of PbBr₂ molecules arriving at the substrate and therefore a huge excess of MAI. A thin film with a perovskite crystal structure forms. The position of the (200) peak is 28.48(2)°, very close to the pure MAPbI₃ perovskite. We then start to increase the PbBr₂ flux arriving at the substrate by linearly increasing the PbBr₂ source temperature.

Two observations can be made: (1) a new peak close to the position of the MAPbBr₃ (200) peak appears. (2) The (200) peak is split into two peaks, with the most intense contribution gradually shifting to higher diffraction angles and the second contribution shifting only slightly to lower angles. The first contribution eventually approaches 29.66° and merges with the new peak at high diffraction angles observed in (1). The second contribution stays nearly constant and only slightly shifts to lower diffraction angles, finishing at 28.24(2)°. In consequence, for a short intermediate time, even three separate peaks can be distinguished in the range between 28° and 30°. We interpret the observed phenomena in the following way: (1) a new, very Br-rich MAPb(I,Br)₃ thin film starts growing on top of the deposited very I-rich MAPb(I,Br)₃ at the beginning, (2) gradually some additional Br is incorporated into the growing film, while some of the initially grown I-rich MAPb(I,Br)₃ is preserved. Over

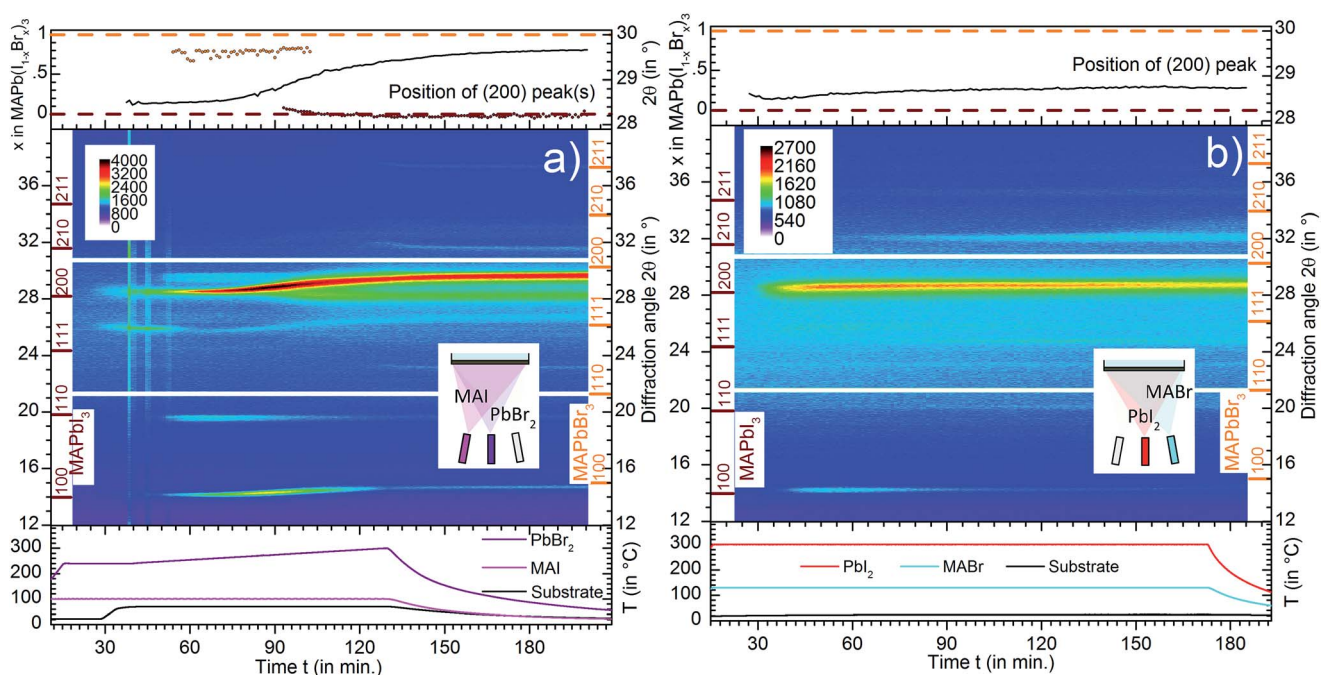


Fig. 5 Growth of mixed MAPb(I,Br)₃ thin films by two-source co-evaporation. (a) Co-evaporation of MAI and PbBr₂. Please note the increasing PbBr₂ substrate temperature resulting in an increasing PbBr₂ flux towards the substrate during the course of the experiment. (b) Static growth of single phase MAPbI₂Br thin films by co-evaporation of MABr and Pbl₂.

the course of the experiment, the most intense (200) peak gradually shifts to the position of the new peak appearing at (1). Our experience with various intents of growing mixed MAPb(I,Br)₃ thin films through the evaporation of MAI and PbBr₂ indicates that this growth route tends to form phase segregations with I-rich and Br-rich thin films co-existing instead of single phase films with mixed composition. In a variety of experiments we tried different substrate temperatures and MAI/PbBr₂ flux ratios, but were not able to find stable growth conditions that allow the deposition of single phase MAPb(I,Br)₃ perovskites with compositions in the middle of the compositional range following this growth route.

II. Co-evaporation of MABr and PbI₂. However, the situation is changed if the halides in the precursors are exchanged and MABr and PbI₂ are co-evaporated instead. With this precursor combination, we were able to grow single phase MAPb_{1-x}Br_x thin films with compositions of *x* between 0.3 and 1 by co-evaporating MABr and PbI₂. Fig. 5b shows the static growth of a single phase MAPb(I_xBr_{1-x})₃ thin film with a thickness of 780 nm, whose (200) position of 28.74°(2) corresponds to an *x* of approximately 0.3. This experiment demonstrates the potential to grow single phase MAPb(I_{1-x}Br_x)₃ thin films without initial phase segregation and under static growth conditions in a vacuum. The film shows a nice homogenous morphology with crystallite sizes around 100–200 nm. A scanning electron micrograph of the film and more additional data on its photoluminescence can be found in the ESI.† From our preliminary experiments we conclude that by varying the MABr/PbI₂ flux ratios and substrate temperature, in principle all compositions between *x* = 0.3 and 1 should be accessible following this MABr/PbI₂ growth route.

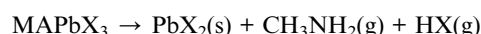
Discussion

There is a heated debate on the intrinsic (in)stability of MAPbI₃, as its stability is a prerequisite for successful application and commercialization as a solar cell absorber. Several recent publications have predicted the thermodynamic instability of MAPbI₃ even at room temperature. Theoretical density functional theory (DFT) calculations resulted in a very small negative (−9.64 kJ mol^{−1})⁴⁶ or even a positive (6.7 kJ mol^{−1})⁴⁷ enthalpy for the formation of MAPbI₃ from its MAI and PbI₂ precursor constituents. Nagabushana *et al.* have suggested a positive enthalpy of the formation of 34.50 kJ mol^{−1} for MAPbI₃ from their experimental solution calorimetry analysis.²³ In contrast to this, our results demonstrate the spontaneous formation of MAPbI₃ even at room temperature. By co-evaporating MAX and PbX₂ (X = I, Br, Cl), single phase perovskite films can be easily obtained. Dense films with good crystallinity giving intense XRD reflections could be formed without substrate heating, giving strong indication that the compound MAPbI₃ is energetically favourable and more stable than its two precursor phases, at least under the conditions used during the growth (high vacuum and MAX oversupply, 25 °C). As an additional check, MAPbI₃ thin films did not show any variations when left inside the vacuum (no air exposure) inside our XRD setup for up to three days.

The previously mentioned publications of Buin *et al.*⁴⁶ and Zhang *et al.*⁴⁷ predict an increasing thermodynamic stability of

the MAPbX₃ perovskites in the sequence I–Br–Cl with the MAPbCl₃ being the most stable. As a matter of fact, the tolerance factor of MAPbCl₃ (Table 1) is the closest to 1 and hence this compound is expected to come closest to the ideal cubic perovskite structure. For inorganic perovskites, the formation reaction becomes more exothermic with an increasing tolerance factor.⁴⁸ From these considerations, one would expect MAPbCl₃ to be the most stable of the three perovskites.

In our experiments, all three single halide perovskites decompose in a vacuum on loss of gaseous species into their corresponding lead halides. Interestingly, the first decrease of the MAPbX₃ signal from the perovskite layers is observed at temperatures higher or similar to the evaporation temperatures used for the MAX temperatures: (MAI: 170 °C/130 °C, MABr: 230 °C/130 °C, MAcl: 110 °C/110 °C). In contrast to predictions, we found that MAPbCl₃ was the least thermally stable as it decomposed at the lowest temperatures with a very sharp transition. Already at 150 °C, nearly all MAPbCl₃ was converted into its lead halide, while this only occurred at 260 °C for MAPbI₃ and MAPbBr₃, both showing much longer transitions. This is in agreement with experiments by Dualeh *et al.*, who measured lower onset temperatures for the sublimation of MAcl (185 °C) than for MAI (234 °C) in a thermogravimetric analysis of precursor powders.⁹ In this work it was also suggested that decomposition of MAPbI₃ and MAPbCl₃ occurs *via* subsequent HX and methyl amine (CH₃NH₂) sublimation, and not in one single step of MAX sublimation. This is in agreement with recently published data on MAPbX₃ powders. Brunetti *et al.* also found the MAPbCl₃ compound to be significantly less stable than its Br/I counterparts on heating under non-ambient conditions.⁴⁹ Based on an additional Knudsen effusion mass spectroscopy and Knudsen effusion mass loss analysis, they proposed the following thermal decomposition pathway under non-ambient conditions:



From their experiments, they calculated comparable decomposition enthalpies for MAPbI₃ and MAPbBr₃, but significantly lower ones for MAPbCl₃ for this specific decomposition route. The standard enthalpy of formation ΔH_f° (298 K) from the elements for the MAPbX₃ compounds is stated by Brunetti as −688.3 kJ mol^{−1} (MAPbCl₃), −567.5 kJ mol^{−1} (MAPbBr₃) and −403.6 kJ mol^{−1} (MAPbI₃). However, the decreasing trend of absolute values is mainly due to the trends observed for the formation of the corresponding lead halides and hydrogen halide species and therefore does not correspond to an increased stability of the MAPbCl₃ compound (Table 2).⁴⁹

Deretzis *et al.* have shown by *in situ* XRD measurements and *ab initio* calculations that MAPbI₃ thin films should be thermodynamically relatively stable at room temperature and in the absence of water. Moisture (60% relative humidity) or thermal stress (150 °C) reduced the lifetime of the perovskite material drastically.⁵⁰ Their DFT calculations support the decomposition pathway postulated by Brunetti, as they show that the calculated dissociation energies for various atomic and molecular defects

Table 2 Comparison of the critical temperature T_c and standard enthalpy of formation from the elements ΔH_f° for the perovskite compounds MAPbX_3 and the precursors. The critical temperature T_c at which approximately half of the perovskite film was decomposed into the lead halide was derived as outlined earlier in the manuscript

X	I	Br	Cl	Ref.
T_c	~ 500 K	~ 520 K	~ 420 K	This work
ΔH_f° MAPbX_3 (kJ mol ⁻¹)	-403.6	-567.5	-688.3	49
ΔH_f° PbX_2 (kJ mol ⁻¹)	-175.5	-278.7	-359.4	23
ΔH_f° MAX (kJ mol ⁻¹)	-200.7	-258.9	-298.3	23

in MAPbI_3 are lowest for HI (1.31 eV). In other words, HI vacancies can be formed with low energetic cost. The volatile HI compound is expected to be readily lost, especially under vacuum conditions. In consequence, Deretzis *et al.* observed an instability of the MAPbI_3 compound and degradation to PbI_2 already at room temperature if subjected to vacuum for prolonged times (1 month), due to dissociation processes at the surface and the loss of volatile HI species. It has to be noted, however, that their samples seem to have been in contact with air during sample preparation and therefore some moisture might have already soaked into them.

In summary, there is still some debate on the gaseous species involved in the thermal decomposition,^{51,52} but the degradation to PbX_2 is well established. The rate and onset of thermal decomposition is also discussed quite controversially and seem to strongly depend on (a) air exposure (b) temperature and the (c) deposition process.

We find MAPbCl_3 to be the least thermally stable of the three investigated MAPbX_3 compounds. As we cannot detect gaseous phases with our experimental setup, we could not verify the stated gaseous decomposition products or discriminate them from MAX. The phase transition temperatures (from the literature) and the critical temperature T_c (from this work) are schematically depicted in Fig. 6.

Finally, from the (200) (MAPbI_3) and (100) (MAPbBr_3 , MAPbCl_3) peak positions of our XRD data we can derive the temperature dependency of the lattice constants of the three cubic perovskite films (Fig. 7). The lattice parameters a of the cubic MAPbI_3 and MAPbCl_3 increase approximately linearly with temperature. From a linear fit to this data, the linear thermal coefficients of expansion at 70 °C can be estimated as $3.6(1) \times 10^{-5} \text{ K}^{-1}$ for MAPbI_3 . This compares well to the reported $4.4 \times 10^{-5} \text{ K}^{-1}$ based on powder diffraction and $4.2 \times 10^{-5} \text{ K}^{-1}$ based on first principles calculations in the quasi-harmonic approximation.⁵³ For MAPbBr_3 , the lattice parameter does not increase linearly in the temperature region where recrystallization and reorientation occurs (100–200 °C). This impedes an accurate analysis of the thermal expansion coefficient in this range and might be caused by stress acting on the film during the recrystallization. We therefore limit the linear fit of the lattice parameter to the temperature range below 60 °C and calculate an α_L of $3.3(1) \times 10^{-5} \text{ K}^{-1}$ at room temperature. In the case of MAPbCl_3 , we derive a linear coefficient of thermal expansion α_L of $2.3(1) \times 10^{-5} \text{ K}^{-1}$ at room temperature.

The opportunity to synthesize mixed perovskites with different halide ratios opens very attractive opportunities to

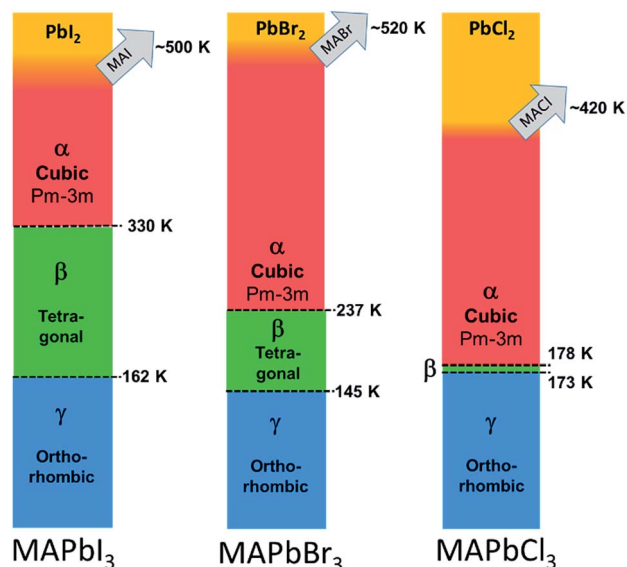


Fig. 6 Schematic representation of the phase transitions and decomposition of MAPbI_3 , MAPbBr_3 and MAPbCl_3 .

tune the bandgap for specific applications. Despite the fact that it is the most investigated system, there is still a dispute if the MAPbI_3 – MAPbBr_3 system is completely miscible or not. Several research groups have reported the synthesis of powders and thin films over the complete range of compositions.^{54–56} Jacobsson *et al.* *e.g.* have prepared $\text{MAPb}(\text{I}_{1-x}\text{Br}_x)_3$ thin films by spin-coating covering the complete range of x from 1 to 0 and band gaps ranging from 1.59 eV to 2.31.⁵⁷ On the other hand, Brivio *et al.* have postulated on the basis of DFT calculations that at 300 K $\text{MAPb}(\text{I}_{1-x}\text{Br}_x)_3$ perovskites in the composition range between $0.3 < x < 0.6$ should be thermodynamically unstable and should

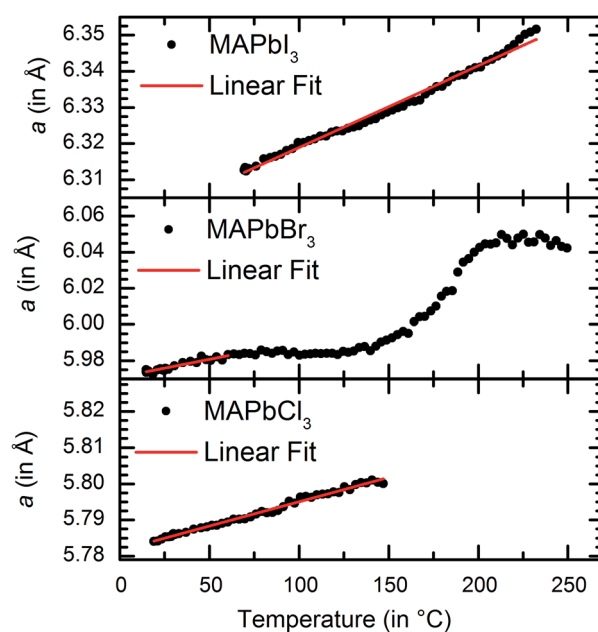


Fig. 7 Temperature dependence of the lattice parameter a of the three MAPbX_3 perovskites studied in this work.

therefore segregate into I-rich and Br-rich phases.⁴⁴ Finally, Hoke *et al.* also found that mixed $\text{MAPb}(\text{I}_{1-x}\text{Br}_x)_3$ perovskites can be synthesized over the complete compositional range by spin-coating. For an increasing Br/I ratio they measured a linear decrease in the lattice parameter, but upon illumination a reversible phase segregation of I-rich and Br-rich phases occurred.⁵⁸ This phenomenon was later reproduced and verified by several research groups.^{29,59}

In our experiments, we found a continuous transition from MAPbI_3 to MAPbBr_3 under continuous supply of MABr. The transition from MAPbBr_3 to MAPbI_3 , however possible, did not take place in a continuous manner. Furthermore, we did not succeed in synthesizing single phase $\text{MAPb}(\text{I}_{1-x}\text{Br}_x)_3$ thin films with $x = 0.3$ from MAI and PbBr_2 precursors. In contrast, in all our attempts phase segregation of different I-rich and Br-rich phases was observed. In contrast to this, evaporation of MABr and PbI_2 precursors lead to the growth of films with the desired stoichiometry without secondary phases even at room temperature.

We interpret these findings in view of the different Pb–X bonding strengths of I and Br and the different ionic radii. In both, the PbX_2 precursors as well as the final perovskite structure, the lead and halide ions build octahedra with similar bond lengths and bond strength. In view of the formation enthalpies of $\text{PbI}_2/\text{PbBr}_2$ or $\text{MAPbI}_3/\text{MAPbBr}_3$, it is energetically much easier to exchange one I by Br than the other way around (see Table 2). Also from purely steric arguments the $\text{Br} \rightarrow \text{I}$ exchange is favoured before the $\text{I} \rightarrow \text{Br}$ exchange, as the smaller Br ion fits easily into the large Pb–I cage of MAPbI_3 , while the large I ion does not fit in or move as easily within a smaller MAPbBr_3 lattice. In consequence, it is easier to substitute I by Br than Br by I. The more promising route towards the synthesis of mixed $\text{MAPb}(\text{I,Br})_3$ thin films by co-evaporation is therefore by evaporating MABr precursors and co-evaporating it with PbI_2 , or partly convert MAPbI_3 thin films by exposing them to MABr.

Our results demonstrate on the one hand the power of *in situ* diagnostics, as we were able to conduct all measurements on pristinely grown thin films under vacuum conditions, *i.e.* without air exposure and directly during the growth. On the other hand, they verify the decomposition pathways and the thermal instability of MAPbX_3 thin films at moderate temperatures, and therefore underline concerns on lifetime. The differences in the thermal decomposition rates reported by the different groups are a clear hint to the importance and influence of the different experimental conditions and the difficulty to obtain reliable and reproducible results for these hybrid perovskite compounds. In terms of mixed $\text{MAPb}(\text{I,Br})_3$ thin films our results highlight the importance of the growth route and the selection of precursor combinations in order to grow single phase materials. They show how MAPbIBr_2 and similar compounds can be synthesized with simple two-source co-evaporation opening a promising perspective towards vacuum-based and low temperature fabrication of top cells for tandem applications.

Conclusions

In conclusion, we have demonstrated that single halide MAPbX_3 ($X = \text{I, Br, Cl}$) perovskite thin films with a cubic crystal structure

can be easily grown by co-evaporation of MAX and PbX_2 precursors. The upper limits for the thermal stability of these films before they decompose into the corresponding lead halides have been determined. Upon application of a linear temperature ramp of 3 K min^{-1} approximately half of the perovskite film had been decomposed at a temperature of $230 \text{ }^\circ\text{C}$ (MAPbI_3), $251 \text{ }^\circ\text{C}$ (MAPbBr_3) and $148 \text{ }^\circ\text{C}$ (MAPbCl_3). The linear increase of the lattice parameter for MAPbI_3 and MAPbCl_3 allowed the determination of the linear coefficient of thermal expansion α_L to be $3.6 \times 10^{-5} \text{ K}^{-1}$ (MAPbI_3), $3.3 \times 10^{-5} \text{ K}^{-1}$ (MAPbBr_3) and $2.3 \times 10^{-5} \text{ K}^{-1}$ (MAPbCl_3).

Furthermore, we could show that upon evaporation of MAI and PbBr_2 , phase segregation takes place and two perovskite phases with stoichiometry close to MAPbI_3 and MAPbBr_3 tend to be present. Pure MAPbBr_3 can be converted into MAPbI_3 if it is heated to $120 \text{ }^\circ\text{C}$ and exposed to MAI vapour, but the transition was not continuous but rather disruptive and not entirely complete. The analogous conversion of $\text{MAPbI}_3 \rightarrow \text{MAPbBr}_3$ took place continuously and completely. Single phase $\text{MAPbI}_2\text{Br}_1$ thin films were successfully synthesized by co-evaporating MABr and PbI_2 precursors. We thus were able to develop a new promising method for the preparation of mixed $\text{MAPb}(\text{I,Br})_3$ thin films by a simple two-source co-evaporation approach.

Conflicts of interest

There are no conflicts to declare.

Acknowledgements

Financial support from the German Federal Ministry of Research and Education (BMBF) under contract number 03EK3570B (StrukturSolar II) is gratefully acknowledged.

References

- 1 A. Kojima, K. Teshima, Y. Shirai and T. Miyasaka, *J. Am. Chem. Soc.*, 2009, **131**, 6050–6051.
- 2 H.-S. Kim, C.-R. Lee, J.-H. Im, K.-B. Lee, T. Moehl, A. Marchioro, S.-J. Moon, R. Humphry-Baker, J.-H. Yum, J. E. Moser, *et al.*, *Sci. Rep.*, 2012, **2**, 591.
- 3 M. M. Lee, J. Teuscher, T. Miyasaka, T. N. Murakami and H. J. Snaith, *Science*, 2012, **338**, 643–647.
- 4 N. Arora, M. I. Dar, A. Hinderhofer, N. Pellet, F. Schreiber, S. M. Zakeeruddin and M. Grätzel, *Science*, 2017, **358**, 768–771.
- 5 W. S. Yang, J. H. Noh, N. J. Jeon, Y. C. Kim, S. Ryu, J. Seo and S. I. Seok, *Science*, 2015, **348**, 1234–1237.
- 6 Q. Dong, Y. Fang, Y. Shao, P. Mulligan, J. Qiu, L. Cao and J. Huang, *Science*, 2015, **347**, 967–970.
- 7 C. Wehrenfennig, G. E. Eperon, M. B. Johnston, H. J. Snaith and L. M. Herz, *Adv. Mater.*, 2013, **26**, 1584–1589.
- 8 B. Conings, J. Drijkoningen, N. Gauquelin, A. Babayigit, J. D'Haen, L. D'Olieslaeger, A. Ethirajan, J. Verbeeck, J. Manca, E. Mosconi, F. D. Angelis and H.-G. Boyen, *Adv. Energy Mater.*, 2015, **5**, 1500477.
- 9 A. Dualeh, P. Gao, S. I. Seok, M. K. Nazeeruddin and M. Grätzel, *Chem. Mater.*, 2014, **26**, 6160–6164.

- 10 J. S. Manser, M. I. Saidaminov, J. A. Christians, O. M. Bakr and P. V. Kamat, *Acc. Chem. Res.*, 2016, **49**, 330–338.
- 11 N. Chander, A. F. Khan, P. S. Chandrasekhar, E. Thouti, S. K. Swami, V. Dutta and V. K. Komarala, *Appl. Phys. Lett.*, 2014, **105**, 033904.
- 12 T. Leijtens, G. E. Eperon, S. Pathak, A. Abate, M. M. Lee and H. J. Snaith, *Nat. Commun.*, 2013, **4**, 2885.
- 13 T. A. Berhe, W.-N. Su, C.-H. Chen, C.-J. Pan, J.-H. Cheng, H.-M. Chen, M.-C. Tsai, L.-Y. Chen, A. A. Dubale and B.-J. Hwang, *Energy Environ. Sci.*, 2016, **9**, 323–356.
- 14 T. Leijtens, K. Bush, R. Checharoen, R. Beal, A. Bowring and M. D. McGehee, *J. Mater. Chem. A*, 2017, **5**, 11483–11500.
- 15 C. Manspeaker, S. Venkatesan, A. Zakhidov and K. S. Martirosyan, *Curr. Opin. Chem. Eng.*, 2017, **15**, 1–7.
- 16 O. Malinkiewicz, C. Roldán-Carmona, A. Soriano, E. Bandiello, L. Camacho, M. K. Nazeeruddin and H. J. Bolink, *Adv. Energy Mater.*, 2014, **4**, 1400345.
- 17 M. Sessolo, C. Momblona, L. Gil-Escrig and H. J. Bolink, *MRS Bull.*, 2015, **40**, 660–666.
- 18 M. Liu, M. B. Johnston and H. J. Snaith, *Nature*, 2013, **501**, 395–398.
- 19 C. Momblona, O. Malinkiewicz, C. Roldán-Carmona, A. Soriano, L. Gil-Escrig, E. Bandiello, M. Scheepers, E. Edri and H. J. Bolink, *APL Mater.*, 2014, **2**, 081504.
- 20 G. Niu, X. Guo and L. Wang, *J. Mater. Chem. A*, 2015, **3**, 8970–8980.
- 21 S. Yang, W. Fu, Z. Zhang, H. Chen and C.-Z. Li, *J. Mater. Chem. A*, 2017, **5**, 11462–11482.
- 22 T. Baikie, Y. Fang, J. M. Kadro, M. Schreyer, F. Wei, S. G. Mhaisalkar, M. Graetzel and T. J. White, *J. Mater. Chem. A*, 2013, **1**, 5628.
- 23 G. P. Nagabhushana, R. Shivaramaiah and A. Navrotsky, *Proc. Natl. Acad. Sci.*, 2016, **113**, 7717–7721.
- 24 N. K. Kumawat, A. Dey, A. Kumar, S. P. Gopinathan, K. L. Narasimhan and D. Kabra, *ACS Appl. Mater. Interfaces*, 2015, **7**, 13119–13124.
- 25 R. Comin, G. Walters, E. S. Thibau, O. Voznyy, Z.-H. Lu and E. H. Sargent, *J. Mater. Chem. C*, 2015, **3**, 8839–8843.
- 26 C. Li, J. Wei, M. Sato, H. Koike, Z.-Z. Xie, Y.-Q. Li, K. Kanai, S. Kera, N. Ueno and J.-X. Tang, *ACS Appl. Mater. Interfaces*, 2016, **8**, 11526–11531.
- 27 A. Sadhanala, S. Ahmad, B. Zhao, N. Giesbrecht, P. M. Pearce, F. Deschler, R. L. Z. Hoyer, K. C. Gödel, T. Bein, P. Docampo, S. E. Dutton, M. F. L. De Volder and R. H. Friend, *Nano Lett.*, 2015, **15**, 6095–6101.
- 28 P. Pistor, J. Borchert, W. Fränzel, R. Csuk and R. Scheer, *J. Phys. Chem. Lett.*, 2014, **5**, 3308–3312.
- 29 E. L. Unger, L. Kegelmann, K. Suchan, D. Sörell, L. Korte and S. Albrecht, *J. Mater. Chem. A*, 2017, **5**, 11401–11409.
- 30 L. Gil-Escrig, A. Miquel-Sempere, M. Sessolo and H. J. Bolink, *J. Phys. Chem. Lett.*, 2015, **6**, 3743–3748.
- 31 V. M. Goldschmidt, *Die Naturwissenschaften*, 1926, **14**, 477–485.
- 32 G. Kieslich, S. Sun and A. K. Cheetham, *Chem. Sci.*, 2014, **5**, 4712–4715.
- 33 S. A. Bretschneider, J. Weickert, J. A. Dorman and L. Schmidt-Mende, *APL Mater.*, 2014, **2**, 040701.
- 34 C. Motta, F. El-Mellouhi, S. Kais, N. Tabet, F. Alharbi and S. Sanvito, *Nat. Commun.*, 2015, **6**, 7026.
- 35 Y. Kawamura and H. Mashiyama, *J. Korean Phys. Soc.*, 1999, **35**, 1437.
- 36 A. Poglitsch and D. Weber, *J. Chem. Phys.*, 1987, **87**, 6373.
- 37 K.-H. Wang, L.-C. Li, M. Shellaiah and K. W. Sun, *Sci. Rep.*, 2017, **7**.
- 38 R. D. Shannon, *Acta Crystallogr., Sect. A: Cryst. Phys., Diffraction, Theor. Gen. Crystallogr.*, 1976, **32**, 751–767.
- 39 J. Borchert, H. Boht, W. Fränzel, R. Csuk, R. Scheer and P. Pistor, *J. Mater. Chem. A*, 2015, **3**, 19842–19849.
- 40 G. Kaune, S. Hartnauer and R. Scheer, *Phys. Status Solidi A*, 2014, **211**, 1991–1996.
- 41 G. Li, J. Y.-L. Ho, M. Wong and H. S. Kwok, *J. Phys. Chem. C*, 2015, **119**, 26883–26888.
- 42 I. C. Smith, M. D. Smith, A. Jaffe, Y. Lin and H. I. Karunadasa, *Chem. Mater.*, 2017, **29**, 1868–1884.
- 43 D. Solis-Ibarra, I. C. Smith and H. I. Karunadasa, *Chem. Sci.*, 2015, **6**, 4054–4059.
- 44 F. Brivio, C. Caetano and A. Walsh, *J. Phys. Chem. Lett.*, 2016, **7**, 1083–1087.
- 45 L. Vegard, *Z. Phys.*, 1921, **5**, 17–26.
- 46 A. Buin, R. Comin, J. Xu, A. H. Ip and E. H. Sargent, *Chem. Mater.*, 2015, **27**, 4405–4412.
- 47 Y.-Y. Zhang, S. Chen, P. Xu, H. Xiang, X. G. Gong, A. Walsh and S.-H. Wei, *Chin. Phys. Lett.*, 2018, **35**, 11.
- 48 A. Navrotsky, *ECS Trans.*, 2012, **45**, 11–17.
- 49 B. Brunetti, C. Cavallo, A. Ciccioli, G. Gigli and A. Latini, *Sci. Rep.*, 2016, **6**.
- 50 I. Deretzi, A. Alberti, G. Pellegrino, E. Smecca, F. Giannazzo, N. Sakai, T. Miyasaka and A. La Magna, *Appl. Phys. Lett.*, 2015, **106**, 131904.
- 51 A. Latini, G. Gigli and A. Ciccioli, *Sustainable Energy Fuels*, 2017, **1**, 1351–1357.
- 52 E. J. Juarez-Perez, Z. Hawash, S. R. Raga, L. K. Ono and Y. Qi, *Energy Environ. Sci.*, 2016, **9**, 3406–3410.
- 53 F. Brivio, J. M. Frost, J. M. Skelton, A. J. Jackson, O. J. Weber, M. T. Weller, A. R. Goñi, A. M. A. Leguy, P. R. F. Barnes and A. Walsh, *Phys. Rev. B: Condens. Matter Mater. Phys.*, 2015, **92**, 144308.
- 54 P. Fedeli, F. Gazza, D. Calestani, P. Ferro, T. Besagni, A. Zappettini, G. Calestani, E. Marchi, P. Ceroni and R. Mosca, *J. Phys. Chem. C*, 2015, **119**, 21304–21313.
- 55 J. H. Noh, S. H. Im, J. H. Heo, T. N. Mandal and S. I. Seok, *Nano Lett.*, 2013, **13**, 1764–1769.
- 56 B.-w. Park, B. Philippe, S. M. Jain, X. Zhang, T. Edvinsson, H. Rensmo, B. Zietz and G. Boschloo, *J. Mater. Chem. A*, 2015, **3**, 21760–21771.
- 57 T. J. Jacobsson, J.-P. Correa-Baena, M. Pazoki, M. Saliba, K. Schenk, M. Grätzel and A. Hagfeldt, *Energy Environ. Sci.*, 2016, **9**, 1706–1724.
- 58 E. T. Hoke, D. J. Slotcavage, E. R. Dohner, A. R. Bowring, H. I. Karunadasa and M. D. McGehee, *Chem. Sci.*, 2015, **6**, 613–617.
- 59 C. M. Sutter-Fella, Y. Li, M. Amani, J. W. Ager, F. M. Toma, E. Yablonovitch, I. D. Sharp and A. Javey, *Nano Lett.*, 2016, **16**, 800–806.

Closing Discussion

One significant finding concerning the growth of the perovskites is that during the co-evaporation of PbI₂ and MAI, MAPbI₃ formed on a substrate with a temperature of 70 °C. There are some theoretical calculations that have determined a positive reaction enthalpy for the reaction PbI₂ + MAI → MAPbI₃, which would imply that the perovskite should not form but instead spontaneously decompose into its constituents at RT [159, 160]. Consequently, a formation at an even higher temperature should not be possible. Our results contradict this and show that, at least under the conditions given, the perovskite can form even at the elevated temperature of 70 °C. Some further support for this was gained by keeping the perovskite in vacuum at RT for 3 days, after which no change in the XRD signal was visible. Thus, at least for this short time frame, no spontaneous decomposition could be detected. By using PbI₂ and MABr as precursors, a MAPb(I_{1-x}Br_x)₃ perovskite with $x \approx 0.3$ could successfully be prepared. The onsets of thermal decomposition for the studied materials were 120 °C for MAPbI₃, 120 °C for MAPbBr₃ and 85 °C for MAPbCl₃. All materials decomposed by losing their MAX component, while PbX₂ remained. This confirms the limited heat stability of these materials while also highlighting that the limiting factor of this stability is likely the MA component. As noted in the paper, some research suggests that the decomposition of the MAPbX₃ perovskites might be initiated by a loss of an HX with subsequent loss of CH₃NH₂. These results hint at the significant role that MA takes in the (in-)stability of these materials. A substitution of this component with a more robust molecule, like FA, or even a fully inorganic atom, like Cs, could therefore have significant impact on the overall robustness of the resulting compound. The latter case will be regarded in the following paper.

Table 4.1: The time it takes for a given halide species to diffuse through a 500 nm thick layer of an I or Br rich MAPbX₃ perovskite. The diffusion constants are taken from Osherov et al. [161].

Time in process	Scenario	$D[\text{cm}^2/\text{s}]$	$t [\text{min}]$
Beginning	Br in I rich MAPbX ₃	8.50×10^{-12}	4.9
Main part	I in I rich MAPbX ₃	8.00×10^{-13}	52.1
End	I in Br rich MAPbX ₃	5.90×10^{-13}	70.6

It is of note that during the conversion from MAbPbI₃ to MAbPbBr₃ via MABr exposure, no peak broadening is observed. If we assume a conversion that starts at the surface and progresses slowly into the layer, the X-rays would come in contact with portions of the crystal that have a variety of different lattice constants. This should lead to a significant broadening of the observed XRD peaks. However, the observed (200) peak shows no broadening but instead just gradually moves from the position expected for MAPbI₃ to the one expected for MAPbBr₃. This indicates that the conversion is progressing homogeneously through the whole layer. Osherov et al. conducted experiments where they investigated the diffusion of I, Br and Cl as foreign ions in MAbPI₃, MAbPBr₃ and MAbPbCl₃, by exposing single crystals of the perovskites to a solution that contained the foreign MA halide at RT. With the data obtained, they calculated the diffusion constants D of the halides in different perovskites at different degrees of conversion

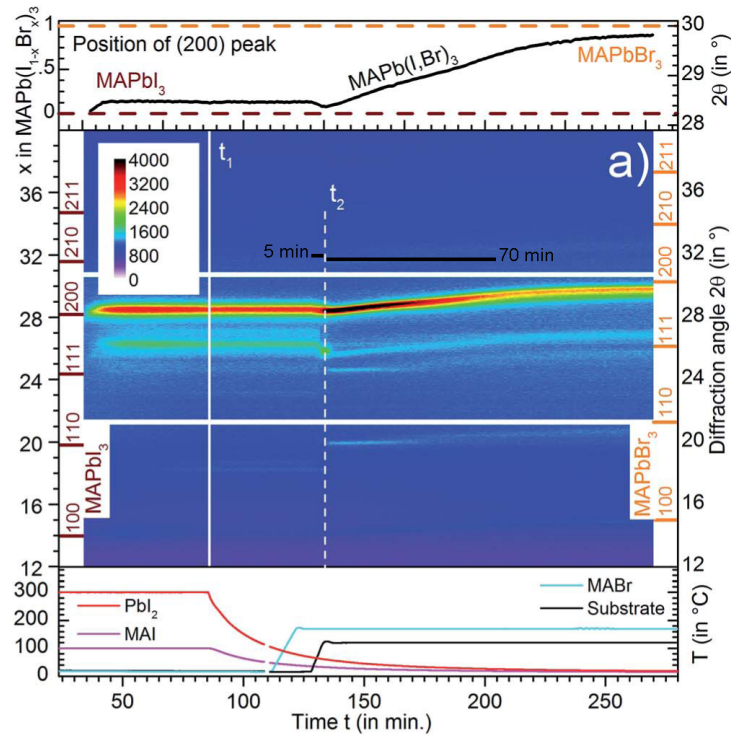


Figure 4.1: Modification of figure 4a of the publication on MAbPbI_3 [Bu1]. Two black bars have been added, one denoting a time of 5 min and one denoting a time of 70 min.

(15% and 85%). Using these diffusion constants, one can calculate the time it would take for the respective halide species to diffuse through a perovskite layer with a thickness of 500 nm. The results are shown in table 4.1. Taking this calculated data into account, there is a possible explanation for the observed XRD data: Br ions diffuse so quickly into the MAbPbI_3 layer (Tab. 4.1 “Beginning”) that they have infused the complete layer in a short timescale. Now the conversion to MAbPbBr_3 occurs homogeneously in the whole layer, the rate limiting factor being the removal of I (Tab. 4.1 “Main part” and “End”). Figure 4.1 shows that the estimated time scales of around 5 min (Br into MAbPbI_3) and 70 min (I out of MAbPbBr_3) correspond very roughly to the observed times of the MAbPbI_3 to MAbPbBr_3 conversion process. A major limitation of this estimate is the fact that Osherov et al. used a very different experimental setup, as they studied the diffusion of MA-halides from a solution into a single crystal, while we looked at polycrystalline thin films in a vacuum chamber, which were exposed to MA-halide vapor produced by a thermal evaporation source. However, these estimates lend credence to the proposed mechanism for the MAbPbI_3 to MAbPbBr_3 conversion, which assumes the outward diffusion of I ions to be the rate limiting factor of the process.

4.3 Preparation and Thermal Stability of CsPbX₃

Preliminary Discussion

Reference: [Bu2]

It is well known by now that the stability limiting component of MAPbI₃ is the organic MA molecule that can easily dissociate under a variety of stressors. There is evidence however, that the photoelectric properties of the perovskites are mainly determined by the inorganic PbX₃ scaffold and only to a lesser degree by the A-site component [162, 163, 93, 164]. Therefore, a promising approach to combat the general instability of MAPbX₃ perovskites is to forgo the organic MA molecule in favor of the inorganic Cs atom. The result are fully inorganic CsPbX₃ perovskites. Hence the next step in my work was to investigate these Cs based perovskites, more specifically CsPbI₃ and CsPbBr₃. Later on, not included in [Bu2], the series was also extended to CsPbCl₃ (see section 5.4). Besides expanding the knowledge on co-evaporated CsPbI₃ and CsPbBr₃, running the same set of experiments on the CsPbX₃ system as we did on the MAPbX₃ system enables us to directly analyze the influence of the MA/Cs cation on the thermal stability. However, there are unique challenges when it comes to implementing CsPbI₃ and CsPbBr₃ in photovoltaic devices: The band gap of CsPbBr₃ is 2.25 eV [165] and thus too large for efficient absorption of sunlight. CsPbI₃ would be a suitable photo absorber, but it can exist in two different crystal structures at room temperature: One is the black α phase with a band gap of 1.73 eV [69], the other is the yellow δ phase, with a band gap of 3.01 eV [166]. There is a tendency of the α phase to undergo a rapid phase transition into the δ phase upon exposure to ambient air. This has also been demonstrated in the paper, as a grown α -CsPbI₃ perovskite remained in the α phase as the vacuum chamber was flooded with nitrogen, but immediately changed into the δ phase upon exposure to ambient air.

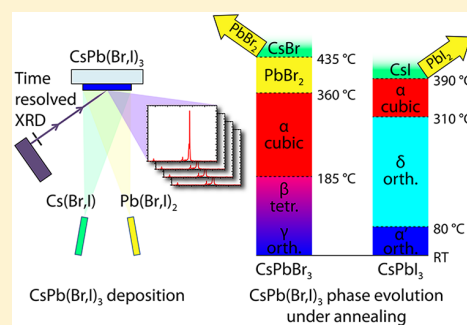
Crystal Phases and Thermal Stability of Co-evaporated CsPbX₃ (X = I, Br) Thin Films

Thomas Burwig, Wolfgang Fränzel, and Paul Pistor*[✉]

Faculty of Natural Sciences II, Martin Luther University Halle-Wittenberg, 06120 Halle (Saale), Germany

Supporting Information

ABSTRACT: We present the growth, phase transitions, and thermal decomposition of CsPbX₃ (X = I, Br) thin films monitored by in situ X-ray diffraction (XRD). The perovskite films are prepared in vacuum via co-evaporation of PbX₂ and CsX (X = I, Br) onto glass substrates. In situ X-ray diffraction allows the observation of phase transitions and decomposition while the samples are heated with a linear temperature ramp. Our experiments reveal the decomposition route for the CsPbX₃ perovskites in high vacuum, with a much higher stability than their hybrid organic–inorganic MAPbX₃ counterparts. We also observe the response of a black CsPbI₃ thin film to exposure to ambient air at room temperature using the same XRD system. Exposing the black CsPbI₃ to ambient air leads to the formation of yellow orthorhombic δ -CsPbI₃, whose crystal structure could be identified by its X-ray diffraction pattern. Additionally, the linear coefficients of expansion are determined for δ -CsPbI₃ and the (020)-orientation of CsPbBr₃.



Within recent years, organo–metal halide perovskites have shown promising results as absorber materials for photovoltaic cells. Most of the current research focuses on perovskites with the general sum formula APbX₃, with X being a halide—mostly Cl, Br, or I—and A being an organic cation like methylammonium (MA) or formamidinium (FA). Some of the greater challenges of current perovskite technologies are concerns about thermal stability^{1,2} as well as a high susceptibility to water-induced damage.^{3–5} There is a growing body of evidence that suggests that the organic A component plays only a minor role for perovskites in regard to their use case as photovoltaic absorbers,^{6–8} with charge carrier mobility and lifetime mostly determined by the PbX₃ framework.⁹ In more recent work, perovskites in which the organic A cation is partially or fully substituted by the inorganic Cs, have seen rising attention.^{6,7,9–11} The motivation behind this substitution is the expectation to increase the stability of the resulting perovskite.^{2,6,12}

CsPbBr₃ has been reported by Hirotsu et al. to exist in an orthorhombic structure (*Pbnm*; *a* = 8.207 Å, *b* = 8.255 Å, *c* = 11.759 Å) at room temperature, with a transition to a tetragonal structure (*P4/mbm*, *a* = 8.259 Å, *b* = 5.897 Å) above 88 °C and to a cubic structure (*Pm3m*, *a* = 5.874 Å) above 130 °C.¹³ The X-ray diffraction (XRD) peak positions that result from these crystal structures will be used to identify the different CsPbBr₃ phases and peaks. In accordance with established convention, the cubic phase of this perovskite will henceforth be referred to as α , the tetragonal phase as β , and the orthorhombic phase as γ . The band gap energy of pure CsPbBr₃ is 2.25 eV,¹⁴ and thus it is too high for efficient absorption of photons within the visible spectrum. However, incorporating I to substitute the Br will decrease its band gap to as low as 1.73 eV.¹⁵

At room temperature, CsPbI₃ can exist in a black, metastable α -phase that has often been assumed to be cubic and a yellow, orthorhombic, nonperovskite δ -phase.¹⁶ The black α -phase has a band gap of 1.73 eV,¹⁵ which renders it suitable for the use as a photovoltaic absorber. This band gap makes it especially useful as a top cell of a silicon tandem solar cell. The yellow δ -phase has a band gap of 3.01 eV,¹⁷ which is far too large for efficiently absorbing visible sunlight. The cubic α -phase, however, has been reported to be stable only for temperatures above 300 °C.^{8,16} The crystal structure of the black α perovskite phase at room temperature has been identified as orthorhombic instead of cubic by some researchers.¹⁸ Because this phase therefore differs from the black α -phase at high temperatures, the room-temperature phase will henceforth be referred to as α' . To identify the phases and the peaks of the CsPbI₃, the works of Trots et al.¹⁹ and Lai et al.¹⁸ have been used. The α' -phase is unstable under ambient air and, if exposed to it, will convert to the δ -phase.^{8,16} Some researchers expect the influx of water molecules into the perovskite matrix to be the driving force behind this phase transition.¹² There have been different successful approaches for increasing the stability of the black CsPbI₃ perovskite at room temperature. Some examples include the solution processing of CsPbI₃ by using alkyl phosphonic acid as a solvent,²⁰ incorporating FA into the A position,²¹ or incorporating Br into the X position.¹¹

We present the growth and thermal decomposition of CsPbBr₃ and CsPbI₃ as well as the response of α' -CsPbI₃ to

Received: July 2, 2018

Accepted: August 7, 2018

Published: August 7, 2018

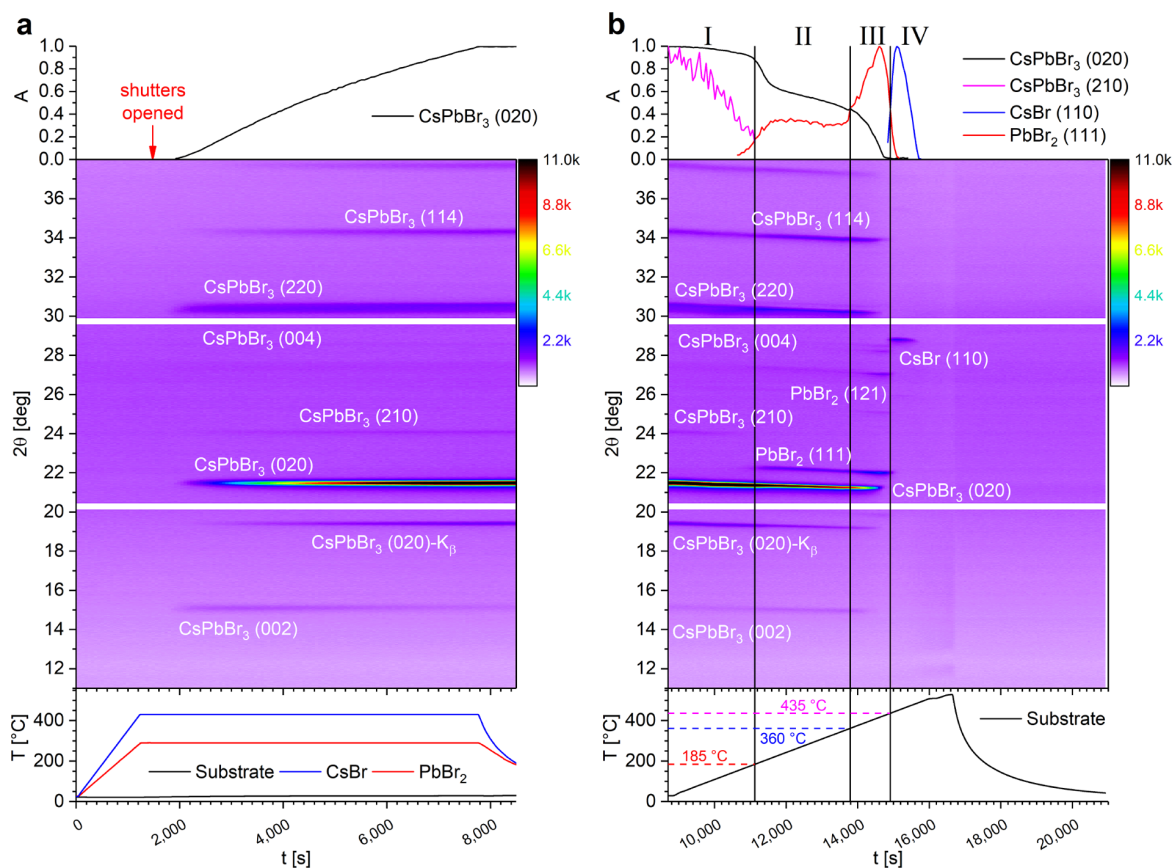


Figure 1. Growth and decomposition of a CsPbBr₃ film. The uppermost chart shows the normalized integrated peak intensity *A*; the middle chart shows a color-map-representation of the XRD scans taken during the experiment; the bottom chart shows the temperature of the evaporation sources and of the substrate. Panel a shows the growth of the perovskite thin film, and panel b shows its annealing and decomposition. The peaks are indexed according to the γ -phase of CsPbBr₃ at room temperature, and this naming is retained throughout the experiment.

ambient air, for the first time monitored by an in situ XRD system. This allows for an easy correlation of the development of the XRD peaks to the temperature and to the applied atmosphere. One major benefit of our approach is the possibility of analyzing the crystal phases without the need for interrupting the process or breaking the vacuum, and therefore the avoidance of air exposure. Furthermore, the setup allows us to easily determine the linear thermal expansion coefficients, which has been carried out for the (020)-plane of the orthorhombic CsPbBr₃ and for the three lattice constants of δ -CsPbI₃.

The results of the growth and decomposition experiments are shown in Figures 1 and 2. Experimental details on the co-evaporation process and in situ XRD measurement setup can be found in the Supporting Information.

In the first experiment (Figure 1), CsBr and PbBr₂ are evaporated simultaneously from two different evaporation sources. After the sources had reached their target temperatures, the source shutters were opened (marked in the graph with a red arrow). Almost immediately, the deposition of a crystalline perovskite thin film starts and can be monitored via XRD with an increasing signal intensity.

To observe the formation and decomposition of the films, the integrated peak intensity of the most intensive peaks is calculated and normalized to one. This normalized, integrated peak area of peak (*hkl*) and component *i* will henceforth be referred to as $A_i^{(hkl)}$ and is plotted in the topmost graphs of Figures 1 and 2. Below these graphs a colormap is shown,

depicting the data of the XRD scans over the course of the experiment. The bottom graph shows the respective temperatures of the substrate and the evaporation sources.

Details on the substrate preparation, the setup, and experimental procedure can be found in the Supporting Information.

During the growth of the CsPbBr₃ (Figure 1a), the most intensive peak of the grown film was the (020) peak at 21.44° with a full width at half-maximum (fwhm) of 0.15°. Additional peaks corresponding to (220), (114), (132), (004), (120), and (002) were also found, named in order of the respective peaks' intensity. An XRD scan of the final CsPbBr₃ film can be found in Figure 3a. All peaks can be assigned to the orthorhombic γ -CsPbBr₃; no secondary phases were identified by XRD. The peaks were indexed according to the γ -phase. Despite possible phase transitions to higher-symmetry perovskite phases, the indices were retained at higher temperatures for easier readability. Laser light scattering (LLS) indicated a film thickness of roughly 1200 nm. The perovskites growth rate was around 0.2 nm s⁻¹.

We were not able to detect the phase transition from γ - to β -CsPbBr₃ predicted at 80 °C,¹³ mainly because the γ - and β -phase have many XRD peaks in common and preferential orientations might inhibit the detection of some lattice reflections. The transition from the β - to the α -phase, however, can be asserted by the decline of the (210) peak as visible by $A_{\text{CsPbBr}_3}^{(210)}$. Because of the low intensity of the (210) peak,

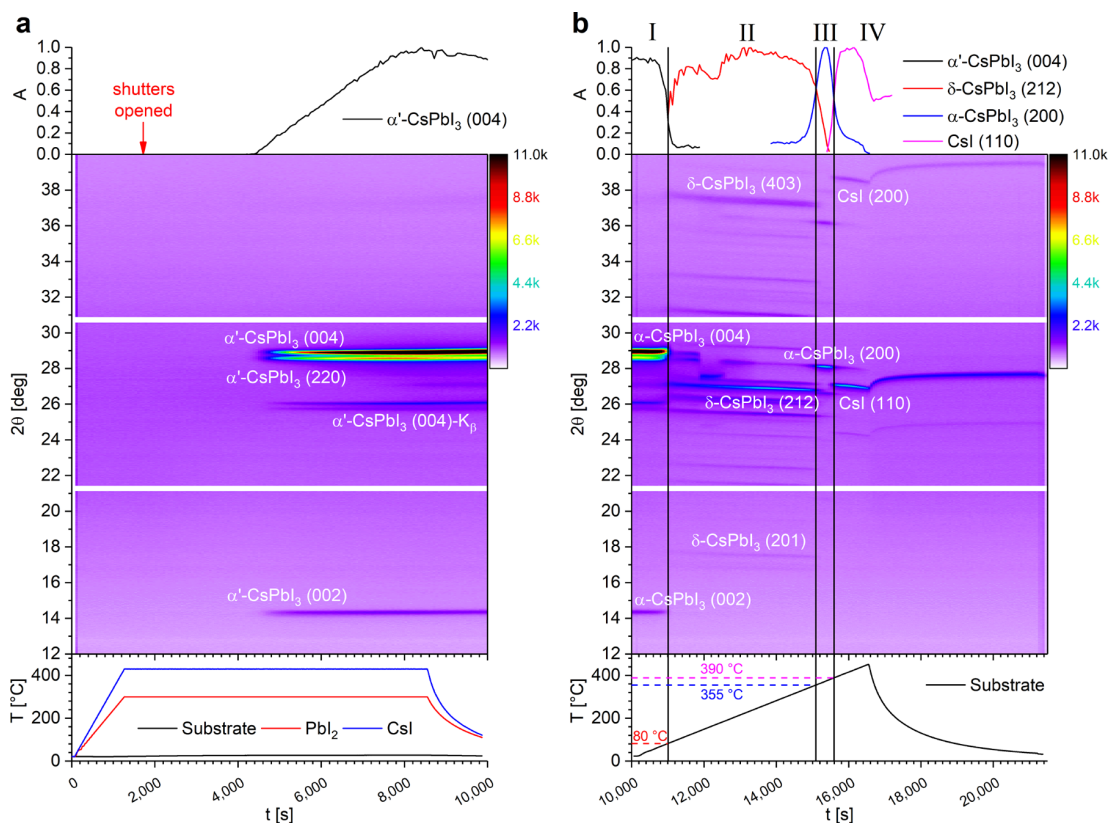


Figure 2. Growth and decomposition of a $CsPbI_3$ film. The uppermost chart shows the normalized integrated peak intensity A ; the middle chart shows a color-map-representation of the XRD-scans taken during the experiment; the bottom chart shows the temperatures of the evaporation sources and of the substrate. Panel a shows the growth and panel b shows the annealing and decomposition of the $CsPbI_3$ perovskite thin film.

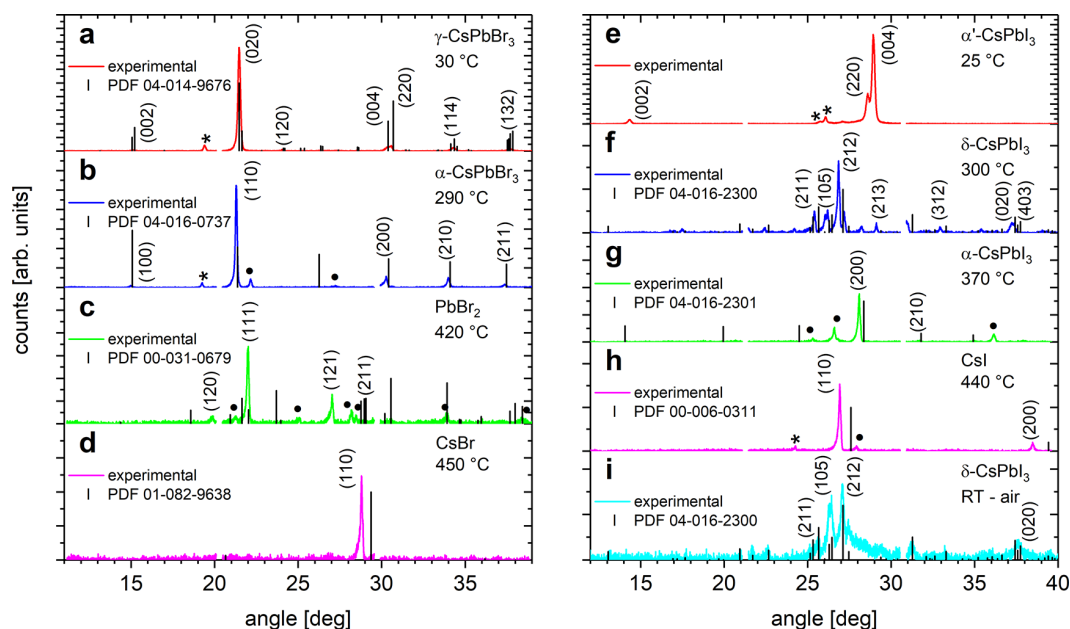


Figure 3. XRD diffractograms showing the materials seen in the experiments that are presented here. Peaks denoted with an asterisk are K_β peaks; peaks with a dot belong to a different material. The references are depicted as black bars.

however, $A_{CsPbBr_3}^{(210)}$ has a low signal-to-noise ratio and the onset of the decline is difficult to determine. The (210) and the (004) peak have fully disappeared at 185 °C, which indicates that pure α - $CsPbBr_3$ is present within section II. This phase

transition is also marked by a rapid decline of $A_{CsPbBr_3}^{(020)}$ and the emergence of $PbBr_2$ within the film, as indicated by a rapid rise of $A_{PbBr_2}^{(200)}$. One possible interpretation of this is that the perovskite is partly decomposing into crystalline $PbBr_2$ while

the CsBr remains in an amorphous state which is not detected by XRD. The (020) CsPbBr₃ peak further diminishes slowly until section III, which starts at 360 °C, where $A_{\text{PbBr}_2}^{(200)}$ rapidly increases and $A_{\text{CsPbBr}_3}^{(020)}$ decreases. $A_{\text{PbBr}_2}^{(020)}$ reaches its maximum at around the same time that $A_{\text{CsPbBr}_3}^{(020)}$ reaches its minimum, indicating a complete decomposition of the perovskite. Shortly afterward, in section IV, beginning at 435 °C, a (110) CsBr peak appears and the PbBr₂ evaporates off of the substrate, leaving behind only the CsBr, which is then fully evaporated soon after. It is notable that the CsBr peak appears only for temperatures >435 °C, when the PbBr₂ has left the film. As noted before, it is possible that the CsBr forms an amorphous phase that crystallizes only at high temperatures when all other components have left the substrate. Another explanation would be that a significant portion of the PbBr₂ covered the substrate's surface, absorbing the majority of the X-ray photons from below. Only when this PbBr₂ vanished from the surface did the CsBr become visible to XRD. To estimate whether this is a realistic proposition, the absorption of PbBr₂ has been calculated for a film that has the full films' thickness directly after the growth of 1200 nm. The result is an absorption of roughly 12%, which renders the aforementioned explanation implausible. We therefore tentatively explain the late appearance of CsBr peaks with an amorphous phase being present at lower temperatures.

The CsPbI₃ experiment is depicted in Figure 2. The XRD peaks of the grown CsPbI₃ film indicate the growth of a black α' -CsPbI₃ film (Figure 2a). The XRD pattern of the grown film is shown in Figure 3e. The position and intensity of these XRD peaks coincide with the results of Lai et al.,¹⁸ and the (*hkl*) indices have been assigned according to their findings. The two most intensive peaks were the (004) peak at 28.92° with a fwhm of 0.18 and the (220) peak at 28.58° with a fwhm of 0.17. The (002) peak was also present. The split (004)–(220) double peak indicates that the black α' -CsPbI₃ indeed exists in an orthorhombic structure and not, as is often assumed, in a cubic structure. According to the laser light scattering, the layer had a thickness of about 700 nm and was grown at a rate of 0.1 nm s⁻¹.

There exists a notable difference to the growth of CsPbBr₃: The first XRD peaks appear only more than 2000 s after the opening of the source shutters, while the LLS indicated a continuous thin-film deposition during this time. We interpret this as an initial amorphous growth phase of the α' -CsPbI₃ perovskite film, which crystallizes and becomes detectable with XRD only at a later time.

One notable feature of the CsPbI₃ decomposition experiment depicted in Figure 2b is the conversion of the black α' -perovskite to the yellow δ -phase at roughly 80 °C, which is marked in Figure 2 as the transition from section I to section II. During this transition, $A_{\alpha'\text{-CsPbI}_3}^{(004)}$ quickly decreases and the (212) peak of the δ -phase emerges. This is in good agreement with the findings of Chen et al., who reported this phase transition at 80 °C.¹¹ In contrast to the CsPbBr₃, which is cubic above 130 °C,^{13,22} the CsPbI₃ will convert from the yellow orthorhombic δ -phase to the cubic α -phase at much higher temperatures. The point at which $A_{\delta\text{-CsPbI}_3}^{(212)}$ drops to 90% of its maximum value can be interpreted as the onset of this phase transition, and this point is reached at roughly 310 °C. $A_{\delta\text{-CsPbI}_3}^{(212)}$ and $A_{\alpha\text{-CsPbI}_3}^{(200)}$ intersect when both reach a value of roughly 0.6 (355 °C). It can be asserted that at this point the majority of the δ -CsPbI₃ has been converted to α -CsPbI₃. At 365 °C $A_{\alpha\text{-CsPbI}_3}^{(200)}$ reaches its maximum while the δ -CsPbI₃ peaks completely disappear.

After the complete conversion, the intensity of the main α -CsPbI₃ peak declines quickly and CsI starts to get visible in the XRD scans. Starting at section IV at 390 °C, $A_{\text{CsI}}^{(110)}$ surpasses $A_{\alpha\text{-CsPbI}_3}^{(200)}$ and at 440 °C, the main peak of the α -CsPbI₃ completely vanishes. The CsI starts evaporating at roughly 430 °C.

The observed behavior illustrates one notable difference that the decomposition routes of the all inorganic Cs-based perovskites show compared to organic–inorganic MAPbX₃ perovskites. The MA-based perovskites decompose in such a way that the MA halide component leaves the film first, leaving behind the lead halide.^{23–25} With the Cs-based perovskites, this relation is reversed: The respective lead halide leaves the film first, and the Cs halide remains. This indicates that the thermal stability of Cs-based perovskites is limited by the lead halide instead of the MA halide component. This provides an explanation for the higher thermal stability that is observed with Cs-based perovskites. When we annealed MAPbX₃ perovskites under identical conditions, we found for MAPbI₃ a decomposition temperature of 230 °C²⁵ compared to the 360 °C of CsPbI₃. The Br analogue MAPbBr₃ was shown to decompose at 250 °C²⁵ compared to CsPbBr₃ with its decomposition at 390 °C.

A selection of XRD-scans that indicate particular materials and phases is compiled in Figure 3. The scans shown depict γ -CsPbBr₃ (a), α -CsPbBr₃ (b), PbBr₂ (c), CsBr (d), α' -CsPbI₃ (e), δ -CsPbI₃ (f), α -CsPbI₃ (g), CsI (h), and δ -CsPbI₃ that was converted from the α' -phase under ambient air (i). The PbBr₂ scan shown in panel c corresponds to the reference data if this is shifted by about 1.75° to smaller angles, with the matching peaks being (111), (121), (211), and (120). This shift is larger than what we would expect due to thermal expansion alone. We tentatively suggest that the Cs might still be partly incorporated into the film, stretching the lattice and leading to the observed shift.

It is well-known that the black α' -phase of CsPbI₃ is unstable in ambient air and that it will convert into the yellow δ -CsPbI₃-phase when exposed to it.^{8,11,16} A black α' -CsPbI₃ film was grown at room temperature in vacuum, and the chamber was subsequently flooded with N₂. The XRD pattern of the film remained unchanged and is displayed in Figure 3e. This indicates at least partial stability of the black α' -CsPbI₃ under atmospheric nitrogen pressure. Subsequently, the chamber was flooded with air, which within seconds leads to a fast color change from black to yellow, accompanied by a sudden shift in the LLS signal. The XRD pattern after this exposure corresponds to the yellow δ -phase and can be seen in Figure 3i. A direct comparison of the XRD pattern before and after the phase transition can be found within the Supporting Information. These results highlight the fact that the phase transition is not driven solely by temperature but also depends significantly on the atmospheric conditions, most probably especially on the moisture level. These results therefore lend credence to the hypothesis that an influx of atmospheric water into the crystal matrix acts as a catalyst for the observed phase transition, as is suggested by Ahmad et al.¹²

Preliminary tests suggest that the stability of the black CsPbI₃ phase to ambient air exposure might be enhanced by incorporating with Br. However, for conclusive results further experiments are needed. Stabilization by mixing I–Br ions has also been reported for example by Sutton et al.²⁶

The thermal expansion coefficients of CsPbBr₃ and δ -CsPbI₃ have been determined by observing the shift of the XRD peaks. The relation between the distance of the lattice plains *d* and

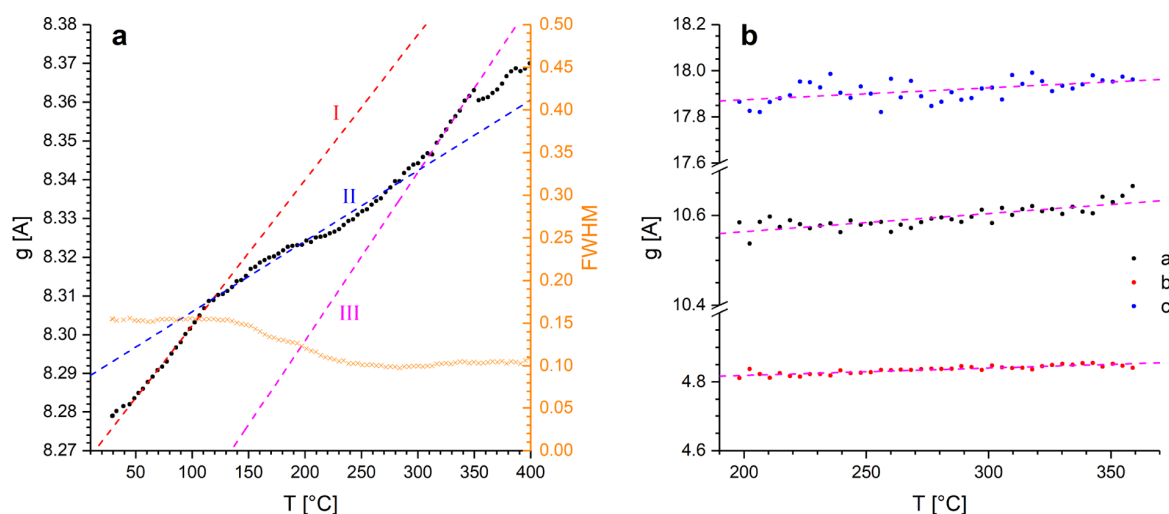


Figure 4. (a) Relation between the lattice plane distance of the (020) plains of CsPbBr₃ and the temperature T . The fwhm of the (020) peak is also shown. (b) This relation for the three lattice constants a , b , and c of the orthorhombic δ -CsPbI₃.

the corresponding XRD peak angle 2θ can be described by Bragg's law. d is calculated as follows:

$$d = \frac{\lambda}{2 \cdot \sin(2\theta)} \quad (1)$$

The thermal expansion of a given lattice constant a is then expressed with the help of the linear thermal expansion coefficient α :

$$a = a_0(1 + \alpha \cdot \Delta T) \quad (2)$$

Here, ΔT is the temperature difference and a_0 is the lattice constant at $\Delta T = 0$. A linear fit of a over the temperature difference ΔT with the form $y = x_0 + m \cdot x$ yields $m = a_0 \cdot \alpha$ as the slope with $x_0 = a_0$. The given uncertainties were calculated from the errors of the fit by gaussian error propagation.

From the development of the lattice plane distance of the CsPbBr₃, three distinct stages can be discerned. The expansion coefficient has been determined separately for the three sections, using the peak at the position that corresponds to the (020) lattice plains in the orthorhombic phase. The expansion coefficient for section I, which reaches up to 115 °C, was determined to be $\alpha_I = (45.4 \pm 0.6) \times 10^{-6} \text{ K}^{-1}$; for section II, reaching up to 315 °C, $\alpha_{II} = (22.0 \pm 0.5) \times 10^{-6} \text{ K}^{-1}$; and for section III, $\alpha_{III} = (52.9 \pm 1.5) \times 10^{-6} \text{ K}^{-1}$. Rodova et al. reported average linear expansion coefficients of $\alpha = 45 \times 10^{-6} \text{ K}^{-1}$ for temperatures below 85 °C, $\alpha = 38 \times 10^{-6} \text{ K}^{-1}$ between 93 °C and 124 °C, and $\alpha = 33 \times 10^{-6} \text{ K}^{-1}$ from 140 °C to 230 °C.¹³ The results for section I lie in good agreement with the expansion coefficient proposed by Rodova et al. for the low-temperature range. The fwhm seen in Figure 1a indicates a transition during section II. This section might be subject to additional distortions induced by the occurrence of PbBr₂ secondary phases. The high-temperature section III exceeds the temperature range examined by Rodova et al. The linear thermal expansion coefficient that was obtained for this section only slightly exceeds that of the low-temperature section I.

During the existence of the α' -CsPbI₃-phase, only the (002), (004), and (220) peaks were visible, which provides only two linearly independent peaks, which is not sufficient for calculating the three lattice parameters of an orthorhombic lattice. To obtain the values for a , b , and c of the orthorhombic δ -CsPbI₃

shown in Figure 4c, the (212), (213), and (312) peaks were factored in. A linear fit of the lattice constants taken over the temperature yielded the values for the linear thermal expansion coefficients with $\alpha_a = (38.6 \pm 4.6) \times 10^{-6} \text{ K}^{-1}$, $\alpha_b = (44.9 \pm 4.1) \times 10^{-6} \text{ K}^{-1}$, and $\alpha_c = (29.1 \pm 7.6) \times 10^{-6} \text{ K}^{-1}$. Trots and Myagkota propose a volumetric expansion coefficient of $\alpha_V = 11.8 \times 10^{-5} \text{ K}^{-1}$,¹⁹ which is in good agreement with our findings, resulting in $\alpha_V = \alpha_a + \alpha_b + \alpha_c = 11.3 \times 10^{-5} \text{ K}^{-1}$.

These results show linear expansion coefficients comparable to those of the MA-based perovskites, where for MAPbI₃ the linear thermal expansion coefficient is $\alpha = 43.3 \times 10^{-6} \text{ K}^{-1}$ and for MAPbBr₃ $\alpha = 33.3 \times 10^{-6} \text{ K}^{-1}$ has been determined.²⁷

In conclusion, we present an upper limit for the thermal stability of CsPbBr₃ at 360 °C and of CsPbI₃ at 390 °C and showed that the decomposition, in contrast to the hybrid MAPbX₃ perovskites, is initiated by the sublimation of the respective materials' lead halide. The results imply that the thermal stability of Cs-based perovskites is limited by the lead halide component and significantly surpasses that of the MA-based perovskites. Under vacuum conditions, we find that CsPbI₃ crystallizes in a black, orthorhombic α' -crystal phase. Upon heating, the film undergoes the phase transitions from a black, orthorhombic α' -phase to a yellow, orthorhombic δ -phase to a black, cubic α -phase.

XRD measurements confirm that black, orthorhombic α' -CsPbI₃ will convert immediately to yellow, orthorhombic δ -CsPbI₃ upon exposure to ambient air, underlining the instability of α -CsPbI₃ in ambient air. The linear thermal expansion coefficient of the (020) plain of CsPbBr₃ has been determined to be $\alpha_I = (45.4 \pm 0.6) \times 10^{-6} \text{ K}^{-1}$ for temperatures below 115 °C, $\alpha_{II} = (22.0 \pm 0.5) \times 10^{-6} \text{ K}^{-1}$ for temperatures below 315 °C, and $\alpha_{III} = (52.9 \pm 1.5) \times 10^{-6} \text{ K}^{-1}$ above 315 °C. For the three lattice constants of the orthorhombic δ -CsPbI₃, the linear thermal expansion coefficients have been determined to be $\alpha_a = (38.6 \pm 4.6) \times 10^{-6} \text{ K}^{-1}$, $\alpha_b = (44.9 \pm 4.1) \times 10^{-6} \text{ K}^{-1}$, and $\alpha_c = (29.1 \pm 7.6) \times 10^{-6} \text{ K}^{-1}$.

■ ASSOCIATED CONTENT

📄 Supporting Information

The Supporting Information is available free of charge on the ACS Publications website at DOI: 10.1021/acs.jpcllett.8b02059.

Substrate cleaning procedure, evaporation temperatures, brand names of used materials, notes regarding the lead bromide X-ray absorption, comparison of CsPbI₃ under N₂ and air (PDF)

AUTHOR INFORMATION

Corresponding Author

*E-mail: paul.pistor@physik.uni-halle.de.

ORCID

Paul Pistor: 0000-0002-9244-915X

Notes

The authors declare no competing financial interest.

ACKNOWLEDGMENTS

Financial support from the German Federal Ministry of Research and Education (BMBF) under Contract Number 03EK3570B (StrukturSolar II) is gratefully acknowledged.

REFERENCES

- (1) Habisreutinger, S. N.; Leijtens, T.; Eperon, G. E.; Stranks, S. D.; Nicholas, R. J.; Snaith, H. J. Carbon Nanotube/Polymer Composites as a Highly Stable Hole Collection Layer in Perovskite Solar Cells. *Nano Lett.* **2014**, *14*, 5561–5568.
- (2) Beal, R. E.; Slotcavage, D. J.; Leijtens, T.; Bowring, A. R.; Belisle, R. A.; Nguyen, W. H.; Burkhard, G. F.; Hoke, E. T.; McGehee, M. D. Cesium Lead Halide Perovskites with Improved Stability for Tandem Solar Cells. *J. Phys. Chem. Lett.* **2016**, *7*, 746–751.
- (3) Leguy, A. M. A.; Hu, Y.; Campoy-Quiles, M.; Alonso, M. I.; Weber, O. J.; Azarhoosh, P.; van Schilfhaarde, M.; Weller, M. T.; Bein, T.; Nelson, J.; et al. Reversible Hydration of CH₃NH₃PbI₃ in Films, Single Crystals, and Solar Cells. *Chem. Mater.* **2015**, *27*, 3397–3407.
- (4) Sheng, R.; Wen, X.; Huang, S.; Hao, X.; Chen, S.; Jiang, Y.; Deng, X.; Green, M. A.; Ho-Baillie, A. W. Y. Photoluminescence Characterisations of a Dynamic Aging Process of Organic–Inorganic CH₃NH₃PbBr₃ Perovskite. *Nanoscale* **2016**, *8*, 1926–1931.
- (5) Yang, J.; Siempelkamp, B. D.; Liu, D.; Kelly, T. L. Investigation of CH₃NH₃PbI₃ Degradation Rates and Mechanisms in Controlled Humidity Environments Using in Situ Techniques. *ACS Nano* **2015**, *9*, 1955–1963.
- (6) Kulbak, M.; Cahen, D.; Hodes, G. How Important is the Organic Part of Lead Halide Perovskite Photovoltaic Cells? Efficient CsPbBr₃ Cells. *J. Phys. Chem. Lett.* **2015**, *6*, 2452–2456.
- (7) Kulbak, M.; Gupta, S.; Kedem, N.; Levine, I.; Bendikov, T.; Hodes, G.; Cahen, D. Cesium Enhances Long-Term Stability of Lead Bromide Perovskite-Based Solar Cells. *J. Phys. Chem. Lett.* **2016**, *7*, 167–172.
- (8) Eperon, G. E.; Paternò, G. M.; Sutton, R. J.; Zampetti, A.; Haghighirad, A. A.; Cacialli, F.; Snaith, H. J. Inorganic Caesium Lead Iodide Perovskite Solar Cells. *J. Mater. Chem. A* **2015**, *3*, 19688–19695.
- (9) Hutter, E. M.; Sutton, R. J.; Chandrashekar, S.; Abdi-Jalebi, M.; Stranks, S. D.; Snaith, H. J.; Savenije, T. J. Vapour-Deposited Cesium Lead Iodide Perovskites: Microsecond Charge Carrier Lifetimes and Enhanced Photovoltaic Performance. *ACS Energy Letters* **2017**, *2*, 1901–1908.
- (10) Saliba, M.; Matsui, T.; Seo, J.-Y.; Domanski, K.; Correa-Baena, J.-P.; Nazeeruddin, M. K.; Zakeeruddin, S. M.; Tress, W.; Abate, A.; Hagfeldt, A.; et al. Cesium-Containing Triple Cation Perovskite Solar Cells: Improved Stability, Reproducibility and High Efficiency. *Energy Environ. Sci.* **2016**, *9*, 1989–1997.
- (11) Chen, C.-Y.; Lin, H.-Y.; Chiang, K.-M.; Tsai, W.-L.; Huang, Y.-C.; Tsao, C.-S.; Lin, H.-W. All-Vacuum-Deposited Stoichiometrically Balanced Inorganic Cesium Lead Halide Perovskite Solar Cells with Stabilized Efficiency Exceeding 11%. *Adv. Mater.* **2017**, *29*, 1605290.
- (12) Ahmad, W.; Khan, J.; Niu, G.; Tang, J. Inorganic CsPbI₃ Perovskite-Based Solar Cells: A Choice for a Tandem Device. *Solar RRL* **2017**, *1*, 1700048.
- (13) Rodova, M.; Brozek, J.; Knizek, K.; Nitsch, K. Phase Transitions in Ternary Caesium Lead Bromide. *J. Therm. Anal. Calorim.* **2003**, *71*, 667–673.
- (14) Stoumpos, C. C.; Malliakas, C. D.; Peters, J. A.; Liu, Z.; Sebastian, M.; Im, J.; Chasapis, T. C.; Wibowo, A. C.; Chung, D. Y.; Freeman, A. J.; et al. Crystal Growth of the Perovskite Semiconductor CsPbBr₃: A New Material for High-Energy Radiation Detection. *Cryst. Growth Des.* **2013**, *13*, 2722–2727.
- (15) Eperon, G. E.; Stranks, S. D.; Menelaou, C.; Johnston, M. B.; Herz, L. M.; Snaith, H. J. Formamidinium Lead Trihalide: A Broadly Tunable Perovskite for Efficient Planar Heterojunction Solar Cells. *Energy Environ. Sci.* **2014**, *7*, 982.
- (16) Møller, C. K. Crystal Structure and Photoconductivity of Cesium Plumbohalides. *Nature* **1958**, *182*, 1436–1437.
- (17) Yunakova, O. N.; Miloslavskii, V. K.; Kovalenko, E. N. Exciton Absorption Spectrum of Thin CsPbI₃ and Cs₄PbI₆ Films. *Opt. Spectrosc.* **2012**, *112*, 91–96.
- (18) Lai, M.; Kong, Q.; Bischak, C. G.; Yu, Y.; Dou, L.; Eaton, S. W.; Ginsberg, N. S.; Yang, P. Structural, Optical, and Electrical Properties of Phase-Controlled Cesium Lead Iodide Nanowires. *Nano Res.* **2017**, *10*, 1107–1114.
- (19) Trots, D.; Myagkota, S. High-Temperature Structural Evolution of Caesium and Rubidium Triiodoplumbates. *J. Phys. Chem. Solids* **2008**, *69*, 2520–2526.
- (20) Wang, C.; Chesman, A. S. R.; Jasieniak, J. J. Stabilizing the Cubic Perovskite Phase of CsPbI₃ Nanocrystals by Using an Alkyl Phosphinic Acid. *Chem. Commun.* **2017**, *53*, 232–235.
- (21) Yi, C.; Luo, J.; Meloni, S.; Boziki, A.; Ashari-Astani, N.; Grätzel, M.; Zakeeruddin, S. M.; Røthlisberger, U.; Grätzel, M. Entropic Stabilization of Mixed A-Cation ABX₃ Metal Halide Perovskites for High Performance Perovskite Solar Cells. *Energy Environ. Sci.* **2016**, *9*, 656–662.
- (22) Cola, M.; Massarotti, V.; Riccardi, R.; Sinistri, C. Binary Systems Formed by Lead Bromide with (Li, Na, K, Rb, Cs and Tl)Br: A DTA and Diffractometric Study. *Z. Naturforsch., A: Phys. Sci.* **1971**, *26*, 1328.
- (23) Dualeh, A.; Gao, P.; Seok, S. I.; Nazeeruddin, M. K.; Grätzel, M. Thermal Behavior of Methylammonium Lead-Trihalide Perovskite Photovoltaic Light Harvesters. *Chem. Mater.* **2014**, *26*, 6160–6164.
- (24) Conings, B.; Drijkoningen, J.; Gauquelin, N.; Babayigit, A.; D'Haen, J.; D'Olieslaeger, L.; Ethirajan, A.; Verbeeck, J.; Manca, J.; Mosconi, E.; et al. Intrinsic Thermal Instability of Methylammonium Lead Trihalide Perovskite. *Adv. Energy Mater.* **2015**, *5*, 1500477.
- (25) Pistor, P.; Burwig, T.; Brzuska, C.; Weber, B.; Fränzel, W. Thermal Stability and Miscibility of Co-Evaporated Methyl Ammonium Lead Halide (MAPbX₃, X = I, Br, Cl) Thin Films Analysed by In Situ X-Ray Diffraction. *J. Mater. Chem. A* **2018**, *6*, 11496.
- (26) Sutton, R. J.; Eperon, G. E.; Miranda, L.; Parrott, E. S.; Kamino, B. A.; Patel, J. B.; Hörantner, M. T.; Johnston, M. B.; Haghighirad, A. A.; Moore, D. T.; et al. Bandgap-Tunable Cesium Lead Halide Perovskites with High Thermal Stability for Efficient Solar Cells. *Adv. Energy Mater.* **2016**, *6*, 1502458.
- (27) Rakita, Y.; Cohen, S. R.; Kedem, N. K.; Hodes, G.; Cahen, D. Mechanical Properties of APbX₃ (A = Cs or CH₃NH₃ X = I or Br) Perovskite Single Crystals. *MRS Commun.* **2015**, *5*, 623–629.

Closing Discussion

While extrapolations from these experiments in vacuum to solar cells under ambient air need to be done with care, the experiments still allow for a reasoned statement about the comparative thermal stability of MA and Cs based perovskites. With this said, the results of the temperature ramp experiments do indeed indicate a significantly improved thermal stability of CsPbI₃ and CsPbBr₃ when compared to the MAPbX₃ perovskites. MAPbI₃ decomposed at around 120 °C, while CsPbI₃, decomposed at roughly 370 °C. Both Cs perovskites decompose via the elimination of the PbX₂ component, leaving behind pure CsX. This supports what was already indicated in the MAPbX₃ case: The component that corresponds to the precursor with the lowest evaporation temperature is also the one that limits the thermal stability of the resulting perovskite, which is MAX for the MAPbX₃ perovskites and PbX₂ for the CsPbX₃ perovskites.

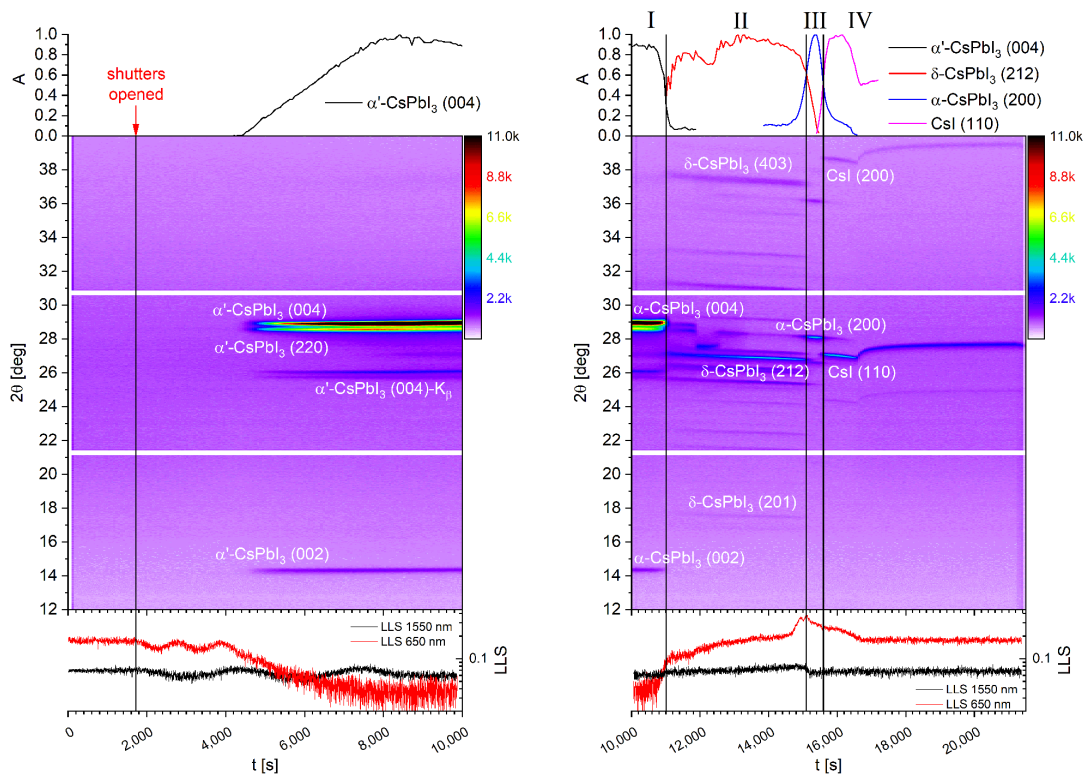


Figure 4.2: Modification of figure 2 shown in the paper, that exchanges the bottom graph with a depiction of the detected LLS signal. The phase transitions have a visible influence on the 650 nm laser light. The LLS signal indicates a growing film prior to the XRD peaks becoming visible.

As is mentioned in the publication, the CsPbI₃ deposition exhibits the notable feature of the grown material being amorphous in the beginning. The shutters are opened at 1722 s into the process while the first peak starts being visible at 4238 s, which means there is a total time

of 2516 s (42 min) that the sample grows amorphously. Notably, during this amorphous growth the sample is transparent to both LLS wavelengths used (650 nm and 1550 nm) and both LLS signals indicate a growing film as soon as the shutters are opened, as can be seen in figure 4.2. As the material transitions to the crystalline CsPbI₃ phase, the 650 nm (1.91 eV) laser significantly loses in detected intensity while it also no longer responds with oscillations to the growing film. This indicates that the film has become opaque to this wavelength and absorbs most of the laser light. α -phase CsPbI₃ has a band gap of 1.73 eV and its absorbance spectrum indicates that it should fully absorb light with a wavelength of 650 nm [69]. It can be concluded that the initial amorphous phase has a higher band gap than the 1.91 eV of the laser. It can also be cautiously hypothesized that it might be possible to grow amorphous CsPbI₃ via thermal co-evaporation onto a substrate at room temperature, yet a final conclusion cannot be drawn from the available data, since the exact nature of the as-grown amorphous phase is unknown. Upon annealing, the α -CsPbI₃ film transitions into the δ phase and this transition coincides with an increase in the measured intensity of the 650 nm laser. Both the 650 nm and the 1550 nm signal slowly increase afterwards, which indicates the decrease of the films thickness.

4.4 Preparation and Thermal Stability of $\text{Cs}_2\text{AgBiBr}_6$

Preliminary Discussion

Reference: [Bu3]

As explained in chapter 2.1.1, not only are there a wide variety of compounds that can be combined to form perovskites, but there are also crystal structures that are derived from the prototypical perovskite crystal structure, like double perovskites. In 2016 Slavney et al. first synthesized the double perovskite $\text{Cs}_2\text{AgBiBr}_6$ and has shown that this perovskite exhibits superior heat and moisture stability compared to MAPbI_3 , while also omitting the toxic Pb that is usually found in other MHPs [40]. The latter is especially significant, as most contenders for Pb free metal-halide perovskites exchange this Pb for Sn, which significantly reduces the stability and the photovoltaic performance of the resulting material. $\text{Cs}_2\text{AgBiBr}_6$ has an indirect band gap of 1.9 eV [40, 167]. This would make it suitable for the top absorber in tandem solar cells, and the material has shown very promising results when used as the absorber in high energy photon detectors [16, 9, 10, 11, 17]. $\text{Cs}_2\text{AgBiBr}_6$ has usually been prepared via solution processing, while the groups that have prepared it via physical vapor deposition did so in a sequential process of depositing BiBr_3 , CsBr and AgBr in a specific order with subsequent annealing [168, 169, 170, 171]. To our knowledge, single-step co-evaporation had not yet been demonstrated before. Of the two related double perovskites $\text{Cs}_2\text{AgBiI}_6$ and $\text{Cs}_2\text{AgBiCl}_6$, the $\text{Cs}_2\text{AgBiI}_6$ is predicted to not be thermodynamically stable at room temperature [172, 50] and $\text{Cs}_2\text{AgBiCl}_6$ has a band gap of 2.2 eV [167], which is too large for efficient photo absorption of visible photons.

This work on $\text{Cs}_2\text{AgBiBr}_6$ presents detailed information on the growth process and, in line with our analysis of other perovskites, presents the phase evolution and thermal decomposition of the material upon annealing. The analysis is conducted via the in situ XRD setup. Additionally, Raman measurements on a $\text{Cs}_2\text{AgBiBr}_6$ sample provide additional evidence of the successful growth of the desired material.

Synthesis and Crystal Structure Evolution of Co-Evaporated $\text{Cs}_2\text{AgBiBr}_6$ Thin Films upon Thermal Treatment

Thomas Burwig, Maxim Guc, Victor Izquierdo-Roca, and Paul Pistor*



Cite This: <https://dx.doi.org/10.1021/acs.jpcc.0c02480>



Read Online

ACCESS |



Metrics & More

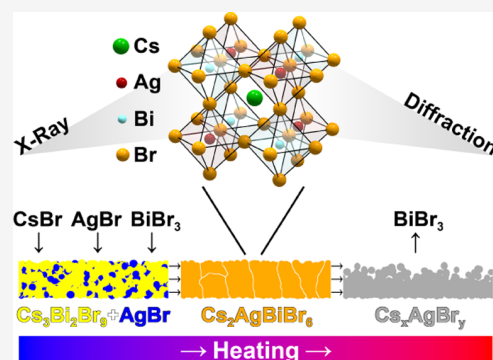


Article Recommendations



Supporting Information

ABSTRACT: Lead-free, highly stable, inorganic double perovskites such as $\text{Cs}_2\text{AgBiBr}_6$ promise to solve two of the main issues that currently hold back the wide-scale application of perovskite-based opto-electronic devices: a lack of stability and the use of toxic lead. Recently, $\text{Cs}_2\text{AgBiBr}_6$ has been shown to be a very promising material for the use in UV and X-ray detectors. In this work, we analyze the film formation of $\text{Cs}_2\text{AgBiBr}_6$ thin films with time-resolved crystal structure analysis using *in situ* X-ray diffraction (XRD). We present an all-vacuum process for the preparation of $\text{Cs}_2\text{AgBiBr}_6$ thin films *via* multisource co-evaporation followed by thermal annealing. The successful synthesis of the double perovskite phase was confirmed by analysis with XRD and Raman spectroscopy. Our *in situ* XRD setup allows us to conduct an extensive temperature-dependent analysis of the phase evolution during annealing of the films during synthesis and also during thermal decomposition. We find a decomposition temperature for the $\text{Cs}_2\text{AgBiBr}_6$ thin films at roughly 300 °C, in between that of MAPbBr_3 and CsPbBr_3 .



INTRODUCTION

In recent years, organic–inorganic hybrid perovskites have gained increasing attention in the field of photovoltaics because of their potential for very cost-efficient production and fast progress in achieving high power conversion efficiencies (PCEs).^{1–3} There is also a growing body of evidence for their high potential as absorbers in UV, X-ray, and γ detectors.^{4–9} Heavy elements such as Pb or Bi give these materials a high stopping power for high-energy photons and they exhibit a remarkable radiation hardness.⁹ The generic perovskite sum formula has the form ABX_3 . The perovskite materials currently most investigated in photovoltaic research are derived from the organic–inorganic lead halide MAPbX_3 ($X = \text{I}, \text{Br}, \text{or Cl}$), which contains the organic molecule methylammonium (MA) on the A position and Pb on the B position. This material exhibits a low stability toward moisture, light, and temperature,^{10–14} mostly induced by the decomposition or removal of the organic MA component.^{12,15–17} Fully inorganic perovskites, such as CsPbX_3 ($X = \text{I}, \text{Br}, \text{or Cl}$), have been studied as alternatives and the results do suggest a much improved stability.^{11,18–20} However, the band gaps of CsPbBr_3 (2.25 eV)²¹ and CsPbCl_3 (2.92 eV)²² are too large for use as efficient solar absorbers. CsPbI_3 is metastable and can exist in two phases at room temperature: a black perovskite phase with a low band gap (1.73 eV)²³ and a yellow δ -phase with a band gap that is too large for efficient solar absorption (3.01 eV).²⁴ Unfortunately, the latter phase is the energetically preferred one under ambient conditions.^{20,25} These inorganic perovskites also still contain the heavy metal Pb, which limits their appeal as a widespread commercial

technology. One approach to tackle this problem is the substitution of Pb with Sn, but Sn-based perovskites, to this day, have fallen short of the PCEs achieved with Pb-based perovskites, with record efficiencies of about 9.6% achieved with FASnI_3 -based solar cells (*JV*-curve scanned in the descending direction).²⁶ The Sn in this material system is also susceptible to oxidization from the Sn^{2+} to the Sn^{4+} state, which further exacerbates the stability problem.²⁷

In search for solutions to these issues, double perovskites have recently attracted notice. It has been shown *via* theoretical calculations that stable “double perovskites” can be formed by substituting two B position ions for two different heterovalent ions.²⁸ These two substituting ions (one monovalent and one trivalent) are labeled B' and B'' here. The substitution results in a double perovskite structure with the generic sum formula $\text{A}_2\text{B}'\text{B}''\text{X}_6$,²⁹ where the B' and B'' ions form a rock-salt-like sublattice. The double perovskite material that has raised most research interest to this date is $\text{Cs}_2\text{AgBiX}_6$, which constitutes a thermodynamically stable system for $X = \text{Br}, \text{Cl}$.^{30,31} The band gap of $\text{Cs}_2\text{AgBiCl}_6$ is 2.2 eV,³² while the band gap of $\text{Cs}_2\text{AgBiBr}_6$ is 1.9 eV.^{32,33} Recent investigations have found that $\text{Cs}_2\text{AgBiBr}_6$

Received: March 20, 2020

Revised: April 2, 2020

Published: April 3, 2020

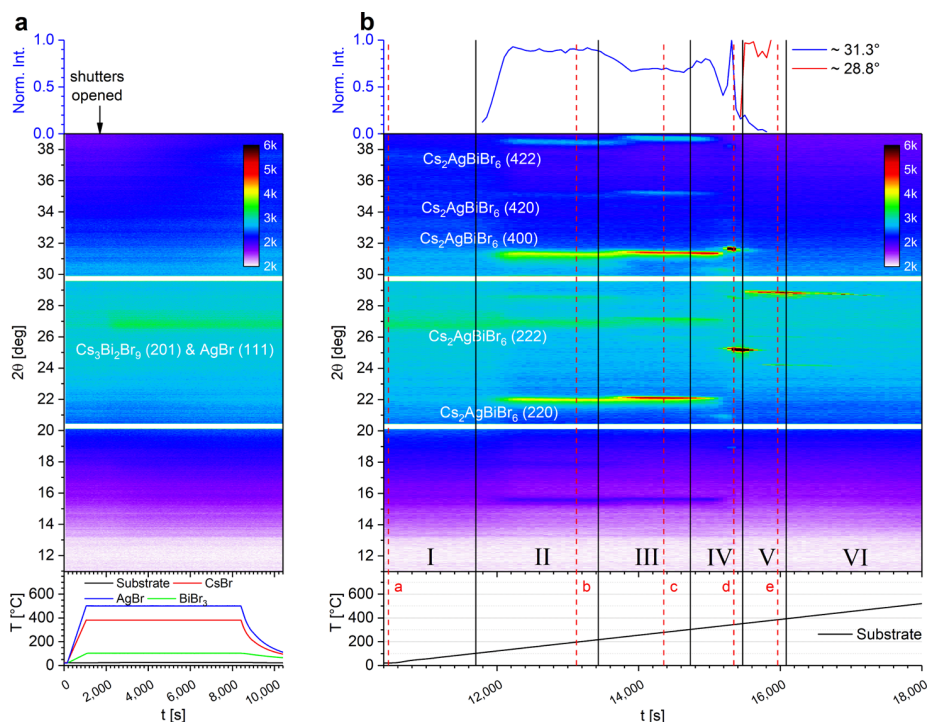


Figure 1. Synthesis and decomposition of a $\text{Cs}_2\text{AgBiBr}_6$ layer. Subfigure (a) shows the deposition of the precursors, and subfigure (b) shows the thermal annealing of the substrate. The uppermost graph shows the normalized, integrated peak intensity of selected peaks. The middle chart shows a colormap depicting the results of the XRD scans taken during the processes, with every column of pixels indicating a complete XRD scan and the colors denoting the counts received at that particular angle. The bottom graph shows the temperatures of the substrate and the evaporation sources. The red lines correspond to the single scans shown in Figure 2.

is highly stable under exposure to moisture, light, mechanical stress, and thermal stress^{5,33–37} and exhibits a lower thermal expansion coefficient compared to the MAPbX_3 perovskites,³⁶ reducing the probability of thermally induced delamination and thermally induced mechanical stress, which constitutes a potential problem for MAPbX_3 -based solar cell devices.³⁸

With remarkable electronic properties resembling that of the lead halide perovskites, $\text{Cs}_2\text{AgBiBr}_6$ has lately allowed astonishing progress in a variety of opto-electronic applications. For example, $\text{Cs}_2\text{AgBiBr}_6$ has been very successfully applied in X-ray and UV detectors.^{8,39} Lei *et al.* reported highly efficient and air-stable $\text{Cs}_2\text{AgBiBr}_6$ photodetectors, with a responsivity of 7.01 A/W, a detectivity of 5.66×10^{11} Jones, an external quantum efficiency of 2146%, and a response time of 956 μs .⁵ Likewise, Steele *et al.* reported highly sensitive X-ray detectors based on $\text{Cs}_2\text{AgBiBr}_6$ single crystals with long charge carrier lifetimes exceeding 1.5 μs and a sensitivity of $316 \mu\text{CGy}^{-1}\text{cm}^{-2}$.⁶ Finally, Yang *et al.* were already able to produce passivated $\text{Cs}_2\text{AgBiBr}_6$ wafers that enabled highly sensitive, low-noise X-ray imaging with good spatial resolution.⁷ Combined with the much improved stability, this material therefore constitutes an extremely promising new material for photodetection and X-ray detection applications. Working solar cell devices using $\text{Cs}_2\text{AgBiBr}_6$ as absorbers have shown a good rectifying diode behavior,^{34,37,40–43} although so far the highest achieved PCE has been limited to 2.5%.⁴⁰ This is mainly due to too low short circuit current densities even when considering the high indirect band gap.³⁰ Possible explanations for the low performances observed so far include a high exciton binding energy⁴⁴ and light-induced phonons that, because of strong Fröhlich coupling, lead to electron scattering.^{44,45} Both factors could significantly reduce the quantity of extracted charge carriers.

Although this still limits the success of $\text{Cs}_2\text{AgBiBr}_6$ as solar cell absorbers, it remains a very promising material for use in direct X-ray and UV detectors.^{5–8,39}

During the vapor deposition of a mix of the respective binary halide precursors, MAPbBr_3 and CsPbBr_3 form spontaneously at room temperature.^{16,20} In contrast to this, synthesis protocols for $\text{Cs}_2\text{AgBiBr}_6$ commonly report annealing steps at temperatures around 250 °C.⁴² Currently, the preparation of $\text{Cs}_2\text{AgBiBr}_6$ thin films has been reported mostly *via* spin coating, which is a process that is inherently difficult to scale up and wastes a large ratio of the precursor material. To our knowledge, only four methods are reported in literature to successfully deposit $\text{Cs}_2\text{AgBiBr}_6$ from the physical vapor phase: direct re-evaporation of already formed $\text{Cs}_2\text{AgBiBr}_6$ crystals,⁴⁶ sequential deposition of $\text{Cs}_3\text{Bi}_2\text{Br}_9$ and AgBr ,⁴⁶ and sequential deposition of either, in order: AgBr , BiBr_3 , and CsBr ³⁷ or CsBr , AgBr , and BiBr_3 .⁴⁰ The sequential deposition methods were followed by annealing in air to 250 °C under ambient or lowered pressure to form the perovskite. Pantaler *et al.* showed that annealing in air can lead to the formation of a BiOBr secondary phase because of the hydrolyzation of BiBr_3 .⁴⁶

In contrast to the former experiments, in this contribution, we report the direct preparation of $\text{Cs}_2\text{AgBiBr}_6$ thin films by co-evaporation and annealing of CsBr , AgBr , and BiBr_3 precursors in a high-vacuum chamber.

EXPERIMENTAL METHODS

Our *in situ* X-ray diffraction (XRD) setup allows us to analyze the crystal structure of the film on the substrate at any given time.^{16,20,47,48} In order to better understand the initial film formation and the phase evolution during annealing, we

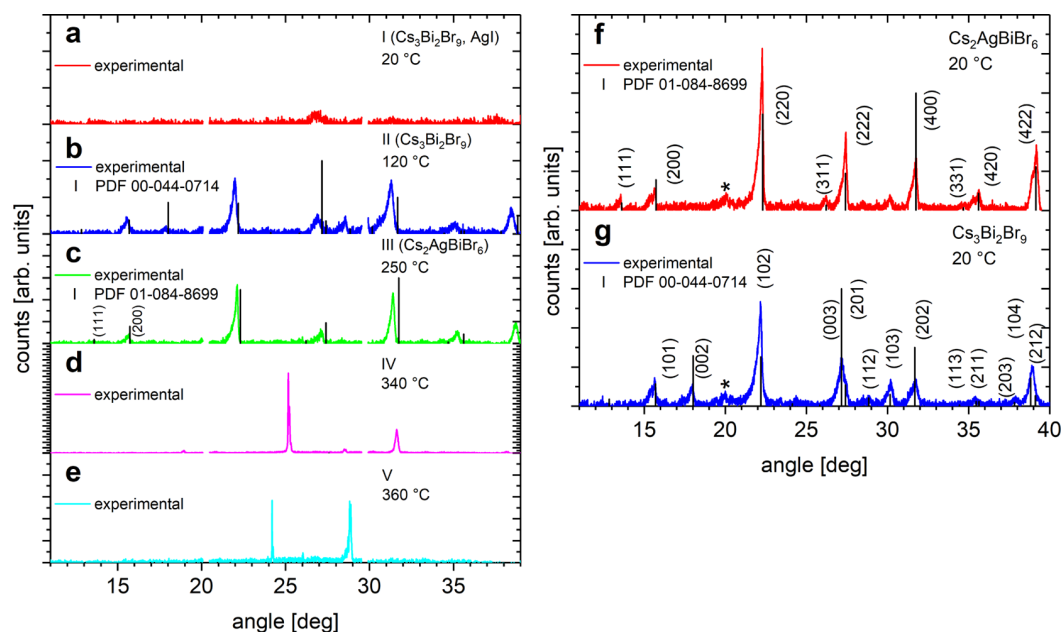


Figure 2. (a–e) XRD scans taken from the decomposition process at different temperatures. The letters correspond to the markers in Figure 1. (f,g) θ/θ scans of $\text{Cs}_2\text{AgBiBr}_6$ and $\text{Cs}_3\text{Bi}_2\text{Br}_9$, respectively.

monitored the presence of different crystal phases and the formation of the desired $\text{Cs}_2\text{AgBiBr}_6$ upon annealing while maintaining the high-vacuum conditions. This provided guidance for the establishment of suitable process parameters for the synthesis of high-quality $\text{Cs}_2\text{AgBiBr}_6$ thin films. Further annealing sheds light onto the thermal degradation pathway of $\text{Cs}_2\text{AgBiBr}_6$. The information gained during the *in situ* process control enables us to develop a process to reproducibly prepare high-quality double perovskite thin films. Finally, we report on the thermal expansion coefficient and decomposition temperature of a $\text{Cs}_2\text{AgBiBr}_6$ film that was prepared with our new approach.

In the first experiment, we examine the phase evolution of a Cs–Bi–Ag–Br precursor film during thermal annealing. For this purpose, the precursors CsBr, AgBr, and BiBr_3 were co-evaporated in a high vacuum of roughly 2×10^{-5} mbar onto a soda lime glass substrate that was kept at room temperature. More experimental details, such as evaporation temperatures and specifications of the materials, can be found in the Supporting Information. After the precursor deposition, the substrates were slowly heated to 550 °C with a temperature ramp of 4 K min^{-1} while retaining the high vacuum. During these experiments, we monitored the evolution of the crystal structure with an *in situ* XRD measurement setup attached to the system that uses a Cu X-ray source and a detector array capable of simultaneously measuring a 2θ angular diffraction range of 28°, with one scan taken every 60 s. More details on the *in situ* XRD system can be found in the referenced publications by Borchert *et al.*⁴⁸ and Pistor *et al.*⁴⁷

RESULTS AND DISCUSSION

A colormap summarizing the XRD measurements of the first experiment, showing the precursor film formation and the phase evolution of $\text{Cs}_2\text{AgBiBr}_6$ upon thermal annealing, is depicted in Figure 1. Figure 1a shows the growth of the precursor film, while Figure 1b depicts the phase evolution during annealing of the film. Every column of pixels in the colormap corresponds to one

full XRD scan, and the color indicates the number of counts that were registered at a given angle. The temperatures of the precursor sources and the substrate are shown in the graphs below the colormaps. For better clarity, the process has been divided into six stages that correspond to the different phases that were observed in the *in situ* XRD. Exemplary XRD scans from each stage are depicted in Figure 2 (subfigures a–e). The position of these scans is marked in the colormap of Figure 1b with red dotted lines. The simultaneous co-evaporation of the precursors CsBr, AgBr, and BiBr_3 onto the substrate at room temperature led to the formation of $\text{Cs}_3\text{Bi}_2\text{Br}_9$ and AgBr (stage I, Figure 2a). At this point, the XRD signal is comparably weak and only one broad peak with low intensity at 26.79° is detected. This peak can be interpreted as a superposition of the (003) peak of $\text{Cs}_3\text{Bi}_2\text{Br}_9$ and the (111) peak of AgBr. Raman measurements of the unannealed precursor layer are provided in the Supporting Information. They show a series of peaks, which indicate the presence of CsBr, BiBr_3 , and/or the overlapping ternary $\text{Cs}_3\text{Bi}_2\text{Br}_9$ phase but not the $\text{Cs}_2\text{AgBiBr}_6$ double perovskite phase. We conclude that our precursor films deposited at room temperature form a rather amorphous or nanocrystalline phase consisting of a mixture of different binary and ternary Cs–Bi–Br and Ag–Br phases.

During the substrate heating with a linear ramp up to a temperature of 550 °C, the first notable change in the XRD signals occurs at 100 °C (stage II, Figure 2b). The (003) peak loses intensity, while other peaks corresponding to $\text{Cs}_3\text{Bi}_2\text{Br}_9$ grow significantly, of which the most intense ones are the (102) peak at 21.97°, the (202) peak at 31.33°, and the (104) peak at 38.43°. We interpret this as a recrystallization of the $\text{Cs}_3\text{Bi}_2\text{Br}_9$ phase in the film. At 230 °C, we observe the first formation of the $\text{Cs}_2\text{AgBiBr}_6$ double perovskite phase (stage III, Figure 2c). The formation is indicated by a sudden increase in intensity and a considerable shift of the XRD peak angles. Most importantly, the peaks at 22.02°, 26.80°, and 31.30° shift upward by about 0.1°. According to our XRD references for $\text{Cs}_3\text{Bi}_2\text{Br}_9$ (PDF 00-044-0714) and $\text{Cs}_2\text{AgBiBr}_6$ (PDF 01-084-8699), this would

correspond well to a phase change from $\text{Cs}_3\text{Bi}_2\text{Br}_9$ to $\text{Cs}_2\text{AgBiBr}_6$.

Continued heating of the substrate led to two further phase transitions and an eventual disappearance of all XRD peaks. The first of these phase transitions occurred at 300 °C (stage IV, Figure 2d). All XRD peaks that were attributed to $\text{Cs}_2\text{AgBiBr}_6$ disappear and a peak at 25.16° becomes detectable, quickly followed by peaks at 18.93°, 28.52°, and 31.62°. This XRD transition could either indicate a phase change toward a different high-temperature phase of $\text{Cs}_2\text{AgBiBr}_6$ or it could be the beginning of decomposition. The XRD peaks did not correspond conclusively to any reference in the Cs–Bi–Ag–Br system that was available to us. In order to gain further insights into this phase, another experiment was conducted, where the process was stopped at this stage and the resulting layer was analyzed with energy-dispersive X-ray spectroscopy (EDX), obtaining a composition of: 29.8% Cs, 12.5% Ag, 8.0% Bi, and 50.0% Br. The loss of Bi at this point makes the beginning decomposition of the perovskite more plausible. At 350 °C (stage V, Figure 2e), another transition occurred, showing XRD peaks at 24.19° and multiple peaks in the range from 28.54° to 28.87°. Again, we did not find any reference that would allow us to unambiguously identify this phase *via* its XRD peaks, so a sample of this phase was prepared and analyzed. The composition, according to EDX, was as follows: 34.1% Cs, 17.2% Ag, 2.5% Bi, and 46.3% Br. These results indicate a very noteworthy drop in the Bi content when compared to the earlier stages in the process. We therefore conclude that these last two phases likely consist of highly oriented CsAgBr_2 , Cs_2AgBr_3 , or both, with the composition of the last phase closely matching Cs_2AgBr_3 . In conclusion, we suggest that the low sublimation temperature of BiBr_3 leads to a decomposition pathway of $\text{Cs}_2\text{AgBiBr}_6$ into Cs_xAgBr_y at temperatures around 300–350 °C. At temperatures above 390 °C (stage VI), the entire set of XRD peaks starts to lose intensity until no peaks were detectable anymore. This remained so after cooling the sample down to room temperature, and after taking out the samples, no layer at all was visible on the glass to the naked eye, indicating that finally all residual layers had re-evaporated from the substrate.

Based on the information we gathered in this experiment, we were able to develop a method for the direct synthesis of $\text{Cs}_2\text{AgBiBr}_6$ thin films. For this purpose, the same precursors were co-evaporated onto a substrate at room temperature and then heated up to 250 °C over 30 min in order to induce the phase change and then kept at that temperature for 30 min. The XRD colormap of an example process of this kind is available in the Supporting Information. A $\theta/2\theta$ -scan of the resulting $\text{Cs}_2\text{AgBiBr}_6$ film measured at room temperature can be seen in Figure 2f, showing the essentially phase-pure synthesis of $\text{Cs}_2\text{AgBiBr}_6$. There is a faint peak at 30.13° that can be attributed to $\text{Cs}_3\text{Bi}_2\text{Br}_9$, hinting at a small amount of $\text{Cs}_3\text{Bi}_2\text{Br}_9$ that might be coexisting as a secondary phase. As a reference, a phase-pure thin film of $\text{Cs}_3\text{Bi}_2\text{Br}_9$ has been grown and its diffractogram is depicted below in Figure 2g for comparison. According to the calculations of Xiao *et al.*, $\text{Cs}_3\text{Bi}_2\text{Br}_9$ can be considered to be a likely secondary phase after the preparation of a $\text{Cs}_2\text{AgBiBr}_6$ perovskite.³¹ A Raman measurement of the annealed $\text{Cs}_2\text{AgBiBr}_6$ layer is provided in Figure 3, together with its photoluminescence spectrum. The observed Raman peaks correspond well to the reference spectrum measured on a $\text{Cs}_2\text{AgBiBr}_6$ single crystal.⁴⁹ EDX measurements of the film indicate a composition close to the one expected for a stoichiometric sample (within the margin of error of our EDX

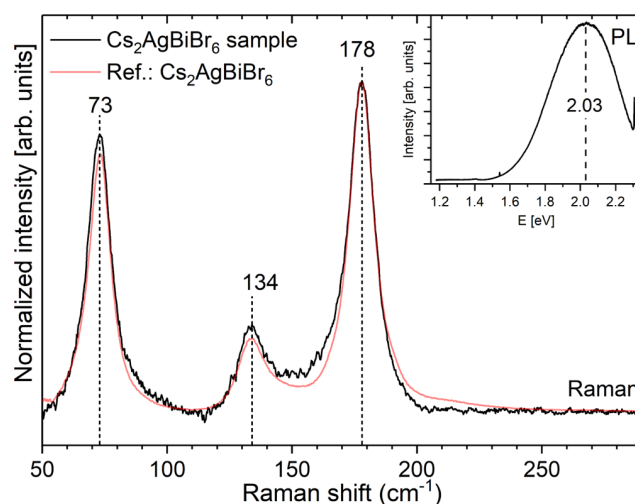


Figure 3. Raman (excitation wavelength 785 nm) and photoluminescence (excitation wavelength 532 nm) spectra of an annealed $\text{Cs}_2\text{AgBiBr}_6$ layer. As a reference, the Raman spectrum of a $\text{Cs}_2\text{AgBiBr}_6$ single crystal grown through slow temperature induced crystallization from an aqueous precursor solution is shown.⁴⁹

system) with 23.7% Cs, 9.3% Ag, 9.7% Bi, and 57.3% Br. Igbari *et al.* reported a slight deviation in the atomic ratios of their vacuum-sublimated $\text{Cs}_2\text{AgBiBr}_6$ from the expected stoichiometry, which manifested as a significantly lowered Br content. It seems that the stoichiometry control of vacuum-deposited films is more challenging when compared to that of spin-coated ones.⁴⁰ An EDX measurement of the initial precursor film (before annealing) shows that its atomic composition is 16.06% Cs, 7.65% Ag, 13.69% Bi, and 62.60% Br, with means that the precursor film has a significantly higher Bi content. It has been reported elsewhere that a surplus of Bi is beneficial for the $\text{Cs}_2\text{AgBiBr}_6$ formation during annealing.^{31,37} We believe the film formation is self-adjusting, with the surplus BiBr_3 evaporating during the annealing because of the low sublimation temperature of BiBr_3 . Scanning electron micrographs of fully formed $\text{Cs}_2\text{AgBiBr}_6$ layers show large, homogeneously distributed grains which can also be found in the Supporting Information. For comparison, we intentionally prepared a $\text{Cs}_3\text{Bi}_2\text{Br}_9$ layer by employing the same method as before (precursor deposition and subsequent annealing) but without co-evaporating AgBr. An XRD scan of the final $\text{Cs}_3\text{Bi}_2\text{Br}_9$ layer is depicted in Figure 2g for comparison. In the first attempt to fabricate solar cell devices with $\text{Cs}_2\text{AgBiBr}_6$ thin films produced this way as absorbers, we could confirm a good rectifying behavior for these films in a device with a $\text{TiO}_2/\text{C60}$ electron- and a Spiro-OMETAD hole-transport layer.⁴³ However, the very low short circuit current densities of below 1 mA/cm² limited the PCE to below 1%. This is in agreement with works presented by other groups, where in all cases low photocurrents limited the device efficiencies, as mentioned earlier. While the potential of $\text{Cs}_2\text{AgBiBr}_6$ as a solar cell absorber therefore might be limited, reports on its use in detection applications still make it a very promising material.

In order to further study the stability and thermal expansion of our final $\text{Cs}_2\text{AgBiBr}_6$ thin films, one of the synthesized thin films was also heated from room temperature to its decomposition, while again monitoring the phase evolution with *in situ* XRD. A colormap of the full process is provided in the Supporting Information. Apart from the thermally induced lattice expansion, no changes were observed up to a temperature of

approximately 300 °C. The decomposition behavior followed the pathway observed before, with the double perovskite starting to decompose again at roughly 300 °C into the phases reported above. Slavney *et al.* conducted an annealing experiment in air, using a temperature ramp of 5 K min⁻¹ and monitoring the sample *via* thermogravimetric analysis. They found a significant mass loss at 430 °C and differential thermal analysis revealed no phase changes up to this point.³³ The difference in the decomposition temperature may be attributed to differences in the temperature ramp, ambient atmosphere, and pressure. Analogous decomposition experiments to the one presented here were conducted previously by our group for MAPbX₃ (X = I, Br, or Cl) and CsPbX₃ (X = I or Br). The highest decomposition temperature of the MAPb-based perovskites was found with MAPbBr₃ at 250 °C,¹⁶ while CsPbI₃ decomposed at 390 °C and CsPbBr₃ decomposed at 360 °C.²⁰ With its decomposition at 300 °C, the Cs₂AgBiBr₆ perovskite exhibits an increased thermal stability in comparison to the MAPbX₃ perovskites, but because of the BiBr₃ loss, it is less thermally stable than the CsPbX₃ system.

Finally, the temperature-dependent *in situ* XRD measurements enabled us to analyze the thermal expansion of the Cs₂AgBiBr₆ perovskite. For these calculations, a cubic crystal symmetry was assumed and the position of the (220) peak was used to calculate the lattice constant *a*. In Figure 4, the lattice

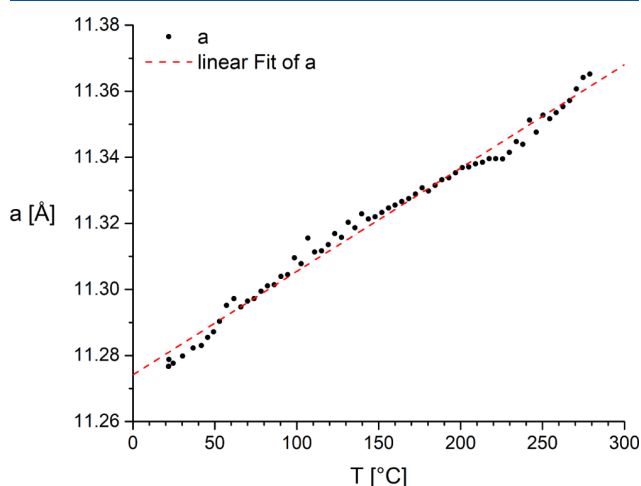


Figure 4. Temperature dependence of the lattice constant *a* of cubic Cs₂AgBiBr₆. The position of the (220) peak was used to calculate *a*.

constant *a* is plotted against the temperature. From a linear fit of the data, the linear expansion coefficient was calculated to be $\alpha_L = (27.75 \pm 0.41) \times 10^{-6} \text{ K}^{-1}$. The error given is the statistical error from the fit. This is in good agreement with the previous findings of Dong *et al.*, who found a linear expansion coefficient of $\alpha_L = (27.8 \pm 0.3) \times 10^{-6} \text{ K}^{-1}$ for this material.³⁶ These results show that the linear expansion coefficient is lower compared to that of both CsPbBr₃ ($\alpha_L \approx 38 \times 10^{-6} \text{ K}^{-1}$)^{20,50} and MAPbBr₃ ($\alpha_L \approx 33 \times 10^{-6} \text{ K}^{-1}$).^{16,50} The higher decomposition temperature and the lower thermal expansion coefficient of Cs₂AgBiBr₆ compared to the MAPbX₃ (X = I, Br, or Cl) perovskites indicate a much increased framework rigidity, which in turn hints at an increased general endurance of this perovskite. This further confirms that the fully inorganic Cs₂AgBiBr₆ exhibits a significantly improved stability when compared to the conventional organic–inorganic lead halide perovskites.

CONCLUSIONS

In conclusion, we successfully analyzed the phase evolution of Cs₂AgBiBr₆ thin films during synthesis and thermal decomposition. The results allowed us to develop a reproducible and simple synthesis method for Cs₂AgBiBr₆ in an all-vacuum process from the physical vapor phase. We find that the Cs₂AgBiBr₆ double perovskite material is only formed at elevated temperatures well above 230 °C. In consequence, in the process presented here, the synthesis is done *via* one-step co-deposition of the precursors CsBr, AgBr, and BiBr₃, followed by thermal annealing to 250 °C. We also investigated the response of a Cs₂AgBiBr₆ thin film to thermal annealing and calculated a linear expansion coefficient of $\alpha_L = (27.8 \pm 0.4) \times 10^{-6} \text{ K}^{-1}$. The decomposition of the double perovskite, caused by the loss of BiBr₃, started at roughly 300 °C. These results indicate a much increased stability of Cs₂AgBiBr₆ when compared to the MAPbX₃ (X = I, Br, or Cl) family of perovskites. This superior stability along with its exceptional opto-electronic properties gives faith in the successful widespread implementation of Cs₂AgBiBr₆ in X-ray and UV detectors.

ASSOCIATED CONTENT

Supporting Information

The Supporting Information is available free of charge at <https://pubs.acs.org/doi/10.1021/acs.jpcc.0c02480>.

Information about the materials used, scanning electron microscopy images of Cs₂AgBiBr₆ layers, full colormap of the preparation process of Cs₂AgBiBr₆, full colormap of the decomposition process starting from Cs₂AgBiBr₆ at room temperature, and Raman measurement on an unannealed precursor layer (PDF)

AUTHOR INFORMATION

Corresponding Author

Paul Pistor – Martin Luther University Halle-Wittenberg, 06120 Halle (Saale), Germany; orcid.org/0000-0002-9244-915X; Email: paul.pistor@physik.uni-halle.de

Authors

Thomas Burwig – Martin Luther University Halle-Wittenberg, 06120 Halle (Saale), Germany; orcid.org/0000-0002-7299-859X

Maxim Guc – Catalonia Institute for Energy Research (IREC), 08930 Barcelona, Spain; orcid.org/0000-0002-2072-9566

Victor Izquierdo-Roca – Catalonia Institute for Energy Research (IREC), 08930 Barcelona, Spain

Complete contact information is available at: <https://pubs.acs.org/doi/10.1021/acs.jpcc.0c02480>

Notes

The authors declare no competing financial interest.

ACKNOWLEDGMENTS

The authors from the MLU gratefully acknowledge the financial support from the German Federal Ministry of Research and Education (BMBF) under contract number 03EK3570B (StrukturSolar II). The authors from the IREC acknowledge the European Regional Development Funds (ERDF, FEDER, Programa Competitivitat de Catalunya 2007–2013) and belong to the M-2E (Electronic Materials for Energy) Consolidated Research Group and the XaRMAE Network of Excellence on Materials for Energy of the Generalitat de Catalunya.

REFERENCES

- (1) Gong, J.; Darling, S. B.; You, F. Perovskite Photovoltaics: Life-Cycle Assessment of Energy and Environmental Impacts. *Energy Environ. Sci.* **2015**, *8*, 1953–1968.
- (2) Rossi, F. D.; Baker, J. A.; Beynon, D.; Hooper, K. E. A.; Meroni, S. M. P.; Williams, D.; Wei, Z.; Yasin, A.; Charbonneau, C.; Jewell, E. H. All Printable Perovskite Solar Modules with 198 cm² Active Area and over 6% Efficiency. *Adv. Mater. Technol.* **2018**, *3*, 1800156.
- (3) Green, M. A.; Hishikawa, Y.; Dunlop, E. D.; Levi, D. H.; Hohl-Ebinger, J.; Yoshita, M.; Ho-Baillie, A. W. Y. Solar Cell Efficiency Tables (Version 55). *Prog. Photovoltaics* **2019**, *27*, 3–12.
- (4) Kim, Y. C.; Kim, K. H.; Son, D.-Y.; Jeong, D.-N.; Seo, J.-Y.; Choi, Y. S.; Han, I. T.; Lee, S. Y.; Park, N.-G. Printable Organometallic Perovskite Enables Large-Area, Low-Dose X-ray Imaging. *Nature* **2017**, *550*, 87–91.
- (5) Lei, L.-Z.; Shi, Z.-F.; Li, Y.; Ma, Z.-Z.; Zhang, F.; Xu, T.-T.; Tian, Y.-T.; Wu, D.; Li, X.-J.; Du, G.-T. High-Efficiency and Air-Stable Photodetectors Based on Lead-Free Double Perovskite Cs₂AgBiBr₆ Thin Films. *J. Mater. Chem. C* **2018**, *6*, 7982–7988.
- (6) Steele, J. A.; Pan, W.; Martin, C.; Keshavarz, M.; Debroye, E.; Yuan, H.; Banerjee, S.; Fron, E.; Jonckheere, D.; Kim, C. W.; et al. Photophysical Pathways in Highly Sensitive Cs₂AgBiBr₆ Double-Perovskite Single-Crystal X-ray Detectors. *Adv. Mater.* **2018**, *30*, 1804450.
- (7) Yang, B.; Pan, W.; Wu, H.; Niu, G.; Yuan, J.-H.; Xue, K.-H.; Yin, L.; Du, X.; Miao, X.-S.; Yang, X.; et al. Heteroepitaxial Passivation of Cs₂AgBiBr₆ Wafers with Suppressed Ionic Migration for X-ray Imaging. *Nat. Commun.* **2019**, *10*, 1989.
- (8) Yang, J.; Bao, C.; Ning, W.; Wu, B.; Ji, F.; Yan, Z.; Tao, Y.; Liu, J. M.; Sum, T. C.; Bai, S.; et al. Stable, High-Sensitivity and Fast-Response Photodetectors Based on Lead-Free Cs₂AgBiBr₆ Double Perovskite Films. *Adv. Opt. Mater.* **2019**, *7*, 1801732.
- (9) Wei, H.; Huang, J. Halide Lead Perovskites for Ionizing Radiation Detection. *Nat. Commun.* **2019**, *10*, 1066.
- (10) Habisreutinger, S. N.; Leijtens, T.; Eperon, G. E.; Stranks, S. D.; Nicholas, R. J.; Snaith, H. J. Carbon Nanotube/Polymer Composites as a Highly Stable Hole Collection Layer in Perovskite Solar Cells. *Nano Lett.* **2014**, *14*, 5561–5568.
- (11) Beal, R. E.; Slotcavage, D. J.; Leijtens, T.; Bowring, A. R.; Belisle, R. A.; Nguyen, W. H.; Burkhard, G. F.; Hoke, E. T.; McGehee, M. D. Cesium Lead Halide Perovskites with Improved Stability for Tandem Solar Cells. *J. Phys. Chem. Lett.* **2016**, *7*, 746–751.
- (12) Leguy, A. M. A.; Hu, Y.; Campoy-Quiles, M.; Alonso, M. I.; Weber, O. J.; Azarhoosh, P.; van Schilfgarde, M.; Weller, M. T.; Bein, T.; Nelson, J.; et al. Reversible Hydration of CH₃NH₃PbI₃ in Films, Single Crystals, and Solar Cells. *Chem. Mater.* **2015**, *27*, 3397–3407.
- (13) Sheng, R.; Wen, X.; Huang, S.; Hao, X.; Chen, S.; Jiang, Y.; Deng, X.; Green, M. A.; Ho-Baillie, A. W. Y. Photoluminescence Characterisations of a Dynamic Aging Process of Organic–Inorganic CH₃NH₃PbBr₃ Perovskite. *Nanoscale* **2016**, *8*, 1926–1931.
- (14) Yang, J.; Siempelkamp, B. D.; Liu, D.; Kelly, T. L. Investigation of CH₃NH₃PbI₃ Degradation Rates and Mechanisms in Controlled Humidity Environments Using in Situ Techniques. *ACS Nano* **2015**, *9*, 1955–1963.
- (15) Akbulatov, A. F.; Luchkin, S. Y.; Frolova, L. A.; Dremova, N. N.; Gerasimov, K. L.; Zhidkov, I. S.; Anokhin, D. V.; Kurmaev, E. Z.; Stevenson, K. J.; Troshin, P. A. Probing the Intrinsic Thermal and Photochemical Stability of Hybrid and Inorganic Lead Halide Perovskites. *J. Phys. Chem. Lett.* **2017**, *8*, 1211–1218.
- (16) Pistor, P.; Burwig, T.; Brzuska, C.; Weber, B.; Fränzel, W. Thermal Stability and Miscibility of Co-evaporated Methyl Ammonium Lead Halide (MAPbX₃, X = I, Br, Cl) Thin Films Analysed by in Situ X-ray Diffraction. *J. Mater. Chem. A* **2018**, *6*, 11496.
- (17) Niu, G.; Guo, X.; Wang, L. Review of Recent Progress in Chemical Stability of Perovskite Solar Cells. *J. Mater. Chem. A* **2015**, *3*, 8970–8980.
- (18) Ahmad, W.; Khan, J.; Niu, G.; Tang, J. Inorganic CsPbI₃ Perovskite-Based Solar Cells: A Choice for a Tandem Device. *Sol. RRL* **2017**, *1*, 1700048.
- (19) Kulbak, M.; Cahen, D.; Hodes, G. How Important Is the Organic Part of Lead Halide Perovskite Photovoltaic Cells? Efficient CsPbBr₃ Cells. *J. Phys. Chem. Lett.* **2015**, *6*, 2452–2456.
- (20) Burwig, T.; Fränzel, W.; Pistor, P. Crystal Phases and Thermal Stability of Co-evaporated CsPbX₃ (X = I, Br) Thin Films. *J. Phys. Chem. Lett.* **2018**, *9*, 4808–4813.
- (21) Stoumpos, C. C.; Malliakas, C. D.; Peters, J. A.; Liu, Z.; Sebastian, M.; Im, J.; Chasapis, T. C.; Wibowo, A. C.; Chung, D. Y.; Freeman, A. J.; et al. Crystal Growth of the Perovskite Semiconductor CsPbBr₃: A New Material for High-Energy Radiation Detection. *Cryst. Growth Des.* **2013**, *13*, 2722–2727.
- (22) Chu, S.; Pan, S.; Li, G. Trap State Passivation and Photoactivation in Wide Band Gap Inorganic Perovskite Semiconductors. *Phys. Chem. Chem. Phys.* **2018**, *20*, 25476–25481.
- (23) Eperon, G. E.; Stranks, S. D.; Menelaou, C.; Johnston, M. B.; Herz, L. M.; Snaith, H. J. Formamidinium Lead Trihalide: A Broadly Tunable Perovskite for Efficient Planar Heterojunction Solar Cells. *Energy Environ. Sci.* **2014**, *7*, 982.
- (24) Yunakova, O. N.; Miloslavskii, V. K.; Kovalenko, E. N. Exciton Absorption Spectrum of Thin CsPbI₃ and Cs₂PbI₆ Films. *Opt. Spectrosc.* **2012**, *112*, 91–96.
- (25) Möller, C. K. Crystal Structure and Photoconductivity of Cesium Plumbohalides. *Nature* **1958**, *182*, 1436.
- (26) Jökar, E.; Chien, C.-H.; Tsai, C.-M.; Fathi, A.; Diau, E. W.-G. Robust Tin-Based Perovskite Solar Cells with Hybrid Organic Cations to Attain Efficiency Approaching 10%. *Adv. Mater.* **2019**, *31*, 1804835.
- (27) Sun, P.-P.; Li, Q.-S.; Yang, L.-N.; Li, Z.-S. Theoretical Insights into a Potential Lead-Free Hybrid Perovskite: Substituting Pb₂ with Ge₂. *Nanoscale* **2016**, *8*, 1503–1512.
- (28) Wang, H.-C.; Pistor, P.; Marques, M. A. L.; Botti, S. Double perovskites as p-type conducting transparent semiconductors: a high-throughput search. *J. Mater. Chem. A* **2019**, *7*, 14705–14711.
- (29) Zhao, X.-G.; Yang, J.-H.; Fu, Y.; Yang, D.; Xu, Q.; Yu, L.; Wei, S.-H.; Zhang, L. Design of Lead-Free Inorganic Halide Perovskites for Solar Cells via Cation-Transmutation. *J. Am. Chem. Soc.* **2017**, *139*, 2630–2638.
- (30) Savory, C. N.; Walsh, A.; Scanlon, D. O. Can Pb-Free Halide Double Perovskites Support High-Efficiency Solar Cells? *ACS Energy Lett.* **2016**, *1*, 949–955.
- (31) Xiao, Z.; Meng, W.; Wang, J.; Yan, Y. Thermodynamic Stability and Defect Chemistry of Bismuth-Based Lead-Free Double Perovskites. *ChemSusChem* **2016**, *9*, 2628–2633.
- (32) Filip, M. R.; Hillman, S.; Haghighirad, A. A.; Snaith, H. J.; Giustino, F. Band Gaps of the Lead-Free Halide Double Perovskites Cs₂AgBiCl₆ and Cs₂AgBiBr₆ from Theory and Experiment. *J. Phys. Chem. Lett.* **2016**, *7*, 2579–2585.
- (33) Slavney, A. H.; Hu, T.; Lindenberg, A. M.; Karunadasa, H. I. A Bismuth-Halide Double Perovskite with Long Carrier Recombination Lifetime for Photovoltaic Applications. *J. Am. Chem. Soc.* **2016**, *138*, 2138–2141.
- (34) Wu, C.; Zhang, Q.; Liu, Y.; Luo, W.; Guo, X.; Huang, Z.; Ting, H.; Sun, W.; Zhong, X.; Wei, S.; et al. The Dawn of Lead-Free Perovskite Solar Cell: Highly Stable Double Perovskite Cs₂AgBiBr₆ Film. *Adv. Sci.* **2018**, *5*, 1700759.
- (35) Igbari, F.; Wang, Z.-K.; Liao, L.-S. Progress of Lead-Free Halide Double Perovskites. *Adv. Energy Mater.* **2019**, *9*, 1803150.
- (36) Dong, L.; Sun, S.; Deng, Z.; Li, W.; Wei, F.; Qi, Y.; Li, Y.; Li, X.; Lu, P.; Ramamurty, U. Elastic Properties and Thermal Expansion of Lead-Free Halide Double Perovskite Cs₂AgBiBr₆. *Comput. Mater. Sci.* **2018**, *141*, 49–58.
- (37) Wang, M.; Zeng, P.; Bai, S.; Gu, J.; Li, F.; Yang, Z.; Liu, M. High-Quality Sequential-Vapor-Deposited Cs₂AgBiBr₆ Thin Films for Lead-Free Perovskite Solar Cells. *Sol. RRL* **2018**, *2*, 1800217.
- (38) Cojocar, L.; Uchida, S.; Sanehira, Y.; Gonzalez-Pedro, V.; Bisquert, J.; Nakazaki, J.; Kubo, T.; Segawa, H. Temperature Effects on the Photovoltaic Performance of Planar Structure Perovskite Solar Cells. *Chem. Lett.* **2015**, *44*, 1557–1559.
- (39) Pan, W.; Wu, H.; Luo, J.; Deng, Z.; Ge, C.; Chen, C.; Jiang, X.; Yin, W.-J.; Niu, G.; Zhu, L.; et al. Cs₂AgBiBr₆ Single-Crystal X-ray

Detectors with a Low Detection Limit. *Nat. Photonics* **2017**, *11*, 726–732.

(40) Igbari, F.; Wang, R.; Wang, Z.-K.; Ma, X.-J.; Wang, Q.; Wang, K.-L.; Zhang, Y.; Liao, L.-S.; Yang, Y. Composition Stoichiometry of Cs₂AgBiBr₆ Films for Highly Efficient Lead-Free Perovskite Solar Cells. *Nano Lett.* **2019**, *19*, 2066.

(41) Gao, W.; Ran, C.; Xi, J.; Jiao, B.; Zhang, W.; Wu, M.; Hou, X.; Wu, Z. High-Quality Cs₂AgBiBr₆ Double Perovskite Film for Lead-Free Inverted Planar Heterojunction Solar Cells with 2.2 % Efficiency. *ChemPhysChem* **2018**, *19*, 1696–1700.

(42) Greul, E.; Petrus, M. L.; Binek, A.; Docampo, P.; Bein, T. Highly Stable, Phase Pure Cs₂AgBiBr₆ Double Perovskite Thin Films for Optoelectronic Applications. *J. Mater. Chem. A* **2017**, *5*, 19972–19981.

(43) Burwig, T.; Heinze, K.; Naumann, V.; Hähnel, A.; Lange, S.; Hagedorf, C.; Scheer, R.; Pistor, P. Co-evaporated Cs₂AgBiBr₆ Double Perovskites for Solar Cells. In *Proceedings of the 36th European Photovoltaic Solar Energy Conference and Exhibition*, 2019; pp 728–732.

(44) Kentsch, R.; Scholz, M.; Horn, J.; Schlettwein, D.; Oum, K.; Lenzer, T. Exciton Dynamics and Electron-Phonon Coupling Affect the Photovoltaic Performance of the Cs₂AgBiBr₆ Double Perovskite. *J. Phys. Chem. C* **2018**, *122*, 25940–25947.

(45) Steele, J. A.; Puech, P.; Keshavarz, M.; Yang, R.; Banerjee, S.; Debroye, E.; Kim, C. W.; Yuan, H.; Heo, N. H.; Vanacken, J.; et al. Giant Electron-Phonon Coupling and Deep Conduction Band Resonance in Metal Halide Double Perovskite. *ACS Nano* **2018**, *12*, 8081–8090.

(46) Pantaler, M.; Fettkenhauer, C.; Nguyen, H. L.; Anusca, I.; Lupascu, D. C. Deposition Routes of Cs₂AgBiBr₆ Double Perovskites for Photovoltaic Applications. *MRS Adv.* **2018**, *3*, 1819–1823.

(47) Pistor, P.; Borchert, J.; Fränzel, W.; Csuk, R.; Scheer, R. Monitoring the Phase Formation of Coevaporated Lead Halide Perovskite Thin Films by in Situ X-ray Diffraction. *J. Phys. Chem. Lett.* **2014**, *5*, 3308–3312.

(48) Borchert, J.; Boht, H.; Fränzel, W.; Csuk, R.; Scheer, R.; Pistor, P. Structural Investigation of Co-evaporated Methyl Ammonium Lead Halide Perovskite Films During Growth and Thermal Decomposition Using Different PbX₂ (X = I, Cl) Precursors. *J. Mater. Chem. A* **2015**, *3*, 19842–19849.

(49) Pistor, P.; Meyns, M.; Guc, M.; Wang, H.-C.; Marques, M. A. L.; Alcobé, X.; Cabot, A.; Izquierdo-Roca, V. Advanced Raman Spectroscopy of Cs₂AgBiBr₆ Double Perovskites and Identification of Cs₃Bi₂Br₉ Secondary Phases. *Scripta Mater.* **2020**, *184*, 24–29.

(50) Rakita, Y.; Cohen, S. R.; Kedem, N. K.; Hodes, G.; Cahen, D. Mechanical Properties of APbX₃ (A = Cs or CH₃NH₃; X = I or Br) Perovskite Single Crystals. *MRS Commun.* **2015**, *5*, 623–629.

Closing Discussion

In contrast to the works of Wu [168], Wang [169], Pantaler [170] and Igrari [171] et al., who used sequential deposition methods, we successfully prepared a $\text{Cs}_2\text{AgBiBr}_6$ perovskite via one step co-evaporation with subsequent annealing to 250° for about 30 min. The results of the ramp experiment show the formation of the perovskite at 230°C and its decomposition at roughly 300°C . The decomposition is initiated by the loss of the BiBr_3 component, leaving behind CsAgBr_2 and Cs_2AgBr_3 . This continues what has been shown for the MA and the Cs based perovskites: That the component that limits the thermal stability of the material is the one whose respective precursor has the lowest sublimation temperature. The results of the Raman measurements confirm, in addition to the XRD and EDX results, that the $\text{Cs}_2\text{AgBiBr}_6$ perovskite has been formed. The measured values coincide well with the reference, which was taken from a work of Pistor et al., who grew a $\text{Cs}_2\text{AgBiBr}_6$ single crystal from solution [173].

Overall, the results on $\text{Cs}_2\text{AgBiBr}_6$ demonstrate for the first time (to my knowledge), that it is possible to prepare this perovskite via an all-vacuum process consisting of a one-step co-evaporation of the precursors BiBr_3 , CsBr and AgBr with a subsequent annealing to 250°C . The perovskite exhibits a thermal stability in between that of the MA and Cs based perovskites. It is unlikely that this material will be used as an efficient absorber for photovoltaic devices (see section 5.2), but it is highly promising as an absorber layer in high energy photon detection devices and for this purpose, its thermal stability is more than sufficient.

In addition to this work, a $\text{Cs}_2\text{AgBiBr}_6$ thin film was analyzed using an SEM and solar cells using $\text{Cs}_2\text{AgBiBr}_6$ absorbers have been prepared. One solar cell was analyzed using a TEM in collaboration with the Fraunhofer CSP. This work is presented in section 5.2.

4.5 Kinetics of the Thermal Decomposition of MAPbI₃

Preliminary Discussion

Reference: [Bu4]

Most studies that examine the thermal stability of metal-halide perovskites, including our earlier studies, follow one of two approaches: One approach is to set a constant environment, defined by temperature, atmospheric gas composition, humidity, etc. and continuously monitor the sample via an in situ measurement method. After a decomposition of the sample is detectable, the *time* it took for that change to be visible is reported. The other approach is to systematically change the experimental conditions, for example via a temperature ramp, and then report on the *conditions* that were in effect during the decomposition, for example a specific temperature. While these approaches are, when taken by themselves, completely viable, they make the comparison of results between different studies very difficult. For metal-halide perovskites several studies have shown that the preparation methods of the materials and the experimental conditions of their decomposition play a crucial role in the measured stability. Thin films tend to be more stable than powders [174], co-evaporated films tend to be more stable than solution processed ones [14], inert atmospheres like vacuum or N₂ lead to higher stabilities than atmospheres containing O₂ [175], and a variety of factors like light and moisture can have a significant impact on the perovskite (see section 2.1.3). The experiments that are put forth by different research groups usually deviate from one another in several of these factors and so it is nearly guaranteed that the materials they use in their experiments will exhibit deviations in their stability. However, if one group uses the first approach presented above and another uses the latter one, their results can end up being inherently incomparable. For example: Kim et al. have identified signs of decomposition on a MAPbI₃ film (prepared via spin coating) after exposing it to 80 °C for 1 h [176] while we observed a beginning decomposition of our MAPbI₃ film (prepared via vacuum co-evaporation) in our temperature ramp experiment at 120 °C [Bu1]. The temperature ramping speed was 3 K min⁻¹, so the temperature difference from 80 °C to 120 °C would have been passed after 13 min and 20 s. In this case, it is impossible to tell whether the two samples were of comparable stability and thus no conclusions can be drawn on how the different preparation methods influenced the stability of the resulting material. Another inherent issue in these approaches is that the results are very critically influenced by the measurement sampling rate and the signal to noise ratio of the setup, which will inevitably lead to an overestimation of the time or temperature of decomposition to some degree. Differences in the qualities of the measurement setups between different research groups can also be obstacles to comparability.

In a consensus statement based on the ISOS procedures regarding the reporting on stability for perovskite photovoltaics, the researchers noted that: “Despite the great emphasis laid on stability-related investigations, publications lack consistency in experimental procedures and parameters reported. It is therefore challenging to reproduce and compare results and thereby develop a deep understanding of degradation mechanisms.” [101] This emphasizes that the lack of comparability constitutes a significant issue in this research field.

A more general method to quantify the thermal stability of a material is the description of the thermal decomposition reaction by a kinetic triplet, which consists of the activation energy

E , the frequency factor A and the reaction model $f(\alpha)$, where α is the extent of reaction, going from 0 at the start of a reaction to 1 at the end. These factors describe how the reaction progresses via the differential equation 2.14. The benefit of this method is that the kinetic triplet can be calculated from any set of data that puts α in relation to t and a large variety of measurement methods can be used to determine α , like TGA, XRD or KEML and KEMS mass spectroscopy, among others. The results can be thought of as a more general description of the thermal decomposition kinetics, as they can be used to try to predict the expected reaction rate for a large range of temperatures. In this way, they also allow for easier comparisons between different research groups and different experimental setups. This paper demonstrates and compares a variety of methods to calculate this kinetic triplet from in situ XRD data obtained during isothermal decomposition.

Reaction kinetics of the thermal decomposition of MAPbI₃ thin films

Thomas Burwig^{✉*} and Paul Pistor^{✉†}

Martin Luther University Halle-Wittenberg, Von-Danckelmann-Platz 3, 06120 Halle (Saale), Germany



(Received 25 March 2021; accepted 1 June 2021; published 21 June 2021)

Despite their outstanding optoelectronic properties, metal halide perovskites have not yet seen widespread use in commercial applications. This is mostly due to their lack of stability with respect to several external factors, e.g., humidity, heat, light, and oxygen. Even though extensive studies have been carried out over the last decade, a lot of questions regarding their thermal stability still remain, and various publications have put forth different approaches for measuring and quantifying the conditions of their decomposition. However, differences in the experimental setups and in the reported values make comparisons of the reported results challenging. We show an approach, where MAPbI₃ thin films are thermally decomposed in high vacuum within a temperature range from 220 °C to 250 °C, while monitoring changes in the crystal structure using an *in situ* x-ray diffraction setup. This process reveals the complete phase evolution of the thin films from MAPbI₃ into PbI₂. The time resolved data was then evaluated in view of the reaction kinetics using three different approaches. First, an Arrhenius fit was applied to $\ln k$ over $1/T$, where the rate constant k was determined by fitting a first order exponential decay onto the decreasing peak area of the most prominent diffraction peaks. Secondly, a model fitting approach was used, where the data was tested against a set of different reaction models. Lastly, a model free isoconversional approach was applied. By doing this, we succeed in characterizing the decomposition and determine the kinetic triplet, consisting of the activation energy E , the frequency factor A , and the reaction model $f(\alpha)$. With the help of the kinetic triplet the decomposition reaction can be expressed in a physically meaningful way and allows us to predict the decomposition dynamics of MAPbI₃ thin films for varying temperatures.

DOI: [10.1103/PhysRevMaterials.5.065405](https://doi.org/10.1103/PhysRevMaterials.5.065405)

I. INTRODUCTION

Metal-halide perovskites (MHPs) have garnered interest in the photovoltaic research community in 2009 and have seen very noteworthy achievements in regard to their power conversion efficiencies when used as absorber layers in solar cells [1]. Due to their remarkable optoelectronic properties they are also being researched for use in LEDs [2–5], lasers [6], and high-energy photodetectors [7,8]. The strongest remaining concern in view of their industrial application is their long term stability. MHPs have been reported to decompose when exposed to environmental influences such as humidity, oxygen, light, and heat [9,10]. There are also certain phenomena pertaining to their stability that are not yet well understood, like self-healing effects observed in certain metal-halide perovskites that would allow for a regeneration of lost performance when stored in the dark [8,11–14]. Another important factor in the stability of perovskite solar cells (PSCs) is their contact layers: Commonly used hole transport layers, such as spiro-OMeTAD, can significantly exacerbate the gradual decline of a PSCs power conversion efficiency [15,16]. Despite this, there are reports of PSCs that have successfully been tested against some of the protocols in the IEC 61215 norm [17,18], but specific testing protocols need to be developed in order to realistically ascertain the

real-world long-term performance of PSCs. Now that the knowledge of metal-halide perovskites and their vulnerabilities has grown significantly over the past few years, there have been recent proposals for standardization in testing for research purposes that take the mentioned phenomena into account [19]. Significant advancements in understanding the perovskites' decomposition pathways and in improving their stability have been made recently. For MAPbI₃, the organic methyl-ammonium (MA) molecule has proven to be a major factor in its instability. Exchanging this molecule, partially or fully, with Cs or formamidinium (FA) has been found to greatly increase the resulting perovskite's durability [20–29]. Our experiments on CsPbI₃ and CsPbBr₃ have also shown a major increase in thermal stability, when MA is exchanged for Cs [30]. 2D perovskites and quasi-2D perovskites have also been shown to exhibit increased stability towards humidity and heat [15,31,32] while showing great promise for applications as LEDs [2,4,5]. While the impact of humidity or photoinduced degradation can be mitigated by encapsulation or the choice of improved contact layers [33–36], the exposure to thermal loads is intrinsic to certain applications such as solar cells.

Therefore, resistance to heat is a major factor for perovskite solar cell absorbers. Yet, up to this day, the results on the thermal stability of perovskites exhibit a large spread and a lot of questions remain open. Notably, there is no consensus on the intrinsic stability of MAPbI₃. The Gibbs free energy for its decomposition into PbI₂ and MAI at room temperature has been calculated to be positive by some groups and negative

*thomas.burwig@physik.uni-halle.de

†paul.pistor@physik.uni-halle.de

by others, while it is more definitely positive for MAPbBr₃ and MAPbCl₃, which renders the latter two intrinsically stable [10]. It is well supported by now, that the stability limiting component in MAPbI₃ is the organic MAI, which might itself decompose into either HI and CH₃NH₂ or CH₃I and NH₃ [10]. Akbulatov *et al.* found that MAPbI₃ first decomposes into PbI₂ and MAI, with the latter one further decomposing into CH₃I and NH₃, while they also observed CH₄, C₂H₄, and HI as additional gaseous species [29]. Other groups disagree on the gaseous species that form from the decomposition of the MA molecule, as they found primarily HI and CH₃NH₂ as decomposition products [37]. The preparation of the perovskite also plays a significant role in the species of gas released. MAPbI₃ thin films prepared by Song *et al.* have been shown to release NH₃ and CH₃I above 100 °C and HI and CH₃NH₂ above 180 °C [38]. In contrast to that, a MAPbI₃ powder by Juarez-Perez *et al.* released all four gaseous species at temperatures above 50 °C [33]. These discrepancies are discussed in detail by Juarez-Perez in Ref. [39]. Wet chemically processed MAPbI₃ can also release solvent residues, for example, DMF, which might influence stability [10]. We chose co-evaporation as the preparation method, because it is industrially attractive, scalable, and results in more stable films as compared to wet-chemical processing [40]. Dewi *et al.* compared the stability of PSCs prepared with co-evaporated MAPbI₃ absorber layers to PSCs with solution processed MAPbI₃ layers. The former ones retained around 80% of their initial power conversion efficiency when stored for 3600 h at 85 °C and 10% RH, while the latter ones had their efficiency drop to almost 0% after only 1000 h [40].

Despite the consensus on the relatively low thermal stability of MAPbI₃, only a few attempts have been made to consistently obtain the kinetic parameters of the decomposition reaction, and, to our knowledge, no attempts have been made so far to derive these directly for MAPbI₃ thin films. In this work, we study the thermal decomposition of absorber-grade, co-evaporated MAPbI₃ thin films in high vacuum. The choice of the preparation method and the absence of atmospheric exposure of these films allow us to exclude any solvent or moisture related impact on the decomposition reaction and to study the intrinsic thermal stability of the MAPbI₃ absorber. In previous works, we used our *in situ* XRD setup to monitor the phase evolution of MHP thin films during a temperature ramp and extracted the onset temperature of decomposition. To do this, thin films were prepared on glass substrates in high vacuum and then, without vacuum break, heated with a ramp of 3 K/min. By observing the phase evolution via the XRD peaks, we could observe, depending on the perovskite under investigation, recrystallization, phase changes, and complete decomposition for temperatures from room temperature up to approximately 400 °C. Using the same method and setup for each experiment, we were able to compare the thermal decomposition onset of different perovskites (MAPbI₃, MAPbBr₃, MAPbCl₃, CsPbI₃, CsPbBr₃, and Cs₂AgBiBr₆) [30,41,42]. As long as the experimental conditions are carefully controlled and kept the same from trial to trial, the results allow for a meaningful comparison of the thermal stability between these materials. However, thermal decomposition experiments that take their data from a single temperature ramp make it difficult to pinpoint the moment of decomposition. Whether

TGA or XRD is used, the onset of the decomposition will be a minute and gradual change in signal that is spread over a long time, and the onset of the decomposition is difficult to specify and relatively imprecise. Additionally, it will depend on the ramping speed and decomposition dynamics, i.e., the slower the decomposition progresses, the higher the reported temperature will be. In Ref. [41] we found that 50% of the MAPbI₃ was decomposed when the temperature ramp had reached around 230 °C. This lies in good agreement with the results of Dualeh *et al.* who found the onset of decomposition of MAPbI₃ at 234 °C using TGA measurements of powder samples [43]. However, as has been rightly pointed out by Zhang *et al.*, the observed decomposition temperature depends strongly on the temperature regime and ramp that is used, as some isothermal experiments show decomposition of MAPbI₃ at much lower temperatures [10]. Using isothermal experiments, multiple groups found a beginning decomposition at the surface of MAPbI₃ already at approximately 80 °C after exposure times of around 1 h [10,44]. There is an obvious disagreement in the onset of decomposition and kinetic parameters between various sets of studies, which calls for clarification.

The ambiguity in the thermal decomposition temperatures and mechanisms in this temperature regime is especially critical, as solar cells can reach operating temperatures of up to 85 °C [17]. Here we provide further analysis of the thermal decomposition of MAPbI₃, the prototypical metal-halide perovskite, in a thin film configuration. As simple decomposition measurements based on one temperature do not suffice to determine the reaction kinetics, we observe the decomposition at four different temperatures close to the decomposition onset temperature established in the previous ramping experiments and aim to obtain the temperature-dependent kinetic parameters of the reaction. Similarly motivated, Yu *et al.* extracted an activation energy E of 120 kJ/mol from isothermal decomposition experiments of powder mixtures of MAPbI₃ diluted in KBr but did not state the corresponding frequency factor [45]. Brunetti *et al.* and Juarez-Perez *et al.* calculated activation energies E of 76 kJ/mol and 93 kJ/mol, respectively, for the thermal decomposition of MAPbI₃ powders and included the corresponding frequency factors A , together with data for other perovskites [37,46]. By determining E and A , the thermal decomposition reaction of a material is quantified in a physically more rigorous way and allows for easier comparisons than the disparate and isolated results that are often reported. It also allows for predictions about the progress of the decomposition for any given combination of time and temperature, with the limitation that the predictions lose accuracy for temperatures that are far away from the values that were used to determine the parameters.

In this work we determine the kinetic triplet of the thermal decomposition of MAPbI₃ thin films, consisting of the activation energy E , the pre-exponential factor A , and the reaction model $f(\alpha)$, where α is the extent of conversion, a value between 0 (beginning of reaction) and 1 (end of reaction). We will first give a short overview over the necessary theory. Afterwards, we explain our experimental process in more detail. For the evaluation of the results we will employ three established methods: Firstly, we assume a first order process and calculate the rate constant k for each experiment

TABLE I. The selection of models that were used for the calculations presented here. This selection was taken from Khawam *et al.* [48], who also go into detail on how to derive these relations. $g(\alpha)$ denotes the integrated reaction model as calculated by equation (5).

Symbol	Model name	$f(\alpha)$	$g(\alpha)$
F0	Zeroth order	1	α
F1	First order; Mampel	$1 - \alpha$	$-\ln(1 - \alpha)$
F2	Second order	$(1 - \alpha)^2$	$(1 - \alpha)^{-1} - 1$
F3	Third order	$(1 - \alpha)^3$	$(1/2)[(1 - \alpha)^{-2} - 1]$
R2	Contracting area	$2(1 - \alpha)^{1/2}$	$1 - (1 - \alpha)^{1/2}$
R3	Contracting volume	$3(1 - \alpha)^{2/3}$	$1 - (1 - \alpha)^{1/3}$
D1	1D diffusion	$1/2\alpha^{-1}$	α^2
D2	2D diffusion	$-1/\ln(1 - \alpha)$	$((1 - \alpha)\ln(1 - \alpha)) + \alpha$
D3	3D diffusion	$2(1 - \alpha)^{2/3}(1 - (1 - \alpha)^{1/3})^{-1}$	$[1 - (1 - \alpha)^{1/3}]^2$
D4	Ginstling-Brounshtein	$3/[2((1 - \alpha)^{-1/3} - 1)]$	$1 - (2/3)\alpha - (1 - \alpha)^{2/3}$
P2	Power law	$2\alpha^{1/2}$	$\alpha^{1/2}$
P3	Power law	$3\alpha^{2/3}$	$\alpha^{1/3}$
P4	Power law	$4\alpha^{3/4}$	$\alpha^{1/4}$
P2/3	Power law	$2/3\alpha^{-1/2}$	$\alpha^{3/2}$
A2	Avrami-Erofeev	$2(1 - \alpha)[- \ln(1 - \alpha)]^{1/2}$	$[- \ln(1 - \alpha)]^{1/2}$
A3	Avrami-Erofeev	$3(1 - \alpha)[- \ln(1 - \alpha)]^{2/3}$	$[- \ln(1 - \alpha)]^{1/3}$
A4	Avrami-Erofeev	$4(1 - \alpha)[- \ln(1 - \alpha)]^{3/4}$	$[- \ln(1 - \alpha)]^{1/4}$
B1	Prout-Tompkins	$\alpha(1 - \alpha)$	$\ln[\alpha/(1 - \alpha)] + c$

through fits to the exponentially decaying XRD peak areas. We then fit an Arrhenius function to $\ln k$ over $1/T$ to determine E and A . Secondly, we use a model fitting approach to determine E , A , and $f(\alpha)$ and evaluate how well the different decomposition models fit to our data. Lastly, we use a model free isoconversional method, where the α dependence of the reaction speed is expressed not with a separate factor $f(\alpha)$ but is instead expressed through α dependent values for E and A . The latter two methods, among others, were presented in detail by Vyazovkin *et al.* [47].

II. THEORY

The activation energy E and the frequency factor A determine the rate constant k according to the formula [47]

$$k = A \cdot \exp\left(-\frac{E}{RT}\right), \quad (1)$$

where R is the universal gas constant and T is the absolute temperature. By using a reaction model $f(\alpha)$ and k , the change in α over the time t can be expressed via the differential equation [47]

$$\frac{d\alpha}{dt} = k(T) \cdot f(\alpha). \quad (2)$$

The reaction model $f(\alpha)$ —for examples see Table I—describes how the overall reaction speed depends on α . Different assumptions about the rate limiting factors of a reaction, e.g., geometrical constraints, diffusion, or density of nucleation sites, lead to the formulation of different reaction models. A good introduction into the different kinds of reaction models and their underlying physical assumptions is given in Refs. [48,49]. A kinetic triplet, consisting of E , A , and $f(\alpha)$, completely defines the progression of a given single-step reaction as a function of temperature and time. Two groups have determined kinetic parameters for the thermal decomposition of MAPbI₃ powders: Juarez-Perez *et al.* found

an $E = 93 \pm 8$ kJ/mol and gave a value for the turnover ratio k_t that was $\ln k_t = 5.6 \pm 0.8$ s⁻¹ with the data being fitted with an n th-order Prout-Tompkins autocatalytic model [46]. Brunetti *et al.* found an activation energy of 80 ± 20 kJ/mol and determined this reaction to be of the first order via DTA measurements [37]. Both groups used MAPbI₃ powder within a He atmosphere for their experiments, while Juarez-Perez made additional experiments in vacuum.

To obtain our data, we conducted isothermal decomposition experiments at four different temperatures and monitored the decomposition by *in situ* x-ray diffraction (XRD). For the analysis, we take the XRD peak area as a measure for the progress of the decomposition. Motivated by the results of Brunetti *et al.*, our first approach was to fit a simple first order exponential decay onto the declining peak area for every experiment:

$$a(t) = a_0 \cdot \exp(-kt) \quad (3)$$

with t as the time, a as the peak area (with a_0 being the area at $t = 0$), and k as the reaction rate. This exponential fit of the data yields a value for k for each isothermal experiment. Then $\ln k$ can be plotted against $1/T$ to obtain an Arrhenius plot of the form:

$$\ln k = \ln A - \frac{E}{RT}, \quad (4)$$

where R is the universal gas constant and T is the absolute temperature. A linear fit of the data points then gives a value for E from the slope and a value for A from the intersection with the y axis.

While this approach is a reasonable starting point, it has a significant drawback: Even if the model fits the data well mathematically, the first order reaction model was assumed *a priori* and alternative decomposition mechanisms are not considered. Generally, a given set of experimental data can be reasonably well fitted to a variety of different reaction models, and the obtained values for E and A may then differ

accordingly in order to compensate for the different model. These considerations were elaborated on in more detail by Vyazovkin *et al.* [47].

In the next stage of analysis, we therefore tested a large set of models against the experimental data, as suggested by Vyazovkin *et al.* This is commonly referred to as the model fitting approach. The selection of reaction models that our data has been tested against is listed in Table I, which displays $f(\alpha)$ and the integrated reaction model $g(\alpha)$, which is calculated as follows:

$$g(\alpha) = \int_0^\alpha [f(\alpha)]^{-1}. \quad (5)$$

To gain an intuition on what $g(\alpha)$ signifies, one can think about it in the following way: $g(\alpha)$ gives a value that, when divided by the rate constant k , gives the time t after which the conversion α is reached. This can be expressed in the following relation:

$$g(\alpha) = k(T) \cdot t. \quad (6)$$

This also means, that when plotting $g(\alpha)$ over t for a set of experimental data at a temperature T , the slope of that plot gives a value for k for that temperature. To reduce the uncertainty that is often seen at the very beginning and at the very end of a process, one can restrict the range of the $g(\alpha)$ over t plot to values between, for example, $\alpha = 0.1$ and $\alpha = 0.9$, which has been done for the evaluations presented here. The results of these fits can then be used to construct a classic Arrhenius plot, where $\ln k$ is plotted over $1/T$ and E and A are calculated in the conventional way. The quality of the linear fit onto the Arrhenius graph gives a good indication of how well the respective model describes the process.

Another way to address the question of which reaction model fits best to the experimental data is to use the following method: The data is first transferred into a reduced time relation. For this, an arbitrary extent of conversion close to the end is chosen, e.g., $\alpha = 0.9$. The time at which this conversion was reached is taken as t_α and then the reduced time t_r is calculated by $t_r = t/t_\alpha$ for all data points. A given model results in a very specific shape of the $\alpha(t_r)$ curve and so this approach can be used to determine how well a particular model fits the experimental data. It is also possible to choose two values for α and normalize between them, so that $t_r = 0$ is at α_1 and $t_r = 1$ is at α_2 . This is especially useful if the exact starting point of the decomposition is difficult to determine. Since this is the case for our data, we chose an approach with $\alpha_1 = 0.1$ and $\alpha_2 = 0.9$. To quantify how well the experimental data fits the calculated curves, one can compute the residual sum of squares S^2 :

$$S_j^2 = \frac{1}{n-1} \sum_{i=1}^n (t_{\text{exp},i} - t_{\text{calc},j}(\alpha_i))^2, \quad (7)$$

where $t_{\text{exp},i}$ are the times of the experimental data points and $t_{\text{calc},j}(\alpha_i)$ are the times predicted by model j for the corresponding value of α . To help with ordering the results, the minimum value for S_j^2 is determined and the normalized residual F_j is calculated [47]:

$$F_j = \frac{S_j^2}{S_{\text{min}}^2}. \quad (8)$$

This value will be 1 for the best fitting model and >1 for all others. It gives an easy to read indication of how much larger S_j^2 is for every model when compared to the best fitting one.

Finally, we test a model free approach, the so-called isoconversional method. The previous approaches assumed a fixed activation energy E and a fixed rate constant A . The α dependence of the reaction speed was found in $f(\alpha)$. In contrast to this, the isoconversional method delivers values for E and A that directly depend on α and thus change over the course of the process. The values for $E(\alpha)$ do not depend on the choice of a reaction model, while the obtained values for $A(\alpha)$ do. This method is especially useful when analyzing multistep reactions but it can also be applied to single step reactions. To calculate the values of $E(\alpha)$ and $A(\alpha)$ for a given α , first $-\ln(t_{\alpha,i})$ is plotted over $1/T_i$ for every temperature T_i . This gives an Arrhenius plot of the following form [47]:

$$-\ln(t_{\alpha,i}) = \ln \left[\frac{A_\alpha}{g(\alpha)} \right] - \frac{E_\alpha}{RT_i}. \quad (9)$$

Again, the values for $E(\alpha)$ and $A(\alpha)$ can be calculated from a linear fit. To obtain the proper dependence of E and A on α this is then done for a selection of values for α .

III. EXPERIMENTAL DETAILS

We prepared and decomposed the MAPbI₃ thin films in a high vacuum chamber under an operating pressure of approximately 10^{-5} mbar. The high vacuum offers a reproducible atmosphere, specifically removing the impact from oxygen and water exposure. The MAPbI₃ was synthesized via co-evaporation of the precursors MAI (evaporated at 110 °C) and PbI₂ (evaporated at 317 °C) onto a soda lime glass substrate that was at room temperature at the time of deposition. The average rate of perovskite growth was 0.6 Å/s and the finished films had a thickness of around 600 nm. During the co-evaporation the chamber pressure rose to around 10^{-4} mbar, mostly due to the partial pressure of the evaporated MAI. The time-resolved *in situ* XRD signature of an exemplary growth process can be found in the supporting information. The MAPbI₃ perovskite undergoes a tetragonal to cubic structural phase change at approximately 60 °C [41,50]. Furthermore, we observed a recrystallization of our thin films in previous experiments. This manifested in a variation of the relative Bragg peak intensities corresponding to the MAPbI₃ phase, indicating a change in the preferential orientation of the thin film. In order to separate these effects from the actual decomposition, the samples have been preheated to 150 °C for 1.5 h in the isothermal decomposition experiments. A sample from a process that was stopped after this pre-annealing was used to confirm that the resulting film still consisted of black perovskite. For the decomposition the samples were subjected to a constant temperature at 220 °C, 230 °C, 240 °C, or 250 °C. This choice of temperatures was informed by our previous temperature ramp experiments. This previous work also contains more information on the growth of the perovskite layers [41]. The supporting information includes a scanning electron microscopic image of a MAPbI₃ layer before annealing as well as an image of a fully decomposed sample.

During the processes the samples were monitored using an *in situ* XRD system that took one scan every minute with a

fixed source-detector geometry. The system uses a Cu x-ray source, whose radiation is filtered through a Ni window. The detector array consists of three Dectris Mythen 1 K modules covering a 2θ range of 28° . The chamber's windows are made of Kapton. Further details on the *in situ* XRD system can be found in Ref. [41]. Exemplary XRD scans of the as-deposited films and of the films annealed to 150°C —taken during the *in situ* XRD analysis—can be found in the supporting information.

One central assumption of these evaluations is the correspondence of the extent of conversion to the intensity of the XRD peaks. Therefore, other factors influencing the peak intensity need to be addressed and, if possible, suppressed. The following paragraphs give an overview over other factors potentially influencing the XRD peak area and how we addressed them:

Recrystallization of the perovskite during the annealing phase: We noticed a recrystallization of the perovskite above 120°C that lead to a change in the relative peak intensities. Because of this we included a pre-annealing to 150°C that was held for 1.5 h before setting the final temperature that lead to the decomposition. While during this pre-annealing step the (100) and (200) peak lose intensity, the increase in intensity of the (222) peak at roughly 24.2° and the (210) peak at roughly 31.3° confirm that, at this temperature, we observe a recrystallization and not the start of the decomposition. For the decomposition at the set temperatures, we then observe a simultaneous and parallel decrease of all XRD peak associated with the perovskite phase, indicating the decomposition as less and less scattering material is available.

A transition into another distinct crystal phase upon heating: The highest temperature phase that is known of MAPbI_3 exhibits a cubic crystal structure with space group $Pm\bar{3}m$ which forms at roughly 60°C [41,50]. The pre-annealing to 150°C should ensure that the film is completely transformed into this high temperature phase.

A melting of the crystal without an actual decomposition: For conventional 3D metal halide perovskites no melting point is known, because the perovskites decompose before a melting point is reached [51].

A layer of educts (specifically PbI_2) that forms on top of the film and thus reduces the XRD intensity: The decomposition of a 600 nm thick MAPbI_3 layer would result in an approximately 300 nm thick PbI_2 layer, due to the molar volume of PbI_2 being roughly half that of MAPbI_3 . The intensity of a beam I_0 will fall to intensity I by going through a film of thickness x as expressed by the relation $I = I_0 \exp(-\mu x)$, where μ is the linear attenuation coefficient of the permeated material. For PbI_2 , with an x-ray beam energy of 8.04 keV, the value for μ is 1.557 cm^{-1} [52]. This would result in a worst-case decrease of the beam intensity by roughly 4.6%, which can be considered negligible.

A deposition of educts on the evaporation chamber windows, which will also reduce the XRD intensity: A deposition of material on the chamber windows would reduce the overall signal strength, thus a few experiments were conducted without exchanging the chamber windows in between trials. The resulting relative decrease in signal strength per experiment was roughly 1%, thus this factor can also be seen as having a negligible influence. The windows were always freshly re-

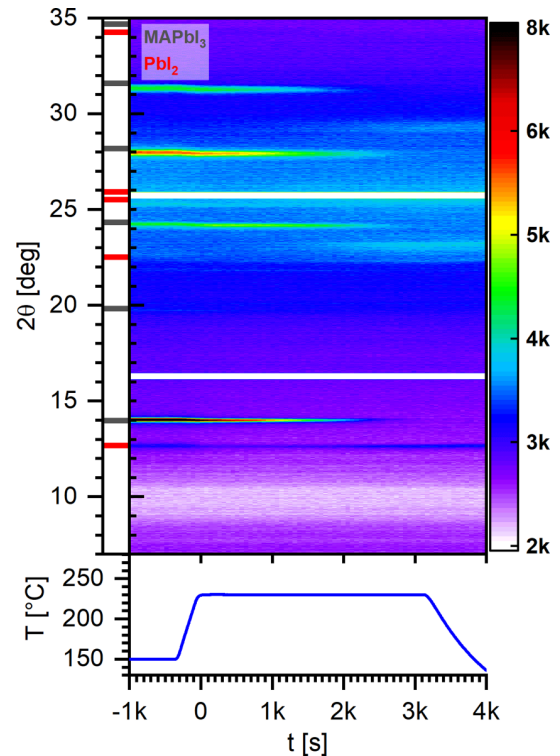


FIG. 1. XRD color map of the decomposition process at 230°C . The x-ray intensity is color coded, with the y axis displaying the detected diffraction angle range and the x axis indicating the evolution in time. The depiction includes the final part of the pre-annealing step at 150°C and the complete decomposition process. The box at the left of the color map shows the XRD references for MAPbI_3 and PbI_2 . The reference for PbI_2 was taken from the PDF database under ID 00-007-0235; the MAPbI_3 reference was calculated using a lattice constant of 6.33 \AA ([41], at 150°C) and assuming the space group $Pm\bar{3}m$ [53].

placed before each experiment for the trials presented in this work.

Presence of an amorphous phase: Any amorphous material would not provide sharp XRD peaks. However, the perovskite is not expected to form an amorphous phase upon heating, and any crystallization of an initially present amorphous phase would lead to an increase in peak intensity and not to the observed decrease. Finally, the clearest indication that the reaction at the final temperature is indeed the thermal decomposition reaction is the increasing XRD peak intensity of the decomposition product PbI_2 .

IV. RESULTS AND EVALUATION

After reaching the respective decomposition temperature, the evolution of the XRD peaks indicates a complete decomposition of the MAPbI_3 perovskite into PbI_2 . As an example, Fig. 1 shows the complete decomposition at a temperature of 230°C . In this graph, the set of *in situ* XRD scans is depicted in a color map, where each column corresponds to one XRD scan, the x axis represents the time scale, and the XRD intensity is color coded. The most intense XRD peak of the MAPbI_3 perovskite in this presentation is the (200)

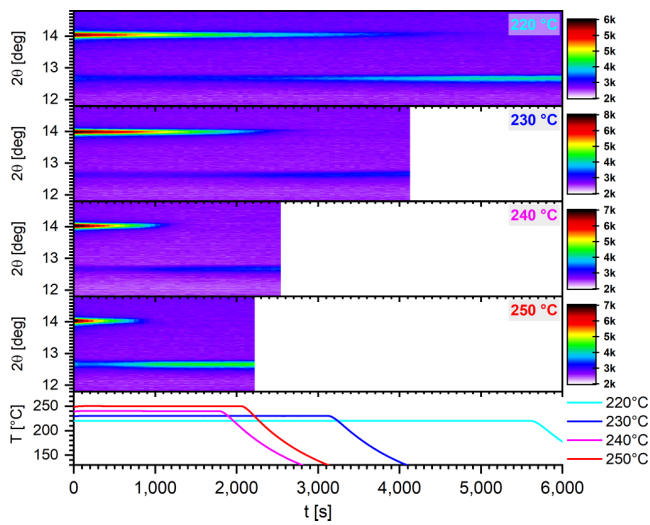


FIG. 2. Overview of the decomposition processes at different temperatures. The color maps show a selected diffraction angle range around the most prominent MAPbI₃ peak [(100) at 14.0°]. The bottom graph shows the substrate temperatures for the different processes. The graphs are scaled so that the reaching of the final temperature is at point $t = 0$. Notably, the (100) MAPbI₃ peak at 14.0° and its k_{β} peak at 12.7° decay with increasing speed as the temperature increases, which indicates an increase in the rate of the decomposition of the MAPbI₃. This decomposition coincides with the growth of the (001) PbI₂ peak at 12.7°.

peak at 28.0°. All MAPbI₃ peaks showed a parallel decline, while the PbI₂ peaks arose directly afterwards. The films after the completed decomposition all had the characteristic yellow color of PbI₂.

Figure 2 compares the evolution of the (100) peak of the MAPbI₃ thin films during the isothermal decomposition for the four decomposition temperatures of 220°C, 230°C, 240°C, and 250°C. For the following evaluation, the area of this peak was chosen as the main indicator for the decomposition of the perovskite, with the peak area before the heating corresponding to a conversion ratio of $\alpha = 0$ and the complete disappearance of the peak corresponding to $\alpha = 1$. In addition to the MAPbI₃ (100) peak, the growing (001) peak of PbI₂, the decomposition product, is visible. It is of note, that the MAPbI₃ layer in the 250°C process contained slightly more lead iodide from the beginning than the other films, according to its XRD signature. A small amount of initial PbI₂ would not make a difference for a first order reaction model, as that would simply equate an already partially reacted film, while the reaction rate stays constant over the course of a first order reaction. The impact on other reaction models, however, would depend strongly on the reaction mechanism. For example, the PbI₂ particles could act as reaction nuclei. In this case, an absolute absence of PbI₂ could lead to a delayed reaction, where even as a temperature is reached, where the reaction would be thermodynamically likely, the absence of any reaction nuclei would hinder the reaction until either a critical temperature is reached, or other small defects or disturbances provide enough of an energetic perturbation for the reaction to occur. In that case, a very small initial amount of PbI₂

TABLE II. Results of the first order approach for the analyzed peaks.

Peak	E (kJ/mol]	$\ln A$ (s ⁻¹)
(100) MAPbI ₃	110.5 ± 17.4	19.3 ± 4.1
(200) MAPbI ₃	105.5 ± 23.3	17.9 ± 5.5
(210) MAPbI ₃	108.7 ± 32.2	18.7 ± 7.6
(001) PbI ₂	114.2 ± 26.7	19.4 ± 6.3

might actually be beneficial for the sake of a thermodynamic analysis. However, since the exact mechanism of this reaction is, as of yet, unknown, it is difficult to exactly predict the influence of excess PbI₂. In any case, its influence is likely greatest at the very start of the reaction and becomes smaller as the reaction, which itself leads to the formation of PbI₂, progresses. Galwey and Brown pointed out in Ref. [49] (Vol. 1, Chap. 3) that some smoothing of the data can be necessary for certain experimental techniques. So, to reduce the impact of measurement noise, each data point has been put through a moving average with the two preceding and the two following data points.

1. First order approach

For the first part of the evaluation we assume a first order model, where the decays of the peak areas are fitted exponentially according to equation (3). For a pure decomposition reaction, the peak intensity of all XRD peaks should decline simultaneously, because the amount of scattering material diminishes, i.e., the relative peak intensities should stay constant. Furthermore, the amount of the reaction product (PbI₂) should increase accordingly. In order to verify this, the evolution of four different XRD peaks is evaluated: The declining normalized peak areas a of the (100), (200), and (210) peaks of MAPbI₃ are plotted in logarithmic scale in Fig. 3. Simultaneously to the decaying of the MAPbI₃ peaks, the area of the PbI₂ (001) peak is rising. It is of note, that the k_{β} peak of the MAPbI₃ (100) reflex overlaps this PbI₂ (001) peak, which leads to some uncertainty in the exact determination of the progress of the PbI₂'s growth. For better comparability, Fig. 3(d) shows $(1 - a)$ for this latter peak. All three MAPbI₃ peaks decay in parallel, which increases the confidence that the observed behavior is in fact a decomposition and not a recrystallization as observed at lower temperatures. The decays show a clear exponential character at the beginning, so these first parts were used for the exponential fits. The reaction rate k was taken from the fits according to equation (3). Then $\ln k$ was plotted against $1/T$ which is shown in Fig. 4. A linear fit of this data resulted in the activation energies and frequency factors shown in Table II.

The results settle around a value for E of roughly 110 ± 20 kJ/mol and a value for $\ln A$ of around 19 ± 5. The evaluations of the four different peaks agree well with each other, demonstrating the consistent behavior of the peaks.

2. Model fitting approach

In this section, different reaction models will be considered and compared in detail for the (100) MAPbI₃ peak, as this peak was the most prominent one. For this model fitting approach the experimental data in the reduced time depiction

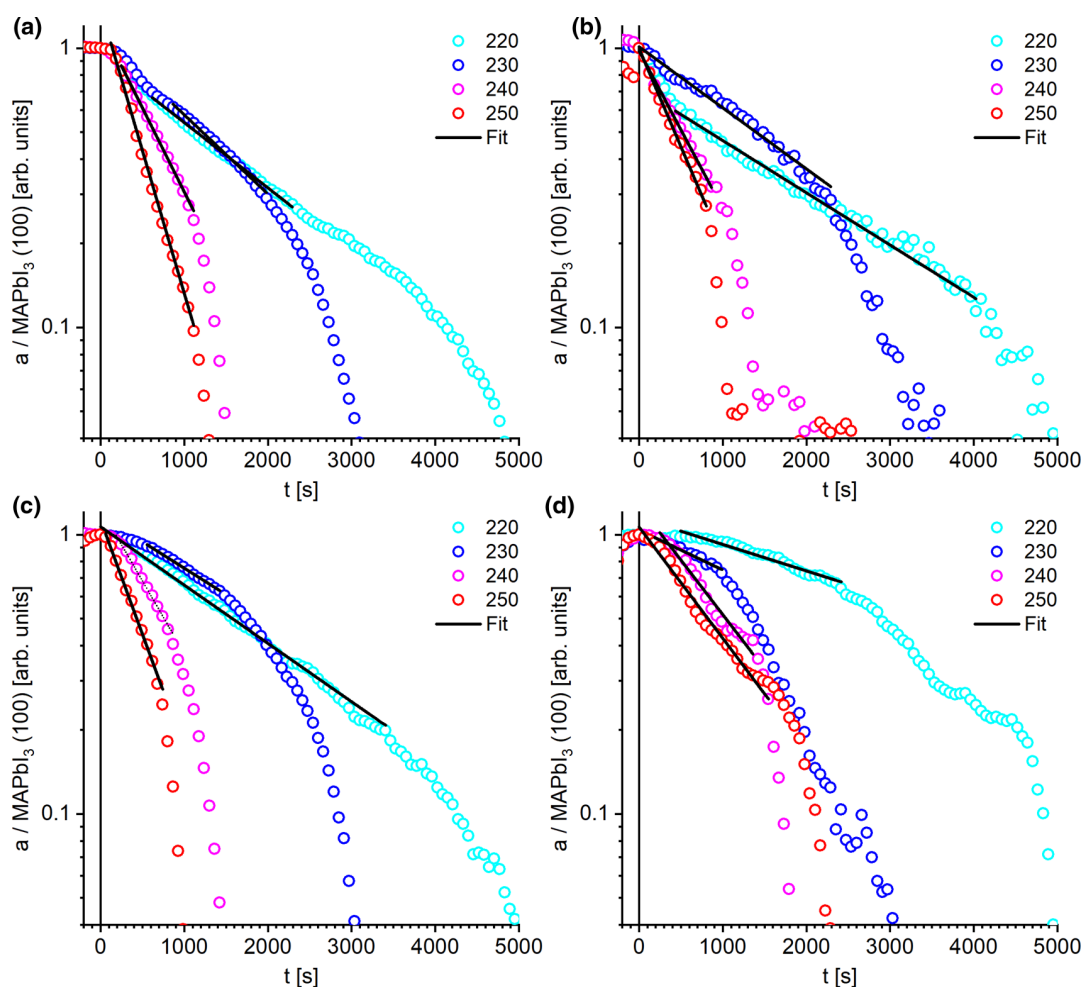


FIG. 3. Logarithmic plots for the time evolution of the peak intensities. (a)–(c) Normalized peak area a for different peaks of MAPbI_3 for all isothermal decomposition experiments. (a) (100) MAPbI_3 ; (b) (200) MAPbI_3 ; (c) (210) MAPbI_3 ; (d) (001) PbI_2 . In the latter case, one minus the normalized peak area, $(1 - a)$, is plotted for better comparability.

will be compared to the predictions from the different models listed in Table I. In the isothermal experiments, the decomposition temperature was not reached instantaneously, but rather ramped up from the 150 °C preheating step to the temperature of isothermal decomposition during 5 min, to avoid overshooting. The actual decomposition begins slightly before the end temperature is reached and so we chose an initial peak intensity before the decline as the starting value for $\alpha = 0$, not the intensity when the decomposition temperature is reached. This way we accept an uncertainty for the first 2–3 data points while assuring that the initial peak area correctly corresponds to $\alpha = 0$. Figure 5 shows the averaged α for the (100) peak from $\alpha = 0.1$ to $\alpha = 0.9$ in comparison to the different models. The residual sum of squares for all models can be found in the supporting information. According to these calculations, the best fitting models are the one-dimensional diffusion (D1), contracting volume (R3), contracting area (R2), the 2/3 power law (P2/3), and the first order (Mampel) model. Individual curves for each temperature are shown in the supporting information.

To determine the activation energies and frequency factors, the $g(\alpha)$ over t plots are prepared as described previ-

ously. Figure 6(a) shows this evaluation exemplarily for the decomposition temperature of 230 °C. The thereby gathered values for k are then used in Arrhenius plots as depicted in Fig. 6(b), which allows for the calculation of E and A . Table III shows the five models that had the lowest values for F , sorted by F in ascending order [see equation (8)]. A table with the results for all models can be found in the supporting information. The activation energies calculated for all models fall around $E \approx 115 \pm 15$ kJ/mol with $\ln A \approx 19$ (s⁻¹), agreeing well with the results for the first order method presented above.

3. Isoconversional approach

The data was also evaluated according to the model free, isoconversional approach as outlined above which resulted in the graph depicted in Fig. 7. Because this method is very susceptible to noise in the data, the data for the peak area has been fitted with a polynomial fit beforehand to smooth it out, before running the calculations. The isoconversional method has the benefit of eliminating the ambiguity that would result from choosing a specific reaction model. The resulting E values are practically constant, indicating a single step reaction. The

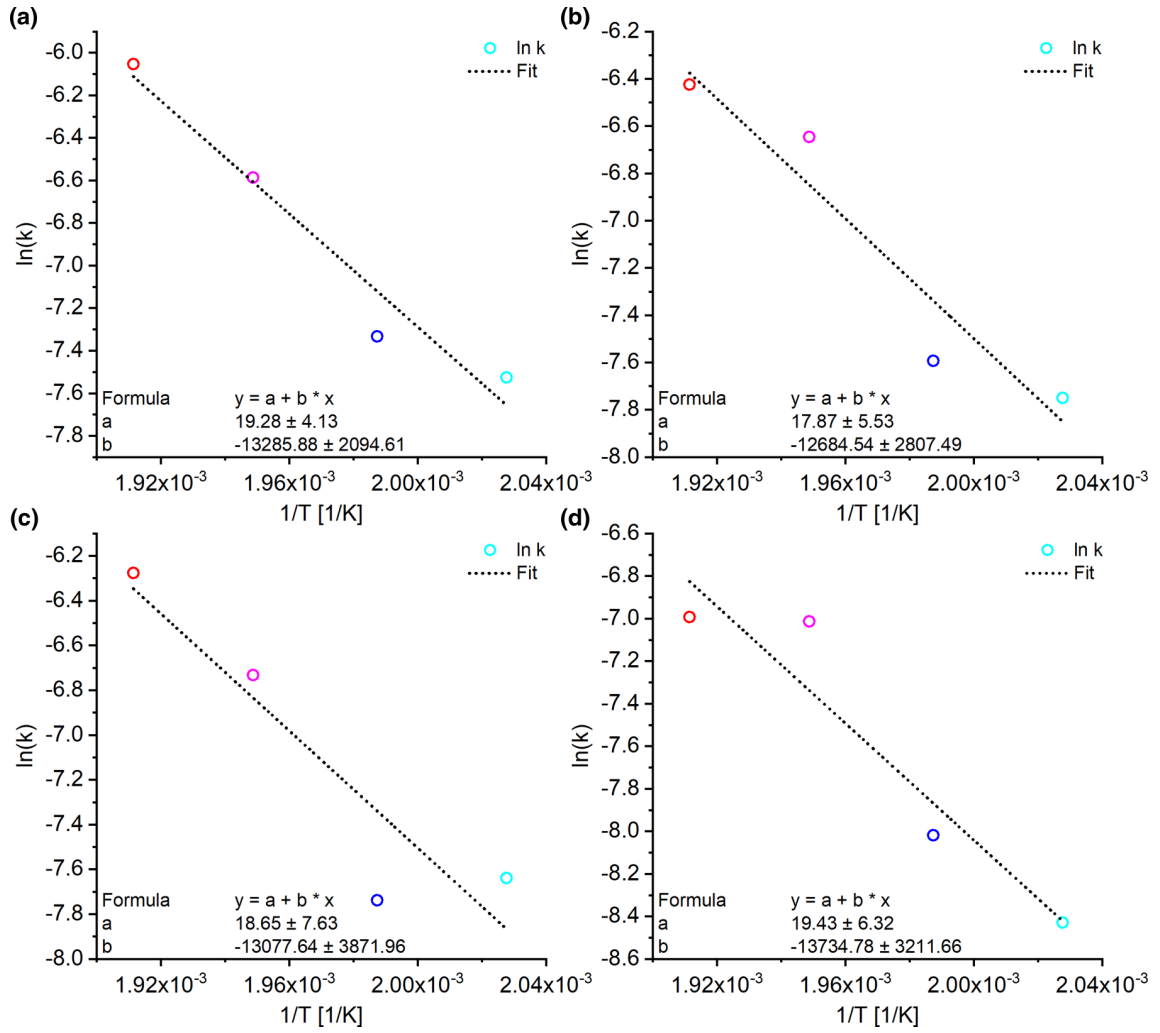


FIG. 4. Arrhenius plots showing the relation of $\ln k$ over $1/T$ for the isothermal experiments and different XRD peaks. The colors represent the different processes and the subfigures represent different XRD peaks. The dotted lines indicate the linear fits. (a) (100) MAPbI₃; (b) (200) MAPbI₃; (c) (210) MAPbI₃; (d) (001) PbI₂.

values for E in the range from $\alpha = 0.1$ to $\alpha = 0.9$ have been averaged to obtain an activation energy of $E(\alpha) = 114.22 \pm 12.12$ kJ/mol. The calculation of A requires the assumption of a reaction model. The choice of the first order model (F1) leads to a value of $\ln A = 21.25 \pm 3.20$ (s⁻¹). These values are, again, in good agreement with the results that were obtained from the previous methods.

4. Comparative evaluation

All perovskite layers decomposed fully into PbI₂ within 15 to 70 min, depending on the temperature. A comparison of the results from the different methods is shown in Table IV. Overall, the results of the three different approaches presented are in accordance with each other and result in values of $E \approx 110 \pm 15$ kJ/mol and $\ln A \approx 19 \pm 4$ (s⁻¹). Using equations

TABLE III. Results of the model fitting approach for the (100) peak of MAPbI₃. E and A were calculated using the data of the isothermal experiments for the models that resulted in the best fits, sorted by the value F , as calculated via equation (8). The error of E is the statistical error from the linear fit.

Model number	Model name	E (kJ/mol)	$\ln A$ (s ⁻¹)	F
D1	One-dimensional diffusion	115.5 ± 11.9	19.7 ± 2.8	1.0
R3	Contracting volume	116.1 ± 12.4	19.2 ± 2.9	6.48
R2	Contracting area	116.6 ± 12.8	19.6 ± 3.0	21.74
P2/3	Power law	116.8 ± 13.0	20.0 ± 3.1	38.15
F1	Mampel (first-order)	115.1 ± 12.0	20.5 ± 2.8	40.75

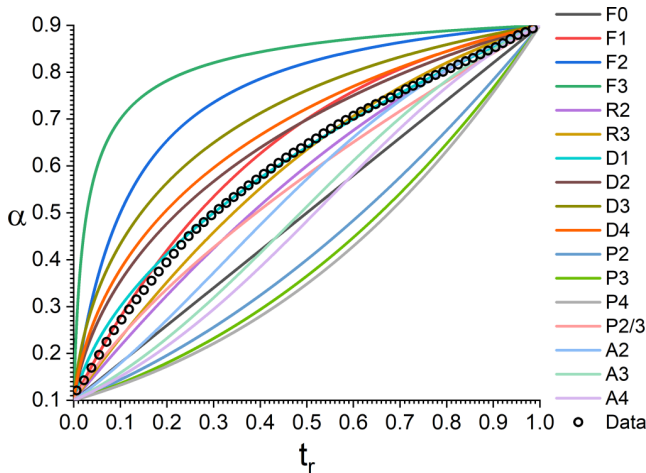


FIG. 5. The relation $\alpha(t_r)$ from $\alpha = 0.1$ to $\alpha = 0.9$, shown for the (100) peak, averaged over all processes. The numbering of the models corresponds to that used in Table I.

(1) and (6) and the values of E and $\ln A$ presented in Table IV, one can calculate at which point in time a certain conversion α would be reached for a given temperature. Many testing protocols, like the IEC 61215 or certain ISOS protocols, specify tests at an elevated temperature of 85°C , which is often seen as the highest temperature that certain spots of a solar module can reach during operation [48]. Similarly, an often used measure is T_{80} , the time it takes for a solar cell to exhibit a relative decrease to 80% of its initial PCE under a given set of conditions. Similarly, we here define T_{80} as the time when 20% of the initial perovskite material would be decomposed. We then use the E and $\ln A$ values of Table IV to calculate the time it would take, according to our results, to decompose a MAPbI_3 layer to $\alpha = 0.2$ at 85°C . For the first order model this conversion ratio would be reached after 2800 h (under the assumption of the model D1 [one-dimensional diffusion] the time would be roughly 2600 h). Dewi *et al.* prepared PSCs with co-evaporated MAPbI_3 and found them to retain roughly 80% of their initial PCE after 3600 h [40], which coincides reasonably well with the time determined by using the first order model. Conversely, we calculated the temperature that a sample can be stored at, to not decompose by more than $\alpha = 0.2$ over the course of 1 h. This temperature is roughly 180°C for both models.

We note that any conclusive decision towards one reaction model or the other has to be taken with care, as a multitude of models can fit a given set of experimental data. For example, in our case, the individual data points obtained for the different

temperatures show some variation in the form of the α versus reduced time plot and could be fitted with various models. We assume that the difficulty to set the exact starting time for the decomposition reaction is the main cause for these variations. The ambiguity of choosing the physical reaction model can take two forms. (1) In practice, a given set of data will probably not perfectly fit a given model. This leads to ambiguity as multiple models with similar behavior can seem to fit the data almost equally well, while the obtained values for E and A will differ accordingly to compensate for the different model. These considerations were elaborated on in more detail by Vyazovkin *et al.* [47]. (2) Different physical processes can lead to the same mathematical description, making a distinction just by the given experimental data impossible. For example, a reaction with a constant number of nucleation sites, which each exhibit one-dimensional growth, could be described with an Avrami-Erofeev model with $n = 1$ (A1). This model, however, is mathematically identical to a first order reaction [49]. To make conclusive statements on the reaction model, further types of analysis, like additional experiments or a microscopic analysis of semidecomposed samples, would be necessary [49].

Another limitation of the experiments presented here is the risk that any factor we did not account for altered the peak area of the analyzed peak apart from the decomposition. A more rigorous approach to obtain the material amount from the XRD data would be a full Rietveld refinement, but such a method would require more peaks to be valuable than what was the case for our thin film samples within our *in situ* XRD setup. The two most visible peaks were the (100) and (200) peaks, which are also co-planar, while the other peaks were relatively weak.

Table V compares our results to the values obtained by other groups. There is some discrepancy between the values, which presumably originates in the different experimental conditions (e.g., thin film vs powder, solvents/moisture affecting the stability) and differences in the value that was measured. One aspect to be considered when comparing the data points for E and A is the so-called compensation effect.

5. Compensation effect

It is not uncommon for experiments on solid state decomposition reactions on the same material to result in different values for E and A . It has been found that these scattered values often follow the equation [49]:

$$\ln(A) = aE + b \quad (10)$$

which defines a linear relation between $\ln(A)$ and E with the slope a and the intersection with the y axis b . The commonality between the data points that fall on this line is a similar overall turnover ratio for a similar temperature. Equation (1) can be rewritten as:

$$A = \exp\left(\frac{E}{RT}\right) k \quad (11)$$

$$\ln(A) = \frac{E}{RT} + \ln(k) \quad (12)$$

TABLE IV. Comparison of the results for E and A from the three evaluation approaches (first order, model fitting, isoconversional approach). The reaction models are labeled according to Table I.

Approach	E (kJ/mol)	$\ln A$ (s^{-1})	Model
First order	110 ± 15	19.3 ± 4.1	F1
Model fitting	116 ± 10	19.7 ± 2.8	D1
Isoconversional	114 ± 10	21.3 ± 3.2	

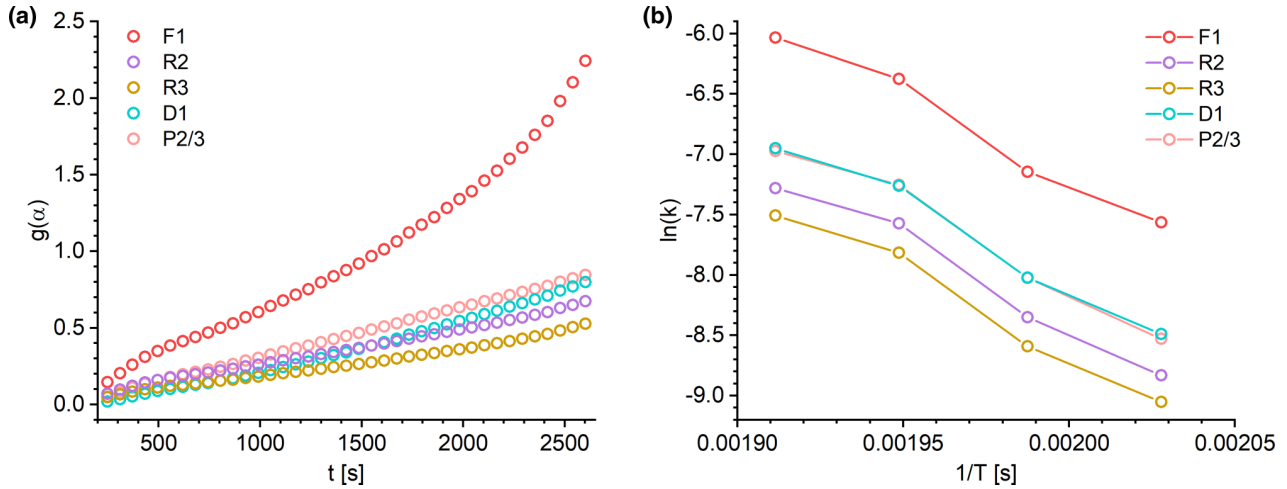


FIG. 6. a: $g(\alpha)$ over t plot for the (100) peak and the process at 230°C. The slope of the graphs gives the respective data points for sub figure b, from which the activation energies and frequency factors can be determined. The model abbreviations correspond to the ones in Table I.

which has the same structure as equation (10), with:

$$a = \frac{1}{RT} \quad (13)$$

$$b = \ln(k). \quad (14)$$

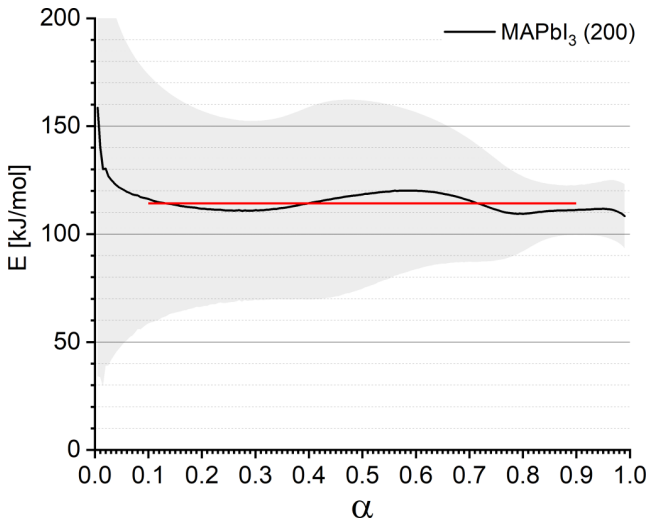


FIG. 7. Result of the isoconversional approach. The gray area shows the statistical error of the curve. The red line indicates the average value of E with its y position and the range of the averaging with its span over the x axis.

The temperature T that is calculated from this relation represents the temperature at which the different sets of E and A agree in their overall reaction rate, which will be k [54]. Figure 8 shows the results presented here together with the results from Brunetti *et al.* and Juarez-Perez *et al.* A linear fit has been calculated for all data points that assume a first order model, which are the results of the first order Arrhenius fits (Table II), the results for model F1 from the model fitting approach (Table III), and the result from Brunetti *et al.* While these data points all fall onto a line, the data point for the growth of the (001) peak of PbI_2 does not fall exactly on this line, likely because there is a small delay in the appearance of the PbI_2 as it initially needs to crystallize. The results for the other models from the model fitting approach likely deviate from the line due to the assumption of completely different reaction models. The parameters that were determined from the fit are $a = 0.315 \pm 0.005$ and $b = -15.6 \pm 0.6$. As calculated with equations (13) and (14), the temperature of agreement is $T = 108.0 \pm 6.6^\circ\text{C}$ and the corresponding reaction rate is $\ln k = -15.6 \pm 0.6$ (s^{-1}).

6. Discussion

With our experiments we provide a systematic analysis of the decomposition velocity for co-evaporated MAPbI_3 thin films in vacuum and provide a complete set of kinetic parameters for the decomposition reaction. They show that while encapsulation strategies and the choice of optimized contact layers might well enhance the stability of perovskite solar cells to moisture and/or illumination, the intrinsic thermal

TABLE V. Comparison of the results and experimental methods of this work with the works of Brunetti *et al.* [37] and Juarez-Perez *et al.* [46].

Source	E (kJ/mol)	$\ln A$ (s^{-1})	Configuration	Preparation	Atmosphere	T regime	Measured value
This work	110 ± 15	19 ± 4	Thin film	Co-evaporation	Vacuum	Isothermal	Time-resolved XRD
[37]	76 ± 21	8.3 ± 5.9	Powder	Solution	He	Isothermal	Rietveld refined XRD
[46]	93 ± 8	5.6 ± 0.8	Powder	Solution	Vacuum & He	Ramp	TGA

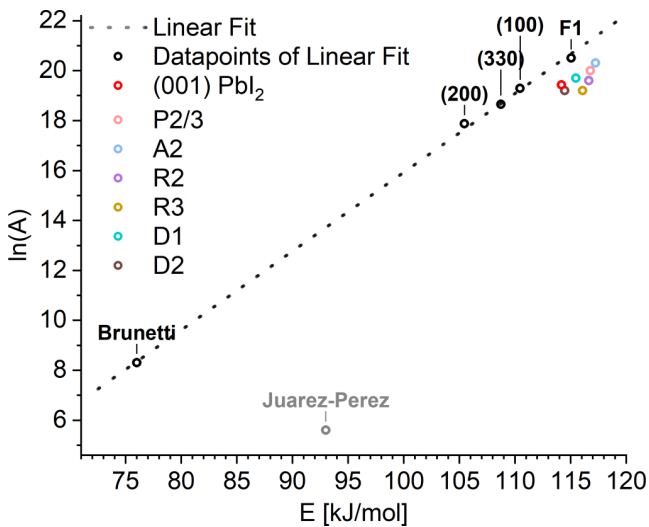


FIG. 8. Our results and the result from Brunetti *et al.* and Juarez-Perez *et al.* for the thermal decomposition of MAPbI₃ as an ln(A) over E plot. All data points that were calculated assuming a first order model (excluding the PbI₂ point) are drawn in black and a linear fit was made over them. The points that are labeled with peak indices are the results of the first order approach, as shown in Table II. This includes the (100), (200) and (330) peaks of MAPbI₃ and the (001) peak of PbI₂. The results of the model fitting approach are labeled with their corresponding reaction model.

(in)stability of MAPbI₃ will remain a concern for commercial solar modules. Encapsulation might also help here, as the volatile decomposition products cannot leave the device, thus enabling a re-formation of the perovskite, in the case that the decomposition reaction is reversible [10]. However, our results show that probably the safest strategy to develop commercial solar modules based on perovskites is the use of alternative, more stable perovskite compositions that exclude the volatile MAI component. As our discussion shows, despite

the differences in experimental procedures and the differences in the nature of the measured values between Brunetti *et al.*, Juarez-Perez *et al.*, and our work, the results can still be meaningfully compared and conclusions can be drawn from that comparison. Because of this, we propose that studies on the thermal stability of MHPs would greatly benefit from focusing more on determining reaction kinetic data.

V. CONCLUSIONS

We monitored the complete thermal decomposition of co-evaporated MAPbI₃ thin films at temperatures from 220 °C to 250 °C with time resolved XRD and, from this data, calculated the activation energy and the frequency factor of this reaction with a first order, a model fitting, and an isoconversional approach. All approaches converge on a value for the activation energy of the thermal decomposition of MAPbI₃ of $E \approx 110 \pm 15$ kJ/mol and $\ln A \approx 19 \pm 4$ (s⁻¹). While the data could be fitted with various reaction models, the best fitting results were obtained for a one-dimensional diffusion model or a contracting geometry model. Simplified calculations with a first order reaction model led to similar results. The activation energy of $E \approx 110 \pm 15$ kJ/mol is larger than the values established by Brunetti *et al.* (80 ± 20 kJ/mol) [37] and Juarez-Perez *et al.* (93 ± 8 kJ/mol) [46], however, the error ranges overlap and co-evaporated MAPbI₃ thin films are plausibly more stable than solution processed powders. When regarding the compensation effect, the results presented here and the results from Brunetti *et al.* fall on a line defined by $\ln A = aE + b$ with $a = 0.315 \pm 0.006$ and $b = -15.6 \pm 0.6$, pointing towards a similar overall turnover ratio at around 110 °C. Supplemental Material available, see Ref. [55].

ACKNOWLEDGMENTS

We gratefully acknowledge the financial support from the German Federal Ministry of Research and Education (BMBF) under Contract No. 03EK3570B (StrukturSolar II).

- [1] M. A. Green, E. D. Dunlop, J. Hohl-Ebinger, M. Yoshita, N. Kopidakis, and A. W. Ho-Baillie, Solar cell efficiency tables (version 55), *Progress in Photovoltaics: Research and Applications* **28**, 3 (2019).
- [2] Q. Shan, J. Song, Y. Zou, J. Li, L. Xu, J. Xue, Y. Dong, B. Han, J. Chen, and H. Zeng, High performance metal halide perovskite light-emitting diode: From material design to device optimization, *Small* **13**, 1701770 (2017).
- [3] Y. Sun, L. Zhang, N. Wang, S. Zhang, Y. Cao, Y. Miao, M. Xu, H. Zhang, H. Li, C. Yi, J. Wang, and W. Huang, The formation of perovskite multiple quantum well structures for high performance light-emitting diodes, *npj Flexible Electronics* **2**, 12 (2018).
- [4] M. Yuan, L. N. Quan, R. Comin, G. Walters, R. Sabatini, O. Voznyy, S. Hoogland, Y. Zhao, E. M. Beaugard, P. Kanjanaboos, Z. Lu, D. H. Kim, and E. H. Sargent, Perovskite energy funnels for efficient light-emitting diodes, *Nat. Nanotechnol.* **11**, 872 (2016).
- [5] N. Wang, L. Cheng, R. Ge, S. Zhang, Y. Miao, W. Zou, C. Yi, Y. Sun, Y. Cao, R. Yang, Y. Wei, Q. Guo, Y. Ke, M. Yu, Y. Jin, Y. Liu, Q. Ding, D. Di, L. Yang, G. Xing, H. Tian, C. Jin, F. Gao, R. H. Friend, J. Wang, and W. Huang, Perovskite light-emitting diodes based on solution-processed self-organized multiple quantum wells, *Nat. Photon.* **10**, 699 (2016).
- [6] S. W. Eaton, M. Lai, N. A. Gibson, A. B. Wong, L. Dou, J. Ma, L.-W. Wang, S. R. Leone, and P. Yang, Lasing in robust cesium lead halide perovskite nanowires, *Proc. Natl. Acad. Sci.* **113**, 1993 (2016).
- [7] Y. C. Kim, K. H. Kim, D.-Y. Son, D.-N. Jeong, J.-Y. Seo, Y. S. Choi, I. T. Han, S. Y. Lee, and N.-G. Park, Printable organometallic perovskite enables large-area, low-dose X-ray imaging, *Nature (London)* **550**, 87 (2017).
- [8] H. Wei and J. Huang, Halide lead perovskites for ionizing radiation detection, *Nat. Commun.* **10**, 1066 (2019).
- [9] R. Sheng, X. Wen, S. Huang, X. Hao, S. Chen, Y. Jiang, X. Deng, M. A. Green, and A. W. Y. Ho-Baillie, Photoluminescence characterisations of a dynamic aging process of organic-inorganic CH₃NH₃PbBr₃ perovskite, *Nanoscale* **8**, 1926 (2016).

- [10] S. Zhang and G. Han, Intrinsic and environmental stability issues of perovskite photovoltaics, *Prog. Energy* **2**, 022002 (2020).
- [11] Y. Rakita, S. R. Cohen, N. K. Kedem, G. Hodes, and D. Cahen, Mechanical properties of APbX_3 ($A = \text{Cs}$ or CH_3NH_3 , $X = \text{I}$ or Br) perovskite single crystals, *MRS Commun.* **5**, 623 (2015).
- [12] W. Nie, J.-C. Blancon, A. J. Neukirch, K. Appavoo, H. Tsai, M. Chhowalla, M. A. Alam, M. Y. Sfeir, C. Katan, J. Even, S. Tretiak, J. J. Crochet, G. Gupta, and A. D. Mohite, Light-activated photocurrent degradation and self-healing in perovskite solar cells, *Nat. Commun.* **7**, 11574 (2016).
- [13] Y. Zhao, J. Wei, H. Li, Y. Yan, W. Zhou, D. Yu, and Q. Zhao, A polymer scaffold for self-healing perovskite solar cells, *Nat. Commun.* **7**, 10228 (2016).
- [14] D. R. Ceratti, Y. Rakita, L. Cremonesi, R. Tenne, V. Kalchenko, M. Elbaum, D. Oron, M. A. C. Potenza, G. Hodes, and D. Cahen, Self-healing inside APbBr_3 halide perovskite crystals, *Adv. Mater.* **30**, 1706273 (2018).
- [15] G. Grancini, C. Roldán-Carmona, I. Zimmermann, E. Mosconi, X. Lee, D. Martineau, S. Narbey, F. Oswald, F. D. Angelis, M. Grätzel, and M. K. Nazeeruddin, One-year stable perovskite solar cells by 2d/3d interface engineering, *Nat. Commun.* **8**, 15684 (2017).
- [16] A. Mei, X. Li, L. Liu, Z. Ku, T. Liu, Y. Rong, M. Xu, M. Hu, J. Chen, Y. Yang, M. Grätzel, and H. Han, A hole-conductor-free, fully printable mesoscopic perovskite solar cell with high stability, *Science* **345**, 295 (2014).
- [17] P. Holzhey and M. Saliba, A full overview of international standards assessing the long-term stability of perovskite solar cells, *J. Mater. Chem. A* **6**, 21794 (2018).
- [18] EPKI, Perovskite-based photovoltaics: A unique chance for European PV-industry, Tech. Rep. (European Perovskite Initiative, 2019).
- [19] M. V. Khenkin, E. A. Katz, A. Abate, G. Bardizza, J. J. Berry, C. Brabec, F. Brunetti, V. Bulović, Q. Burlingame, A. D. Carlo, R. Cheacharoen, Y.-B. Cheng, A. Colmann, S. Cros, K. Domanski, M. Dusza, C. J. Fell, S. R. Forrest, Y. Galagan, D. D. Girolamo, M. Grätzel, A. Hagfeldt, E. von Hauff, H. Hoppe, J. Kettle, H. Köbler, M. S. Leite, S. Liu, Y.-L. Loo, J. M. Luther, C.-Q. Ma, M. Madsen, M. Manceau, M. Matheron, M. McGehee, R. Meitzner, M. K. Nazeeruddin, A. F. Nogueira, Ç. Odabaşı, A. Osherov, N.-G. Park, M. O. Reese, F. D. Rossi, M. Saliba, U. S. Schubert, H. J. Snaith, S. D. Stranks, W. Tress, P. A. Troshin, V. Turkovic, S. Veenstra, I. Visoly-Fisher, A. Walsh, T. Watson, H. Xie, R. Yıldırım, S. M. Zakeeruddin, K. Zhu, and M. Lira-Cantu, Consensus statement for stability assessment and reporting for perovskite photovoltaics based on ISOS procedures, *Nat. Energy* **5**, 35 (2020).
- [20] G. Niu, W. Li, J. Li, X. Liang, and L. Wang, Enhancement of thermal stability for perovskite solar cells through cesium doping, *RSC Advances* **7**, 17473 (2017).
- [21] X. Li, J. Wu, S. Wang, and Y. Qi, Progress of all-inorganic cesium lead-free perovskite solar cells, *Chem. Lett.* **48**, 989 (2019).
- [22] G. A. Tosado, Y.-Y. Lin, E. Zheng, and Q. Yu, Impact of cesium in phase and device stability of triple cation Pb-Sn double halide perovskite films and solar cells, *J. Mater. Chem. A* **6**, 17426 (2018).
- [23] R. E. Beal, D. J. Slotcavage, T. Leijtens, A. R. Bowring, R. A. Belisle, W. H. Nguyen, G. F. Burkhard, E. T. Hoke, and M. D. McGehee, Cesium lead halide perovskites with improved stability for tandem solar cells, *J. Phys. Chem. Lett.* **7**, 746 (2016).
- [24] B. Wook Park and S. I. Seok, Intrinsic instability of inorganic-organic hybrid halide perovskite materials, *Adv. Mater.* **31**, 1805337 (2019).
- [25] E. Smecca, Y. Numata, I. Deretzis, G. Pellegrino, S. Boninelli, T. Miyasaka, A. L. Magna, and A. Alberti, Stability of solution-processed MAPbI_3 and FAPbI_3 layers, *Phys. Chem. Chem. Phys.* **18**, 13413 (2016).
- [26] A. F. Akbulatov, S. A. Tsarev, M. Elshobaki, S. Y. Luchkin, I. S. Zhidkov, E. Z. Kurmaev, S. M. Aldoshin, K. J. Stevenson, and P. A. Troshin, Comparative intrinsic thermal and photochemical stability of Sn(II) complex halides as next-generation materials for lead-free perovskite solar cells, *J. Phys. Chem. C* **123**, 26862 (2019).
- [27] M. Saliba, T. Matsui, J.-Y. Seo, K. Domanski, J.-P. Correa-Baena, M. K. Nazeeruddin, S. M. Zakeeruddin, W. Tress, A. Abate, A. Hagfeldt, and M. Grätzel, Cesium-containing triple cation perovskite solar cells: improved stability, reproducibility and high efficiency, *Energy Environ. Sci.* **9**, 1989 (2016).
- [28] A. F. Akbulatov, S. Y. Luchkin, L. A. Frolova, N. N. Dremova, K. L. Gerasimov, I. S. Zhidkov, D. V. Anokhin, E. Z. Kurmaev, K. J. Stevenson, and P. A. Troshin, Probing the intrinsic thermal and photochemical stability of hybrid and inorganic lead halide perovskites, *J. Phys. Chem. Lett.* **8**, 1211 (2017).
- [29] A. F. Akbulatov, V. M. Martynenko, L. A. Frolova, N. N. Dremova, I. Zhidkov, S. A. Tsarev, S. Y. Luchkin, E. Z. Kurmaev, S. M. Aldoshin, K. J. Stevenson, and P. A. Troshin, Intrinsic thermal decomposition pathways of lead halide perovskites APbX_3 , *Sol. Energy Mater. Sol. Cells* **213**, 110559 (2020).
- [30] T. Burwig, W. Fränzel, and P. Pistor, Crystal phases and thermal stability of co-evaporated CsPbX_3 ($X = \text{I}, \text{Br}$) thin films, *J. Phys. Chem. Lett.* **9**, 4808 (2018).
- [31] G. Grancini and M. K. Nazeeruddin, Dimensional tailoring of hybrid perovskites for photovoltaics, *Nat. Rev. Mater.* **4**, 4 (2018).
- [32] G. Liu, H. Zheng, X.-X. Xu, L. Zhu, A. Alsaedi, T. Hayat, X. Pan, and S. Dai, Efficient solar cells with enhanced humidity and heat stability based on benzylammonium-caesium-formamidinium mixed-dimensional perovskites, *J. Mater. Chem. A* **6**, 18067 (2018).
- [33] E. J. Juarez-Perez, L. K. Ono, M. Maeda, Y. Jiang, Z. Hawash, and Y. Qi, Photodecomposition and thermal decomposition in methylammonium halide lead perovskites and inferred design principles to increase photovoltaic device stability, *J. Mater. Chem. A* **6**, 9604 (2018).
- [34] S. Nam, C. T. K. Mai, and I. Oh, Ultrastable photoelectrodes for solar water splitting based on organic metal halide perovskite fabricated by lift-off process, *ACS Appl. Mater. Interfaces* **10**, 14659 (2018).
- [35] A. Senocrate, T. Acartürk, G. Y. Kim, R. Merkle, U. Starke, M. Grätzel, and J. Maier, Interaction of oxygen with halide perovskites, *J. Mater. Chem. A* **6**, 10847 (2018).
- [36] T. Leijtens, K. Bush, R. Cheacharoen, R. Beal, A. Bowring, and M. D. McGehee, Towards enabling stable lead halide perovskite

- solar cells, interplay between structural, environmental, and thermal stability, *J. Mater. Chem. A* **5**, 11483 (2017).
- [37] B. Brunetti, C. Cavallo, A. Ciccio, G. Gigli, and A. Latini, On the thermal and thermodynamic (in)stability of methylammonium lead halide perovskites, *Sci. Rep.* **6**, 31896 (2016).
- [38] Z. Song, C. Wang, A. B. Phillips, C. R. Grice, D. Zhao, Y. Yu, C. Chen, C. Li, X. Yin, R. J. Ellingson, M. J. Heben, and Y. Yan, Probing the origins of photodegradation in organic-inorganic metal halide perovskites with time-resolved mass spectrometry, *Sustainable Energy Fuels* **2**, 2460 (2018).
- [39] E. J. Juarez-Perez, Comment on “Probing the origins of photodegradation in organic-inorganic metal halide perovskites with time-resolved mass spectrometry,” *ChemRxiv* (2019), doi:10.26434/chemrxiv.7295585.
- [40] H. A. Dewi, J. Li, H. Wang, B. Chaudhary, N. Mathews, S. Mhaisalkar, and A. Bruno, Excellent intrinsic long-term thermal stability of co-evaporated MAPbI₃ solar cells at 85 °C, *Adv. Funct. Mater.* **31**, 2100557 (2021).
- [41] P. Pistor, T. Burwig, C. Brzuska, B. Weber, and W. Fränzel, Thermal stability and miscibility of co-evaporated methyl ammonium lead halide (MAPbX₃, X = I, Br, Cl) thin films analysed by in situ X-ray diffraction, *J. Mater. Chem. A* **6**, 11496 (2018).
- [42] T. Burwig, M. Guc, V. Izquierdo-Roca, and P. Pistor, Synthesis and crystal structure evolution of co-evaporated Cs₂ AgBiBr₆ thin films upon thermal treatment, *J. Phys. Chem. C* **124**, 9249 (2020).
- [43] A. Dualeh, P. Gao, S. I. Seok, M. K. Nazeeruddin, and M. Grätzel, Thermal behavior of methylammonium lead-trihalide perovskite photovoltaic light harvesters, *Chem. Mater.* **26**, 6160 (2014).
- [44] N.-K. Kim, Y. H. Min, S. Noh, E. Cho, G. Jeong, M. Joo, S.-W. Ahn, J. S. Lee, S. Kim, K. Ihm, H. Ahn, Y. Kang, H.-S. Lee, and D. Kim, Investigation of thermally induced degradation in CH₃NH₃PbI₃ perovskite solar cells using in-situ synchrotron radiation analysis, *Sci. Rep.* **7**, 4645 (2017).
- [45] X. Yu, Y. Qin, and Q. Peng, Probe decomposition of methylammonium lead iodide perovskite in N₂ and O₂ by in situ infrared spectroscopy, *J. Phys. Chem. A* **121**, 1169 (2017).
- [46] E. J. Juarez-Perez, L. K. Ono, and Y. Qi, Thermal degradation of formamidinium based lead halide perovskites into sym-triazine and hydrogen cyanide observed by coupled thermogravimetry-mass spectrometry analysis, *J. Mater. Chem. A* **7**, 16912 (2019).
- [47] S. Vyazovkin and C. A. Wight, Model-free and model-fitting approaches to kinetic analysis of isothermal and nonisothermal data, *Thermochim. Acta* **340–341**, 53 (1999).
- [48] A. Khawam and D. R. Flanagan, Solid-state kinetic models: basics and mathematical fundamentals, *J. Phys. Chem. B* **110**, 17315 (2006).
- [49] M. Brown, *Handbook of Thermal Analysis and Calorimetry* (Elsevier, Amsterdam, New York, 1998).
- [50] T. Baikie, N. S. Barrow, Y. Fang, P. J. Keenan, P. R. Slater, R. O. Piltz, M. Gutmann, S. G. Mhaisalkar, and T. J. White, A combined single crystal neutron/X-ray diffraction and solid-state nuclear magnetic resonance study of the hybrid perovskites CH₃NH₃PbX₃ (X = I, Br, Cl), *J. Mater. Chem. A* **3**, 9298 (2015).
- [51] A. Singh, M. K. Jana, and D. B. Mitzi, Reversible crystal-glass transition in a metal halide perovskite, *Adv. Mater.* **33**, 2005868 (2020).
- [52] NIST, *Nist X-ray form factor, atten. scatt. tables form page* (2018).
- [53] T. Baikie, Y. Fang, J. M. Kadro, M. Schreyer, F. Wei, S. G. Mhaisalkar, M. Graetzel, and T. J. White, Synthesis and crystal chemistry of the hybrid perovskite CH₃NH₃PbI₃ for solid-state sensitised solar cell applications, *J. Mater. Chem. A* **1**, 5628 (2013).
- [54] P. D. Garn, An examination of the kinetic compensation effect, *J. Therm. Anal.* **7**, 475 (1975).
- [55] See Supplemental Material at <http://link.aps.org/supplemental/10.1103/PhysRevMaterials.5.065405> for a θ - 2θ scan of a MAPbI₃ thin film, the *in situ* XRD scans of the four processes after preparation and right before the transition from 150 °C to the temperature of decomposition, SEM images of a freshly prepared MAPbI₃ layer and of a decomposed layer, the color map of the growth of a MAPbI₃ thin film, the reduced time plot for all four processes, and a table with all results from the model fitting approach.

Closing Discussion

The analysis yielded an activation energy E for the thermal decomposition of MAPbI₃ of 110(15) kJ mol⁻¹ and an $\ln A$ of 19(1). As stated in the publication, this would lead to a decomposition of 20% of the material after 2800 h at 85 °C, which again highlights that pure MAPbI₃ is probably not suitable for use as an absorber layer in a solar cell. Of course, this extrapolation to real world use needs to take into account, that the MAPbI₃ layers that were studied here were prepared and decomposed in vacuum. A real solar cell would not be exposed to vacuum and it would be encapsulated, potentially allowing the re-formation of the perovskite from the products of the decomposition [52]. On a final note, the results for E and A are nicely comparable to the results of Juarez-Perez et al. and Brunetti et al., despite the very different methods of preparation and evaluation, which highlights the practical appeal of this approach to analysis.

4.6 Kinetics of the Thermal Decomposition of FAPbI₃

Preliminary Discussion

Reference: [Bu5]

After having studied the thermal decomposition of MAPbI₃ extensively, we wanted to look at a perovskite with a different A cation. Metal-halide perovskites that are based on formamidinium (FA), another organic molecule, have been shown to exhibit an increased stability towards a variety of environmental factors. According to Zhang et al., FA bonds more strongly to the halides in MHPs, which should reduce ion migration and in turn increase the stability of the material [177]. FAPbI₃ based perovskite solar cells have been shown to exhibit a much improved temperature [69] and photostability [70] than their MA based counterpart, while also being able to achieve comparable PCEs [178, 179]. Therefore, FAPbI₃ is a relevant candidate for expanding on the reaction kinetical study of hybrid MHPs. Similarly to MAPbI₃, most publications that study the stability of FAPbI₃ focus on wet chemically processed FAPbI₃ thin films and powders. Again, we want to complement these studies by looking at co-evaporated FAPbI₃ thin films and use similar techniques for obtaining and evaluating the data as we have done in the case of MAPbI₃ in order to enable a direct comparison. In addition to the isothermal decomposition experiments, the phase evolution of FAPbI₃ during growth and decomposition by a temperature ramp will also be the subject of this paper, as it has not yet been presented in a publicized format. A point that is often stressed by researchers who work on the analysis of solid-state decomposition reactions, is the utility of supplemental types of analysis on semi-decomposed samples to allow insights into the progression of the decomposition. For this reason, we prepared a sample that exhibited varying stages of decomposition on its surface and analyzed it via SEM and EDX.

Thermal decomposition kinetics of FAPbI₃ thin films

Thomas Burwig^{✉*} and Karl Heinze

Martin Luther University Halle-Wittenberg, Von-Danckelmann-Platz 3, 06120 Halle (Saale), Germany

Paul Pistor^{✉†}

Martin Luther University Halle-Wittenberg, Von-Danckelmann-Platz 3, 06120 Halle (Saale), Germany
and Universidad Pablo de Olavide, Carretera de Utrera 1, 41013 Sevilla, Spain



(Received 7 February 2022; accepted 3 June 2022; published 27 June 2022)

In the realm of organic-inorganic-hybrid metal-halide perovskites, FAPbI₃ is seeing increasing attention as a potentially more stable alternative to MAPbI₃. To add to our previous paper, where we studied the reaction kinetics of the thermal decomposition of MAPbI₃, here we analyze the compositional change and crystal phase evolution during the thermal decomposition of FAPbI₃ thin films. To this end, we prepare the perovskite using thermal coevaporation and monitor the growth and thermal decomposition in vacuum with an *in situ* x-ray diffraction setup. The experimental procedure has been carried out via three approaches: producing a partially decomposed sample with the help of a graded temperature profile, using a temperature ramp and a set of isothermal decomposition experiments. From this data we analyze and calculate the stoichiometry and phase changes, the activation energy E and the frequency factor A of the thermal decomposition process, in addition to the thermal expansion coefficient during heating. We compare our results to the ones obtained for MAPbI₃ thin films by the same experimental method, confirming the enhanced thermal stability of FAPbI₃.

DOI: [10.1103/PhysRevMaterials.6.065404](https://doi.org/10.1103/PhysRevMaterials.6.065404)

I. INTRODUCTION

Since the first successful demonstration of metal-halide perovskites as photoabsorbers in 2009 [1], this organic-inorganic semiconductor family has gained a lot of interest for a variety of applications, which, besides photovoltaics, include high energy photon detectors [2,3], LEDs [4–7], and lasers [8]. In all of these applications, metal-halide perovskites, such as the prototypical methyl ammonium lead iodide (MAPbI₃) and derivatives based on Cs, formamidinium (FA), Sn, Br, or Cl, have shown significant potential for enabling efficient, low-cost optoelectronic devices. The most significant drawback of these perovskite-based devices, however, is their lack of stability towards a variety of environmental factors such as heat, moisture, or UV illumination [9]. In this paper we will focus on thermal stability aspects and the decomposition kinetics of the perovskite absorber formamidinium lead iodide FAPbI₃, complementing our previous paper on MAPbI₃ [10].

Solar cells can reach up to 85 °C under operating conditions [11] and, in contrast to moisture-related degradation, thermal decomposition cannot be alleviated by encapsulation. Therefore it is vital to understand the thermal decomposition pathways and kinetics for these materials in view of any application where the material is subjected to heat. For the workhorse material MAPbI₃ it has become clear that severe degradation may occur at comparatively low temperatures, close to the operating conditions of solar cells, while the exact

onset of degradation is still a matter of dispute [12]. This uncertainty applies even more so to the recently strongly investigated perovskite FAPbI₃, where less stability studies are available. As Zhang *et al.* point out, the observed decomposition depends significantly on the chosen temperature regime, as isothermal experiments usually found decompositions at much lower temperatures than ramp experiments [12]. Our earlier results on the thermal stability of MAPbI₃, using a temperature ramp, showed a 50 % decomposition at 230 °C [13] and Dualeh *et al.* found an onset of the decomposition of MAPbI₃ at 234 °C, again using a temperature ramp [14]. In contrast to this, Kim *et al.* have found a detectable decomposition of MAPbI₃ at 80 °C after 1 h [15]. This conflict is an example for one of several problems, which impede the formation of a complete and clear picture of the degradation mechanisms in current research: (i) As already noted, the choice of temperature regime significantly affects results. (ii) Degradation studies of completed solar cells often report only the decline in performance over time for a given temperature, lacking substantial information on the exact degree of decomposition. (iii) Many studies analyzing perovskite decomposition only report the degree of decomposition for one set of time and temperature, which does not allow for the extraction of kinetic parameters. This can also lead to difficulties when comparing the results of different research groups, especially when different conditions (e.g., different temperatures) are chosen for the trials. (iv) Materials with different morphologies (single crystal, powder, thin film) can be expected to degrade differently [16]. (v) The synthesis method can play a significant role in the stability of the resulting material. For example, solvent residues that remain after wet chemical preparation can decrease the stability [17]. (vi) The

*thomas.burwig@physik.uni-halle.de

†paul.pistor@physik.uni-halle.de

history of the investigated samples cannot be excluded as a factor for their stability. Samples that have been exposed to air (and thus to moisture, light, etc.) can reasonably be expected to show a different decomposition behavior. (vii) When temporarily exposing the samples to environmental factors, such as ambient air or light, these factors are often difficult to precisely quantify or are often not seen as “report-worthy” by the researchers.

It is for these reasons that in the current study we explicitly investigate thin films with properties similar to those applied in solar cells (e.g., in regard to thickness), that were prepared solvent-free in vacuum by coevaporation and investigated *in situ* within the vacuum chamber without air exposure at any time.

In the past, we have reported the synthesis, phase evolution and thermal decomposition of a variety of different perovskite thin films that were prepared by coevaporation in vacuum and studied via temperature ramp experiments with *in situ* x-ray diffraction (XRD) analysis. The materials studied so far include MAPbI₃, MAPbBr₃, MAPbCl₃ [13], CsPbI₃, CsPbBr₃ [18], and also the double perovskite Cs₂AgBiBr₆ [19,20]. To add to this list, FAPbI₃ will be studied in this paper.

While single temperature ramp experiments give a general idea of the thermal stability limits of a material and allow for a qualitative comparison of different materials, for a more detailed and general view of the decomposition kinetics, sets of isothermal measurements or sets of different temperature ramps are needed. In a previous paper, we elaborated on the kinetics of the thermal decomposition of MAPbI₃ in detail, by determining the kinetic triplet of this reaction. This consists of the activation energy E , the frequency factor A , and the reaction model $f(\alpha)$, where α is the extent of reaction [10]. These kinetic parameters allow for a generalization of the decomposition behavior over a larger temperature range and for more meaningful comparisons to other experiments. It has been shown by a large number of studies, that the major limiting component for the thermal stability of MAPbI₃ is the organic MA molecule [13,18,21–30]. Therefore, we study the impact of exchanging the MA molecule with FA to see how this modification influences the thermal stability of the resulting material. Solar cells that use FAPbI₃ absorber layers have been shown to be more resilient towards temperature [31] and moisture [32], which makes this material a promising object of study.

To our knowledge, there are three research groups that have investigated the reaction kinetics of the thermal decomposition of FAPbI₃: Juarez-Perez *et al.* used a wet-chemically prepared powder in vacuum and He atmosphere [33]. Pool *et al.* used spin coated thin films that were annealed under N₂ atmosphere [34]. Luongo *et al.* prepared a powder via dry grinding of the precursors and heated the samples up in Ar and He [35]. All of these trials use multiple temperature ramps to determine the kinetic data of the reaction and none of them use preparation methods that are likely candidates for use in industrial applications. Our goal is to complement these findings with isothermally acquired data on coevaporated thin films. The different preparation methods, experimental parameters and resulting values for E and A are compiled in Table III.

In order to be comparable to our previous experiments on the MA based perovskites [13], we first prepare FAPbI₃ in

high vacuum via coevaporation of FAI and PbI₂. With an *in situ* x-ray diffraction setup, we are able to monitor the crystallization and phase evolution of the thin films at any time of the experiment. Afterwards, without breaking the vacuum, we perform three sets of decomposition measurements. First, a sample is decomposed using a temperature ramp in order to determine the general temperature range where a measurable decomposition is to be expected. In addition, we decompose FAPbI₃ thin films using a set of isothermal experiments in the temperature range between 230 °C and 290 °C. From this data we calculate the activation energy E and the frequency factor A for this process. The data is first analyzed under the assumption of a first-order model, where the rate constants k are determined by fitting an exponential decay onto the data. Then a more general approach is used, where the data is tested against a variety of different reaction models. Finally, we partially decompose a FAPbI₃ sample by applying a temperature gradient over the length of the sample, enabling us to investigate the morphology and stoichiometry changes during the decomposition via scanning electron microscopy (SEM) and energy-dispersive x-ray spectroscopy (EDX).

II. THEORY

A. FAPbI₃ crystal structure

Similarly to CsPbI₃, FAPbI₃ is a polymorph and can exist in different crystal phases at room temperature. The black, photoactive α phase has a band gap of 1.48 eV [31] and is sometimes identified with a cubic symmetry [$Pm\bar{3}m$, $a = b = c = 6.3620(8)$ Å] [36], while other reports assign a trigonal symmetry [$P\bar{3}m1$, $a = b = 8.9817(13)$ Å, $c = 11.006(2)$ Å] [37]. The δ phase is photo inactive, orange in appearance, has a band gap of 2.14 eV [38] and has a hexagonal crystal structure [$P6_3mc$, $a = b = 8.6603(14)$ Å, $c = 7.9022(6)$ Å] [37]. The α phase is stable for temperatures above 130 °C, while at lower temperatures the perovskite will gradually transform into the δ phase, even in an inert gas atmosphere [38,39]. A partial exchange of FA with MA [39] or of I with Br [40] has been shown to increase the stability of the photoactive α phase under ambient conditions.

B. Reaction kinetics

In general, the extent of conversion α of a reaction changes over the time t according to the following formula [41]:

$$\frac{d\alpha}{dt} = k(T)f(\alpha) \quad (1)$$

Here, T is the absolute temperature, k is the reaction rate and $f(\alpha)$ is the reaction model. α is defined as being 0 at the start of the reaction and 1 at the end. The data presented in this paper is tested against the same models as the MAPbI₃ samples in our previous work in Ref. [10]. The complete list of tested reaction models can be found in the Supplemental Material [42]. The selection of models was taken from Ref. [43], which also goes into detail about how these models are derived. The reaction rate $k(T)$ is defined as [41]:

$$k(T) = A \exp\left(-\frac{E}{RT}\right), \quad (2)$$

where R is the universal gas constant, E is the activation energy, and A is the pre-exponential factor. In principle, the kinetic parameters of a thermal decomposition reaction can be determined by a single temperature ramp experiment. However, as has been explained by Vyazovkin *et al.*, an experiment that uses a temperature ramp changes T and α simultaneously, which leads to a very high uncertainty in any determined kinetic parameters. If only a single temperature ramp experiment is used, this makes the results next to unusable [41]. For this reason, we use four isothermal experiments with different temperatures to determine the kinetic parameters of the degradation. For the first evaluation approach, we assumed the reaction model to be of first order, where an equation of the form

$$y = ae^{-kx} \quad (3)$$

is fitted onto the data. Then $\ln k$ is plotted over $1/T$ for each isothermal experiment. An equivalent form of Eq. (2) is:

$$\ln k = \ln A - \frac{E}{RT}. \quad (4)$$

This has the same structure as the equation:

$$y = m + nx. \quad (5)$$

Therefore, a linear fit of the data for $y = \ln k$ over $x = 1/T$ can then be identified with this equation, which allows the calculation of $\ln A = m$ and $E = -nR$.

The second evaluation method used to analyze the kinetic data was a model fitting approach, which includes a variety of common reaction models. For this, different integrated reaction models $g(\alpha)$ are used, where $g(\alpha)$ follows from the reaction model $f(\alpha)$ by integration [41]:

$$g(\alpha) = \int_0^\alpha [f(\alpha)]^{-1}. \quad (6)$$

$g(\alpha)$ gives a unitless measure for the time it takes for the reaction to achieve a certain extend of conversion and, in this way, it relates the time t with the reaction rate $k(T)$ [41]:

$$g(\alpha) = k(T) \cdot t. \quad (7)$$

A plot of $g(\alpha)$ over t can be linearly fitted to yield a value for $k(T)$. Then, similarly to the first approach, $\ln k$ can then be plotted over $1/T$ and the kinetic parameters can be determined using an Arrhenius fit.

In our analysis, the peak area evolution of certain characteristic XRD peaks is assumed to be proportional to the amount of a given material within the film. The validity of this assumption has been discussed at length in our previous paper [10], and we only summarize the main points here. Besides a decomposition of the material, there are two main effects that could reduce the area of the detected peaks:

A layer of product (PbI₂) covers the film and reduces the detected x-ray intensity. To calculate the absorption B of a layer of PbI₂ with linear attenuation coefficient μ , coverage c , and thickness d when hit by x-rays with an incidence angle of θ , one can use the following formula:

$$B = c(1 - e^{-\mu x}) \quad (8)$$

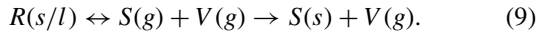
where $x = 2d/\sin \theta$ is the distance the x-rays travel through the film. To make an assessment as to the value of these

parameters, the SEM images of the partial decomposition experiment, which are shown in Figs. 4 and 5, can be helpful to consider. Figure 5(d) shows an image with material contrast and, as can be seen there, the PbI₂ does not form a solid layer on top of the perovskite, but has a coverage of roughly 50%. The cross-sectional image in Fig. 4(d) indicates a PbI₂ thickness of around 100 nm. The attenuation coefficient of PbI₂ for x-rays with an energy of 8.04 keV is 1556.51 cm⁻¹ [44]. With the above mentioned values this would lead to an absorption of $B = 4.4\%$. This in itself can be considered negligible. While it is difficult to assess which extent of conversion corresponds to the SEM images, there is no PbI₂ at the beginning, therefore at $\alpha = 0$ the absorption is $B = 0\%$. Since the evaluation of the isothermal experiments focuses on the first half of the decomposition, the impact of the PbI₂ absorption should be very limited. Additionally, the results for E and A that were based on the declining FAPbI₃ peak were very similar to the ones obtained from the growing PbI₂ peak, and since the PbI₂ is formed above the perovskite, the results based on the PbI₂ peak should not be affected at all by this phenomenon.

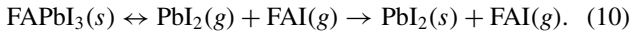
A recrystallization or reorientation of the material. There is the known transition from the δ phase to the α phase of FAPbI₃ at around 130 °C [38,39]. As can be seen in the colormap in Fig. 2 by the change in relative peak intensities, the FAPbI₃ film does respond to the increasing temperature by recrystallizing or changing the preferential orientation of the crystal grains. To limit the effect of this on the results of the isothermal decomposition experiments, an intermediate temperature at 160 °C was held for at least 20 min, before heating to the respective isothermal decomposition. It is also of note that the results for E and A that used the growing PbI₂ peak as their basis where similar to the values obtained from studying the declining FAPbI₃ peak. Since the growing PbI₂ peak should not be influenced by a recrystallization of the FAPbI₃ educt, this is a good indication that this phenomenon has no major impact on our results.

We would like to insert a short comment on an ongoing dispute concerning the interpretation of solid-state decomposition analysis. When using the Arrhenius approach to determine the reaction kinetics of a decomposition reaction from the solid state, it is of note, that the applicability of the Arrhenius equation to this class of reactions is, at this point, a contentious topic. This has to do with the fact that the base assumptions behind the Arrhenius model pertain to the theory of gases and liquids: The atoms, ions, or molecules in the reactant species move freely with a kinetic energy that is proportional to the temperature of the substance. If a collision with an energy of at least E occurs, it leads to a reaction. The frequency factor A describes how often these collisions happen and the term of the Maxwell-Boltzmann distribution [$\exp(-\frac{E}{RT})$, see Eq. (2)] gives the relative fraction of collisions that occur with an energy of at least E . Further restrictions as to which collisions lead to a reaction—such as requiring the collisions of specific bonds—are usually incorporated into the frequency factor [45]. According to Garn, the energies within solids are too equally spread out to allow for the application of Maxwell-Boltzmann statistics and thus there exists no distinct activated species [46]. This violates one of the central assumptions of the Arrhenius model and

immediately raises the question, what an empirically determined activation energy from a conventional Arrhenius plot actually signifies. A recent discussion of the current state of the theory of solid state decomposition is given in Ref. [47]. A promising contribution to this topic was made by L'vov, who developed the theory of congruent dissociative volatilization (CDV) that aims to close this explanatory gap. His theory is derived in detail in Refs.[48–50]. This theory retains the validity of the empiric relation described by Eq. (4), but here the activation energy E is assigned to the molar enthalpy $\Delta_r H_T^\circ/\nu$, thus relating the empirically determined value E to an actual physical property of the studied material. Just as important, it gives a theoretical foundation to the application of the Arrhenius relation. Additionally, it provides an explanation for the often observed “compensation effect”, where similar experiments on the same substance lead to disparate results for A and E that, however, follow the relation $\ln A = aE + b$. The CDV theory proposes the following model reaction for solid-state decompositions:



Here, a reactant R (liquid or gas) first reacts into two gaseous products, one of which volatile (V), that remains a gas, and one nonvolatile (S), that subsequently condenses to form a solid. When applied to the thermal decomposition of FAPbI₃ (ignoring any further decomposition of the FAI component) the equation is:



Such a recondensation of PbI₂ would explain the very high crystallinity of the reaction product, as it was observed in our experiments. In our current paper, we are unable to add significant further insight into the applicability of the CDV theory. However, for completeness we mention it here in order to offer an alternative physical interpretation for the commonly extracted activation energies. Independent from the above discussion on their physical interpretation, the experimental data presented in this paper and the kinetic parameters extracted in the following sections allow to determine the temperature dependence of the degradation kinetics of FAPbI₃ in an empirical way, enabling the comparison with MAPbI₃ and the prediction of the degree of decomposition for a given set of time and temperature.

III. EXPERIMENTAL DETAILS

The sample preparation and posttreatment took place within a high vacuum chamber under a base pressure of 2×10^{-5} mbar. The FAPbI₃ thin films were deposited using thermal coevaporation of the precursors PbI₂ at 350 °C and FAI at 195 °C from Al₂O₃ crucibles. The pressure within the chamber increased to 7×10^{-5} mbar during the deposition of the films, mostly due to the evaporation of FAI. The target sample thickness was around 310 nm with an average growth rate of 0.13 \AA s^{-1} . After the preparation, without interrupting the vacuum, the samples were heated via radiative heat from a carbon heating element at the back of the sample holder. During the whole process, including growth and annealing, the samples were observed using an *in situ* XRD system. The system had a fixed source-sample-detector geometry during

the whole process and recorded one measurement every 60 s. The x-ray source was made of Cu and a Ni filter was used to reduce the strength of the Cu k_β reflexes. The detector was composed of three Dectris Mythen 1 K modules, that together cover a 2θ range of 28°. More information about the preparation and analysis apparatus can be found in Ref. [13].

In line with previous experiments, we first exposed a freshly deposited FAPbI₃ layer to a temperature ramp of 3.6 Kmin^{-1} , starting at room temperature, to investigate the phase evolution and to determine the onset of decomposition.

For the isothermal experiments, the samples were heated to either 230 °C, 250 °C, 270 °C, or 290 °C. In order to ensure that the initial FAPbI₃ thin film was completely in the photoactive α phase and in order to avoid recrystallization effects observed at lower temperatures, an intermediate temperature step at 160 °C for at least 20 min was introduced prior to applying the actual isothermal decomposition temperature.

For the preparation of the partially decomposed sample, half of the sample was covered by a stainless steel plate, partially shielding the sample from the heater. This cover was applied after the FAPbI₃ deposition, in a nitrogen filled glovebox attached to the deposition chamber, therefore ensuring that the sample would not come into contact with ambient air. The decomposition process kept the sample at 250 °C for 50 min. Due to the shield, the sample was effectively exposed to a temperature gradient over its length.

IV. RESULTS

A. Growth

To grow the perovskite, FAI and PbI₂ have been thermally coevaporated in a high vacuum chamber. More details on the growth conditions can be found in Sec. III. A colormap representation of the growth process is shown in Fig. 1. The XRD peaks that became detectable upon the formation of the perovskite correspond well to either the black α phase or the yellow δ phase of FAPbI₃. The peaks of the α phase have been indexed using the PDF reference 00-069-0999 and the δ -phase peaks have been indexed according to Han *et al.*'s work in Ref. [38]. The visible peaks of the α phase are: (100) [13.92°], (110) [19.70°], (111) [24.51°], (200) [28.00°], (210) [31.39°]. From the δ phase, the following peaks are detected: (002) [22.39°], (021) [25.36°], ($\bar{1}$ 22) [30.52°], (004) [32.80°]. Additionally, the ($\bar{1}$ 30) peak of the δ phase might exist, but is overlaid by the (210) peak of the α phase. The δ phase vanished after heating the samples to 160 °C for twenty minutes and only the α phase remained.

B. Temperature ramp experiment

To identify any phase changes that might occur during annealing, a freshly prepared film was subjected to a temperature ramp. Below 160 °C, for the peaks assigned to the α -FAPbI₃ phase, no decomposition but only a recrystallization was observed, which manifested in variations of the relative peak intensities. For temperatures above 230 °C, the intensities of the perovskite peaks rapidly decreased until disappearing above approximately 270 °C, as can be observed in Fig. 2. In parallel to the decomposition of FAPbI₃, PbI₂ is formed. For temperatures above 290 °C, the PbI₂ decomposes and

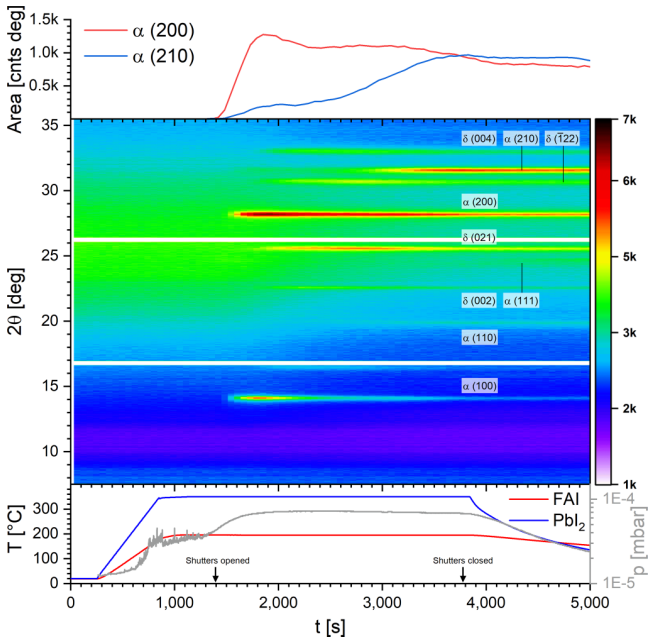


FIG. 1. Colormap of the growth of the FAPbI₃ perovskite that was used in the isothermal decomposition experiment at 290 °C. Every column of pixels corresponds to one XRD scan and the color indicates the number of counts received at the respective angle. The bottom graph shows the temperatures of the crucibles, the opening and closing times of the shutters and the chamber pressure. The XRD peaks are labeled by phase and miller index.

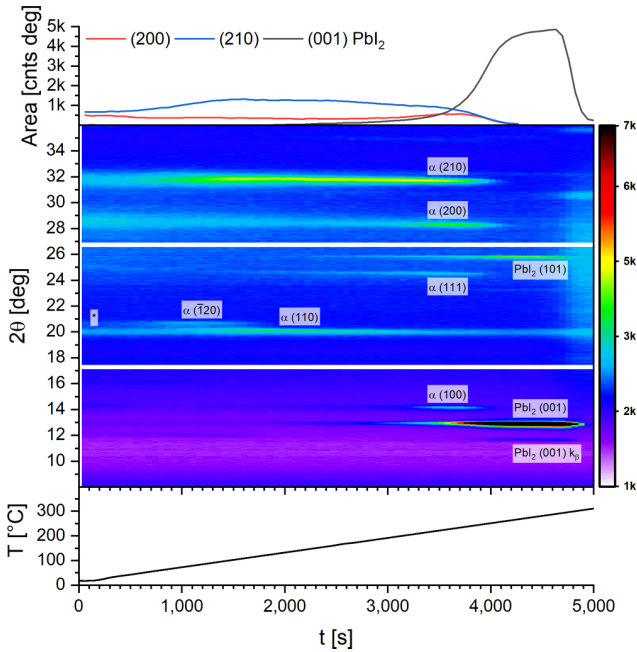


FIG. 2. Colormap of the temperature ramp experiment of the thermal decomposition of FAPbI₃. The top graph shows the integrated intensity of the (200) and (210) peaks of the α phase and the bottom graph shows the sample's temperature. An additional peak detected at 20° for this deposition run was identified with contamination of the Kapton window and is labeled with an asterisk in the graph. Notably, the (110) peak of the α phase overlays this peak for a time before the perovskite fully disappears.

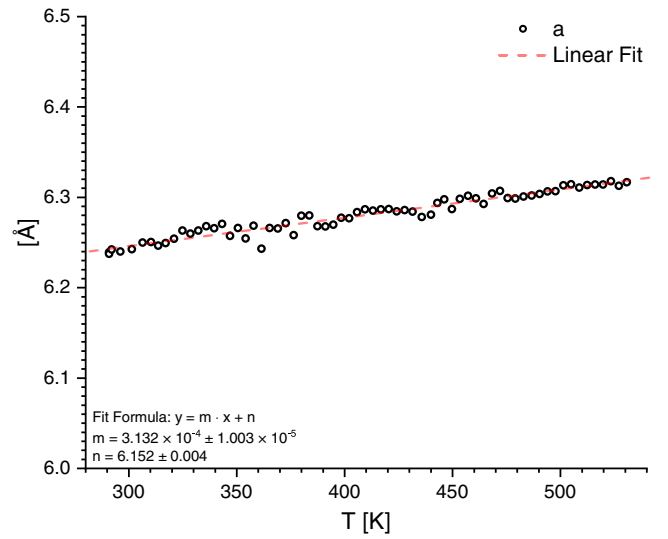


FIG. 3. Dependence of the lattice constant a on the temperature T together with a linear fit over the data. a has been calculated using the position of the (200) FAPbI₃ peak.

some metallic lead is detected. It is of note that with this experimental setup we cannot detect organic (and possibly volatile) decomposition products and as such we cannot make a comment as to whether the decomposition is driven by the dissociation of the FA molecule itself, as is the case for MAPbI₃, or whether the FA molecule stays intact during the decomposition. However, in works by Juarez-Perez et al. the FA decomposition products HCN and NH₃ have been detected during the thermal decomposition of FAPbI₃ and FAPbBr₃ [33].

Since the positions of the XRD peaks directly depend on the lattice constant of the analyzed material, their shift upon heating with a temperature ramp allows for the calculation of the thermal expansion coefficient of a material. Figure 3 shows the change of the lattice constant in relation to the temperature together with a linear fit of the data, as calculated from the (200) peak. α_L was also calculated from the positions of the (100), (110), (111), and (210) FAPbI₃ peaks in the XRD pattern for each scan. Since most of these other peaks were only faintly visible or not very sharp, a weighted average was taken and the result was $\alpha_L = 48.08 \pm 1.32 \times 10^{-6} \text{ K}^{-1}$. The results for the separate peaks can be found in the Supplemental Material [42]. Due to the deviations in the results for the different peaks, we would estimate the actual relative uncertainty of the end result to be closer to 10%, resulting in a final value of $\alpha_L = 48 \pm 5 \times 10^{-6} \text{ K}^{-1}$. This value for the linear thermal expansion coefficient for FAPbI₃ is higher than the value we obtained, using the same method, for MAPbI₃ thin films in Ref. [13], which is $36 \pm 1 \times 10^{-6} \text{ K}^{-1}$.

C. Partial decomposition - SEM/EDX analysis

As described in Sec. III, one sample was partially decomposed by applying a temperature gradient over its surface. One sample was taken out of the vacuum chamber prior to annealing, serving as an untreated reference sample. The sample turned orange upon exposure to ambient air, which indicates

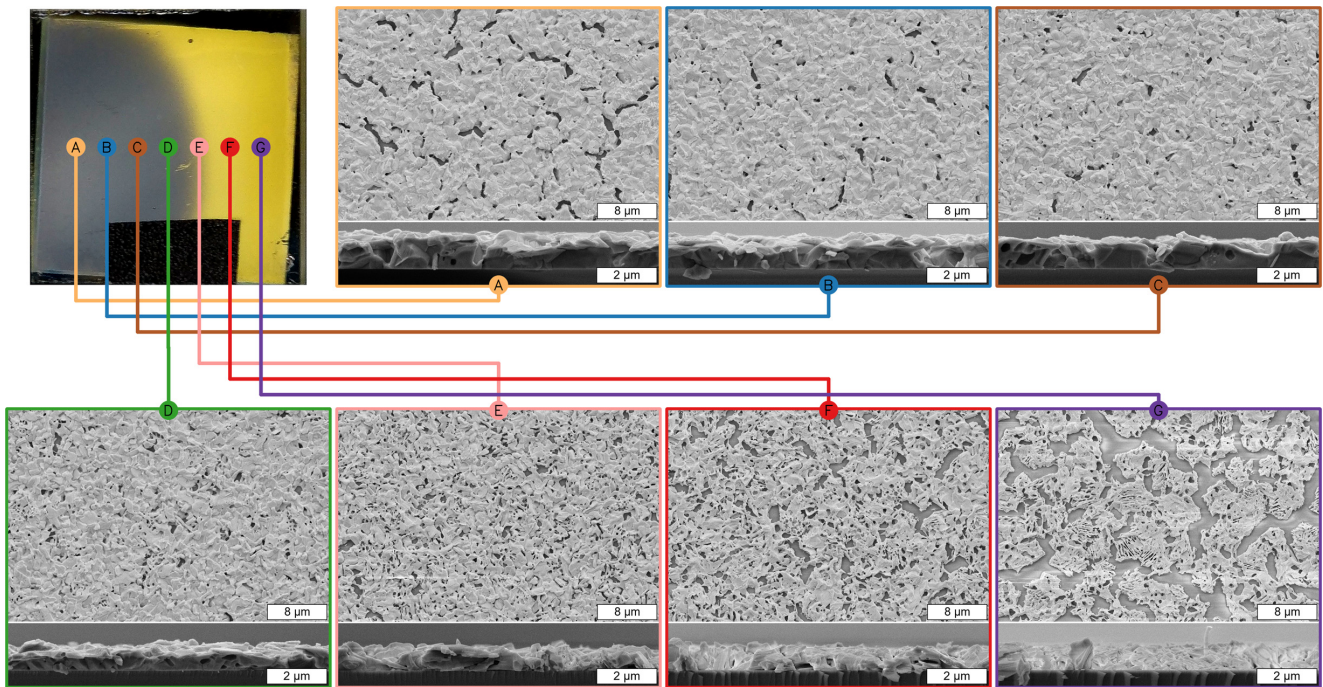


FIG. 4. Cross-sectional and top view SEM images of the partially decomposed sample. The photograph at the top left marks the approximate areas where the SEM images were taken. The cross section images correspond approximately to the positions of the surface images.

the transition from the α to the δ phase. This untreated sample was analyzed with a scanning electron microscope (SEM) in this state. The resulting images are shown in Figs. 5(a) and 5(b). The images were taken by two detectors (consecutively, not simultaneously): an Everhart-Thornley secondary electron detector (ET-SE) and an in-lens secondary electron detector (IL-SE). The ET-SE image (a), shows a smooth layer with full coverage and particles of roughly 300 nm in average size. The IL-SE image (b), which provides a higher material contrast, suggests a very homogeneous layer without any visible secondary phases.

The succession of SEM images shown in Fig. 4 provides an insight into the progress of the reaction and the resulting morphology change on a microscopic scale. Going from left to right (lower to higher annealing temperature), the sample first shows only very small signs of decomposition while the decomposition gets more pronounced towards the right side. Image A is an exception to this, because the metal rail that blocked the thermal radiation let some heat through on the leftmost side. Because of this, the part of the sample which is least decomposed is shown in images B and C. Some rifts are already visible at these positions, while the layer still covers most of the sample. At point D, roughly in the middle of the sample, some pores and voids appear. The cross section shows a declining layer thickness and hints at flat platelets forming at the top of the layer. Their characteristic form suggests a hexagonal crystal structure, as expected for the decomposition product PbI_2 , that was detected with XRD. Figures 5(c) and 5(d) show the same spot of the image with a larger magnification and, in addition to the ET-SE image, also shows an IL-SE image. Due to the higher material contrast

of the IL-SE image, two clearly distinct phases are visible. The brighter part of the image with the hexagonal platelet structures is assigned to PbI_2 , as indicated above. The slightly darkened spot in the middle is likely an artifact of the IL-SE system, as those detectors can sometimes lead to a small dark area at the center of the image. Overall, this image gives the impression that FAPbI_3 (in dark) is overlaid by the brighter PbI_2 , consistent with the cross-section image of D in Fig. 4, indicating the formation of a PbI_2 top layer. The next image (E) shows an increase in porousness and the PbI_2 platelets are now clearly visible in the cross section. This is also the part of the sample where, in the photo, the dark perovskite area gives way to the yellow PbI_2 . In image F, which in the photo is already completely yellow, the layer coverage has decreased significantly. The pores from before have now started forming elongated ridges. On position G, the sample exhibits a very low surface coverage and what remains of the layer is highly furrowed. The cross section underlines this by showing a layer that has significantly lost in thickness and looks more like a loose scattering of material, rather than a solid layer. EDX measurements of the $[\text{I}]/[\text{Pb}]$ ratio (IP) taken on positions A, D, and G, which are shown in Table I, are consistent with these visual observations. Positions A's and D's IPs are close to the value expected for FAPbI_3 ($\text{IP} \approx 3$), while the results for position G indicate that PbI_2 has been formed ($\text{IP} \approx 2$), which is consistent with the expectations.

D. Isothermal decomposition - First order approach

To calculate the kinetic parameters of the thermal decomposition reaction, a set of isothermal decomposition

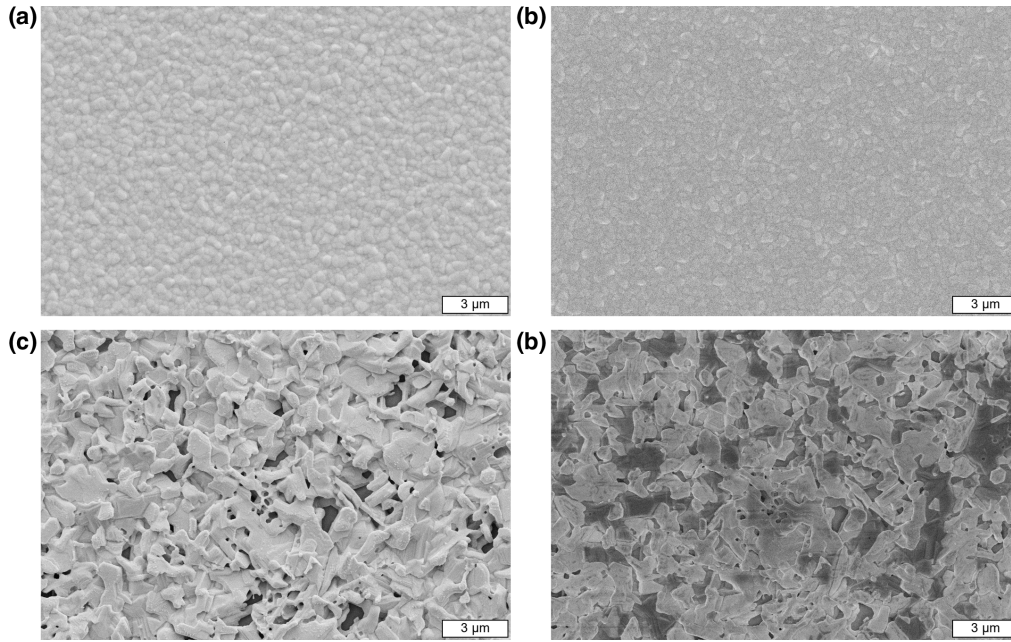


FIG. 5. (a) Everhart-Thornley secondary electron (ET-SE) micrograph of an untreated sample. (b) Micrograph using the in-lens secondary electron detector (IL-SE) of the same area of an untreated sample. (c) ET-SE image of the partially decomposed sample at position *D* (see Fig. 4). (d) IL-SE image of the same area of the partially decomposed sample.

experiments has been conducted at temperatures of 230 °C, 250 °C, 270 °C, and 290 °C. In the first experiment at 230 °C, the area of the perovskite peaks declined by only 50 % over 3.5 h. An overview of the results is depicted in Fig. 6. The sample annealed at 250 °C showed recrystallization prior to decomposition: After the final temperature of 250 °C was reached, the (111) and (200) peaks gained notably in intensity over several minutes before declining. The (210) peak did not exhibit this behavior. After the initial increase, the following decline of the (111) and (200) peaks was far more rapid than that of the (210) peak. In consequence, the initial recrystallization might lead to an overestimation of the subsequent intensity decay and reaction rate k , when considering merely the (111) and (200) peaks. For these reasons, the evaluation is focused on the decline of the FAPbI₃ (210) peak. Since the decomposition of FAPbI₃ results in a crystalline PbI₂ layer, the formation of this reaction product also constitutes an indicator for the progress of the decomposition reaction and is decoupled from any recrystallization effects occurring in the FAPbI₃ layer. Therefore, the rise of the PbI₂ (001) peak is used as a second variable for the calculation of the reaction

rate k . For better comparability with the declining peak areas of the FAPbI₃ reflexes, the normalized peak areas a of the PbI₂ reflexes are given as $(1 - a)$ in Fig. 7.

In order to determine a first estimate for the reaction rate k , the data points were fitted using the exponential equation of Eq. (3). Since the exact beginning of the decomposition can be difficult to determine, the first 4 to 5 data points were ignored and the fit was conducted down to a normalized peak

TABLE I. EDX measurements of different positions in Fig. 4. The values are given as the amount of I atoms per one Pb atom, which is the [I]/[Pb] ratio, also referred to here as IP. For FAPbI₃ the expected IP is 3 and for PbI₂ it is 2.

Position	I per Pb (IP)
A	3.2
D	2.9
G	2.1

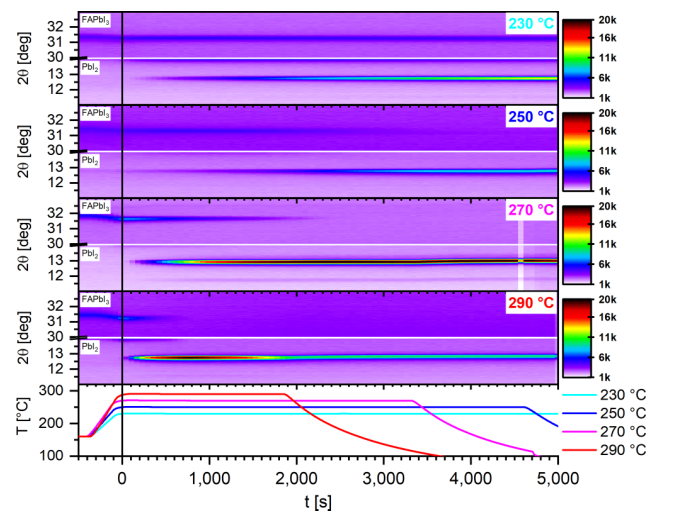


FIG. 6. Colormaps of the decomposition experiments. The decay of the (210) FAPbI₃ peak is visible in the 30° to 33° range and the growth of the (001) PbI₂ peak is visible in the 11° to 14° range. The substrate temperatures for each of these experiments are shown in the bottom graph.

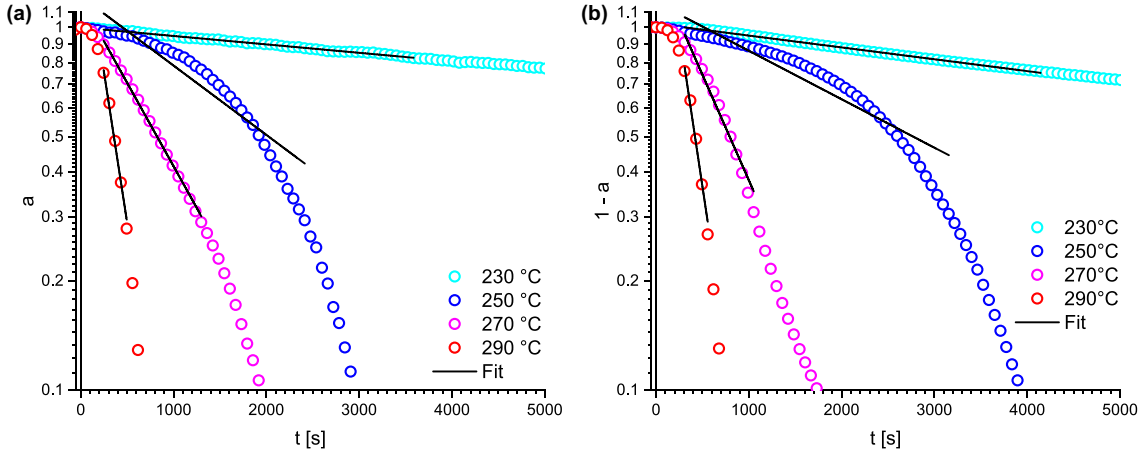


FIG. 7. Logarithmic plots of the time evolution of the normalized peak areas a together with the linear fits. (a) Normalized peak area a for the (210) peak of FAPbI₃. (b) The evolution of the (001) PbI₂ peak. In this latter case, one minus the normalized peak area ($1 - a$) is plotted for better comparability.

area a of 0.3. This is possible because for a first-order decay, the speed of the reaction does not depend on the extent of the reaction. The 250 °C process does not fit this exponential decay as well as the others, but the fit range was chosen by the same criteria for consistency. The process using 230 °C is the only exception to this, since the area of the perovskite peaks only dropped to 50 % during the course of the experiment. However, since it showed a very consistent exponential decay, the result is quite insensitive to the choice of the fit range. After obtaining a value for each experiment, $\ln k$ has been plotted over $1/T$ to achieve an Arrhenius-type plot, which is

depicted in Fig. 8 for the (210) peak of FAPbI₃ and the (001) peak of PbI₂, together with the plot resulting from averaging over the k values for the (210) FAPbI₃ peak and the (001) PbI₂ peak. The exponential fits shown in Fig. 7 provide a statistical error σ for each value of k and these errors have been used in the Arrhenius fits to weight the data according to $w_i = 1/\sigma_i$. The resulting fit for the averaged values of k yielded values for the activation energy $E = 165.3 \pm 4.9 \text{ kJ mol}^{-1}$ and the pre-exponential factor $\ln A = 29.9 \pm 1.2$. The results of these evaluations are summarized in Table II.

E. Model-fitting approach

Our paper on MAPbI₃ (Ref. [10]) showed the difficulty to determine a specific reaction model from our data. In addition, the obtained E and A values did not significantly deviate from the ones obtained from the manual first order fitting method. We made a similar comparison with the same set of reaction models for the data on FAPbI₃ obtained here. The outcome was similar to the MAPbI₃ case, as the linearity of the $g(\alpha)$ over t plot (a rough measure for how well a model fits the reaction) and the values for E and A were similar for many of the models. The specific results for all models are included in the supporting information [42]. The evaluation of the (210) FAPbI₃ peak with the different reaction models resulted in values of $E \approx 150 \pm 24 \text{ kJ mol}^{-1}$ and $\ln A = 26 \pm 5$, while the (001) PbI₂ peak yielded $E \approx 160 \pm 16 \text{ kJ mol}^{-1}$ and $\ln A = 28 \pm 4$.

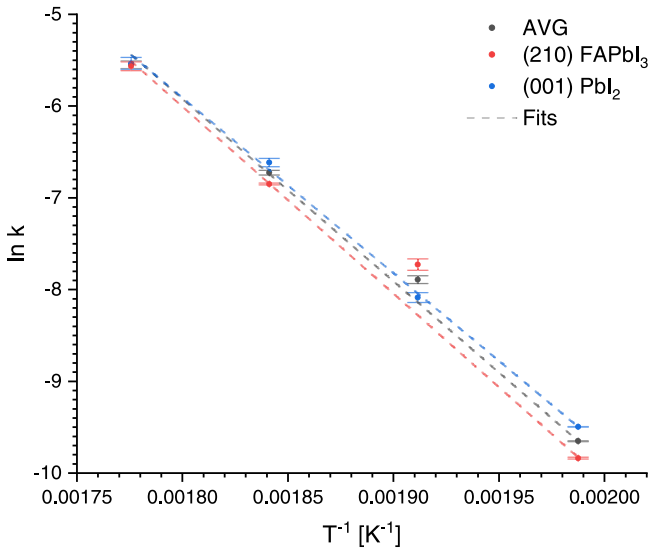


FIG. 8. Arrhenius plot showing $\ln k$ values over $1/T$ for the (210) peak of FAPbI₃ and the (001) peak of PbI₂. “AVG” denotes the averaged k values. The values for k are determined from the exponential fits of the graphs shown in Fig. 7. The errors of $\ln k$, as calculated from the statistical errors of the exponential fits, are marked with horizontal lines. For the linear fits, the data points were weighted with these errors σ according to $w_i = 1/\sigma_i$.

TABLE II. Results of the first order approach for the (210) FAPbI₃ peak and the (001) PbI₂ peak. The result that was obtained by averaging the k values of these two peaks for each temperature is denoted as “AVG”.

Peak	E [kJ mol ⁻¹]	$\ln A$ [s ⁻¹]
(210) FAPbI ₃	169.1 ± 3.6	30.6 ± 0.9
(001) PbI ₂	159.1 ± 2.9	28.5 ± 0.7
AVG	165.3 ± 4.9	29.9 ± 1.2

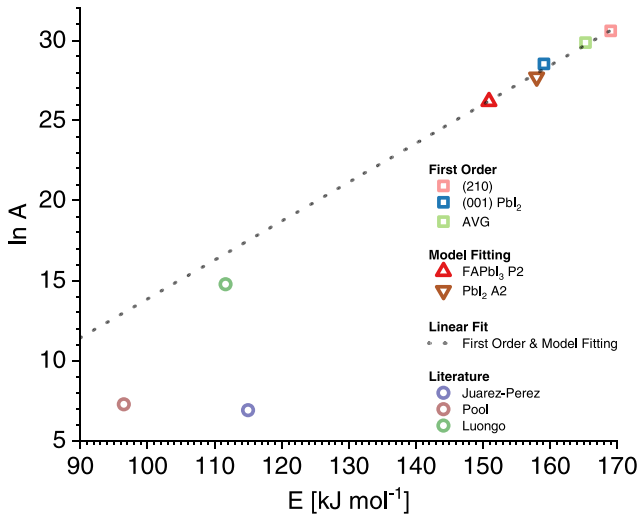


FIG. 9. The results of this paper depicted as an $\ln A$ over E plot, together with the results of Juarez-Perez *et al.* [33], Pool *et al.* [34], and Luongo *et al.* [35]. The linear fit is indicated by the dotted line.

F. Compensation effect

Just as in our previous paper, we again found that the results of the various methods and reaction models follow a line with the form

$$\ln A = aE + b. \quad (11)$$

The $\ln A$ over E data is plotted in Fig. 9. This behavior is generally known as the compensation effect, which refers to the phenomenon that similar experiments on the decomposition of a material can lead to a significant spread of E and $\ln A$ values, while those values are coupled by a linear dependence. The line described by Eq. (11) implies that there is a temperature T at which these processes agree on a specific turnover ratio k . From the values of a and b one can calculate these values for T and k :

$$T = \frac{1}{Ra} \quad (12)$$

$$\ln k = b. \quad (13)$$

A linear fit of the data presented in Fig. 9 gave values of $a = 0.243 \pm 0.022$ and $b = -10.453 \pm 3.553$, which results in a temperature of agreement of $T = 222 \pm 45$ °C and a corresponding turnover ratio of $\ln k = 10.453 \pm 3.553$. L'vov's

theory of CDV explains the compensation effect with the buildup of product gases in the reactor, that influence the values for E and A according to Eq. (11). Unfortunately, since all our experiments were conducted in high vacuum, this explanation does not apply to our case. A more likely explanation is the simple fact that, because the evaluations used the same experimental data, their results need to agree on the overall turnover ratio to some degree, but the specific values for E and A are more sensitive to small deviations in the data and the choice of the evaluation method.

When comparing the results of our paper with the other works mentioned in Table III, the results of Luongo *et al.* are close to the linear fit line shown in Fig. 9, hinting at an overall similar rate of decomposition.

V. DISCUSSION

The activation energy of the thermal decomposition of FAPbI₃ that has been determined in this paper ($E = 165$ kJ mol⁻¹) is significantly larger than that which has been determined for MAPbI₃ ($E = 110$ kJ mol⁻¹) in our previous paper [10]. However, it needs to be stressed that this does not by itself indicate a higher thermal stability, i.e., a lower rate of thermal decomposition at any given temperature. To make such an assessment, the rate constant A needs to be taken into account as well. According to Eq. (2), the activation energy E determines how k changes with a change in temperature T , while the rate constant A is a scalar factor onto the exponential term that, especially in the field of solid-state decompositions, can vary by many orders of magnitude between different processes [51]. To get an understanding of how the values for E and A , taken together, translate into the thermal stability of a material, one can use Eq. (2) to calculate $k(T)$. Figure 10 shows the calculated $k(T)$ relation for FAPbI₃ and MAPbI₃ (with E and A taken from Ref. [10]), together with the experimentally determined values for k . The figure also shows the temperature difference between $k(T)$ of MAPbI₃ and $k(T)$ of FAPbI₃ for a given rate k . From this it can be estimated that the start of the decomposition of FAPbI₃ is shifted upwards by about 45 °C when compared to MAPbI₃, while the temperature difference between the two curves becomes smaller as the temperature increases.

Overall, the results confirm the higher thermal stability of FAPbI₃ when compared to MAPbI₃. While Fig. 10 implies an upwards shift of the temperature of thermal decomposition by only roughly 45 °C, the increased stability becomes more apparent when looking at the predicted decomposition

TABLE III. Comparison of the results and experimental methods of this work with the works of Juarez-Perez *et al.* [33], Pool *et al.* [34], and Luongo *et al.* [35]. The results of Luongo *et al.* are divided into three parts. A: *In situ* XRD of the whole decomposition process; B: Differential scanning calorimetry (DSC) of the first decomposition step; C: DSC of the second decomposition step.

Source	E [kJ mol ⁻¹]	$\ln A$ [s ⁻¹]	Configuration	Preparation	Atmosphere	T-regime	Measured value
This paper	165.3 ± 4.9	29.9 ± 1.2	Thin film	Coevaporation	Vacuum	Isothermal	Time-resolved XRD
[33]	115 ± 3	6.9 ± 0.2	Powder	Solution + Mortar	Vacuum & He	Ramp	TGA
[34]	96.5 ± 13.1	7.260 ± 0.007	Thin Film	Spin-coating	N ₂	Ramp	Time-resolved XRD
[35] A	112 ± 9	14.8 ± 2.0	Powder	Grinding of precursors	He	Ramp	Time-resolved XRD
[35] B	205 ± 20	–	Powder	Grinding of precursors	Ar	Ramp	DSC
[35] C	410 ± 20	–	Powder	Grinding of precursors	Ar	Ramp	DSC

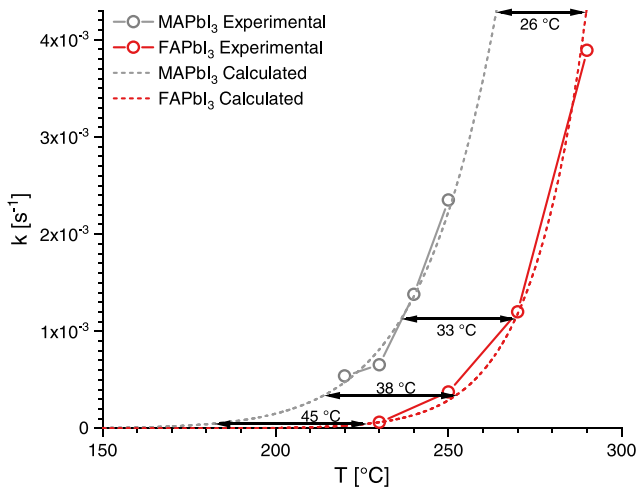


FIG. 10. Comparison of how the rate constant of the thermal decomposition k depends on the temperature T for MAPbI₃ (data taken from our earlier work in Ref. [10]) and FAPbI₃ (data taken from this paper). The circles represent the k values obtained from the measurements and the dotted lines are calculations using Eq. (2), with $E = 110.5 \text{ kJ mol}^{-1}$ and $\ln A = 19.3$ for MAPbI₃ and $E = 165.3 \text{ kJ mol}^{-1}$ and $\ln A = 29.9$ in the case of FAPbI₃. The arrows show the difference in temperature between the two calculated curves for the same value of k .

behavior at lower temperatures. In our paper on MAPbI₃ [10] we calculated the time in which the perovskite would decompose by 20% to $\alpha = 0.2$ at 85 °C and the result was 2800 h (around 120 d). For FAPbI₃ to decompose to the same extent at 85 °C, it would take roughly 8 000 000 h (around 900 years). A similar calculation stated that for MAPbI₃ to not decompose by more than 20% within 1 h it would need to be

stored below 180 °C. In the case of FAPbI₃ this temperature would be 230 °C. Zhang *et al.* note that, compared to MA, FA is a larger molecule with a smaller dipole moment and, in perovskites, has a larger bonding strength to the halides, which reduces halide ion migration and explains the higher stability commonly observed with FA-based perovskites [52,53].

VI. CONCLUSIONS

In conclusion, we have determined the kinetic parameters for the thermal decomposition of coevaporated FAPbI₃ thin films, deriving an activation energy of $E = 165.3 \pm 4.9 \text{ kJ mol}^{-1}$ and a pre-exponential factor of $\ln A = 29.9 \pm 1.2$. The data indicates that the onset of decomposition occurs at higher temperatures compared to MAPbI₃, which confirms the higher thermal stability of the FA-based perovskite. The temperature ramp experiment indicated the start of the decomposition of FAPbI₃ to occur at roughly 230 °C, which is in good agreement with what would be expected from the determined values for E and A . The linear expansion coefficient was determined to be $\alpha_L = 48 \pm 5 \times 10^{-6} \text{ K}^{-1}$. The SEM analysis of the partially decomposed sample indicated a decomposition that started from the top of the layer, forming PbI₂, and progressed through the whole layer while significantly reducing its surface coverage.

ACKNOWLEDGMENTS

We gratefully acknowledge financial support from the German Federal Ministry of Research and Education (BMBF) under Contract No. 03EK3570B (StrukturSolar II) and from the Spanish Ministerio de Universidades under the Beatriz Galindo Senior Program No. BG20/00194.

There are no conflicts of interest to disclose.

- [1] A. Kojima, K. Teshima, Y. Shirai, and T. Miyasaka, Organometal halide perovskites as visible-light sensitizers for photovoltaic cells, *J. Am. Chem. Soc.* **131**, 6050 (2009).
- [2] Y. C. Kim, K. H. Kim, D.-Y. Son, D.-N. Jeong, J.-Y. Seo, Y. S. Choi, I. T. Han, S. Y. Lee, and N.-G. Park, Printable organometallic perovskite enables large-area, low-dose x-ray imaging, *Nature (London)* **550**, 87 (2017).
- [3] H. Wei and J. Huang, Halide lead perovskites for ionizing radiation detection, *Nat. Commun.* **10**, 1066 (2019).
- [4] Q. Shan, J. Song, Y. Zou, J. Li, L. Xu, J. Xue, Y. Dong, B. Han, J. Chen, and H. Zeng, High performance metal halide perovskite light-emitting diode: From material design to device optimization, *Small* **13**, 1701770 (2017).
- [5] Y. Sun, L. Zhang, N. Wang, S. Zhang, Y. Cao, Y. Miao, M. Xu, H. Zhang, H. Li, C. Yi, J. Wang, and W. Huang, The formation of perovskite multiple quantum well structures for high performance light-emitting diodes, *npj Flex. Electron.* **2**, 12 (2018).
- [6] M. Yuan, L. N. Quan, R. Comin, G. Walters, R. Sabatini, O. Voznyy, S. Hoogland, Y. Zhao, E. M. Beauregard, P. Kanjanaboos, Z. Lu, D. H. Kim, and E. H. Sargent, Perovskite energy funnels for efficient light-emitting diodes, *Nat. Nanotechnol.* **11**, 872 (2016).
- [7] N. Wang, L. Cheng, R. Ge, S. Zhang, Y. Miao, W. Zou, C. Yi, Y. Sun, Y. Cao, R. Yang *et al.*, Perovskite light-emitting diodes based on solution-processed self-organized multiple quantum wells, *Nat. Photonics* **10**, 699 (2016).
- [8] S. W. Eaton, M. Lai, N. A. Gibson, A. B. Wong, L. Dou, J. Ma, L.-W. Wang, S. R. Leone, and P. Yang, Lasing in robust cesium lead halide perovskite nanowires, *Proc. Natl. Acad. Sci. USA* **113**, 1993 (2016).
- [9] C. C. Boyd, R. Cheacharoen, T. Leijtens, and M. D. McGehee, Understanding degradation mechanisms and improving stability of perovskite photovoltaics, *Chem. Rev.* **119**, 3418 (2019).
- [10] T. Burwig and P. Pistor, Reaction kinetics of the thermal decomposition of MAPbI₃ thin films, *Phys. Rev. Materials* **5**, 065405 (2021).
- [11] P. Holzhey and M. Saliba, A full overview of international standards assessing the long-term stability of perovskite solar cells, *J. Mater. Chem. A* **6**, 21794 (2018).

- [12] S. Zhang and G. Han, Intrinsic and environmental stability issues of perovskite photovoltaics, *Prog. Energy* **2**, 022002 (2020).
- [13] P. Pistor, T. Burwig, C. Brzuska, B. Weber, and W. Fränzel, Thermal stability and miscibility of co-evaporated methyl ammonium lead halide (MAPbX₃, X = I, Br, Cl) thin films analysed by *in situ* x-ray diffraction, *J. Mater. Chem. A* **6**, 11496 (2018).
- [14] A. Dualeh, P. Gao, S. I. Seok, M. K. Nazeeruddin, and M. Grätzel, Thermal behavior of methylammonium lead-trihalide perovskite photovoltaic light harvesters, *Chem. Mater.* **26**, 6160 (2014).
- [15] N.-K. Kim, Y. H. Min, S. Noh, E. Cho, G. Jeong, M. Joo, S.-W. Ahn, J. S. Lee, S. Kim, K. Ihm, *et al.*, Investigation of thermally induced degradation in CH₃NH₃PbI₃ perovskite solar cells using *in-situ* synchrotron radiation analysis, *Sci. Rep.* **7**, 4645 (2017).
- [16] E. J. Juarez-Perez, Comment on probing the origins of photodegradation in organic-inorganic metal halide perovskites with time-resolved mass spectrometry, sustainable energy & fuels, *ChemRxiv* (2018), doi: 10.26434/chemrxiv.7295585.v2.
- [17] H. A. Dewi, J. Li, H. Wang, B. Chaudhary, N. Mathews, S. Mhaisalkar, and A. Bruno, Excellent intrinsic long-term thermal stability of co-evaporated MAPbI₃ solar cells at 85 °C, *Adv. Funct. Mater.* **31**, 2100557 (2021).
- [18] T. Burwig, W. Fränzel, and P. Pistor, Crystal phases and thermal stability of co-evaporated CsPbX₃ (X = I, Br) thin films, *J. Phys. Chem. Lett.* **9**, 4808 (2018).
- [19] T. Burwig, K. Heinze, V. Naumann, A. Hähnel, S. Lange, C. Hagendorf, R. Scheer, and P. Pistor, Co-evaporated Cs₂AgBiBr₆ double perovskites for solar cells, in *Proceedings of the 36th European Photovoltaic Solar Energy Conference and Exhibition* (WIP, Marseille, France, 2019) pp. 728–732.
- [20] T. Burwig, M. Guc, V. Izquierdo-Roca, and P. Pistor, Synthesis and crystal structure evolution of co-evaporated Cs₂AgBiBr₆ thin films upon thermal treatment, *J. Phys. Chem. C* **124**, 9249 (2020).
- [21] G. Niu, W. Li, J. Li, X. Liang, and L. Wang, Enhancement of thermal stability for perovskite solar cells through cesium doping, *RSC Adv.* **7**, 17473 (2017).
- [22] X. Li, J. Wu, S. Wang, and Y. Qi, Progress of all-inorganic cesium lead-free perovskite solar cells, *Chem. Lett.* **48**, 989 (2019).
- [23] G. A. Tosado, Y.-Y. Lin, E. Zheng, and Q. Yu, Impact of cesium in phase and device stability of triple cation Pb-Sn double halide perovskite films and solar cells, *J. Mater. Chem. A* **6**, 17426 (2018).
- [24] R. E. Beal, D. J. Slotcavage, T. Leijtens, A. R. Bowring, R. A. Belisle, W. H. Nguyen, G. F. Burkhard, E. T. Hoke, and M. D. McGehee, Cesium lead halide perovskites with improved stability for tandem solar cells, *J. Phys. Chem. Lett.* **7**, 746 (2016).
- [25] B. Wook Park and S. I. Seok, Intrinsic instability of inorganic-organic hybrid halide perovskite materials, *Adv. Mater.* **31**, 1805337 (2019).
- [26] E. Smecca, Y. Numata, I. Deretzis, G. Pellegrino, S. Boninelli, T. Miyasaka, A. L. Magna, and A. Alberti, Stability of solution-processed MAPbI₃ and FAPbI₃ layers, *Phys. Chem. Chem. Phys.* **18**, 13413 (2016).
- [27] A. F. Akbulatov, S. A. Tsarev, M. Elshobaki, S. Y. Luchkin, I. S. Zhidkov, E. Z. Kurmaev, S. M. Aldoshin, K. J. Stevenson, and P. A. Troshin, Comparative intrinsic thermal and photochemical stability of Sn(II) complex halides as next-generation materials for lead-free perovskite solar cells, *J. Phys. Chem. C* **123**, 26862 (2019).
- [28] M. Saliba, T. Matsui, J.-Y. Seo, K. Domanski, J.-P. Correa-Baena, M. K. Nazeeruddin, S. M. Zakeeruddin, W. Tress, A. Abate, A. Hagfeldt, and M. Grätzel, Cesium-containing triple cation perovskite solar cells: Improved stability, reproducibility and high efficiency, *Energy Environ. Sci.* **9**, 1989 (2016).
- [29] A. F. Akbulatov, S. Y. Luchkin, L. A. Frolova, N. N. Dremova, K. L. Gerasimov, I. S. Zhidkov, D. V. Anokhin, E. Z. Kurmaev, K. J. Stevenson, and P. A. Troshin, Probing the intrinsic thermal and photochemical stability of hybrid and inorganic lead halide perovskites, *J. Phys. Chem. Lett.* **8**, 1211 (2017).
- [30] A. F. Akbulatov, V. M. Martynenko, L. A. Frolova, N. N. Dremova, I. Zhidkov, S. A. Tsarev, S. Y. Luchkin, E. Z. Kurmaev, S. M. Aldoshin, K. J. Stevenson, and P. A. Troshin, Intrinsic thermal decomposition pathways of lead halide perovskites APbX₃, *Sol. Energy Mater. Sol. Cells* **213**, 110559 (2020).
- [31] G. E. Eperon, S. D. Stranks, C. Menelaou, M. B. Johnston, L. M. Herz, and H. J. Snaith, Formamidinium lead trihalide: A broadly tunable perovskite for efficient planar heterojunction solar cells, *Energy Environ. Sci.* **7**, 982 (2014).
- [32] J.-W. Lee, D.-J. Seol, A.-N. Cho, and N.-G. Park, High-efficiency perovskite solar cells based on the black polymorph of HC(NH₂)₂PbI₃, *Adv. Mater.* **26**, 4991 (2014).
- [33] E. J. Juarez-Perez, L. K. Ono, and Y. Qi, Thermal degradation of formamidinium based lead halide perovskites into sym-triazine and hydrogen cyanide observed by coupled thermogravimetry-mass spectrometry analysis, *J. Mater. Chem. A* **7**, 16912 (2019).
- [34] V. L. Pool, B. Dou, D. G. V. Campen, T. R. Klein-Stockert, F. S. Barnes, S. E. Shaheen, M. I. Ahmad, M. F. A. M. van Hest, and M. F. Toney, Thermal engineering of FAPbI₃ perovskite material via radiative thermal annealing and *in situ* XRD, *Nat. Commun.* **8**, 14075 (2017).
- [35] A. Luongo, B. Brunetti, S. V. Cipriotti, A. Cicciooli, and A. Latini, Thermodynamic and kinetic aspects of formamidinium lead iodide thermal decomposition, *J. Phys. Chem. C* **125**, 21851 (2021).
- [36] M. T. Weller, O. J. Weber, J. M. Frost, and A. Walsh, Cubic perovskite structure of black formamidinium lead iodide, α -[HC(NH₂)₂]PbI₃, at 298 K, *J. Phys. Chem. Lett.* **6**, 3209 (2015).
- [37] C. C. Stoumpos, C. D. Malliakas, and M. G. Kanatzidis, Semiconducting tin and lead iodide perovskites with organic cations: Phase transitions, high mobilities, and near-infrared photoluminescent properties, *Inorg. Chem.* **52**, 9019 (2013).
- [38] Q. Han, S.-H. Bae, P. Sun, Y.-T. Hsieh, Y. M. Yang, Y. S. Rim, H. Zhao, Q. Chen, W. Shi, G. Li, and Y. Yang, Single crystal formamidinium lead iodide (FAPbI₃): Insight into the structural, optical, and electrical properties, *Adv. Mater.* **28**, 2253 (2016).
- [39] A. Binek, F. C. Hanusch, P. Docampo, and T. Bein, Stabilization of the trigonal high-temperature phase of formamidinium lead iodide, *J. Phys. Chem. Lett.* **6**, 1249 (2015).
- [40] X. Zheng, C. Wu, S. K. Jha, Z. Li, K. Zhu, and S. Priya, Improved phase stability of formamidinium lead triiodide perovskite by strain relaxation, *ACS Energy Lett.* **1**, 1014 (2016).

- [41] S. Vyazovkin and C. A. Wight, Model-free and model-fitting approaches to kinetic analysis of isothermal and nonisothermal data, *Thermochim. Acta* **340-341**, 53 (1999).
- [42] See Supplemental Material at <http://link.aps.org/supplemental/10.1103/PhysRevMaterials.6.065404> for all models used for the the model fitting approach, the results of the model fitting approach, full colormaps of the isothermal decomposition experiments and results for the linear expansion coefficient calculated from multiple peaks.
- [43] A. Khawam and D. R. Flanagan, Solid-state kinetic models: Basics and mathematical fundamentals, *J. Phys. Chem. B* **110**, 17315 (2006).
- [44] NIST, NIST x-ray form factor, atten. scatt. tables form page <https://physics.nist.gov/PhysRefData/FFast/html/form.html> (2018).
- [45] A. K. Galwey, What theoretical and/or chemical significance is to be attached to the magnitude of an activation energy determined for a solid-state decomposition?, *J. Therm. Anal. Calorim.* **86**, 267 (2006).
- [46] P. Garn, Kinetics of decomposition of the solid state, *Thermochim. Acta* **135**, 71 (1988).
- [47] A. K. Galwey, Thermal reactions involving solids: A personal view of selected features of decompositions, thermal analysis and heterogeneous catalysis, *J. Therm. Anal. Calorim.* **142**, 1123 (2020).
- [48] B. V. L'vov, The physical approach to the interpretation of the kinetics and mechanisms of thermal decomposition of solids: The state of the art, *Thermochim. Acta* **373**, 97 (2001).
- [49] B. V. L'vov, *Thermal Decomposition of Solids and Melts* (Springer Netherlands, Dordrecht, 2007).
- [50] B. V. L'vov and A. K. Galwey, Toward a general theory of heterogeneous reactions, *J. Therm. Anal. Calorim.* **113**, 561 (2013).
- [51] H. F. Cordes, Preexponential factors for solid-state thermal decomposition, *J. Phys. Chem.* **72**, 2185 (1968).
- [52] T. Zhang, X. Meng, Y. Bai, S. Xiao, C. Hu, Y. Yang, H. Chen, and S. Yang, Profiling the organic cation-dependent degradation of organolead halide perovskite solar cells, *J. Mater. Chem. A* **5**, 1103 (2017).
- [53] A. Oranskaia and U. Schwingenschlögl, Suppressing x-migrations and enhancing the phase stability of cubic FAPbX₃ (X = Br, I), *Adv. Energy Mater.* **9**, 1901411 (2019).

Closing Discussion

The kinetic parameters of the thermal decomposition of FAPbI₃ have been determined as $E = 125.1(84) \text{ kJ mol}^{-1}$ and $\ln A = 21.1(19)$. For comparison, the values found for MAPbI₃ were $E = 110(15) \text{ kJ mol}^{-1}$ and $\ln A = 19(4)$. A higher value for E , however, does not automatically result in a higher thermal stability, especially when the value for A is also higher to compensate. A more readable comparison of what these values mean in practice is depicted in figure 10 in the publication. This graphic compares the experimental and calculated values for $k(T)$ for MAPbI₃ and FAPbI₃ and also shows the difference in temperature, where MAPbI₃ and FAPbI₃ show the same value for k . The calculated points are predictions for $k(T)$ using the before mentioned values for E and A . The overall scaling of k over T is similar for both materials, due to the similar activation energies, but the decomposition of FAPbI₃ is moved upwards on the T axis by about 45 °C. This confirms that FAPbI₃ has higher thermal stability than MAPbI₃. In view of the potentially high operational temperature of solar cells of up to 85 °C [60], this difference can have a significant impact for a solar cell's overall longevity.

Chapter 5

Additional Results

5.1 General Notes

In addition to the experiments that were presented in detail in chapter 4, experiments have been conducted on the preparation and thermal decomposition of other MHPs that have not yet been published. Solar cells using $\text{Cs}_2\text{AgBiBr}_6$ absorbers have been prepared and the resulting layer stack has been analyzed using TEM, in collaboration with researchers from the Fraunhofer CSP. The results were presented the proceedings of the EU PVSEC 2019 conference (reference [Bu6]) and are commented on in section 5.2. A common observation made during the experiments presented in this work, was that small changes in the relative onset times of the precursor's evaporation, as well as the observed increase in chamber pressure upon evaporation of the organic halides, seem to have a large influence on the resulting thin films and on solar cells prepared with these films. For this reason, experiments were conducted and analyzed by Karl Heinze, to investigate how the increase in chamber pressure due to MAI evaporation and the onset time of MAI evaporation influence the performance of MAPbI_3 solar cells [Bu7]. The results are shown in section 5.3. Finally, the results of the temperature ramp experiments on the different perovskites are compared in section 5.5.

5.2 $\text{Cs}_2\text{AgBiBr}_6$ Solar Cells

Preliminary Discussion

Reference: [Bu6]

To complement the results on $\text{Cs}_2\text{AgBiBr}_6$, some $\text{Cs}_2\text{AgBiBr}_6$ thin films were prepared using the simultaneous co-evaporation of precursors with subsequent annealing — as presented in reference [Bu3] — and the resulting films were used to prepare solar cells. In collaboration with the Fraunhofer CSP, one of the solar cells was analyzed using a TEM.

CO-EVAPORATED Cs₂AgBiBr₆ DOUBLE PEROVSKITES FOR SOLAR CELLSThomas Burwig^a, Karl Heinze^a, Volker Naumann^b, Angelika Hähnel^b, Stefan Lange^b, Christian Hagendorf^b, Roland Scheer^a, and Paul Pistor^a^aMartin-Luther-Universität Halle-Wittenberg, Von-Danckelmann-Platz 3, 06120 Halle (Saale), Germany^bFraunhofer-Center für Silizium-Photovoltaik CSP, Otto-Eißfeldt-Straße 12, 06120 Halle (Saale), Germany

ABSTRACT: Lead halide perovskites constitute a promising material for various opto-electronic applications, most prominently photovoltaics. The organic-inorganic perovskites that have been mostly investigated for use as photovoltaic absorbers, e.g. MAPbI₃, face two main issues that hinder their large-scale application: A lack of stability towards environmental factors and the fact that they contain lead. The double perovskite Cs₂AgBiBr₆ presents a significantly more stable and lead-free alternative. We present a dry vacuum synthesis of Cs₂AgBiBr₆ thin films by a two-stage co-evaporation process that leads to homogeneous layers with large crystals. Our first trials for their implementation as absorbers in solar cells yielded rectifying diodes, but only a low efficiency of 0.5 % (descending scan direction) due to very low current densities. The JV-curves of the double perovskites are compared to devices with a co-evaporated MAPbI₃ absorber, with which we obtain an efficiency of 9.8 % (descending scan direction). Transmission electron microscopy of a cross-section of the Cs₂AgBiBr₆ solar cell reveals large grains in the micrometre-range. While the photoconversion efficiency seems limited, the homogenous, controlled deposition and good crystallinity of the obtained Cs₂AgBiBr₆ layers makes our preparation method attractive for other opto-electronic applications not depending on optical absorption, such as X-ray- and UV-detectors.

Keywords: Perovskite, Deposition, Thin Film Solar Cell, Lead Free

1 INTRODUCTION

Organic-inorganic lead halide perovskites have seen an immense attention in the photovoltaic research community due to their outstanding photo-electric properties and comparably low production costs. This material class can combine a large variety of different constituents with varying properties. Most of these compounds have, to date, been investigated with photovoltaic applications in mind. However, the large spectrum of possible perovskites is also suited for a wide range of other opto-electronic applications. As such, lead halide perovskites have been investigated for the use in lasers, LEDs, visible-light-, UV- and X-ray-detectors, to name a few. [1, 2, 3, 4, 5, 6, 7, 8]

The main obstacle for the successful large-scale application of metal halide perovskites in solar cells is the limited stability [9, 10, 11] and the use of lead, especially when regarding the most investigated organic-inorganic hybrid perovskites such as MAPbI₃. The search for more stable alternatives has led to the investigation of fully inorganic perovskites. [12, 13] CsPbI₃, for example, shows a significantly increased thermal stability. [14, 15] However, it still contains lead and holds its own challenges, as CsPbI₃ tends to convert into a high-band-gap, non-perovskites phase when exposed to air. [16, 17]

These overall promising results, however, have motivated the quest for alternative constituents. Sn is, from a purely chemical consideration, a viable substitute for Pb, but Sn-based perovskites suffer from decreased stability due to Sn preferring the Sn⁴⁺ oxidation state over the Sn²⁺ state, further exacerbating one of the main issues. [18] A recently suggested new approach is to substitute two Pb²⁺ ions not with two other bivalent ions but with one monovalent and one trivalent ion instead, e.g. Ag¹⁺ and Bi³⁺. This leads to the formation of a so-called double perovskite with the sum formula Cs₂AgBiBr₆. First promising investigations of this material have confirmed a significant increase in stability towards moisture, light and heat. [19, 20, 21, 22, 23] Its high band gap of about 1.9 eV [23, 24] is above the ideal band gap for single junction solar cells but is still suitable for top cells in tandem

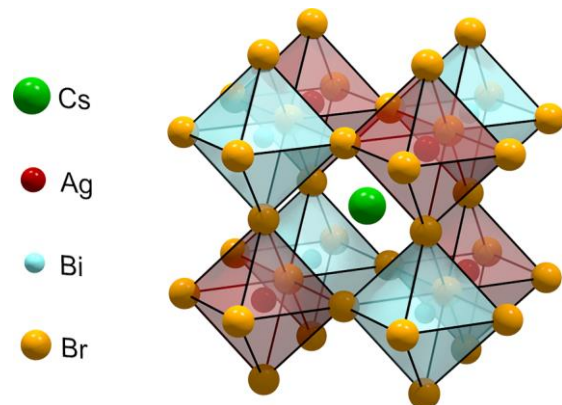


Figure 1 Sketch of the crystal structure of the double perovskite Cs₂AgBiBr₆.

applications. As a result, several attempts to use Cs₂AgBiBr₆ layers as absorbers in solar cells have very recently been launched, resulting in efficiencies of up to 2.5%. [19, 21, 25, 26, 27] Further investigations to use Cs₂AgBiBr₆ as an X-ray-detector have yielded very encouraging results, as Cs₂AgBiBr₆ exhibits a comparably high specific detectivity and fast response times. [6, 7, 8] As a direct X-ray-detector it could be a viable alternative to state-of-the-art Se-based devices as it could potentially reduce both material costs and the dosage of X-rays required during image acquisition. However, most research covering Cs₂AgBiBr₆ perovskites focuses on layers prepared via spin coating, which is a method that is inherently difficult to scale up and where large amounts of the precursor solution are wasted in the process. The publications that investigated vacuum deposited films used a sequential deposition method followed by an annealing step in air under ambient pressure or in a low pressure environment. [19, 21, 25, 31] Air annealing might induce the formation of a BiOBr secondary phase [31], which in turn can deteriorate the overall film quality. Here we present a simple, simultaneous co-evaporation process followed by a mild annealing yielding smooth and

homogenous $\text{Cs}_2\text{AgBiBr}_6$ layers, with the complete process taking place in an uninterrupted high vacuum. The morphology and microstructure of the resulting films are investigated via transmission electron microscopy (TEM). $\text{Cs}_2\text{AgBiBr}_6$ double perovskite layers are further processed to solar cells in the regular n-i-p structure with $\text{TiO}_2/\text{C}_{60}$ and spiro-OMeTAD as electron and hole selective contacts, respectively. The performance of solar cells with these lead-free perovskite absorbers is evaluated and compared to co-evaporated MAPbI_3 absorbers.

2 EXPERIMENTAL PROCEDURE

The $\text{Cs}_2\text{AgBiBr}_6$ layers were prepared via co-evaporation in a vacuum chamber under a base pressure of $2 \cdot 10^{-5}$ mbar. The precursors CsBr (380 °C), AgBr (500 °C) and BiBr_3 (100 °C) were evaporated simultaneously onto the unheated substrate. After the deposition of the precursors, the substrate was heated to 250 °C, kept at that temperature for 30 min and was then allowed to cool down. To prepare the MAPbI_3 layers, MAI (110 °C) and PbI_2 (320 °C) were co-evaporated onto a substrate at room temperature. The layer was subsequently annealed to 100 °C for 10 min on a hotplate in a nitrogen-filled glovebox.

A cross-sectional TEM lamella was prepared by focused ion beam (FIB) combined with SEM using a Dual-FIB/SEM FEI Versa 3D. Subsequently, transmission electron microscopy (TEM) and energy-dispersive X-ray spectroscopy (EDX) were carried out by use of a TEM/STEM FEI TecnaiG2 F20. The TEM analysis was done one day after preparation of the lamella and in the meantime the lamella was stored in a nitrogen flooded chamber.

To prepare the solar cells, FTO substrates were first cleaned in an ultrasonic bath using first a 2 % Hellmanex solution, followed by isopropyl alcohol, followed by acetone, for 30 min each. Then, a solution of titanium diisopropoxide bis(acetylacetonate) in ethanol (2.5 vol%) was spin coated (30 s at 3000 rpm) on top of the substrates. To form a compact TiO_2 layer, the substrates were subsequently annealed for 1 h in air at 500 °C. Afterwards, the samples were placed inside the vacuum chamber, which was evacuated to a pressure of roughly $2 \cdot 10^{-5}$ mbar. A layer of C_{60} (10 - 15 nm) was thermally evaporated (370 °C) onto the unheated substrates before depositing the perovskite on top. After the perovskite preparation was finished, spiro-OMeTAD was spin coated following a recipe from Saliba et al. [32] and the samples were left under a dry air atmosphere over night to ensure the lithium doping of the layer. To prepare the back contact, gold was thermally evaporated on top of the solar cells in a vacuum chamber. The active solar cell area was 9.6 mm² and during the JV-measurements the solar cells were illuminated with a simulated solar spectrum using a halogen lamp and a light intensity of approximately 100 mW/cm².

3 RESULTS

The simultaneous co-evaporation of CsBr, BiBr_3 and AgBr with subsequent annealing at 250°C resulted in smooth, slightly transparent films of yellow colour. A top view of a $\text{Cs}_2\text{AgBiBr}_6$ layer that was grown on glass was obtained using a scanning electron microscope (SEM) and is depicted in Figure 2. The image shows large grains with

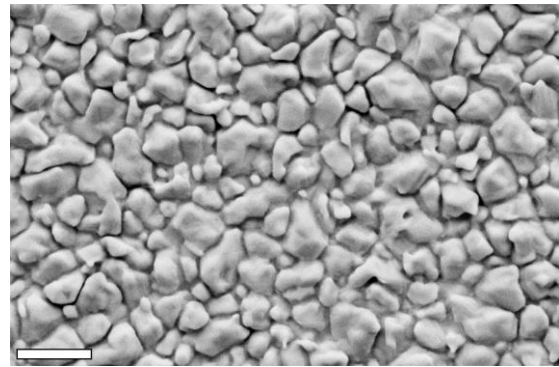


Figure 2 SEM image of a $\text{Cs}_2\text{AgBiBr}_6$ layer grown on glass. The bar indicates a length of 1 μm .

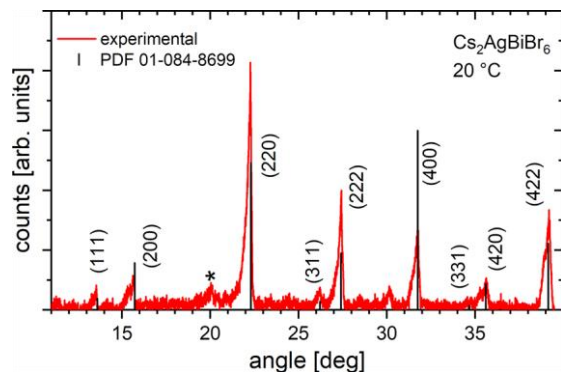


Figure 3 XRD scan of a $\text{Cs}_2\text{AgBiBr}_6$ perovskite layer on glass. The asterisk indicates the K_{β} peak of the (220) diffraction.

a size in the order of roughly 0.5 to 0.8 μm . Figure 3 shows an X-ray diffractogram (XRD) of the same film, confirming the successful synthesis of the $\text{Cs}_2\text{AgBiBr}_6$ double perovskite. The main diffraction peaks of $\text{Cs}_2\text{AgBiBr}_6$ are labelled with the indices of the corresponding lattice plains. A calculated reference pattern for $\text{Cs}_2\text{AgBiBr}_6$ which is based on the PDF reference with No. PDF-01-084-8699 is included for comparison. All peaks can be attributed to $\text{Cs}_2\text{AgBiBr}_6$, except one low intensity peak at roughly 30.1°, which is associated with a small amount of a remaining $\text{Cs}_3\text{Bi}_2\text{Br}_9$ secondary phase.

Standard MAPbI_3 solar cells in the conventional n-i-p architecture (FTO/ $\text{TiO}_2/\text{C}_{60}$ /Perovskite/spiro-OMeTAD/Au) were prepared by co-evaporating MAI and PbI_2 to form the absorbing perovskite layer as described in the experimental section. Working solar cells with co-evaporated MAPbI_3 perovskite absorbers and efficiencies between 6 - 10 % were obtained. Hysteresis effects that influence the shape of the JV-curve depending on the scan direction were observed, mainly affecting the fill factor of the devices. JV-curves in ascending and descending scan directions are depicted in Figure 4.

Co-evaporated $\text{Cs}_2\text{AgBiBr}_6$ layers were also implemented as absorbers in the same layer configuration. The results of the JV-measurements of a $\text{Cs}_2\text{AgBiBr}_6$ -based solar cell are shown in Figure 6. These solar cells show a slightly higher voltage of 1010 mV, as would be expected due to the higher band gap, and a reasonable fill factor of 67.8% in the descending scan direction. However, the short circuit current density is less than 10 times smaller ($< 1 \text{ mA/cm}^2$) compared to the MAPbI_3 -based solar cells, resulting in poor power conversion efficiencies below 1 %. To gain further insight into the

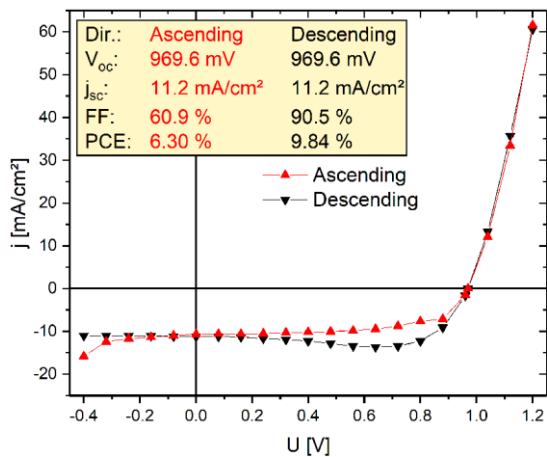


Figure 4 JV-curve of a solar cell with an MAPbI₃ absorber layer.

film morphology and how it might interact with adjacent layers, a TEM-analysis with supplementary EDX was conducted. A TEM-image of a cross section of a complete Cs₂AgBiBr₆ solar cell is presented in Figure 5. According to these results, the thickness of the Cs₂AgBiBr₆ layer is around 1 μm. Large crystallites with grains extending over the whole layer thickness can be clearly distinguished. EDX analysis indicated that the crystallites contain Cs, Ag, Bi and Br in the expected amounts for the double perovskite.

Below the crystallites a seemingly amorphous matrix phase can be observed. This matrix phase between the TiO₂ and the perovskite shows an absence of Ag, a high C content and a high concentration of voids. A likely explanation for these voids is a surplus of BiBr₃ that was not fully incorporated into the perovskite before annealing. Since BiBr₃ in high vacuum sublimates well before the annealing temperature of 250 °C is reached, any BiBr₃ that was not incorporated into the crystal structure can be expected to leave the film, leaving behind voids. In addition, the C₆₀ might have resublimated during annealing and is found to be spread around inside the matrix phase, presumably lining the insides of the observed voids. In accordance with the XRD analysis, the amorphous and silver poor matrix is most likely a residual Cs₃Bi₂Br₉ secondary phase. With the current results it cannot yet be determined whether these phenomena are intrinsic to the preparation process or if the growth on C₆₀ plays a large role in the formation of the observed morphology.

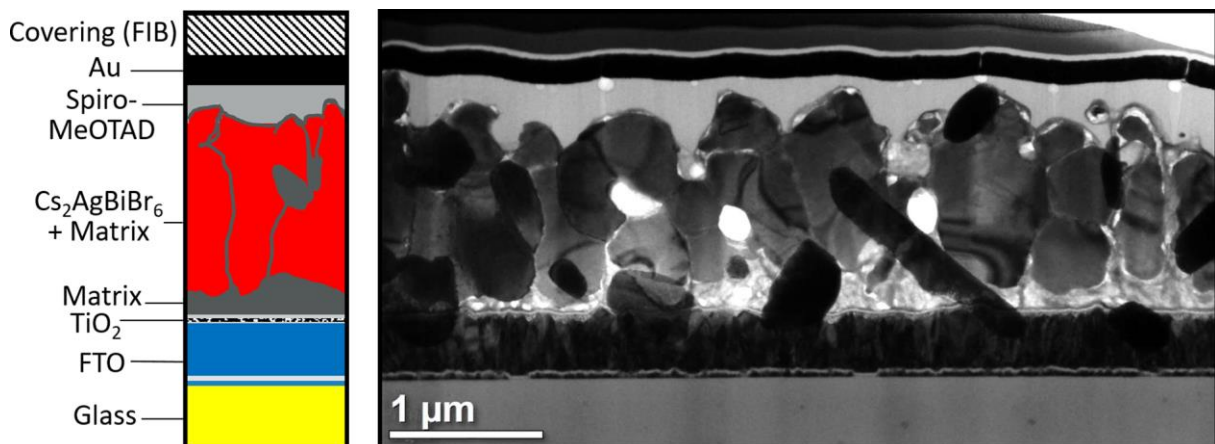


Figure 5 TEM image of a cross section of a Cs₂AgBiBr₆ solar cell with a schematic depiction of the layer stack.

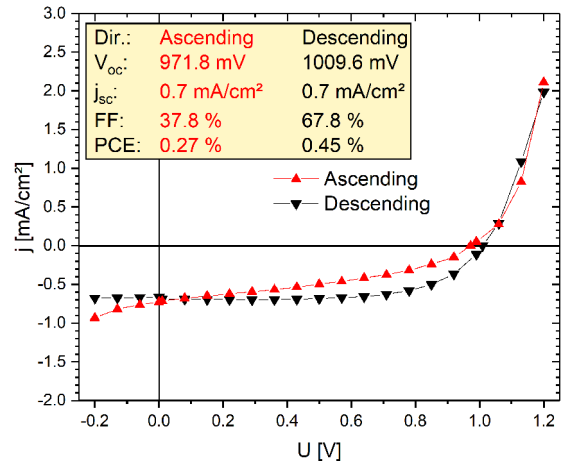


Figure 6 JV-curve of a solar cell with a Cs₂AgBiBr₆ absorber layer.

4 DISCUSSION

The solar cell trials with the Cs₂AgBiBr₆ absorber yielded functional, rectifying diodes in a conventional perovskite solar cell configuration. However, JV-measurements under illumination reveal a poor performance with reasonable voltage and fill factor, but a very low photo-current and a PCE of 0.5 % (descending scan direction). Using an MAPbI₃ absorber in the same configuration resulted in a PCE of 9.8 % (descending scan direction) and a significantly larger photo-current. Our results on Cs₂AgBiBr₆ solar cells are consistent with existing literature on the subject, which show similar voltages, but also a very low current for this type of solar cell. [19, 21, 25, 26, 27]

Solar cells made with this perovskite have not yet exceeded a PCE of 2.5 % [25, 27], which is comparably low, even when regarding the high and indirect band gap of the material. [28] There are multiple possible factors that could contribute to the observed results: 1: Inherent properties of the material, such as an indirect band gap, which lowers absorption [28], and a comparably high exciton binding energy, which renders effective charge extraction more difficult. [29] 2: Effects that occur within the material under illumination, such as light-induced phonons that lead to electron scattering due to a significant Fröhlich coupling. [29, 30] 3: We used a cell design with contact layers that were still unoptimized, which, even in the MAPbI₃ case, showed a comparably low photo-current. These contact layers have also not been adjusted

to Cs₂AgBiBr₆ and might therefore not be fully compatible with this higher band gap absorber. This could, for example, result in a poor band alignment. 4: The observed matrix side-phase could have a negative impact but is unlikely to be the main reason for the poor performance.

Further analysis is necessary to clearly answer the question, if the observed limitations are intrinsic to the new absorber material or if they could be mitigated through optimized device configurations.

5 CONCLUSIONS

In conclusion, we successfully synthesized Cs₂AgBiBr₆ perovskite layers in a dry, all-vacuum co-evaporation process. We obtained homogeneous layers with good crystallinity, large crystallites and good coverage. Trials with solar cells using unoptimized contact layers showed a PCE of 9.8 % (descending scan direction) for MAPbI₃-based solar cells and a low PCE of 0.5 % (descending scan direction) for the Cs₂AgBiBr₆-based solar cells. The main limitation of the Cs₂AgBiBr₆-based solar cells was a very low short circuit current density. These results are in line with the results of other groups, which show subpar performance of Cs₂AgBiBr₆ absorbers with low photocurrents. [19, 21, 25, 26, 27] While some improvement can be expected by further optimization of the contact layers and the co-evaporation process with respect to secondary phases, our results indicate a subpar solar harvesting performance of the Cs₂AgBiBr₆ perovskite. However, a scalable process for homogenous Cs₂AgBiBr₆ thin films with large grains is presented, bearing promise for opto-electronic applications that do not rely on the absorption of photons within the visible light spectrum, such as X-ray- or UV-detectors.

5 ACKNOWLEDGEMENTS

Financial support from the German Federal Ministry of Research and Education (BMBF) under contract number 03EK3570B (StrukturSolar II) is gratefully acknowledged.

6 REFERENCES

- [1] Y. Fu, H. Zhu, C. C. Stoumpos, Q. Ding, J. Wang, M. G. Kanatzidis, X. Zhu and S. Jin, "Broad Wavelength Tunable Robust Lasing from Single-Crystal Nanowires of Cesium Lead Halide Perovskites (CsPbX, X = Cl, Br, I)," *ACS Nano*, vol. 10, pp. 7963-7972, 7 2016.
- [2] J. Chen, S. Zhou, S. Jin, H. Li and T. Zhai, "Crystal organometal halide perovskites with promising optoelectronic applications," *Journal of Materials Chemistry C*, vol. 4, pp. 11-27, 18 12 2015.
- [3] S. W. Eaton, M. Lai, N. A. Gibson, A. B. Wong, L. Dou, J. Ma, L.-W. Wang, S. R. Leone and P. Yang, "Lasing in robust cesium lead halide perovskite nanowires," *Proceedings of the National Academy of Sciences*, vol. 113, pp. 1993-1998, 23 2 2016.
- [4] L. Xi, C. B. Boothroyd, T. Salim, S. Borghardt, Y. Ming Lam and B. E. Kardynał, "Facile in situ synthesis of stable luminescent organic-inorganic lead halide perovskite nanoparticles in a polymer matrix," *Journal of Materials Chemistry C*, vol. 5, pp. 7207-7214, 2017.
- [5] Y. Tang, M. Liang, B. Chang, H. Sun, K. Zheng, T. Pullerits and Q. Chi, "Lead-free double halide perovskite Cs₃BiBr₆ with well-defined crystal structure and high thermal stability for optoelectronics," *Journal of Materials Chemistry C*, 2019.
- [6] L.-Z. Lei, Z.-F. Shi, Y. Li, Z.-Z. Ma, F. Zhang, T.-T. Xu, Y.-T. Tian, D. Wu, X.-J. Li and G.-T. Du, "High-efficiency and air-stable photodetectors based on lead-free double perovskite Cs₂AgBiBr₆ thin films," *Journal of Materials Chemistry C*, vol. 6, pp. 7982-7988, 2018.
- [7] J. A. Steele, W. Pan, C. Martin, M. Keshavarz, E. Debroye, H. Yuan, S. Banerjee, E. Fron, D. Jonckheere, C. W. Kim, W. Baekelant, G. Niu, J. Tang, J. Vanacken, M. V. Auweraer, J. Hofkens and M. B. J. Roeffaers, "Photophysical Pathways in Highly Sensitive Cs₂AgBiBr₆ Double-Perovskite Single-Crystal X-Ray Detectors," *Advanced Materials*, vol. 30, p. 1804450, 9 2018.
- [8] B. Yang, W. Pan, H. Wu, G. Niu, J.-H. Yuan, K.-H. Xue, L. Yin, X. Du, X.-S. Miao, X. Yang, Q. Xie and J. Tang, "Heteroepitaxial passivation of Cs₂AgBiBr₆ wafers with suppressed ionic migration for X-ray imaging," *Nature Communications*, vol. 10, 4 2019.
- [9] A. Dualeh, P. Gao, S. I. Seok, M. K. Nazeeruddin and M. Grätzel, "Thermal Behavior of Methylammonium Lead-Trihalide Perovskite Photovoltaic Light Harvesters," *Chemistry of Materials*, vol. 26, pp. 6160-6164, 10 2014.
- [10] R. Sheng, X. Wen, S. Huang, X. Hao, S. Chen, Y. Jiang, X. Deng, M. A. Green and A. W. Y. Ho-Baillie, "Photoluminescence characterisations of a dynamic aging process of organic-inorganic CH₃NH₃PbBr₃ perovskite," *Nanoscale*, vol. 8, pp. 1926-1931, 2016.
- [11] J. Yang, B. D. Siempelkamp, D. Liu and T. L. Kelly, "Investigation of CH₃NH₃PbI₃ Degradation Rates and Mechanisms in Controlled Humidity Environments Using in Situ Techniques," *ACS Nano*, vol. 9, pp. 1955-1963, 2 2015.
- [12] M. Kulbak, D. Cahen and G. Hodes, "How Important Is the Organic Part of Lead Halide Perovskite Photovoltaic Cells? Efficient CsPbBr₃ Cells," *The Journal of Physical Chemistry Letters*, vol. 6, pp. 2452-2456, 2 7 2015.
- [13] W. Ahmad, J. Khan, G. Niu and J. Tang, "Inorganic CsPbI₃ Perovskite-Based Solar Cells: A Choice for a Tandem Device," *Solar RRL*, vol. 1, p. 1700048, 6 2017.
- [14] R. E. Beal, D. J. Slotcavage, T. Leijtens, A. R. Bowring, R. A. Belisle, W. H. Nguyen, G. F. Burkhard, E. T. Hoke and M. D. McGehee, "Cesium Lead Halide Perovskites with Improved Stability for Tandem Solar Cells," *The Journal of Physical Chemistry Letters*, vol. 7, pp. 746-751, 2 2016.
- [15] T. Burwig, W. Fränzel and P. Pistor, "Crystal Phases and Thermal Stability of Co-evaporated CsPbX₃ (X = I, Br) Thin Films," *The Journal of Physical Chemistry Letters*, vol. 9, pp. 4808-4813, 8 2018.

- [16] C. H. R. K. N. MOLLER, "Crystal Structure and Photoconductivity of Cesium Plumbobalides," *Nature*, vol. 182, pp. 1436-1436, 11 1958.
- [17] G. E. Eperon, G. M. Paternò, R. J. Sutton, A. Zampetti, A. A. Haghighirad, F. Cacialli and H. J. Snaith, "Inorganic caesium lead iodide perovskite solar cells," *Journal of Materials Chemistry A*, vol. 3, pp. 19688-19695, 29 9 2015.
- [18] P.-P. Sun, Q.-S. Li, L.-N. Yang and Z.-S. Li, "Theoretical insights into a potential lead-free hybrid perovskite: substituting Pb²⁺ with Ge²⁺," *Nanoscale*, vol. 8, pp. 1503-1512, 2016.
- [19] M. Wang, P. Zeng, S. Bai, J. Gu, F. Li, Z. Yang and M. Liu, "High-Quality Sequential-Vapor-Deposited Cs₂AgBiBr₆ Thin Films for Lead-Free Perovskite Solar Cells," *Solar RRL*, vol. 2, p. 1800217, 9 2018.
- [20] L. Dong, S. Sun, Z. Deng, W. Li, F. Wei, Y. Qi, Y. Li, X. Li, P. Lu and U. Ramamurty, "Elastic properties and thermal expansion of lead-free halide double perovskite Cs₂AgBiBr₆," *Computational Materials Science*, vol. 141, pp. 49-58, 1 2018.
- [21] C. Wu, Q. Zhang, Y. Liu, W. Luo, X. Guo, Z. Huang, H. Ting, W. Sun, X. Zhong, S. Wei, S. Wang, Z. Chen and L. Xiao, "The Dawn of Lead-Free Perovskite Solar Cell: Highly Stable Double Perovskite Cs₂AgBiBr₆ Film," *Advanced Science*, vol. 5, p. 1700759, 12 2017.
- [22] F. Igbari, Z.-K. Wang and L.-S. Liao, "Progress of Lead-Free Halide Double Perovskites," *Advanced Energy Materials*, vol. 9, p. 1803150, 2 2019.
- [23] A. H. Slavney, T. Hu, A. M. Lindenberg and H. I. Karunadasa, "A Bismuth-Halide Double Perovskite with Long Carrier Recombination Lifetime for Photovoltaic Applications," *Journal of the American Chemical Society*, vol. 138, pp. 2138-2141, 24 2 2016.
- [24] M. R. Filip, S. Hillman, A. A. Haghighirad, H. J. Snaith and F. Giustino, "Band Gaps of the Lead-Free Halide Double Perovskites Cs₂BiAgCl₆ and Cs₂BiAgBr₆ from Theory and Experiment," *The Journal of Physical Chemistry Letters*, vol. 7, pp. 2579-2585, 6 2016.
- [25] F. Igbari, R. Wang, Z.-K. Wang, X.-J. Ma, Q. Wang, K.-L. Wang, Y. Zhang, L.-S. Liao and Y. Yang, "Composition Stoichiometry of Cs₂AgBiBr₆ Films for Highly Efficient Lead-Free Perovskite Solar Cells," *Nano Letters*, 2 2019.
- [26] W. Gao, C. Ran, J. Xi, B. Jiao, W. Zhang, M. Wu, X. Hou and Z. Wu, "High-Quality Cs₂AgBiBr₆ Double Perovskite Film for Lead-Free Inverted Planar Heterojunction Solar Cells with 2.2% Efficiency," *ChemPhysChem*, vol. 19, pp. 1696-1700, 5 2018.
- [27] E. Greul, M. L. Petrus, A. Binek, P. Docampo and T. Bein, "Highly stable, phase pure Cs₂AgBiBr₆ double perovskite thin films for optoelectronic applications," *Journal of Materials Chemistry A*, vol. 5, pp. 19972-19981, 2017.
- [28] C. N. Savory, A. Walsh and D. O. Scanlon, "Can Pb-Free Halide Double Perovskites Support High-Efficiency Solar Cells?," *ACS Energy Letters*, vol. 1, pp. 949-955, 10 2016.
- [29] R. Kentsch, M. Scholz, J. Horn, D. Schlettwein, K. Oum and T. Lenzer, "Exciton Dynamics and Electron-Phonon Coupling Affect the Photovoltaic Performance of the Cs₂AgBiBr₆ Double Perovskite," *The Journal of Physical Chemistry C*, vol. 122, pp. 25940-25947, 10 2018.
- [30] J. A. Steele, P. Puech, M. Keshavarz, R. Yang, S. Banerjee, E. Debroye, C. W. Kim, H. Yuan, N. H. Heo, J. Vanacken, A. Walsh, J. Hofkens and M. B. J. Roeffaers, "Giant Electron-Phonon Coupling and Deep Conduction Band Resonance in Metal Halide Double Perovskite," *ACS Nano*, vol. 12, pp. 8081-8090, 8 2018.
- [31] M. Pantaler, C. Fettkenhauer, H. L. Nguyen, I. Anusca and D. C. Lupascu, "Deposition routes of Cs₂AgBiBr₆ double perovskites for photovoltaic applications," *MRS Advances*, vol. 3, pp. 1819-1823, 2018.
- [32] M. Saliba, J.-P. Correa-Baena, C. M. Wolff, M. Stollerfoht, N. Phung, S. Albrecht, D. Neher and A. Abate, "How to Make over 20% Efficient Perovskite Solar Cells in Regular (n-i-p) and Inverted (p-i-n) Architectures," *Chemistry of Materials*, vol. 30, pp. 4193-4201, 6 2018.

Closing Discussion

Cs₂AgBiBr₆ films were successfully prepared using vacuum co-evaporation and implemented in solar cell devices. The films exhibited a morphology with excellent coverage and no visible pin holes, however, the sample whose cross section was analyzed using the TEM showed very large voids in the bulk of the absorber. As stated in the paper, a likely cause of this could be the sublimation of BiBr₃ before it is incorporated into the Cs₂AgBiBr₆ layer. To counter this, and adjustment of the annealing temperature can be considered. Whether it should be an adjustment towards higher or lower temperatures, depends on whether it is the sublimation of BiBr₃ or the formation of Cs₂AgBiBr₆ that is more thermally activated. However, the usable temperature range for such an adjustment is quite narrow. As our paper on the Cs₂AgBiBr₆ ramp experiment shows, the perovskite formed at 230 °C and decomposed at 300 °C [Bu3]. A more applicable way of combating a BiBr₃ void formation would be to use a surplus of BiBr₃ for the initial deposition. Such a surplus has been reported as beneficial for the formation of Cs₂AgBiBr₆ by other groups [50, 169]. A counter against the claim that these voids were formed by a loss of BiBr₃ is the fact that the EDX measurements (see reference [Bu3]) showed a composition that was in line with the expected Cs₂AgBiBr₆, with a slight Cs surplus. Void formation due to loss of BiBr₃ would lead to a severe deficiency of Bi in the resulting layer, especially when considering the size of the voids. It was also observed that the center sample tends to form more voids than the samples further out away from the center of the substrate holder. Since the outer samples are closer to the heating element, they are exposed to a higher temperature than the center one and they might also experience a slightly different precursor flux compared to the central sample. With a PCE of only 0.5 %, while a comparable MAPbI₃ solar cell achieved 9.8 %, there is a strong indication that this material might not be suitable for the use case of a photovoltaic absorber. Multiple research groups have prepared solar cells with Cs₂AgBiBr₆ [168, 180, 169, 181, 171], but the highest PCE that has been achieved, as of this time, was 2.84 % [182]. The analyses by Savory et al. and Kentsch et al. deliver a sound reasoning why devices with a Cs₂AgBiBr₆ absorber show such low current densities [172, 183]. In spite of this, their inherent stability and comparative ease of preparation make them a prime candidate for the use in high energy photon and X-Ray detectors [9, 10, 11, 17].

5.3 Influence of MAI Onset on Growth of MAPbI₃

Preliminary Discussion

Reference: [Bu7]

There are a lot of aspects pertaining to the vacuum-based synthesis of perovskite thin films that are still poorly understood. It is well accepted by now, that the preparation method of a perovskite can have a profound impact on its properties, for instance its stability. But even small changes in the perovskites preparation conditions, like the difference between the onset of the MAI and PbI₂ evaporation in co-evaporated films, can significantly influence the properties of the resulting material.

Closing Discussion

Delaying the onset of MAI influx onto the substrate relative to the PbI₂ influx lead to a substantial increase in the PCE of resulting solar cells from 3% (simultaneous onset) to around 14% (MAI delayed by 8 min). This indicates that the initial seed layer formed by the PbI₂ is beneficial to the quality of the resulting MAPbI₃ film. However, there seems to be an optimum delay, as the layer prepared with a longer MAI onset delay of 16 min showed a PCE of 12%. In addition to the onset time of MAI, the increase in chamber pressure that results from the evaporation of MAI has also been found to be a useful indicator for the performance of the resulting solar cells. A pressure of 7.5×10^{-5} mbar has resulted in the best solar cells with a PCE of 14%, while a lower pressure of 4×10^{-5} mbar achieved 13% and a higher pressure of 1.5×10^{-4} mbar resulted in non-functional solar cells.

In summary, the relative onset times of the evaporation of MAI to PbI₂ and the increase in chamber pressure due to MAI evaporation are two often overlooked parameters in the preparation of co-evaporated MHP solar cells. This contribution has successfully shown for the first time that both the monitoring and careful control of these two factors is of paramount importance for achieving well performing MAPbI₃ solar cells.

5.4 Additional Decomposition Experiments

Additional experiments on the preparation and thermal decomposition have been conducted on the compounds CsPbCl_3 , CsSnBr_3 and FAPbBr_3 . These experiments share the same general approach, where the sample was first prepared using vacuum co-evaporation, followed by a heating ramp until full thermal decomposition. For the sake of conciseness, they are not elaborated on in the same detail as the other trials. Instead, the details on the processes can be found in appendix A.3: Table A.2 shows the precursors used and the respective crucible temperatures, the resulting film's thickness and the temperature ramp speed of the decomposition experiments. The appendix also contains $\theta - 2\theta$ scans of the fully prepared layers and colormaps of the decomposition processes.

5.5 Comparison of Thermal Stabilities

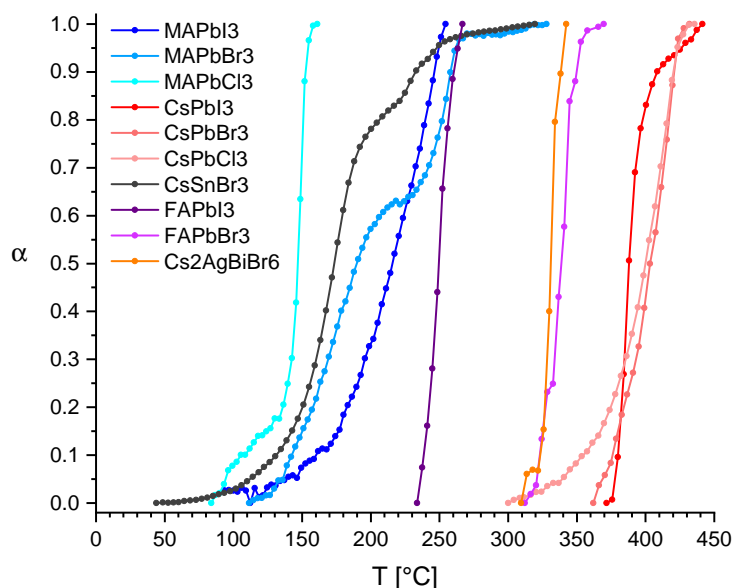


Figure 5.1: Comparison of the thermal stability of a variety of metal-halide perovskites. The data was obtained from temperature ramp experiments and the plot relates the temperature at a point in time with the extent of conversion at that temperature.

An efficient way to compare the thermal stabilities of different perovskites is to thermally decompose them using temperature ramp experiments. As has been discussed in section 2.4, calculating a kinetic triplet from non-isothermal data alone can lead to highly ambiguous results. However, as long as the experimental conditions between the non-isothermal trials are kept the same, one can still make comparative assessments of the thermal stabilities and decomposition temperatures of different perovskites. An overview of the results of the temperature ramp decomposition experiments is depicted in figure 5.1. It shows the decomposition as the extent of conversion α over the temperature. As has been discussed in section 2.1.3, the MA is likely the limiting factor of the stability of the MAPbX_3 -perovskites. This seems to be confirmed by these results, given that the MHPs containing MA are less stable than the FA and Cs based MHPs, with the exception of CsSnBr_3 . All CsPbX_3 perovskites have reached $\alpha = 0.5$ at roughly 400°C and therefore show a very similar stability when compared to one another. Their thermal stability is also notably higher than that of all other perovskites that have been analyzed in this work. This seems plausible, as Cs is not an organic molecule and that, as an element, it cannot itself decompose. Another likely factor in the lower stability of the perovskites with organic cations is the relatively weak hydrogen bonding between the organic molecule and the PbX_3 cage. This already weak bonding seems to further diminish for elevated temperatures [184]. An exchange of the Pb with either Sn or Ag and Bi decreased the thermal stability notably. The lowering in stability in the Sn-case might be due to the fact that in order for Sn to be properly incorpo-

rated into the perovskite's crystal structure, it needs to exist in the oxidation state of Sn^{2+} , yet Sn^{2+} has a high susceptibility to further oxidize into Sn^{4+} [185], in which case the perovskite's structure cannot be maintained. According to Oranskaia et al. the increased stability that FA based perovskites show compared to MA based ones lies in the FA molecule's larger volume and stronger binding to the perovskites halides [186]. The double perovskite $\text{Cs}_2\text{AgBiBr}_6$ shows a thermal stability comparable to FAPbBr_3 . This is lower compared to the CsPbX_3 perovskites, but still significantly above CsSnBr_3 .

Chapter 6

Summary and Outlook

Metal-halide perovskites (MHPs) are a promising material for a large variety of optoelectronic applications. Due to their roots in the realm of organic solar cells and the ease of setup and usage of spin coating systems, most current research focuses on solution processed films. However, co-evaporation is a more scalable preparation method and, as has been shown by other researchers, can produce more robust films [14]. This is especially relevant, given that a lack of stability is the main concern regarding a large-scale application of perovskites for solar cell absorbers. Due to the recency of this materials' attention in photovoltaic research, there are still many open questions related to the properties of MHPs in general, and for co-evaporated thin film MHPs in particular. Thus, the main aim of this work is to contribute to the understanding of the complex phase relations and interrelations of process parameters and growth paths for co-evaporated organic-inorganic and fully inorganic metal-halide perovskite thin films. The vacuum co-evaporation chamber with in situ XRD analysis capabilities allowed for an all-vacuum preparation with simultaneous observation of the crystal structures of the emerging phases. In this way, a large variety of perovskites were examined with a focus on their growth, their response to an increase in temperature and their thermal decomposition.

Due to the fact that MAPbI₃ is the prototypical and most studied MHP, the first set of experiments focused on the MAPbX₃ system (X = I, Br, Cl). The samples were grown on glass substrates, using an all-vacuum co-evaporation process, and were then subjected to a temperature ramp. The data obtained from in situ XRD allowed to gain insights into the responses of the samples to the increase in temperature. These responses include phase changes, thermal expansion and decomposition. Notably, the MAPbI₃ perovskite started to decompose at roughly 120 °C, leaving behind PbI₂. However, the temperature of thermal decomposition, as determined by a ramp experiment, gives only a lower bound for the onset of the decomposition. An experiment using a slower temperature ramp, or an isothermal temperature regime, would likely identify a decomposition at lower temperatures. The maximum operating temperature of a solar cell is often given as around 85 °C [60], to which the observed 120 °C are concerningly close. The Br containing perovskite showed no notably increased stability and the Cl variant decomposed at even lower temperatures. This highlights that the increase in stability from solution processing to co-evaporation does not satisfactorily resolve the issue of perovskite stability in the case of the MAPbX₃ (X = I, Br, Cl) perovskites. In addition, the fact that the remainder

of the decomposition reaction is PbX_2 ($X = \text{I}, \text{Br}, \text{Cl}$) gives an indication that it might be the organic MA component that is the culprit for the low thermal stability. Experiments that converted MAPbI_3 to MAPbBr_3 by exposing MAPbI_3 to MABr vapor indicated a continuous and complete conversion of the former to the latter. The inverse conversion, from MAPbBr_3 to MAPbI_3 using MAI vapor, showed a discontinuity in the XRD peaks, which indicates that the sample became amorphous during the transition. The result of the conversion was a crystalline MAPbI_3 layer and a smaller amount of MAPbBr_3 . These results have been discussed in respect to the difference in ion radius between I and Br and the differing diffusion speed of the halides within the perovskites.

Because of the potential role of MA in the low thermal stability of the MHPs, the next set of experiments omitted MA as the cation in favor of Cs. The experiments on CsPbX_3 ($X = \text{I}, \text{Br}$) were conducted analogous to the ones on MAPbX_3 ($X = \text{I}, \text{Br}, \text{Cl}$) and the results of the temperature ramp experiments confirmed the significantly increased stability of the Cs based perovskites, with CsPbI_3 starting its decomposition at around 370°C . Furthermore, the remaining species was CsX ($X = \text{I}, \text{Br}$), indicating that the thermal stability of the Cs perovskites is limited not by the A site component, but by the PbX_3 ($X = \text{I}, \text{Br}$) system. It stands to reason then, that an exchange of this B site component would modify the thermal stability, either upward or downward. Moreover, exchanging lead for a non-toxic alternative might decrease health concerns. This led to a consideration of $\text{Cs}_2\text{AgBiBr}_6$ as the next candidate perovskite.

Exchanging the B site ion Pb^{2-} with both Ag^- and Bi^{3-} forms $\text{Cs}_2\text{AgBiBr}_6$. The promise of this material is the combination of the high stability of the Cs based perovskites with the benefit of being lead free, as Sn based alternatives, even CsSnBr_3 , show a very low stability due to the propensity of Sn^{2+} to form Sn^{4+} [185]. The preparation of $\text{Cs}_2\text{AgBiBr}_6$ followed the same procedure as for the other perovskites, which is the simultaneous co-evaporation of the precursor materials, but included an additional annealing step to 250°C , which is necessary to allow the precursors to react and form the double perovskite. The temperature ramp experiment showed that, interestingly, the perovskite started its decomposition at roughly 300°C by losing BiBr_3 , which is only 50°C higher than the temperature needed for its preparation. This places the thermal stability of the material in between the MA and the Cs perovskites. While the thermal stability seems high enough for the use as a solar cell absorber material, experiments with $\text{Cs}_2\text{AgBiBr}_6$ -based solar cells have shown a very low performance, limited mainly by a low photocurrent [172, 183, 187]. The best PCE achieved to this date using this material was 2.84% [182]. However, the works of other groups have shown very promising results for this material for the use in high energy photon detectors [9, 10, 11, 17].

The isothermal decomposition experiments yielded results on the activation energy E and the frequency factor A of the thermal decomposition reaction. The values obtained for MAPbI_3 were $E = 110(15) \text{ kJ mol}^{-1}$ and $\ln A = 19(1)$ and the values for FAPbI_3 were $E = 125.1(84) \text{ kJ mol}^{-1}$ and $\ln A = 21.1(19)$. When taking together E and A , these results imply an overall higher thermal stability of FAPbI_3 when compared to MAPbI_3 , which leads to an increased decomposition temperature by roughly 45°C . This is illustrated in Figure 10 in reference [Bu5].

All perovskites with an organic A component decomposed by losing said component, leaving the Pb halide behind. For the purely inorganic perovskites with Cs on their A-site, it was the PbX_2 that left the film first, leaving CsX behind. In the case of $\text{Cs}_2\text{AgBiBr}_6$, the BiBr_3 was lost

first, followed by AgBr, leaving CsBr behind. Overall, the main deciding factor for the thermal stability of an ABX_3 MHP seems to be the A-site and B-site component. When keeping the same B and X anions and varying the A cation, the stability is highest for Cs based perovskites, followed by FA, followed by MA. When keeping the same A and X components and varying B, Pb-based MHP where the most stable, followed by AgBi, followed by Sn. The halide X seems to have the least impact on stability, but a tentative assessment can be made from the data: When keeping the same A and B components and varying X, I and Br based perovskites exhibit similar stability, with the exception of $FAPbX_3$ ($X = I, Br$), where $FAPbBr_3$ decomposed at significantly higher temperatures. Cl based perovskites showed a tendency towards a slightly lower thermal stability compared to their I and Br variations.

In summary, a large variety of ABX_3 type perovskites and one $AB^1B^2X_3$ type perovskite have been analyzed with focus on their preparation via co-evaporation and their thermal stability. The in situ XRD system allowed to determine the phase formation pathways for the synthesis reactions. Process parameters have been found that allow for the single-phase growth of all studied perovskites, except $Cs_2AgBiBr_6$, where a potential $Cs_3Bi_2Br_9$ secondary phase could not be excluded. All perovskites, except $Cs_2AgBiBr_6$, could be synthesized at room temperature. The comparison of MHPs with differing A, B and X components allows for in depth insights into how the different constituents of the perovskite influence the stability of the resulting compound. Moreover, the results of the calculation of the activation energy E and the pre-exponential factor A of the thermal decomposition reaction have been shown to enable a more meaningful comparison of the thermal stability of different material systems. Due to the flexibility of the reaction kinetical methods, we suggest that further research should incorporate approaches that result in values for E and A to enhance comparability and thus help to build a consistent and interlinked knowledge base for further work on MHPs. Now that a large amount of data has been gathered on a variety of ABX_3 perovskites and one $AB^1B^2X_3$ perovskite, the ground is laid for subsequent research to focus on the following aspects:

- Expanding the reaction kinetical approach to the other perovskites that were analyzed in this work
- Growth and properties of perovskites with mixed A, B and X constituents
- Influence of variations in the preparation conditions of the perovskites, such as the substrate temperature during growth and after-growth-annealing temperatures, or delaying the temporal onset of certain precursors, as has already been shown in reference [Bu7]
- Influence of the substrate material on the growth and properties of the perovskites
- Correlation of preparation conditions and XRD data with the performance of solar cells that use the perovskite as an absorber
- Full-stack preparation of solar cells within the vacuum chamber

Appendix A

Appendix

A.1 Estimation of X-ray Induced Damage

The X-ray setup uses a current of $I = 40$ mA and an acceleration voltage of $U = 35$ kV, which corresponds to a total of power of $P = 1400$ W introduced into the X-ray source. The radiative output P_{rad} of an X-ray tube with $U < 0.5$ MV can be estimated by [188]:

$$P_{rad} = k \cdot Z \cdot I \cdot U^2 \quad (\text{A.1})$$

where $k = 1.1 \cdot 10^{-9}$ is an empirically determined constant, Z is the atomic number of the target material (Cu with $Z = 29$). The resulting value is $P_{rad} \approx 1.56$ W. The overall power per area P_A introduced into the sample by the X-rays is:

$$P_A = \frac{P_{rad} \cdot \sin \theta}{4\pi r^2} \quad (\text{A.2})$$

where $\theta = 20^\circ$ is the incidence angle of the X-rays and $r = 0.4$ m is the distance of the X-ray source to the sample. The result is $P_A = 2.66 \times 10^{-5}$ W cm⁻². Over an experiment with a length of 8 h the total energy introduced per area is $E_t = 0.77$ J cm⁻². Svanström et al. found a value for the radiolysis rate constant of $k_r = 1.68 \times 10^{-18}$ cm² photon⁻¹ (see equation 3.4) [155]. Since our setup uses X-rays with a different energy distribution, we translate the value of k_r from *per photon* to *per energy*. The photon energy of 3 keV corresponds to 4.81×10^{-16} J. The value of k_r in respect to energy is therefore $k_{rE} = 3.50 \times 10^{-3}$ cm² J⁻¹. The exponential term of equation 3.4 can now be calculated: $\exp\{-k_{rE} \cdot E_t\} \approx 0.9973$.

A.2 Evaporation Temperatures for the Preparation of Various MHPs

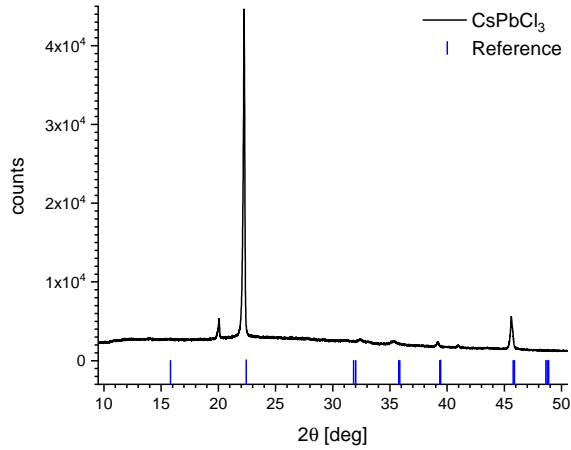
Table A.1: Crucible temperatures that were used to prepare the perovskite layers which were analyzed in this thesis.

Material	AX Prec. (T [°C])	BX ₂ Prec. (T [°C])
MAPbI ₃	MAI (110 – 130)	PbI ₂ (320)
MAPbBr ₃	MABr (130)	PbBr ₂ (300)
MAPbCl ₃	MACl (110)	PbCl ₂ (360)
CsPbI ₃	CsI (430)	PbI ₂ (300)
CsPbBr ₃	CsBr (430)	PbBr ₂ (290)
FAPbI ₃	FAI (195)	PbI ₂ (350)
Cs ₂ AgBiBr	CsBr (382)	AgBr (501) / BiBr ₃ (103)

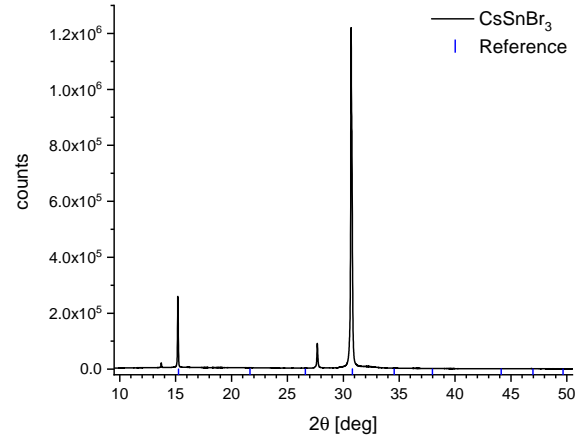
Table A.2: Crucible temperatures used in the additional experiments mentioned in section 5.4.

Material	AX Prec. (T [°C])	BX ₂ Prec. (T [°C])	Thick. [nm]	T-Ramp [°C min ⁻¹]
CsPbCl ₃	CsCl (510)	PbCl ₂ (337)	1030	4
CsSnBr ₃	CsBr (430)	SnBr ₂ (175)	700	4
FAPbBr ₃	FABr (90)	PbBr ₂ (266)	500	4

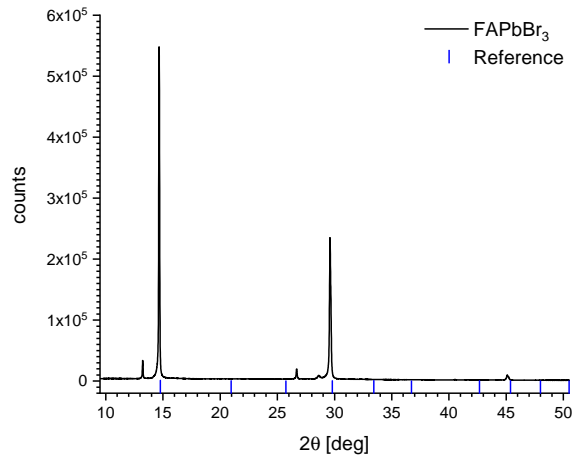
A.3 XRD Results of the Additional Experiments



(a) $\theta-2\theta$ scan of a CsPbCl₃ sample. The reference was taken from the PDF database and has the entry ID 00-018-0366.



(b) $\theta-2\theta$ scan of a CsSnBr₃ sample. The reference was taken from the PDF database and has the entry ID 04-006-8981.



(c) $\theta-2\theta$ scan of a FAPbBr₃ sample. The reference was calculated assuming a primitive cubic crystal symmetry and a lattice constant of 5.9944 Å.

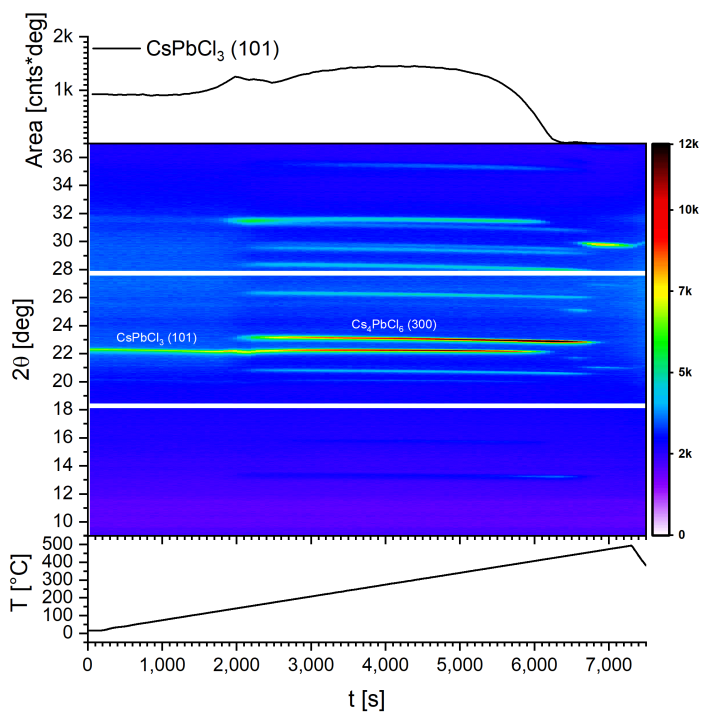


Figure A.2: Color map of the CsPbCl₃ decomposition process.

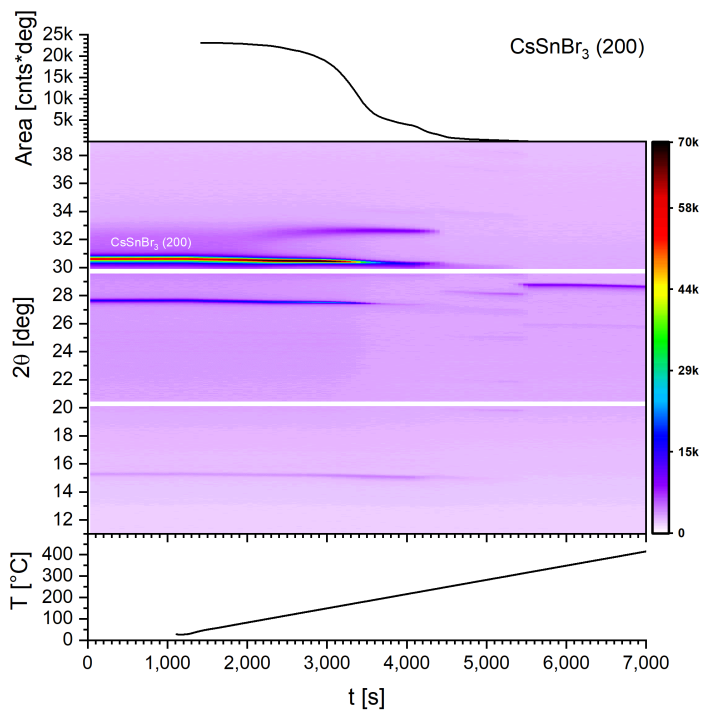


Figure A.3: Color map of the CsSnBr₃ decomposition process.

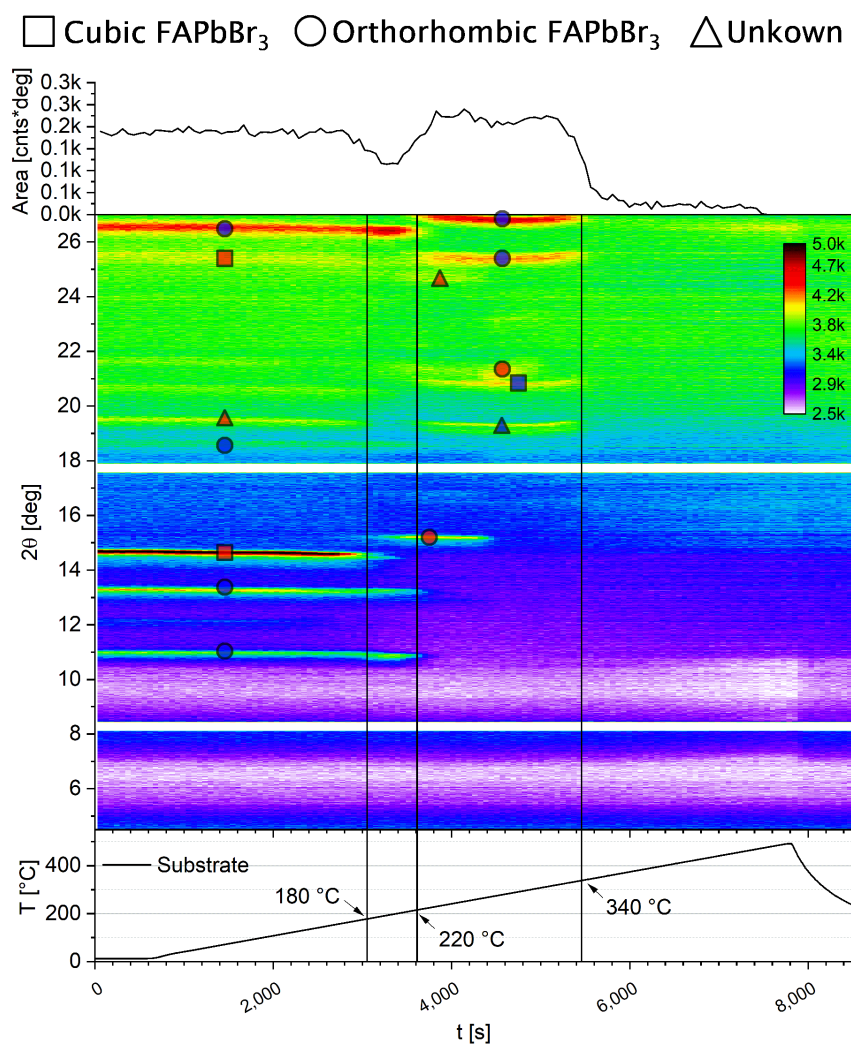


Figure A.4: Color map of the FAPbBr₃ decomposition process. This process has shown a multitude of different phases whose evolution is difficult to interpret. To get a better overview, the different phases are marked by different shapes depending on which phase would correspond to the XRD peaks: Squares denote cubic FAPbBr₃, circles denote orthorhombic FAPbBr₃ and triangles denote an unkown phase. In addition, they were marked either blue or red. The dissapperance of the first set of blue marked peaks coincides with the appearance of the second set of blue marked peaks. In the same way, the dissapperance of the first set of red marked peaks coincides with the appearance of the second set of red marked peaks.

List of Figures

2.1	a: Perovskite crystal structure with the sum formula ABX_3 . b: Double perovskite crystal structure with the sum formula $A_2B^1B^2X_6$	10
2.2	Different architectures of perovskite solar cells. a: Dye-Sensitized Solar Cell (DSSC); b: Meso-Superstructured Solar Cell (MSSC); c: Pillared Structure Solar Cell; d: Planar Heterojunction Solar Cell [113] <small>Licensed under CC BY-NC-ND: https://creativecommons.org/licenses/by-nc-nd/4.0/</small>	24
2.3	Stylized depiction of the band diagram of a p-i-n solar cell. ϵ_{BG} is the band gap of the absorber, ϵ_C is the energy level of the conduction band, ϵ_V is the energy level of the valence band and ϵ_{FC} and ϵ_{FV} are the quasi Fermi levels.	26
2.4	Qualitative depiction of how the surface free energy, volume free energy and total free energy of a droplet scale with its radius.	29
2.5	Example for peaks with $I_{\max} = 1$ in Gaussian shape ($\beta = 1$) and Lorentzian shape ($w = 0.5$).	40
2.6	Electron beam damage on an improperly formed $MAPbI_xBr_{3-x}$ layer.	44
3.1	Left: A photo of the inside of the evaporation chamber. The sample holder is at the top with the quartz scale visible just below. The thermal evaporation sources are at the bottom. The entry and exit slits for the X-rays are visible at the sides of the chamber and they are covered with Kapton on the outside. The circular hole at the right is the connection to the vacuum pumps. Right: Schematic depiction of the evaporation chamber together with the XRD system. The X-rays enter and exit the evaporation chamber through the Kapton windows. The consecutive XRD scans can be translated into color maps.	46
3.2	Rotational axes in relation to the sample plane, as they are referred to in the text. The blue line is the XRD beam, which lies in the plane spanned by the χ and φ axes.	52
4.1	Modification of figure 4a of the publication on $MAbPbI_3$ [Bu1]. Two black bars have been added, one denoting a time of 5 min and one denoting a time of 70 min.	69
4.2	Modification of figure 2 shown in the paper, that exchanges the bottom graph with a depiction of the detected LLS signal. The phase transitions have a visible influence on the 650 nm laser light. The LLS signal indicates a growing film prior to the XRD peaks becoming visible.	77

5.1	Comparison of the thermal stability of a variety of metal-halide perovskites. The data was obtained from temperature ramp experiments and the plot relates the temperature at a point in time with the extent of conversion at that temperature.	128
A.2	Color map of the CsPbCl ₃ decomposition process.	136
A.3	Color map of the CsSnBr ₃ decomposition process.	136
A.4	Color map of the FAPbBr ₃ decomposition process. This process has shown a multitude of different phases whose evolution is difficult to interpret. To get a better overview, the different phases are marked by different shapes depending on which phase would correspond to the XRD peaks: Squares denote cubic FAPbBr ₃ , circles denote orthorhombic FAPbBr ₃ and triangles denote an unknown phase. In addition, they were marked either blue or red. The disappearance of the first set of blue marked peaks coincides with the appearance of the second set of blue marked peaks. In the same way, the disappearance of the first set of red marked peaks coincides with the appearance of the second set of red marked peaks.	137

List of Tables

2.1	The selection of models that were used for the calculations presented here. This selection was taken from Khawam et al. [144], who also go into detail on how to derive these relations. $g(\alpha)$ denotes the integrated reaction model as calculated by equation 2.19.	34
3.1	Absorption A calculated by equation 3.3 for a layer of product under the assumption of $\theta = 20^\circ$, $d = 100$ nm and $c = 50\%$	51
4.1	The time it takes for a given halide species to diffuse through a 500 nm thick layer of an I or Br rich MAPbX ₃ perovskite. The diffusion constants are taken from Osheroov et al. [161].	68
A.1	Crucible temperatures that were used to prepare the perovskite layers which were analyzed in this thesis.	134
A.2	Crucible temperatures used in the additional experiments mentioned in section 5.4.134	

Bibliography

- [1] Akihiro Kojima, Kenjiro Teshima, Yasuo Shirai, et al. “Organometal Halide Perovskites as Visible-Light Sensitizers for Photovoltaic Cells”. In: *Journal of the American Chemical Society* 131.17 (2009), pp. 6050–6051. DOI: 10.1021/ja809598r.
- [2] NREL. *Best Research-Cell Efficiency Chart*. National Renewable Energy Laboratory. Jan. 3, 2022. URL: <https://www.nrel.gov/pv/cell-efficiency.html>.
- [3] Haotong Wei and Jinsong Huang. “Halide lead perovskites for ionizing radiation detection”. In: *Nature Communications* 10.1 (2019). DOI: 10.1038/s41467-019-08981-w.
- [4] Francesca De Rossi, Jenny A. Baker, David Beynon, et al. “All Printable Perovskite Solar Modules with 198 cm² Active Area and Over 6% Efficiency”. In: *Advanced Materials Technologies* (2018), p. 1800156. DOI: 10.1002/admt.201800156.
- [5] Ilke Celik, Adam B. Philips, Zhaoning Song, et al. “Energy Payback Time (EPBT) and Energy Return on Energy Invested (EROI) of Perovskite Tandem Photovoltaic Solar Cells”. In: *IEEE Journal of Photovoltaics* 8.1 (2018), pp. 305–309. DOI: 10.1109/jphotov.2017.2768961.
- [6] Jian Gong, Seth B. Darling, and Fengqi You. “Perovskite photovoltaics: life-cycle assessment of energy and environmental impacts”. In: *Energy & Environmental Science* 8.7 (2015), pp. 1953–1968. DOI: 10.1039/c5ee00615e.
- [7] T. Ibn-Mohammed, S.C.L. Koh, I.M. Reaney, et al. “Perovskite solar cells: An integrated hybrid lifecycle assessment and review in comparison with other photovoltaic technologies”. In: *Renewable and Sustainable Energy Reviews* 80 (2017), pp. 1321–1344. DOI: 10.1016/j.rser.2017.05.095.
- [8] Yong Churl Kim, Kwang Hee Kim, Dae-Yong Son, et al. “Printable organometallic perovskite enables large-area, low-dose X-ray imaging”. In: *Nature* 550.7674 (2017), pp. 87–91. DOI: 10.1038/nature24032.
- [9] Ling-Zhi Lei, Zhi-Feng Shi, Ying Li, et al. “High-efficiency and air-stable photodetectors based on lead-free double perovskite Cs₂AgBiBr₆ thin films”. In: *Journal of Materials Chemistry C* 6.30 (2018), pp. 7982–7988. DOI: 10.1039/c8tc02305k.
- [10] Julian A. Steele, Weicheng Pan, Cristina Martin, et al. “Photophysical Pathways in Highly Sensitive Cs₂AgBiBr₆ Double-Perovskite Single-Crystal X-Ray Detectors”. In: *Advanced Materials* 30.46 (2018), p. 1804450. DOI: 10.1002/adma.201804450.

- [11] Bo Yang, Weicheng Pan, Haodi Wu, et al. “Heteroepitaxial passivation of Cs₂AgBiBr₆ wafers with suppressed ionic migration for X-ray imaging”. In: *Nature Communications* 10.1 (2019). DOI: 10.1038/s41467-019-09968-3.
- [12] Jie Yang, Chunxiong Bao, Weihua Ning, et al. “Stable, High-Sensitivity and Fast-Response Photodetectors Based on Lead-Free Cs₂AgBiBr₆ Double Perovskite Films”. In: *Advanced Optical Materials* (2019), p. 1801732. DOI: 10.1002/adom.201801732.
- [13] *European Restriction on Hazardous Substances (RoHS)*. Feb. 29, 2020. URL: <http://eur-lex.europa.eu/legal-content/EN/TXT/?uri=CELEX:32011L0065>.
- [14] Herlina Arianita Dewi, Jia Li, Hao Wang, et al. “Excellent Intrinsic Long-Term Thermal Stability of Co-Evaporated MAPbI₃ Solar Cells at 85 °C”. In: *Advanced Functional Materials* 31.22 (Feb. 2021), p. 2100557. DOI: 10.1002/adfm.202100557.
- [15] Mingzhen Liu, Michael B. Johnston, and Henry J. Snaith. “Efficient planar hetero-junction perovskite solar cells by vapour deposition”. In: *Nature* 501.7467 (Sept. 2013), pp. 395–398. DOI: 10.1038/nature12509.
- [16] Weicheng Pan, Haodi Wu, Jiajun Luo, et al. “Cs₂AgBiBr₆ single-crystal X-ray detectors with a low detection limit”. In: *Nature Photonics* 11.11 (2017), pp. 726–732. DOI: 10.1038/s41566-017-0012-4.
- [17] Zheng Zhang, Da Cao, Zhengjie Huang, et al. “Gamma-Ray Detection Using Bi-Poor Cs₂AgBiBr₆ Double Perovskite Single Crystals”. In: *Advanced Optical Materials* 9.8 (Mar. 2021), p. 2001575. DOI: 10.1002/adom.202001575.
- [18] V. M. Goldschmidt. “Die Gesetze der Krystallochemie”. In: *Die Naturwissenschaften* 14.21 (1926), pp. 477–485. DOI: 10.1007/bf01507527.
- [19] M. A. Peña and J. L. G. Fierro. “Chemical Structures and Performance of Perovskite Oxides”. In: *Chemical Reviews* 101.7 (May 2001), pp. 1981–2018. DOI: 10.1021/cr980129f.
- [20] Chonghea Li, Xionggang Lu, Weizhong Ding, et al. “Formability of ABX₃(X= F, Cl, Br, I) halide perovskites”. In: *Acta Crystallographica Section B Structural Science* 64.6 (2008), pp. 702–707. DOI: 10.1107/s0108768108032734.
- [21] Marina R. Filip and Feliciano Giustino. “The geometric blueprint of perovskites”. In: *Proceedings of the National Academy of Sciences* 115.21 (2018), pp. 5397–5402. DOI: 10.1073/pnas.1719179115.
- [22] Christopher J. Bartel, Christopher Sutton, Bryan R. Goldsmith, et al. “New tolerance factor to predict the stability of perovskite oxides and halides”. In: *Science Advances* 5.2 (2019), eaav0693. DOI: 10.1126/sciadv.aav0693.
- [23] Zhenzhu Li, Qichen Xu, Qingde Sun, et al. “Stability Engineering of Halide Perovskite via Machine Learning”. In: (Mar. 16, 2018). arXiv: <http://arxiv.org/abs/1803.06042v1> [cond-mat.mtrl-sci]. URL: <http://arxiv.org/pdf/1803.06042v1>.
- [24] Zhenzhu Li, Qichen Xu, Qingde Sun, et al. “Thermodynamic Stability Landscape of Halide Double Perovskites via High-Throughput Computing and Machine Learning”. In: *Advanced Functional Materials* 29.9 (2019), p. 1807280. DOI: 10.1002/adfm.201807280.

- [25] Tom Baikie, Yanan Fang, Jeannette M. Kadro, et al. "Synthesis and crystal chemistry of the hybrid perovskite CH₃NH₃PbI₃ for solid-state sensitised solar cell applications". In: *Journal of Materials Chemistry A* 1.18 (2013), p. 5628. DOI: 10.1039/c3ta10518k.
- [26] Stefaan De Wolf, Jakub Holovsky, Soo-Jin Moon, et al. "Organometallic Halide Perovskites: Sharp Optical Absorption Edge and Its Relation to Photovoltaic Performance". In: *The Journal of Physical Chemistry Letters* 5.6 (Mar. 2014), pp. 1035–1039. DOI: 10.1021/jz500279b.
- [27] Yong Wang, M. Ibrahim Dar, Luis K. Ono, et al. "Thermodynamically stabilized β -CsPbI₃-based perovskite solar cells with efficiencies >18%". In: *Science* 365.6453 (2019), pp. 591–595. DOI: 10.1126/science.aav8680.
- [28] Haizhou Lu, Yuhang Liu, Paramvir Ahlawat, et al. "Vapor-assisted deposition of highly efficient, stable black-phase FAPbI₃ perovskite solar cells". In: *Science* 370.6512 (Oct. 2020). DOI: 10.1126/science.abb8985.
- [29] Naresh K. Kumawat, Amrita Dey, Aravindh Kumar, et al. "Band Gap Tuning of CH₃-NH₃Pb(Br_{1-x}Cl_x)₃ Hybrid Perovskite for Blue Electroluminescence". In: *ACS Applied Materials & Interfaces* 7.24 (June 2015), pp. 13119–13124. DOI: 10.1021/acsami.5b02159.
- [30] Yuiga Nakamura, Naoyuki Shibayama, Akiko Hori, et al. "Crystal Systems and Lattice Parameters of CH₃NH₃Pb(I_{1-x}Br_x)₃ Determined Using Single Crystals: Validity of Vegard's Law". In: *Inorganic Chemistry* 59.10 (Mar. 2020), pp. 6709–6716. DOI: 10.1021/acs.inorgchem.9b03421.
- [31] Michele Saba, Michele Cadelano, Daniela Marongiu, et al. "Correlated electron-hole plasma in organometal perovskites". In: *Nature Communications* 5.1 (Sept. 2014). DOI: 10.1038/ncomms6049.
- [32] Pronoy Nandi, Chandan Giri, Boby Joseph, et al. "CH₃NH₃PbI₃, A Potential Solar Cell Candidate: Structural and Spectroscopic Investigations". In: *The Journal of Physical Chemistry A* 120.49 (Dec. 2016), pp. 9732–9739. DOI: 10.1021/acs.jpca.6b09718.
- [33] Paolo Umari, Edoardo Mosconi, and Filippo De Angelis. "Infrared Dielectric Screening Determines the Low Exciton Binding Energy of Metal-Halide Perovskites". In: *The Journal of Physical Chemistry Letters* 9.3 (Jan. 2018), pp. 620–627. DOI: 10.1021/acs.jpcllett.7b03286.
- [34] Z. Yang, A. Surrente, K. Galkowski, et al. "Impact of the Halide Cage on the Electronic Properties of Fully Inorganic Cesium Lead Halide Perovskites". In: *ACS Energy Letters* 2.7 (June 2017), pp. 1621–1627. DOI: 10.1021/acsenenergylett.7b00416.
- [35] Christian Wehrenfennig, Giles E. Eperon, Michael B. Johnston, et al. "High Charge Carrier Mobilities and Lifetimes in Organolead Trihalide Perovskites". In: *Advanced Materials* 26.10 (Dec. 2013), pp. 1584–1589. DOI: 10.1002/adma.201305172.
- [36] Laura M. Herz. "Charge-Carrier Mobilities in Metal Halide Perovskites: Fundamental Mechanisms and Limits". In: *ACS Energy Letters* 2.7 (2017), pp. 1539–1548. DOI: 10.1021/acsenenergylett.7b00276.

- [37] Yucheng Liu, Zhou Yang, and Shengzhong Frank Liu. “Recent Progress in Single-Crystalline Perovskite Research Including Crystal Preparation, Property Evaluation, and Applications”. In: *Advanced Science* 5.1 (Nov. 2017), p. 1700471. DOI: 10.1002/advs.201700471.
- [38] Roberto Brenes, Dengyang Guo, Anna Osherov, et al. “Metal Halide Perovskite Polycrystalline Films Exhibiting Properties of Single Crystals”. In: *Joule* 1.1 (Sept. 2017), pp. 155–167. DOI: 10.1016/j.joule.2017.08.006.
- [39] Kenjiro Miyano, Neeti Tripathi, Masatoshi Yanagida, et al. “Lead Halide Perovskite Photovoltaic as a Model p–i–n Diode”. In: *Accounts of Chemical Research* 49.2 (Jan. 2016), pp. 303–310. DOI: 10.1021/acs.accounts.5b00436.
- [40] Adam H. Slavney, Te Hu, Aaron M. Lindenberg, et al. “A Bismuth-Halide Double Perovskite with Long Carrier Recombination Lifetime for Photovoltaic Applications”. In: *Journal of the American Chemical Society* 138.7 (Feb. 24, 2016), pp. 2138–2141. ISSN: 0002-7863. DOI: 10.1021/jacs.5b13294. (Visited on 06/26/2017).
- [41] Wan-Jian Yin, Tingting Shi, and Yanfa Yan. “Unusual defect physics in CH₃NH₃PbI₃ perovskite solar cell absorber”. In: *Applied Physics Letters* 104.6 (Feb. 2014), p. 063903. DOI: 10.1063/1.4864778.
- [42] Jun Haruyama, Keitaro Sodeyama, Liyuan Han, et al. “Termination Dependence of Tetragonal CH₃NH₃PbI₃ Surfaces for Perovskite Solar Cells”. In: *The Journal of Physical Chemistry Letters* 5.16 (Aug. 2014), pp. 2903–2909. DOI: 10.1021/jz501510v.
- [43] Andrei Buin, Patrick Pietsch, Jixian Xu, et al. “Materials Processing Routes to Trap-Free Halide Perovskites”. In: *Nano Letters* 14.11 (Oct. 2014), pp. 6281–6286. DOI: 10.1021/nl502612m.
- [44] Michael L. Agiorgousis, Yi-Yang Sun, Hao Zeng, et al. “Strong Covalency-Induced Recombination Centers in Perovskite Solar Cell Material CH₃NH₃PbI₃”. In: *Journal of the American Chemical Society* 136.41 (Oct. 2014), pp. 14570–14575. DOI: 10.1021/ja5079305.
- [45] Aron Walsh, David O. Scanlon, Shiyu Chen, et al. “Self-Regulation Mechanism for Charged Point Defects in Hybrid Halide Perovskites”. In: *Angewandte Chemie International Edition* 54.6 (Dec. 2014), pp. 1791–1794. DOI: 10.1002/anie.201409740.
- [46] H. Zhu, K. Miyata, Y. Fu, et al. “Screening in crystalline liquids protects energetic carriers in hybrid perovskites”. In: *Science* 353.6306 (Sept. 2016), pp. 1409–1413. DOI: 10.1126/science.aaf9570.
- [47] Alessandro Pecchia, Desirée Gentilini, Daniele Rossi, et al. “Role of Ferroelectric Nanodomains in the Transport Properties of Perovskite Solar Cells”. In: *Nano Letters* 16.2 (Jan. 2016), pp. 988–992. DOI: 10.1021/acs.nanolett.5b03957.
- [48] Shamim Shahrokhi, Wenxiu Gao, Yutao Wang, et al. “Emergence of Ferroelectricity in Halide Perovskites”. In: *Small Methods* 4.8 (May 2020), p. 2000149. DOI: 10.1002/smt.202000149.

- [49] Xia Li, Shaoqing Chen, Peng-Fei Liu, et al. "Evidence for Ferroelectricity of All-Inorganic Perovskite CsPbBr₃ Quantum Dots". In: *Journal of the American Chemical Society* 142.7 (2020), pp. 3316–3320. DOI: 10.1021/jacs.9b12254.
- [50] Zewen Xiao, Weiwei Meng, Jianbo Wang, et al. "Thermodynamic Stability and Defect Chemistry of Bismuth-Based Lead-Free Double Perovskites". In: *ChemSusChem* 9.18 (2016), pp. 2628–2633. DOI: 10.1002/cssc.201600771.
- [51] I.L. Ivanov, A.S. Steparuk, M.S. Bolyachkina, et al. "Thermodynamics of formation of hybrid perovskite-type methylammonium lead halides". In: *The Journal of Chemical Thermodynamics* 116 (Jan. 2018), pp. 253–258. DOI: 10.1016/j.jct.2017.09.026.
- [52] Sam Zhang and Guifang Han. "Intrinsic and environmental stability issues of perovskite photovoltaics". In: *Progress in Energy* 2.2 (2020), p. 022002. DOI: 10.1088/2516-1083/ab70d9.
- [53] Daniel Prochowicz, Pankaj Yadav, Michael Saliba, et al. "Reduction in the Interfacial Trap Density of Mechanochemically Synthesized MAPbI₃". In: *ACS Applied Materials & Interfaces* 9.34 (Aug. 2017), pp. 28418–28425. DOI: 10.1021/acsami.7b06788.
- [54] Jun Yin, Hui Qu, Jing Cao, et al. "Vapor-assisted crystallization control toward high performance perovskite photovoltaics with over 18% efficiency in the ambient atmosphere". In: *Journal of Materials Chemistry A* 4.34 (2016), pp. 13203–13210. DOI: 10.1039/c6ta04465d.
- [55] Sonia R. Raga, Luis K. Ono, and Yabing Qi. "Rapid perovskite formation by CH₃NH₂ gas-induced intercalation and reaction of PbI₂". In: *Journal of Materials Chemistry A* 4.7 (2016), pp. 2494–2500. DOI: 10.1039/c5ta10055k.
- [56] Huichao Zhang, Xu Fu, Ying Tang, et al. "Phase segregation due to ion migration in all-inorganic mixed-halide perovskite nanocrystals". In: *Nature Communications* 10.1 (Mar. 2019). DOI: 10.1038/s41467-019-09047-7.
- [57] Nengxu Li, Xiuxiu Niu, Qi Chen, et al. "Towards commercialization: the operational stability of perovskite solar cells". In: *Chemical Society Reviews* 49.22 (2020), pp. 8235–8286. DOI: 10.1039/d0cs00573h.
- [58] Dae-Yong Son, Seul-Gi Kim, Ja-Young Seo, et al. "Universal Approach toward Hysteresis-Free Perovskite Solar Cell via Defect Engineering". In: *Journal of the American Chemical Society* 140.4 (Jan. 2018), pp. 1358–1364. DOI: 10.1021/jacs.7b10430.
- [59] Mojtaba Abdi-Jalebi, Zahra Andaji-Garmaroudi, Stefania Cacovich, et al. "Maximizing and stabilizing luminescence from halide perovskites with potassium passivation". In: *Nature* 555.7697 (Mar. 2018), pp. 497–501. DOI: 10.1038/nature25989.
- [60] Philippe Holzhey and Michael Saliba. "A full overview of international standards assessing the long-term stability of perovskite solar cells". In: *Journal of Materials Chemistry A* 6.44 (2018), pp. 21794–21808. DOI: 10.1039/c8ta06950f.
- [61] Ludmila Cojocaru, Satoshi Uchida, Yoshitaka Sanehira, et al. "Temperature Effects on the Photovoltaic Performance of Planar Structure Perovskite Solar Cells". In: *Chemistry Letters* 44.11 (2015), pp. 1557–1559. DOI: 10.1246/cl.150781.

- [62] Andrea Pisoni, Jaćim Jaćimović, Osor S. Barišić, et al. “Ultra-Low Thermal Conductivity in Organic–Inorganic Hybrid Perovskite $\text{CH}_3\text{NH}_3\text{PbI}_3$ ”. In: *The Journal of Physical Chemistry Letters* 5.14 (July 2014), pp. 2488–2492. DOI: 10.1021/jz5012109.
- [63] Aurélien M. A. Leguy, Yinghong Hu, Mariano Campoy-Quiles, et al. “Reversible Hydration of $\text{CH}_3\text{NH}_3\text{PbI}_3$ in Films, Single Crystals, and Solar Cells”. In: *Chemistry of Materials* 27.9 (2015), pp. 3397–3407. DOI: 10.1021/acs.chemmater.5b00660.
- [64] Jeffrey A. Christians, Pierre A. Miranda Herrera, and Prashant V. Kamat. “Transformation of the Excited State and Photovoltaic Efficiency of $\text{CH}_3\text{NH}_3\text{PbI}_3$ Perovskite upon Controlled Exposure to Humidified Air”. In: *Journal of the American Chemical Society* 137.4 (Jan. 2015), pp. 1530–1538. DOI: 10.1021/ja511132a.
- [65] Jinli Yang, Braden D. Siempelkamp, Danyi Liu, et al. “Investigation of $\text{CH}_3\text{NH}_3\text{PbI}_3$ Degradation Rates and Mechanisms in Controlled Humidity Environments Using in Situ Techniques”. In: *ACS Nano* 9.2 (Feb. 2015), pp. 1955–1963. ISSN: 1936-0851. DOI: 10.1021/nn506864k. URL: <https://doi.org/10.1021/nn506864k>.
- [66] Hong Fang and Puru Jena. “Super-ion inspired colorful hybrid perovskite solar cells”. In: *Journal of Materials Chemistry A* 4.13 (2016), pp. 4728–4737. DOI: 10.1039/c5ta09646d.
- [67] Lingling Zheng, Yao-Hsien Chung, Yingzhuang Ma, et al. “A hydrophobic hole transporting oligothiophene for planar perovskite solar cells with improved stability”. In: *Chem. Commun.* 50.76 (2014), pp. 11196–11199. DOI: 10.1039/c4cc04680c.
- [68] Qi Wang, Bo Chen, Ye Liu, et al. “Scaling behavior of moisture-induced grain degradation in polycrystalline hybrid perovskite thin films”. In: *Energy & Environmental Science* 10.2 (2017), pp. 516–522. DOI: 10.1039/c6ee02941h.
- [69] Giles E. Eperon, Samuel D. Stranks, Christopher Menelaou, et al. “Formamidinium lead trihalide: a broadly tunable perovskite for efficient planar heterojunction solar cells”. In: *Energy & Environmental Science* 7.3 (2014), p. 982. DOI: 10.1039/c3ee43822h.
- [70] Jin-Wook Lee, Dong-Jin Seol, An-Na Cho, et al. “High-Efficiency Perovskite Solar Cells Based on the Black Polymorph of $\text{HC}(\text{NH}_2)_2\text{PbI}_3$ ”. In: *Advanced Materials* 26.29 (June 2014), pp. 4991–4998. DOI: 10.1002/adma.201401137.
- [71] Guoqing Tong, Luis K. Ono, and Yabing Qi. “Recent Progress of All-Bromide Inorganic Perovskite Solar Cells”. In: *Energy Technology* 8.4 (Apr. 2020), p. 1900961. DOI: 10.1002/ente.201900961.
- [72] Yu An, Juanita Hidalgo, Carlo Andrea Ricardo Perini, et al. “Structural Stability of Formamidinium- and Cesium-Based Halide Perovskites”. In: *ACS Energy Letters* 6.5 (Apr. 2021), pp. 1942–1969. DOI: 10.1021/acsenenergylett.1c00354.
- [73] Alessandro Senocrate, Tolga Acartürk, Gee Yeong Kim, et al. “Interaction of oxygen with halide perovskites”. In: *Journal of Materials Chemistry A* 6.23 (2018), pp. 10847–10855. DOI: 10.1039/c8ta04537b.

- [74] Nicholas Aristidou, Christopher Eames, Irene Sanchez-Molina, et al. “Fast oxygen diffusion and iodide defects mediate oxygen-induced degradation of perovskite solar cells”. In: *Nature Communications* 8.1 (May 2017). DOI: 10.1038/ncomms15218.
- [75] Nicholas Aristidou, Irene Sanchez-Molina, Thana Chotchuangchutchaval, et al. “The Role of Oxygen in the Degradation of Methylammonium Lead Trihalide Perovskite Photoactive Layers”. In: *Angewandte Chemie International Edition* 54.28 (May 2015), pp. 8208–8212. DOI: 10.1002/anie.201503153.
- [76] Hsinhan Tsai, Reza Asadpour, Jean-Christophe Blancon, et al. “Light-induced lattice expansion leads to high-efficiency perovskite solar cells”. In: *Science* 360.6384 (2018), pp. 67–70. DOI: 10.1126/science.aap8671.
- [77] Silvia G. Motti, Daniele Meggiolaro, Alex J. Barker, et al. “Controlling competing photochemical reactions stabilizes perovskite solar cells”. In: *Nature Photonics* 13.8 (May 2019), pp. 532–539. DOI: 10.1038/s41566-019-0435-1.
- [78] Monojit Bag, Lawrence A. Renna, Ramesh Y. Adhikari, et al. “Kinetics of Ion Transport in Perovskite Active Layers and Its Implications for Active Layer Stability”. In: *J. Am. Chem. Soc.* 137.40 (Oct. 2015), pp. 13130–13137. DOI: 10.1021/jacs.5b08535.
- [79] Federico Brivio, Clovis Caetano, and Aron Walsh. “Thermodynamic Origin of Photoinstability in the CH₃NH₃Pb(I_{1-x}Br_x)₃Hybrid Halide Perovskite Alloy”. In: *The Journal of Physical Chemistry Letters* 7.6 (2016), pp. 1083–1087. DOI: 10.1021/acs.jpcllett.6b00226.
- [80] Eric T. Hoke, Daniel J. Slotcavage, Emma R. Dohner, et al. “Reversible photo-induced trap formation in mixed-halide hybrid perovskites for photovoltaics”. In: *Chemical Science* 6.1 (Dec. 1, 2014), pp. 613–617. ISSN: 2041-6539. DOI: 10.1039/C4SC03141E. URL: <http://pubs.rsc.org/en/content/articlelanding/2015/sc/c4sc03141e> (visited on 08/31/2017).
- [81] Emilio J. Juarez-Perez, Luis K. Ono, Maki Maeda, et al. “Photodecomposition and thermal decomposition in methylammonium halide lead perovskites and inferred design principles to increase photovoltaic device stability”. In: *Journal of Materials Chemistry A* 6.20 (2018), pp. 9604–9612. DOI: 10.1039/c8ta03501f.
- [82] Felix Lang, Norbert H. Nickel, Jürgen Bundesmann, et al. “Radiation Hardness and Self-Healing of Perovskite Solar Cells”. In: *Advanced Materials* 28.39 (Aug. 2016), pp. 8726–8731. DOI: 10.1002/adma.201603326.
- [83] Pankaj Yadav, Daniel Prochowicz, Essa A. Alharbi, et al. “Intrinsic and interfacial kinetics of perovskite solar cells under photo and bias-induced degradation and recovery”. In: *Journal of Materials Chemistry C* 5.31 (2017), pp. 7799–7805. DOI: 10.1039/c7tc02652h.
- [84] Davide Raffaele Ceratti, Yevgeny Rakita, Llorenç Cremonesi, et al. “Self-Healing Inside APbBr₃ Halide Perovskite Crystals”. In: *Advanced Materials* 30.10 (2018), p. 1706273. DOI: 10.1002/adma.201706273.

- [85] Wanyi Nie, Jean-Christophe Blancon, Amanda J. Neukirch, et al. “Light-activated photocurrent degradation and self-healing in perovskite solar cells”. In: *Nature Communications* 7.1 (2016). DOI: 10.1038/ncomms11574.
- [86] Ronen Gottesman, Laxman Gouda, Basanth S. Kalanoor, et al. “Photoinduced Reversible Structural Transformations in Free-Standing CH₃NH₃PbI₃ Perovskite Films”. In: *J. Phys. Chem. Lett.* 6.12 (June 2015), pp. 2332–2338. DOI: 10.1021/acs.jpcllett.5b00994.
- [87] Mark V. Khenkin, Anoop K. M., Iris Visoly-Fisher, et al. “Dynamics of Photoinduced Degradation of Perovskite Photovoltaics: From Reversible to Irreversible Processes”. In: *ACS Appl. Energy Mater.* 1.2 (Jan. 2018), pp. 799–806. DOI: 10.1021/acsaem.7b00256.
- [88] Sang-Won Lee, Seongtak Kim, Soohyun Bae, et al. “UV Degradation and Recovery of Perovskite Solar Cells”. In: *Scientific Reports* 6.1 (Dec. 2016). DOI: 10.1038/srep38150.
- [89] Mark V. Khenkin, Anoop K. M., Iris Visoly-Fisher, et al. “Reconsidering figures of merit for performance and stability of perovskite photovoltaics”. In: *Energy & Environmental Science* 11.4 (2018), pp. 739–743. DOI: 10.1039/c7ee02956j.
- [90] CHR. KN. MOLLER. “Crystal Structure and Photoconductivity of Cæsium Plumbahalides”. In: *Nature* 182.4647 (1958), pp. 1436–1436. DOI: 10.1038/1821436a0.
- [91] Andreas Binek, Fabian C. Hanusch, Pablo Docampo, et al. “Stabilization of the Trigonal High-Temperature Phase of Formamidinium Lead Iodide”. In: *The Journal of Physical Chemistry Letters* 6.7 (2015), pp. 1249–1253. DOI: 10.1021/acs.jpcllett.5b00380.
- [92] Qifeng Han, Sang-Hoon Bae, Pengyu Sun, et al. “Single Crystal Formamidinium Lead Iodide (FAPbI₃): Insight into the Structural, Optical, and Electrical Properties”. In: *Advanced Materials* 28.11 (Jan. 2016), pp. 2253–2258. DOI: 10.1002/adma.201505002.
- [93] Giles E. Eperon, Giuseppe M. Paternò, Rebecca J. Sutton, et al. “Inorganic caesium lead iodide perovskite solar cells”. In: *Journal of Materials Chemistry A* 3.39 (Sept. 29, 2015), pp. 19688–19695. ISSN: 2050-7496. DOI: 10.1039/C5TA06398A. URL: <http://pubs.rsc.org/en/content/articlelanding/2015/ta/c5ta06398a> (visited on 10/24/2017).
- [94] Zhiwen Qiu, Nengxu Li, Zijian Huang, et al. “Recent Advances in Improving Phase Stability of Perovskite Solar Cells”. In: *Small Methods* 4.5 (Mar. 2020), p. 1900877. DOI: 10.1002/smt.201900877.
- [95] Xiaojia Zheng, Congcong Wu, Shikhar K. Jha, et al. “Improved Phase Stability of Formamidinium Lead Triiodide Perovskite by Strain Relaxation”. In: *ACS Energy Lett.* 1.5 (Oct. 2016), pp. 1014–1020. DOI: 10.1021/acsenergylett.6b00457.
- [96] G. Grancini, C. Roldán-Carmona, I. Zimmermann, et al. “One-Year stable perovskite solar cells by 2D/3D interface engineering”. In: *Nature Communications* (June 1, 2017). DOI: 10.1038/ncomms15684.
- [97] Guangda Niu, Xudong Guo, and Liduo Wang. “Review of recent progress in chemical stability of perovskite solar cells”. In: *Journal of Materials Chemistry A* 3.17 (2015), pp. 8970–8980. DOI: 10.1039/c4ta04994b.

- [98] Hui-Seon Kim, Ja-Young Seo, and Nam-Gyu Park. “Impact of Selective Contacts on Long-Term Stability of CH₃NH₃PbI₃ Perovskite Solar Cells”. In: *J. Phys. Chem. C* 120.49 (Dec. 2016), pp. 27840–27848. DOI: 10.1021/acs.jpcc.6b09412.
- [99] Tomas Leijtens, Giles E. Eperon, Sandeep Pathak, et al. “Overcoming ultraviolet light instability of sensitized TiO₂ with meso-superstructured organometal tri-halide perovskite solar cells”. In: *Nature Communications volume 4* 4.1 (Dec. 2013). DOI: 10.1038/ncomms3885.
- [100] Yuichi Kato, Luis K. Ono, Michael V. Lee, et al. “Silver Iodide Formation in Methyl Ammonium Lead Iodide Perovskite Solar Cells with Silver Top Electrodes”. In: *Advanced Materials Interfaces* 2.13 (July 2015), p. 1500195. DOI: 10.1002/admi.201500195.
- [101] Mark V. Khenkin, Eugene A. Katz, Antonio Abate, et al. “Consensus statement for stability assessment and reporting for perovskite photovoltaics based on ISOS procedures”. In: *Nature Energy* 5.1 (2020), pp. 35–49. DOI: 10.1038/s41560-019-0529-5.
- [102] EPKI. *Perovskite-based photovoltaics: A unique chance for European PV-industry*. Tech. rep. European Perovskite Initiative, Sept. 1, 2019. URL: https://www.zsw-bw.de/uploads/media/EPKI_Perovskite_White_Paper_2019-09_01.pdf.
- [103] Silver-Hamill Turren-Cruz, Anders Hagfeldt, and Michael Saliba. “Methylammonium-free, high-performance, and stable perovskite solar cells on a planar architecture”. In: *Science* 362.6413 (Oct. 2018), pp. 449–453. DOI: 10.1126/science.aat3583.
- [104] Yana Vaynzof. “The Future of Perovskite Photovoltaics—Thermal Evaporation or Solution Processing?” In: *Advanced Energy Materials* 10.48 (Nov. 2020), p. 2003073. DOI: 10.1002/aenm.202003073.
- [105] Daniel Pérez del Rey, Pablo P. Boix, Michele Sessolo, et al. “Interfacial Modification for High-Efficiency Vapor-Phase-Deposited Perovskite Solar Cells Based on a Metal Oxide Buffer Layer”. In: *The Journal of Physical Chemistry Letters* 9.5 (Feb. 2018), pp. 1041–1046. DOI: 10.1021/acs.jpcllett.7b03361.
- [106] Jia Li, Hao Wang, Xin Yu Chin, et al. “Highly Efficient Thermally Co-evaporated Perovskite Solar Cells and Mini-modules”. In: *Joule* 4.5 (May 2020), pp. 1035–1053. DOI: 10.1016/j.joule.2020.03.005.
- [107] Jiangshan Feng, Yuxiao Jiao, Hui Wang, et al. “High-throughput large-area vacuum deposition for high-performance formamidine-based perovskite solar cells”. In: *Energy & Environmental Science* 14.5 (2021), pp. 3035–3043. DOI: 10.1039/d1ee00634g.
- [108] Xingyue Liu, Xianhua Tan, Zhiyong Liu, et al. “Sequentially vacuum evaporated high-quality CsPbBr₃ films for efficient carbon-based planar heterojunction perovskite solar cells”. In: *Journal of Power Sources* 443 (Dec. 2019), p. 227269. DOI: 10.1016/j.jpowsour.2019.227269.
- [109] Peipei Du, Liang Wang, Jinghui Li, et al. “Thermal Evaporation for Halide Perovskite Optoelectronics: Fundamentals, Progress, and Outlook”. In: *Advanced Optical Materials* 10.4 (Dec. 2021), p. 2101770. DOI: 10.1002/adom.202101770.

- [110] Jeong-Hyeok Im, Chang-Ryul Lee, Jin-Wook Lee, et al. “6.5% efficient perovskite quantum-dot-sensitized solar cell”. In: *Nanoscale* 3.10 (2011), p. 4088. DOI: 10.1039/c1nr10867k.
- [111] Michael M. Lee, Joël Teuscher, Tsutomu Miyasaka, et al. “Efficient Hybrid Solar Cells Based on Meso-Superstructured Organometal Halide Perovskites”. In: *Science* 338.6107 (Nov. 2012), pp. 643–647. DOI: 10.1126/science.1228604.
- [112] Julian Burschka, Norman Pellet, Soo-Jin Moon, et al. “Sequential deposition as a route to high-performance perovskite-sensitized solar cells”. In: *Nature* 499.7458 (July 2013), pp. 316–319. DOI: 10.1038/nature12340.
- [113] Nam-Gyu Park. “Perovskite solar cells: an emerging photovoltaic technology”. In: *Materials Today* 18.2 (2015), pp. 65–72. DOI: 10.1016/j.mattod.2014.07.007.
- [114] Ab Latif Wani, Anjum Ara, and Jawed Ahmad Usmani. “Lead toxicity: a review”. In: *Interdisciplinary Toxicology* 8.2 (June 2015), pp. 55–64. DOI: 10.1515/intox-2015-0009.
- [115] Chengbo Wang, Yuting Zhang, Feidan Gu, et al. “Illumination Durability and High-Efficiency Sn-Based Perovskite Solar Cell under Coordinated Control of Phenylhydrazine and Halogen Ions”. In: *Matter* 4.2 (Feb. 2021), pp. 709–721. DOI: 10.1016/j.matt.2020.11.012.
- [116] Ping-Ping Sun, Quan-Song Li, Li-Na Yang, et al. “Theoretical insights into a potential lead-free hybrid perovskite: substituting Pb²⁺ with Ge²⁺”. In: *Nanoscale* 8.3 (2016), pp. 1503–1512. DOI: 10.1039/c5nr05337d.
- [117] Nam-Gyu Park, Michael Grätzel, Tsutomu Miyasaka, et al. “Towards stable and commercially available perovskite solar cells”. In: *Nature Energy* 1.11 (Oct. 2016). DOI: 10.1038/nenergy.2016.152.
- [118] Petr Melnikov and Lourdes Zélia Zanoni. “Clinical Effects of Cesium Intake”. In: *Biological Trace Element Research* 135 (June 1, 2010), pp. 1–9. DOI: 10.1007/s12011-009-8486-7.
- [119] Garland T. Johnson, Trent R. Lewis, and William D. Wagner. “Acute toxicity of cesium and rubidium compounds”. In: *Toxicology and Applied Pharmacology* 32.2 (1975), pp. 239–245. ISSN: 0041-008X. DOI: [https://doi.org/10.1016/0041-008X\(75\)90216-1](https://doi.org/10.1016/0041-008X(75)90216-1). URL: <https://www.sciencedirect.com/science/article/pii/0041008X75902161>.
- [120] Hiroshi Higuchi and Takayuki Negami. “Largest highly efficient 203 × 203 mm² CH₃NH₃PbI₃ perovskite solar modules”. In: *Japanese Journal of Applied Physics* 57.8S3 (July 2018), 08RE11. DOI: 10.7567/jjap.57.08re11.
- [121] Sang-Won Lee, Soohyun Bae, Donghwan Kim, et al. “Historical Analysis of High-Efficiency, Large-Area Solar Cells: Toward Upscaling of Perovskite Solar Cells”. In: *Advanced Materials* 32.51 (Oct. 2020), p. 2002202. DOI: 10.1002/adma.202002202.
- [122] Khagendra P. Bhandari, Jennifer M. Collier, Randy J. Ellingson, et al. “Energy payback time (EPBT) and energy return on energy invested (EROI) of solar photovoltaic systems: A systematic review and meta-analysis”. In: *Renewable and Sustainable Energy Reviews* 47 (July 2015), pp. 133–141. DOI: 10.1016/j.rser.2015.02.057.

- [123] Andreas Binek, Michiel L. Petrus, Niklas Huber, et al. “Recycling Perovskite Solar Cells To Avoid Lead Waste”. In: *ACS Applied Materials & Interfaces* 8.20 (May 2016), pp. 12881–12886. DOI: 10.1021/acsami.6b03767.
- [124] Byeong Jo Kim, Dong Hoe Kim, Seung Lee Kwon, et al. “Selective dissolution of halide perovskites as a step towards recycling solar cells”. In: *Nature Communications* 7.1 (May 2016). DOI: 10.1038/ncomms11735.
- [125] Priyanka Chhillar, Bhanu Pratap Dhamaniya, Viresh Dutta, et al. “Recycling of Perovskite Films: Route toward Cost-Efficient and Environment-Friendly Perovskite Technology”. In: *ACS Omega* 4.7 (July 2019), pp. 11880–11887. DOI: 10.1021/acsomega.9b01053.
- [126] Xiyuan Feng, Qing Guo, Jingwei Xiu, et al. “Close-loop recycling of perovskite solar cells through dissolution-recrystallization of perovskite by butylamine”. In: *Cell Reports Physical Science* 2.2 (Feb. 2021), p. 100341. DOI: 10.1016/j.xcrp.2021.100341.
- [127] Eran Edri, Saar Kirmayer, Sabyasachi Mukhopadhyay, et al. “Elucidating the charge carrier separation and working mechanism of CH₃NH₃PbI₃-xCl_x perovskite solar cells”. In: *Nature Communications* 5.1 (Mar. 2014). DOI: 10.1038/ncomms4461.
- [128] Peter Würfel. *Physics of solar cells from basic principles to advanced concepts*. Weinheim: Wiley-VCH Verlag GmbH & Co. KGaA, 2016. ISBN: 9783527413119.
- [129] Qingsong Shan, Jizhong Song, Yousheng Zou, et al. “High Performance Metal Halide Perovskite Light-Emitting Diode: From Material Design to Device Optimization”. In: *Small* 13.45 (2017), p. 1701770. DOI: 10.1002/smll.201701770.
- [130] Nana Wang, Lu Cheng, Rui Ge, et al. “Perovskite light-emitting diodes based on solution-processed self-organized multiple quantum wells”. In: *Nature Photonics* 10.11 (2016), pp. 699–704. DOI: 10.1038/nphoton.2016.185.
- [131] Peter William Atkins, Julio De Paula, and James Keeler. *Physical chemistry*. eng. Eleventh edition. Peter Atkins, Fellow of Lincoln College, University of Oxford, Oxford, UK, Julio de Paula, Professor of Chemistry, Lewis and Clark College, Portland, Oregon, USA, James Keeler, Senior Lecturer in Chemistry and Fellow of Selwyn College, University of Cambridge, Cambridge, UK., Includes index. New York, NY : Oxford University Press, 2018. ISBN: 9780198769866.
- [132] Milton Ohring. *Materials science of thin films : deposition and structure*. San Diego, CA: Academic Press, 2002. ISBN: 0125249756.
- [133] J. A. Venables and G. D. T. Spiller. “Nucleation and Growth of Thin Films”. In: *Surface Mobilities on Solid Materials*. Springer US, 1983, pp. 341–404. DOI: 10.1007/978-1-4684-4343-1_16.
- [134] Weijie Chen, Jingwen Zhang, Guiying Xu, et al. “A Semitransparent Inorganic Perovskite Film for Overcoming Ultraviolet Light Instability of Organic Solar Cells and Achieving 14.03% Efficiency”. In: *Advanced Materials* 30.21 (Apr. 2018), p. 1800855. DOI: 10.1002/adma.201800855.

- [135] Sergey Vyazovkin and Charles A Wight. “Model-free and model-fitting approaches to kinetic analysis of isothermal and nonisothermal data”. In: *Thermochimica Acta* 340-341 (1999), pp. 53–68. DOI: 10.1016/s0040-6031(99)00253-1.
- [136] A. K. Galwey. “What theoretical and/or chemical significance is to be attached to the magnitude of an activation energy determined for a solid-state decomposition?” In: *Journal of Thermal Analysis and Calorimetry* 86.1 (Aug. 2006), pp. 267–286. DOI: 10.1007/s10973-005-7157-y.
- [137] Keith J. Laidler. “The development of the Arrhenius equation”. In: *Journal of Chemical Education* 61.6 (June 1984), p. 494. DOI: 10.1021/ed061p494.
- [138] Michael Brown and Andrew Galwey. *Handbook of thermal analysis and calorimetry*. Amsterdam Netherlands New York: Elsevier, 1998. ISBN: 9780444820853.
- [139] Andrew K. Galwey and Michael E. Brown. “A theoretical justification for the application of the Arrhenius equation to kinetics of solid state reactions (mainly ionic crystals)”. In: *Proceedings of the Royal Society of London. Series A: Mathematical and Physical Sciences* 450.1940 (Sept. 1995), pp. 501–512. DOI: 10.1098/rspa.1995.0097.
- [140] Andrew K. Galwey. “Thermal reactions involving solids: a personal view of selected features of decompositions, thermal analysis and heterogeneous catalysis”. In: *Journal of Thermal Analysis and Calorimetry* 142.3 (Mar. 2020), pp. 1123–1144. DOI: 10.1007/s10973-020-09461-w.
- [141] Paul D. Garn. “Kinetics of decomposition of the solid state”. In: *Thermochimica Acta* 135 (Oct. 1988), pp. 71–77. DOI: 10.1016/0040-6031(88)87368-4.
- [142] Boris V L’vov. “The physical approach to the interpretation of the kinetics and mechanisms of thermal decomposition of solids: the state of the art”. In: *Thermochimica Acta* 373.2 (June 2001), pp. 97–124. DOI: 10.1016/s0040-6031(01)00507-x.
- [143] Boris V. L’vov. *Thermal Decomposition of Solids and Melts*. Springer Netherlands, 2007. DOI: 10.1007/978-1-4020-5672-7.
- [144] Ammar Khawam and Douglas R. Flanagan. “Solid-State Kinetic Models: Basics and Mathematical Fundamentals”. In: *The Journal of Physical Chemistry B* 110.35 (2006), pp. 17315–17328. DOI: 10.1021/jp062746a.
- [145] Anthony West. *Grundlagen der Festkörperchemie*. WeinheimNew YorkCambridgeBasel: VCH, 1992. ISBN: 3527281037.
- [146] H.G.J. Moseley. “XCIII. The high-frequency spectra of the elements”. In: *The London, Edinburgh, and Dublin Philosophical Magazine and Journal of Science* 26.156 (1913), pp. 1024–1034. DOI: 10.1080/14786441308635052.
- [147] Mario Birkholz. *Thin film analysis by X-ray scattering*. Weinheim: Wiley-VCH, 2006. ISBN: 3527310525. DOI: 10.1002/3527607595. URL: <https://onlinelibrary.wiley.com/doi/book/10.1002/3527607595>.
- [148] J. I. Langford and A. J. C. Wilson. “Scherrer after sixty years: A survey and some new results in the determination of crystallite size”. In: *Journal of Applied Crystallography* 11.2 (Apr. 1978), pp. 102–113. DOI: 10.1107/s0021889878012844.

- [149] Brendan J. Griffin. “A comparison of conventional Everhart-Thornley style and in-lens secondary electron detectors—a further variable in scanning electron microscopy”. In: *Scanning* 33.3 (May 2011), pp. 162–173. DOI: 10.1002/sca.20255.
- [150] JEOL. *Scanning Electron Microscope A To Z - Basic Knowledge For Using The SEM*. JEOL Ltd. Dec. 22, 2021. URL: https://www.jeol.co.jp/en/applications/pdf/sm/sem_atoz_all.pdf.
- [151] Junhui Ran, Ondrej Dyck, Xiaozheng Wang, et al. “Electron-Beam-Related Studies of Halide Perovskites: Challenges and Opportunities”. In: *Advanced Energy Materials* 10.26 (Feb. 2020), p. 1903191. DOI: 10.1002/aenm.201903191.
- [152] Günter Sauerbrey. “Verwendung von Schwingquarzen zur Wägung dünner Schichten und zur Mikrowägung”. In: *Zeitschrift für Physik* 155.2 (Apr. 1959), pp. 206–222. DOI: 10.1007/bf01337937.
- [153] Stefan Hartnauer. “Phasenbildung am System Cu-Zn-Sn-(In,Ga)-S-Se untersucht mit Echtzeitmethoden für Chalkogenid-Dünnschichtsolarzellen”. PhD thesis. Martin-Luther-Universität Halle-Wittenberg, Dec. 2016. URL: <https://digital.bibliothek.uni-halle.de/hs/content/titleinfo/2508836>.
- [154] A. K. Srivastava and P. Sakthivel. “Quartz-crystal microbalance study for characterizing atomic oxygen in plasma ash tools”. In: *Journal of Vacuum Science & Technology A: Vacuum, Surfaces, and Films* 19.1 (Jan. 2001), pp. 97–100. DOI: 10.1116/1.1335681.
- [155] Sebastian Svanström, Alberto García Fernández, Tamara Sloboda, et al. “X-ray stability and degradation mechanism of lead halide perovskites and lead halides”. In: *Physical Chemistry Chemical Physics* (2021). DOI: 10.1039/d1cp01443a.
- [156] Akash Singh, Manoj K. Jana, and David B. Mitzi. “Reversible Crystal–Glass Transition in a Metal Halide Perovskite”. In: *Advanced Materials* (Dec. 2020), p. 2005868. DOI: 10.1002/adma.202005868.
- [157] Adhita Asma Nurunnizar and Rahmat Hidayat. “The Influence of Humid Atmosphere during the MAPbI₃ Perovskite Layer Preparation on the Characteristics of Its Solar Cells”. In: *Journal of Physics: Conference Series* 1245 (Aug. 2019), p. 012065. DOI: 10.1088/1742-6596/1245/1/012065.
- [158] Jeffrey P. Spindler, John W. Hamer, and Marina E. Kondakova. “OLED Manufacturing Equipment and Methods”. In: *Handbook of Advanced Lighting Technology*. Springer International Publishing, 2017, pp. 417–441. DOI: 10.1007/978-3-319-00176-0_26.
- [159] G. P. Nagabhushana, Radha Shivaramaiah, and Alexandra Navrotsky. “Direct calorimetric verification of thermodynamic instability of lead halide hybrid perovskites”. In: *Proceedings of the National Academy of Sciences* 113.28 (2016), pp. 7717–7721. DOI: 10.1073/pnas.1607850113.
- [160] Dmitry S. Tsvetkov, Maxim O. Mazurin, Vladimir V. Sereda, et al. “Formation Thermodynamics, Stability, and Decomposition Pathways of CsPbX₃ (X = Cl, Br, I) Photovoltaic Materials”. In: *The Journal of Physical Chemistry C* 124.7 (2020), pp. 4252–4260. DOI: 10.1021/acs.jpcc.9b11494.

- [161] Aya Osherov, Yishay Feldman, Ifat Kaplan-Ashiri, et al. “Halide Diffusion in MAPbX₃: Limits to Topotaxy for Halide Exchange in Perovskites”. In: *Chemistry of Materials* 32.10 (Apr. 2020), pp. 4223–4231. DOI: 10.1021/acs.chemmater.0c00496.
- [162] Michael Kulbak, David Cahen, and Gary Hodes. “How Important Is the Organic Part of Lead Halide Perovskite Photovoltaic Cells? Efficient CsPbBr₃ Cells”. In: *The Journal of Physical Chemistry Letters* 6.13 (July 2, 2015), pp. 2452–2456. ISSN: 1948-7185. DOI: 10.1021/acs.jpcllett.5b00968. URL: <http://dx.doi.org/10.1021/acs.jpcllett.5b00968> (visited on 06/29/2017).
- [163] Michael Kulbak, Satyajit Gupta, Nir Kedem, et al. “Cesium Enhances Long-Term Stability of Lead Bromide Perovskite-Based Solar Cells”. In: *The Journal of Physical Chemistry Letters* 7.1 (2015), pp. 167–172. DOI: 10.1021/acs.jpcllett.5b02597.
- [164] Eline M. Hutter, Rebecca J. Sutton, Sanjana Chandrashekar, et al. “Vapour-Deposited Cesium Lead Iodide Perovskites: Microsecond Charge Carrier Lifetimes and Enhanced Photovoltaic Performance”. In: *ACS Energy Letters* 2.8 (Aug. 11, 2017), pp. 1901–1908. ISSN: 2380-8195. DOI: 10.1021/acsenerylett.7b00591. URL: <https://www.ncbi.nlm.nih.gov/pmc/articles/PMC5569666/> (visited on 10/24/2017).
- [165] Constantinos C. Stoumpos, Christos D. Malliakas, John A. Peters, et al. “Crystal Growth of the Perovskite Semiconductor CsPbBr₃: A New Material for High-Energy Radiation Detection”. In: *Crystal Growth & Design* 13.7 (July 3, 2013), pp. 2722–2727. ISSN: 1528-7483. DOI: 10.1021/cg400645t. URL: <http://dx.doi.org/10.1021/cg400645t> (visited on 06/29/2017).
- [166] O. N. Yunakova, V. K. Miloslavskii, and E. N. Kovalenko. “Exciton absorption spectrum of thin CsPbI₃ and Cs₄PbI₆ films”. In: *Optics and Spectroscopy* 112.1 (2012), pp. 91–96. DOI: 10.1134/s0030400x12010249.
- [167] Marina R. Filip, Samuel Hillman, Amir Abbas Haghighirad, et al. “Band Gaps of the Lead-Free Halide Double Perovskites Cs₂BiAgCl₆ and Cs₂BiAgBr₆ from Theory and Experiment”. In: *The Journal of Physical Chemistry Letters* 7.13 (2016), pp. 2579–2585. DOI: 10.1021/acs.jpcllett.6b01041.
- [168] Cuncun Wu, Qiaohui Zhang, Yang Liu, et al. “The Dawn of Lead-Free Perovskite Solar Cell: Highly Stable Double Perovskite Cs₂AgBiBr₆ Film”. In: *Advanced Science* 5.3 (2017), p. 1700759. DOI: 10.1002/advs.201700759.
- [169] Ming Wang, Peng Zeng, Sai Bai, et al. “High-Quality Sequential-Vapor-Deposited Cs₂AgBiBr₆ Thin Films for Lead-Free Perovskite Solar Cells”. In: *Solar RRL* 2.12 (2018), p. 1800217. DOI: 10.1002/solr.201800217.
- [170] Martina Pantaler, Christian Fettikeyhauer, Hoang L. Nguyen, et al. “Deposition routes of Cs₂AgBiBr₆ double perovskites for photovoltaic applications”. In: *MRS Advances* 3.32 (2018), pp. 1819–1823. DOI: 10.1557/adv.2018.151.
- [171] Femi Igbari, Rui Wang, Zhao-Kui Wang, et al. “Composition Stoichiometry of Cs₂AgBiBr₆ Films for Highly Efficient Lead-Free Perovskite Solar Cells”. In: *Nano Letters* (2019). DOI: 10.1021/acs.nanolett.9b00238.

- [172] Christopher N. Savory, Aron Walsh, and David O. Scanlon. “Can Pb-Free Halide Double Perovskites Support High-Efficiency Solar Cells?” In: *ACS Energy Letters* 1.5 (2016), pp. 949–955. DOI: 10.1021/acsenerylett.6b00471.
- [173] Paul Pistor, Michaela Meyns, Maxim Guc, et al. “Advanced Raman spectroscopy of Cs₂AgBiBr₆ double perovskites and identification of Cs₃Bi₂Br₉ secondary phases”. In: *Scripta Materialia* 184 (July 2020), pp. 24–29. DOI: 10.1016/j.scriptamat.2020.03.040.
- [174] Emilio J. Juarez-Perez. “Comment on “Probing the Origins of Photodegradation in Organic-Inorganic Metal Halide Perovskites with Time-Resolved Mass Spectrometry”, Sustainable Energy & Fuels, 2018”. In: *ChemRxiv* (). DOI: 10.26434/chemrxiv.7295585.v2. URL: https://chemrxiv.org/articles/preprint/Comment_on_Probing_the_Origins_of_Photodegradation_in_OrganicInorganic_Metal_Halide_Perovskites_with_Time-Resolved_Mass_Spectrometry_Sustainable_Energy_Fuels_2018/7295585.
- [175] Xiaozhou Yu, Ying Qin, and Qing Peng. “Probe Decomposition of Methylammonium Lead Iodide Perovskite in N₂ and O₂ by in Situ Infrared Spectroscopy”. In: *The Journal of Physical Chemistry A* 121.6 (Feb. 2017), pp. 1169–1174. DOI: 10.1021/acs.jpca.6b12170.
- [176] Nam-Koo Kim, Young Hwan Min, Seokhwan Noh, et al. “Investigation of Thermally Induced Degradation in CH₃NH₃PbI₃ Perovskite Solar Cells using In-situ Synchrotron Radiation Analysis”. In: *Scientific Reports* 7.1 (2017). DOI: 10.1038/s41598-017-04690-w.
- [177] Teng Zhang, Xiangyue Meng, Yang Bai, et al. “Profiling the organic cation-dependent degradation of organolead halide perovskite solar cells”. In: *Journal of Materials Chemistry A* 5.3 (2017), pp. 1103–1111. DOI: 10.1039/c6ta09687e.
- [178] Tianqi Niu, Jing Lu, Ming-Chun Tang, et al. “High performance ambient-air-stable FAPbI₃ perovskite solar cells with molecule-passivated Ruddlesden-Popper/3D heterostructured film”. In: *Energy & Environmental Science* 11.12 (2018), pp. 3358–3366. DOI: 10.1039/c8ee02542h.
- [179] Yong Zhang, Seongrok Seo, Soo Yeon Lim, et al. “Achieving Reproducible and High-Efficiency (> 21%) Perovskite Solar Cells with a Presynthesized FAPbI₃ Powder”. In: *ACS Energy Letters* 5.2 (Dec. 2019), pp. 360–366. DOI: 10.1021/acsenerylett.9b02348.
- [180] Enrico Greul, Michiel L. Petrus, Andreas Binek, et al. “Highly stable, phase pure Cs₂-AgBiBr₆ double perovskite thin films for optoelectronic applications”. In: *Journal of Materials Chemistry A* 5.37 (2017), pp. 19972–19981. DOI: 10.1039/c7ta06816f.
- [181] Weiyin Gao, Chenxin Ran, Jun Xi, et al. “High-Quality Cs₂AgBiBr₆ Double Perovskite Film for Lead-Free Inverted Planar Heterojunction Solar Cells with 2.2% Efficiency”. In: *ChemPhysChem* 19.14 (2018), pp. 1696–1700. DOI: 10.1002/cphc.201800346.

- [182] Xiaoqing Yang, Yonghui Chen, Pengyun Liu, et al. “Simultaneous Power Conversion Efficiency and Stability Enhancement of Cs₂AgBiBr₆ Lead-Free Inorganic Perovskite Solar Cell through Adopting a Multifunctional Dye Interlayer”. In: *Advanced Functional Materials* 30.23 (Apr. 2020), p. 2001557. DOI: 10.1002/adfm.202001557.
- [183] Robin Kentsch, Mirko Scholz, Jonas Horn, et al. “Exciton Dynamics and Electron-Phonon Coupling Affect the Photovoltaic Performance of the Cs₂AgBiBr₆ Double Perovskite”. In: *The Journal of Physical Chemistry C* 122.45 (2018), pp. 25940–25947. DOI: 10.1021/acs.jpcc.8b09911.
- [184] Jin-Wook Lee and Nam-Gyu Park. “Chemical Approaches for Stabilizing Perovskite Solar Cells”. In: *Advanced Energy Materials* 10.1 (Nov. 2019), p. 1903249. DOI: 10.1002/aenm.201903249.
- [185] Femi Igbari, Zhao-Kui Wang, and Liang-Sheng Liao. “Progress of Lead-Free Halide Double Perovskites”. In: *Advanced Energy Materials* 9.12 (2019), p. 1803150. DOI: 10.1002/aenm.201803150.
- [186] Aleksandra Oranskaia and Udo Schwingenschlögl. “Suppressing X-Migrations and Enhancing the Phase Stability of Cubic FAPbX₃ (X = Br, I)”. In: *Advanced Energy Materials* 9.32 (July 2019), p. 1901411. DOI: 10.1002/aenm.201901411.
- [187] Giulia Longo, Suhas Mahesh, Leonardo R. V. Buizza, et al. “Understanding the Performance-Limiting Factors of Cs₂AgBiBr₆ Double-Perovskite Solar Cells”. In: *ACS Energy Letters* 5.7 (June 2020), pp. 2200–2207. DOI: 10.1021/acseenergylett.0c01020.
- [188] Hanno Krieger. *Strahlungsquellen für Technik und Medizin*. Springer Spektrum, p. 515. ISBN: 9783662558263.

Acknowledgments

I want to thank Prof. Dr. Roland Scheer for the opportunity to work in his research group and in this way allow me to create this thesis. I highly appreciated his consistent support and the many helpful discussions. In addition, I want to thank Dr. Paul Pistor for supervising my work while letting me and this thesis profit from his knowledge and for providing me with encouragement and valuable feedback. It was a joy to work with Karl Heinze on the topic of metal-halide perovskites and I hope that we benefited both in equal measure from the mutual assistance. The laboratory managers Dr. Wolfgang Fränzel and Dr. Heiko Kempa and the technicians Ulrich Fahnert and Thomas Richter saw to a well-maintained laboratory environment and Torsten Hölscher was always ready to support me with any technical issues. Leonard Wägele, Thomas Schneider, Chris Bluhm, Matthias Maiberg and all the other members of the photovoltaics research group enabled many insightful discussions, research related and otherwise, and they made my work there a very joyful and enriching experience. Björn Weber of the research group for organic chemistry helped me out with the occasional chemistry related problem. I appreciate the efforts of the teams at the fine mechanics and electronics workshops and of Dr. Bodo Fuhrmann and his team at the IZM for making a clean room available. I also want to thank my friends and family for the many enjoyable moments and the moral support over the years of my work on this thesis. Finally, I want to thank the doctorate committee and the reviewers and I hope they enjoy engaging with my work just as I did.

Eidesstattliche Erklärung

Hiermit erkläre ich an Eides statt, dass ich, Thomas Burwig, die vorliegende Arbeit *Growth and Thermal Decomposition of Metal-Halide Perovskite Thin Films Analyzed by In Situ X-Ray Diffraction* selbstständig und unter ausschließlicher Verwendung der angegebenen Literatur und Hilfsmittel erstellt habe. Alle wörtlichen oder sinngemäßen Zitate sind als solche gekennzeichnet.

Die Arbeit wurde bisher in gleicher oder ähnlicher Form keiner anderen Prüfungsbehörde vorgelegt und auch nicht veröffentlicht.

Halle (Saale), den

Thomas Burwig

Thomas Burwig

Curriculum Vitae

Education

- 02/2017– Present **Doctoral Studies (Physics)**, *Martin-Luther-Universität Halle-Wittenberg*, Halle (Saale)
- 10/2014– 01/2017 **Master of Science (Physics)**, *Martin-Luther-Universität Halle-Wittenberg*, Halle (Saale)
Final grade: 1.6
- 10/2011– 08/2014 **Bachelor of Science (Physics)**, *Martin-Luther-Universität Halle-Wittenberg*, Halle (Saale)
Final grade: 2.2
- 08/2003– 08/2011 **Abitur**, *Gymnasium Landsberg*, Landsberg
Final grade: 1.9

Work Experience

- 01/2019– Present **Software Developer**, *DENKweit GmbH*, Halle (Saale)
Assignment: Development of software for A.I. based industry applications
- 02/2018– 12/2018 **Software Developer**, *Fraunhofer CSP*, Halle (Saale)
Assignment: Development of software for A.I. based industry applications
- 02/2017– 06/2020 **Research Associate**, *Martin-Luther-Universität Halle-Wittenberg*, Halle (Saale)
Assignment: Research on perovskites for photovoltaic applications
- 10/2013– 02/2014 **Scientific Assistant**, *Martin-Luther-Universität Halle-Wittenberg*, Halle (Saale)
Assignment: Checking of weekly exercises in theoretical physics

Languages

- German Native speaker
- English Very good command in speech and writing, officially acquired CEF level: B2